University of Southampton

Faculty of Engineering, Science and Mathematics

Optoelectronics Research Centre

Bending losses in large mode area holey fibres

by

Joanne Claire Baggett

Thesis submitted for the degree of Doctor of Philosophy

30th June 2004

UNIVERSITY OF SOUTHAMPTON

ABSTRACT

FACULTY OF ENGINEERING, SCIENCE & MATHEMATICS

OPTOELECTRONICS RESEARCH CENTRE

Doctor of Philosophy

Bending losses in large mode area holey fibres

by Joanne Claire Baggett

The aims of the study presented here are to develop methods of accurately predicting bend loss in arbitrary index fibres, to use these techniques to explore the potential offered by holey fibres in the large-mode-area, single-mode regime, and to place their performance in context against conventional step-index fibres.

Large-mode-area optical fibres are required in high power and transmission applications in which low nonlinear effects and high damage thresholds are essential. For many of these applications, good beam quality is also a critical issue and, as a result, single-mode guidance is desirable. Holey fibres are an attractive route towards large-mode-area fibres due to their ability to remain *endlessly* single-mode independent of the structure scale when the holes are small. In this regime, low values of numerical aperture are an intrinsic fibre property, which has obvious merit for extreme mode areas and short wavelength applications where single-mode operation is required. However, as with any fibre, the fundamental limit on mode area for practical applications is bend loss.

At the time of this study, very little was understood about the factors that influence bend loss in a holey fibre, or how the losses compared to those of similarly sized conventional solid fibres. The novel waveguides properties of holey fibres result in bending losses that increase towards both short and long wavelengths, while the bending losses of conventional fibres increase towards long wavelengths only. Consequently, it is not obvious how these two fibre types will compare in terms of bend loss.

In the study presented here, numerical and experimental techniques have been developed that are capable of accurately evaluating the bending losses, the fundamental mode area and the modedness of holey fibres. Note that these techniques are also applicable to conventional solid fibres, which is essential in order to form accurate comparisons. These techniques are applied here to the problem of understanding the bending losses of large-mode-area holey fibres and are successfully used to assess the practical limits that bend loss imposes on large-mode-area holey fibres designed for single-mode operation. These properties are also evaluated for a range of equivalent conventional fibres, the results of which are used to benchmark the potential of holey fibre technology in this regime. The results of this study reveal that the performance of large-mode-area holey and conventional fibres at any given wavelength are similar, and that holey fibres offer advantages for broadband applications. Methods of improving bend loss in holey fibres are also investigated, and it is shown that more complex hole arrangements can be used to improve bend loss in a holey fibre.

Contents

List of Figures

List of Tables

Declaration of Authorship

I, Joanne Claire Baggett, declare that the thesis entitled *Bending losses in large mode area holey fibres* and the work presented in it is my own unless otherwise indicated. I confirm that:

- this work was done wholly or mainly while in candidature for a research degree at this University;
- no part of this thesis has perviously been submitted as part of another degree or any other qualification at this university or at any other institution;
- where I have consulted the published work of others, this is clearly attributed;
- where I have quoted from the work of others, the source is always given. With the exception of such quotations, this thesis is entirely my own work;
- I have acknowledged all main sources of help;
- where the thesis is based on work done jointly with others, I have made clear exactly what was done by others and what I have contributed myself;
- all publications containing parts of this work are listed on the following page.

Joanne Baggett

June 2004

Publications

The material in this thesis is closely based on the following publications:

Journal papers

- J. C. Baggett, T. M. Monro, K. Furusawa, D. J. Richardson, Understanding bending losses in holey optical fibers, Opt. Comm. **227** (4-6) 317-335 (2003).
- J. C. Baggett, T. M. Monro, K. Furusawa, D. J. Richardson, Comparative study of large mode holey and conventional fibers, Opt. Lett. **26** (14) 1045-1047 (2001).

Conference Papers

- J. C. Baggett, T. M. Monro, K. Furusawa, D. J. Richardson, Distinguishing transition and pure bend losses in holey fibers, CLEO'2002 Long Beach, California 19-24 May 2002 paper CMJ6.
- T. M. Monro, J. C. Baggett, K. Furusawa, D. J. Richardson, Comparative study of bend loss in large mode holey and conventional fibers, CLEO'2001 Baltimore, Maryland 6-11 May 2001 paper CTuAA1.

Other publications:

Journal papers

- M. Fuochi, J. R. Hayes, K. Furusawa, W. Belardi, J. C. Baggett, T. M. Monro, and D. J. Richardson, Polarization mode dispersion reduction in spun large mode area silica holey fibers, Opt. Express 12, 1972-1977 (2004),

  http://www.opticsexpress.org/abstract.cfm?URI=OPEX-12-9-1972
- J. C. Gates, C. W. J. Hillman, J. C. Baggett, K. Furusawa, T. M. Monro, and W. S. Brocklesby, Structure and propagation of modes of large mode area holey fibers, Opt. Express 12, 847-852 (2004),

  http://www.opticsexpress.org/abstract.cfm?URI=OPEX-12-5-847

- T. Südmeyer, F. Brunner, E. Innerhofer, R. Paschotta, K. Furusawa, J. C. Baggett, T. M. Monro, D. J. Richardson, U. Keller, Nonlinear femtosecond pulse compression at high average power levels using a large mode area holey fiber, Opt. Lett. **28** (20) 1951-1953 (2003).

- J. H. V. Price, T. M. Monro, K. Furusawa, W. Belardi, J. C. Baggett, S. Coyle, C. Netti, J. J. Baumberg, R. Paschotta, D. J. Richardson, UV generation in a pure silica holey fiber, Appl. Phys. B **77** (2/3) 291-298 (2003).

- S. Hoogland, J. J. Baumberg, S. Coyle, J. C. Baggett, M. J. Coles, H. J. Coles, Self-organized patterns and spatial solitons in liquid-crystal microcavities, Phys. Rev. A **66** 055801 (2002).

- D. A. Guilhot, J. Baggett, I. Musgrave, University of Southampton takes science into the schools, Optics and Photonics News (OSA Student Chapter) (2002).

- T. M. Monro, W. Belardi, K. Furusawa, J. C. Baggett, N. G. R. Broderick, D. J. Richardson, Sensing with microstructured optical fibers, Journal of Measurement Science and Technology, **12** (7) pp.854-8 (2001).

- J. C. Baggett, T. M. Monro, W. Belardi, K. Furusawa, D. J. Richardson, Assorted core air-clad fiber, Electron. Lett. **36** (25) pp.2065-6 (2000).

Conference Papers

- D. J. Richardson, K. Furusawa, H. Ebendorff-Heidepriem, P. Petropoulos, V. Finazzi, J. C. Baggett, W. Belardi, T. Kogure, J. H. Lee, Z. Yusoff, J. Nilsson, Y. Jeong, J. K. Sahu, T. M. Monro, Practical applications of holey optical fibers, OFC 2004 Los Angeles 22-27 Feb 2004 (Invited).

- Joanne C. Baggett, Denis A. Guilhot, Ian O. Musgrave and Errica Bricchi, The Lightwave Road Show, ETOP 2003 Tuscan 6-8 Oct. 2003 (Invited).

- T. Südmeyer, F. Brunner, J.C. Baggett, K. Furusawa, E. Innerhofer, U. Keller, T. M. Monro, R. Paschotta and D. J. Richardson, Sub-40-fs pulses with 18-W average power from a passively mode-locked thin disk Yb:YAG laser with nonlinear fiber compression, CLEO 2003 Baltimore 3-5 June 2003 paper CWM3.

- S. Coyle, S. Hoogland, J. C. Baggett, J. J. Baumberg, M. Coles and H. Coles, Pattern formation and spatial solitons in bistable liquid crystal microcavities, CLEO'2003 Baltimore 3-5 2003 June QTuG26.

- T. M. Monro, K. Furusawa, J. H. Lee, J. H. V. Price, Z. Yusoff, J. C. Baggett, D. J. Richardson, Advances in holey fibers, Photonics West 2003 San Francisco 25-31 Jan 2003 (Invited).

- T. M. Monro, V. Finazzi, J. C. Baggett, D. J. Richardson, Modelling the optical properties of microstructured optical fibers, JEE'2002 Toulouse, France 6-8 Mar 2002 (Invited).

- S. J. Hoogland, J. J. Baumberg, S. Coyle, J. Baggett and H.F. Coles, Spatial Solitons in Liquid-Crystal microcavities, Pt.2 IOP Novel Techniques for Optical Thin Films, London 14 Nov 2001.

- T. M. Monro, J. C. Baggett, W. Belardi, K. Furusawa, J. H. V. Price, D. J. Richardson, Holey fibers: Properties applications and future directions, ICTON 2001 Cracow Poland 18-21 Jun (2001).

- K. Furusawa, T. M. Monro, J. C. Baggett, P. Petropoulos, P. W. Turner, D. J. Richardson, A mode-locked ytterbium doped holey fiber laser, CLEO'2001 Baltimore 6-11 May 2001 CWC2

- J. C. Baggett, T. M. Monro, W. Belardi, K. Furusawa, D. J. Richardson, Assorted core air-clad fiber, CLEO'2001 Baltimore 6-11 May 2001 CTuAA4 (2001).

The most exciting phrase to hear in science,
the one that heralds new discoveries, is not
'Eureka!' (I found it!), but 'That's funny ...'

Isaac Asimov (1920 – 1992)

List of abbreviations

a	The core radius of a step-index fibre.
A_{eff}	The effective mode area of a fibre.
A_{eff}^{bent}	The effective mode area of the fundamental mode of the bent fibre.
A_{eff}^{FM}	The effective mode area of the fundamental mode of the straight fibre.
C_{loss}^{HOM}	The confinement loss of a higher order mode.
d	The hole diameter in a holey fibre.
ESI	Effective step-index.
FM	Fundamental mode.
FSM	Fundamental space filling mode (the fundamental cladding mode of a holey fibre).
HF	Holey fibre.
$\triangle$HF	Triangular-core holey fibre.
HOM	Higher-order mode.
MM	Multi-mode.
NA	The numerical aperture: NA = $\sqrt{{n_{core}}^2 - {n_{clad}}^2}$.
n_{air}	The refractive index of air (= 1.0).
n_{av}	The volume average refractive index of a holey fibre.
n_{clad}	The cladding index.
n_{core}	The core index.
n_{doped}	The refractive index of doped glass.
n_{eff}	The effective modal index.
n_{FM}	The effective modal index of the fundamental fibre mode.
n_{FSM}	The effective cladding index of a holey fibre.
n_{glass}	The refractive index of glass.
n^{HOMx}	The effective modal index of the x-polarised higher-order mode.
n^{HOMy}	The effective modal index of the y-polarised higher-order mode.
n_{silica}	The refractive index of silica glass.

R_c	The critical bend radius.
$\mathrm{R_c^{FM}}$	The critical bend radius of the fundamental fibre mode.
$\mathrm{R_c^{HOM}}$	The critical bend radius of a higher-order fibre mode.
R_o	The bend radius.
SM	Single-mode.
V	The V-parameter of a step-index fibre: $\mathrm{V} = 2\pi a \mathrm{NA}/\lambda$.
β	The propagation constant.
β_b	The propagation constant of the mode of the bent fibre.
β_{FSM}	The propagation constant of the FSM.
θ	The angular rotation around a bend of radius R_o.
Λ	The hole-to-hole spacing in a holey fibre.
λ	The wavelength of light.
τ	The fitting factor in the model of pure bend loss developed here.
ϕ	The angular orientation of the fibre in the bend.

Part I

Background

Chapter 1

Introduction to microstructured fibres

1.1 Introduction

Over the past 25 years, conventional optical fibres have revolutionised communications and have become vital components in many technologies, from sensing and medical imaging to high power applications, including laser welding and machining and active devices such as fibre lasers and amplifiers. In recent years, two new types of optical fibre have enlivened this well-established field, bringing with them a wide range of novel optical properties. These new fibres, known collectively as microstructured fibres, can be made entirely from one type of glass as they need not rely on dopants for guidance. Instead, the cladding region is peppered with many small holes that run the entire fibre length, creating a longitudinally uniform air/glass microstructure. Although the first microstructured fibres were fabricated in the early 1970's by Kaiser *et al.* at Bell labs [1, 2], the current burst in activity stems from the first demonstration of guidance within such structures in 1996 [3]. This explosive growth is fuelled by the many unusual and useful optical properties exhibited by these fibres, many of which are impossible to achieve using conventional methods.

Microstructured fibres are separated into two distinct categories, defined by the way in which they guide light: (1) *Holey fibres*, which guide light due to average index effects, and (2) *Photonic crystal* or *Band-gap fibres*, which guide light due to photonic band-gap effects. Typical examples of these two fibre types are shown respectively in Figs 1.1 (a) and (b). In both fibre types, the cladding is formed by an array of air holes that run the full fibre length. These air holes are typically arranged on a hexagonal lattice and the defining

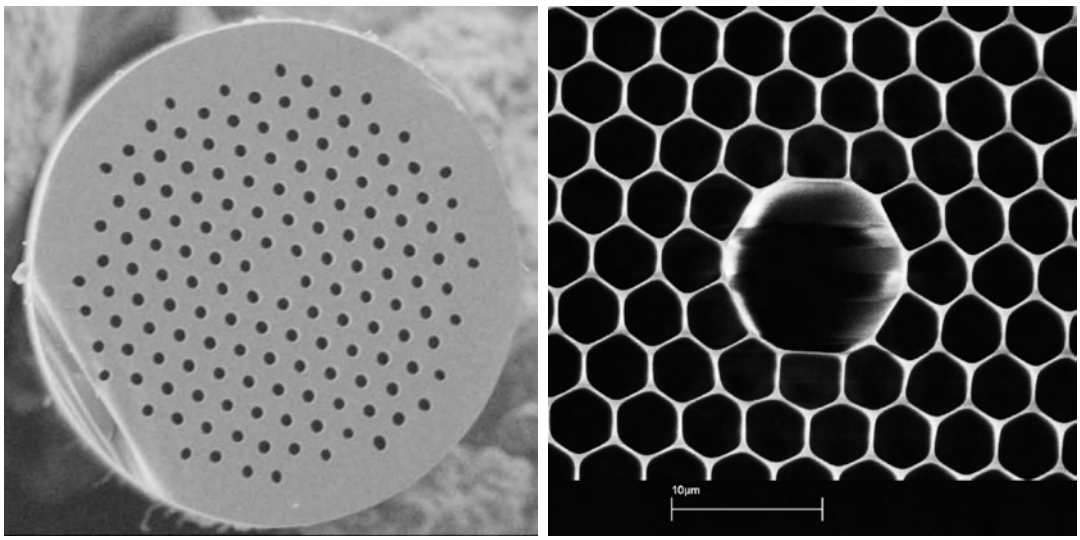

(a) (b)

Figure 1.1: (a) SEM image of a typical index guiding *Holey fibre* and (b) SEM image of a typical *Photonic band-gap fibre*. Both fibres were made at the ORC.

parameters are the hole-to-hole spacing Λ, and the hole diameter d.

In holey fibres, the air holes that define the cladding act to lower the average, or effective refractive index of this region relative to that of the solid core. As a result, light is guided within the core via a modified form of total internal reflection. Whilst this mechanism is similar to the way in which conventional step-index fibres guide light, the wavelength scale features in a holey fibre lead to a strongly wavelength dependent cladding index. This property is responsible for the host of unusual optical properties unique to holey fibres, including single-mode guidance at all wavelengths [4], which has great practical significance for broadband and short wavelength applications, in addition to a host of novel dispersive properties [5, 6, 7, 8]. Furthermore, simply by scaling the cladding geometry, single-mode holey fibres with effective mode areas ($A_{\text{eff}}^{\text{FM}}$) ranging from approximately 1.5 to 600 μm^2 at 1550 nm can be created [9, 10]. Such small values of $A_{\text{eff}}^{\text{FM}}$ have enormous potential for highly nonlinear applications, whilst large-mode-area fibres are essential for applications involving high optical powers.

In contrast to holey fibres, in which the mechanisms responsible for guidance share similarities with conventional fibres, photonic band-gap fibres represent a fundamentally different class of waveguide. In a photonic band-gap fibre, the cladding air holes are arranged in a perfectly periodic fashion. For certain geometries the cladding can form a two-dimensional photonic crystal with band-gaps at well defined optical frequencies [11]. Wavelengths within

the band-gap cannot propagate in the cladding region and are thus confined to the core of the fibre. The most attractive property of this fibre type arises from the fact that the core need not be defined by a high index region, as is necessary in an index-guiding fibre. Instead, the fibre core can be created by a low-index defect, and via careful design of the cladding can result in a fibre in which light is guided within a hollow air-core [12]. Such waveguides offer potentially lower values of loss and nonlinearity than is possible in conventional solid core waveguides, which has obvious advantages for long-haul transmission and high power applications.

Note that holey fibres are often referred to as *photonic crystal* fibres within the literature. However, the average index effects responsible for guidance in holey fibres do not rely on any periodicity within the air hole lattice [13]. Consequently, here the term *photonic crystal* is reserved for band-gap fibres, in which periodicity is essential to the guidance mechanism.

In the following sections of this chapter, these two classes of microstructured fibre are discussed in more detail. Holey fibres are considered within Section 1.2, in which the unique modal properties and flexible fabrication techniques that give rise to a wide range of novel fibre designs and optical properties are discussed. A summary of the numerical techniques used to model the modal properties of holey fibres is presented in Section 1.4. The second class of microstructured fibre, the photonic band-gap fibre, is discussed in Section 1.3. However, please note that band-gap fibres are only discussed briefly and are not considered in any detail in the work presented in this thesis.

1.2 Holey fibres

1.2.1 Introduction

The wide range of novel optical properties that can be realised using holey fibre technology are possible as a result of two main factors: (1) the wavelength scale air-holes that define the cladding result in an average, or *effective* cladding index that is strongly dependent on both the wavelength of light and the geometry of the cladding; (2) the typical methods of holey fibre fabrication are extremely flexible and thus permit a wide range of fibre geometries to be created.

In the following section, the way in which these two factors combine to enable a whole host of novel optical properties, many of which are impossible to achieve in conventional fibres, is discussed. The novel cladding index of a holey fibre is explored in Section 1.2.2,

and the directly related phenomenon of endlessly single-mode guidance is illustrated in Section 1.2.3 via analogy with step-index fibres. In Section 1.2.4, the basic holey fibre fabrication techniques are outlined, which facilitates the following description of the wide range of fibre types and associated modal properties that can be engineered, as presented in Sections 1.2.5, 1.2.6 and 1.2.7.

1.2.2 The effective cladding index

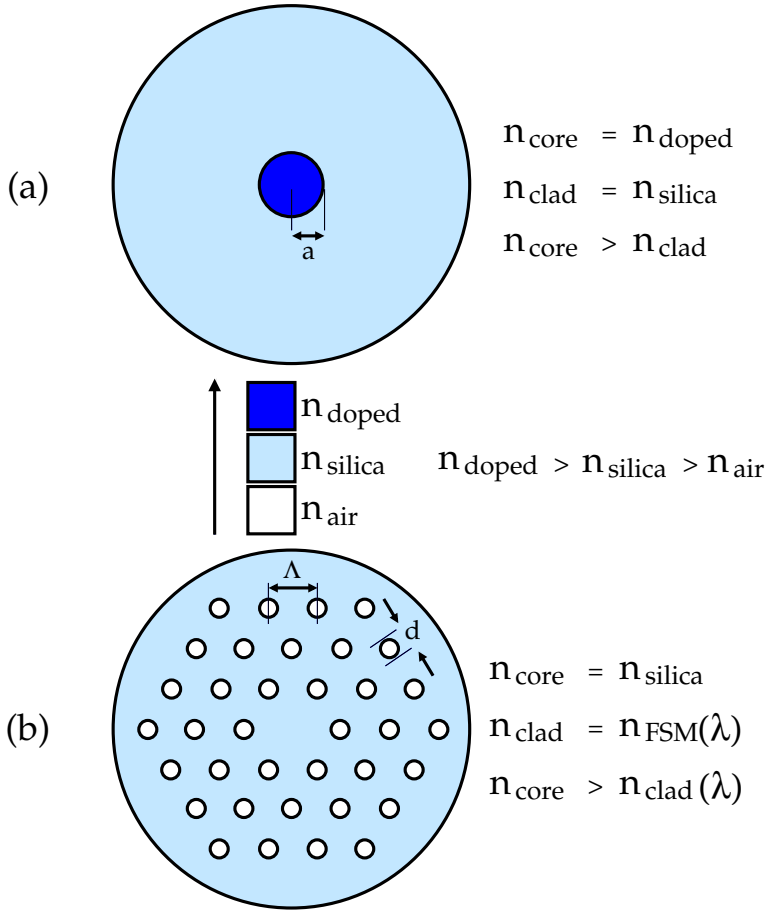

Figure 1.2: Sketch of an idealised transverse refractive index profile for (a) a typical conventional step-index fibre and (b) a typical holey fibre. Here, n_{silica} is the refractive index of silica glass, n_{doped} represents the raised refractive index of a doped silica glass and n_{air} is the refractive index of air. n_{FSM} is the effective refractive index of the holey fibre cladding, which is also known as the effective index of the fundamental space filling mode (FSM) of the cladding.

Fig. 1.2 shows schematic representations of an idealised transverse refractive index profile for (a) a typical conventional step-index fibre and (b) a typical holey fibre. A typical conventional step-index fibre, as shown in Fig. 1.2 (a), consists of two uniform solid layers of silica glass; an inner core with a refractive index of n_{core}, surrounded by an outer

cladding layer with a refractive index of n_{clad}. Light is guided in the fibre core via total internal reflection if the condition $n_{core} > n_{clad}$ is satisfied. Typically, the refractive index of the core is raised by doping the glass in this region with elements such as germanium or phosphorous. However, the condition $n_{core} > n_{clad}$ can also be satisfied by doping the cladding glass with elements such as boron and fluorine, which act to lower the refractive index of silica.

A typical holey fibre, as shown in Fig. 1.2 (b) is made entirely from pure silica and the cladding region is defined by an array of air holes arranged in a triangular lattice. The omission of one central air hole within this array forms the solid fibre core. The defining parameters of a holey fibre are the hole-to-hole spacing, Λ, and the hole size, d. The air holes in the cladding act to lower the average, or *effective* refractive index of this region (n_{FSM}) relative to that of the solid core (n_{silica}) and light is thus guided in the solid core via a modified version of total internal reflection since ($n_{core} \equiv n_{silica}$) > ($n_{clad} \equiv n_{FSM}$). Note that this mechanism does not rely on any periodicity of the air hole lattice and light is guided even for a completely random hole distribution [13]. However, the cladding of a holey fibre usually possesses a periodic geometry due to the typical method of fabrication, as discussed in Section 1.2.4.

Due to the fact that the hole size and spacing in a holey fibre are both similar in scale to the wavelength of light (Λ is typically of the order of 1 to 20 μm, and d is typically of the order of 0.5 to 10 μm), the effective cladding index is strongly wavelength dependent. The effective cladding index of a holey fibre, n_{FSM}, is defined as the effective modal index of the lowest-order cladding mode, which is often referred to as the fundamental space filling mode (FSM) [14, 15], and can be evaluated by considering an infinite periodic structure with the parameters of the cladding. As such, n_{FSM} is determined by the spatial distribution of the FSM, which becomes more confined to the silica regions as the wavelength decreases, resulting in an effective cladding index that increases towards short wavelengths. One way of evaluating n_{FSM} is to solve the wave equation using periodic boundary conditions for a single hexagonal unit cell that is centred on an air hole, as shown in the inset in Fig. 1.3. By approximating the hexagonal boundary by a circular one of radius $\Lambda/2$ (indicated by the dashed line inside the hexagonal until cell in Fig. 1.3), this problem can be vastly simplified, enabling a general circular symmetric mode solution [4, 15, 16]. The effective index of the lowest-order mode of this annular region of silica thus represents an approximate form of n_{FSM} of the (infinite) holey fibre cladding. Both scalar and vector versions of this approach

have been developed [15, 16], the latter of which returns values of n_{FSM} that are in agreement with values calculated using a more rigourous numerical model to 2-3 significant figures for a range of fibre structures and wavelengths (see Sections 1.4 and 3.5.1 for more details on the numerical techniques commonly used to evaluate n_{FSM}).

Calculated values of n_{FSM} for a holey fibre with $\Lambda = 7.5$ μm are plotted in Fig. 1.3 as a function of Λ/λ, for a range of d/Λ as indicated on the figure. These values of n_{FSM} are calculated for each fibre as a function of wavelength using the vector approach of the circular unit cell method described above [15]. The dashed line in Fig. 1.3 indicates the (constant) refractive index of silica used in these calculations (1.444). A constant value of refractive index is used here for simplicity, which enables results calculated for a single structure to be scaled with wavelength (if the refractive index is a constant value at all wavelengths, Maxwell's equations become scale invariant). This assumption is approximate, since the refractive index of silica is wavelength dependent (see appendix C). However, the refractive index of silica is a weak function of wavelength, varying by approximately 3% in the wavelength range $300 - 1600$ nm and this approximation is often successfully used when evaluating holey fibre properties [4, 16, 17]. This figure shows that the effective index of a holey fibre cladding increases towards short wavelengths, and that in the short wavelength extreme, n_{FSM} tends towards the refractive index of silica itself. In addition, it can also be seen from Fig. 1.3 that the overall value of n_{FSM} increases as the relative hole size (d/Λ) decreases. This results from the fact that the fraction of the modal field in the air depends on the relative size of the wavelength of light and the cladding parameters, d and Λ. As the cladding features become smaller with respect to the wavelength of light, the modal field can penetrate further into each air hole, thus lowering the effective index of the mode. Although not indicated by Fig. 1.3, in the long wavelength extreme, n_{FSM} tends to an asymptotic value close to the volume average refractive index.

1.2.3 Endlessly single-mode guidance

The wavelength dependence of the effective cladding index is the fundamental difference between holey and conventional fibres, in which the cladding index is typically only weakly dependent on wavelength, and it is this property that is responsible for the many novel optical properties exhibited by holey fibres. The most notable of these unusual properties is the ability of a holey fibre to guide a single-mode at all wavelengths, a phenomenon known as endlessly single-mode guidance, which is explained here via analogy with step-

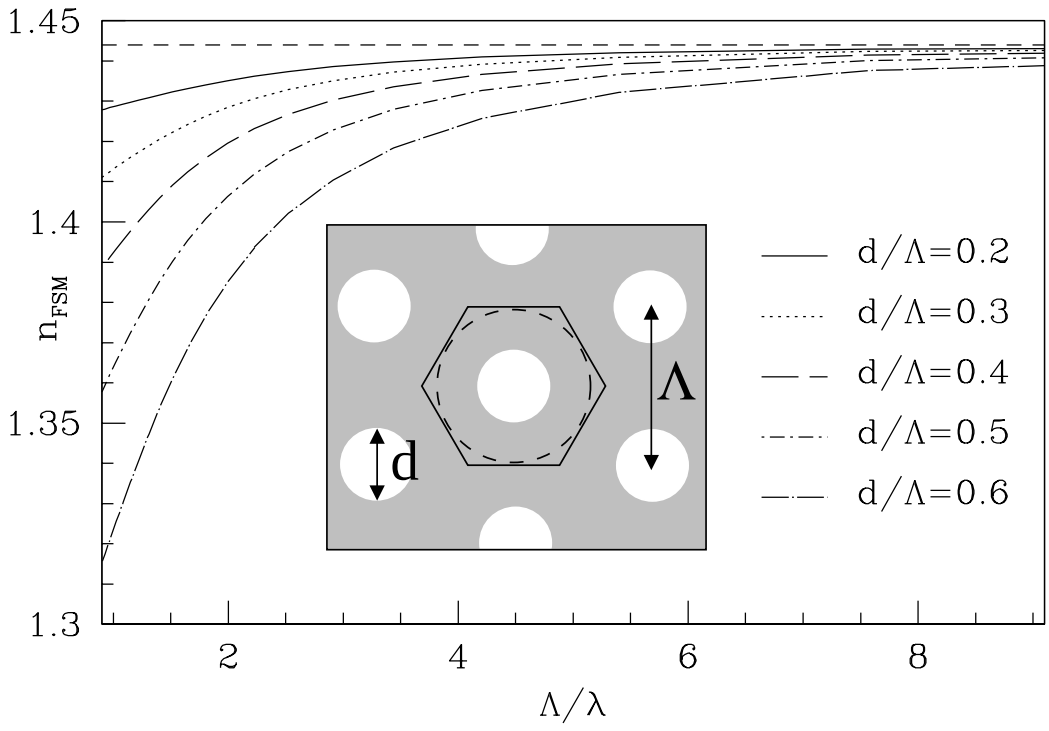

Figure 1.3: The effective modal index of the fundamental space filling mode (FSM) of a holey fibre with $\Lambda = 7.5$ μm for several different values of d/Λ (as indicated on the figure) as a function of Λ/λ, calculated using the method from Ref. [15]. The refractive index of silica is assumed to be constant in this case, with a value of 1.444 and is indicated on the figure by the dashed line.

index fibres.

Although the modal properties of holey fibres and step-index fibres are very different spectrally, the modal properties of a holey fibre can, to first approximation, be evaluated by considering an *equivalent* step-index (ESI) fibre at any given wavelength [4], as discussed in Section 1.4.2. An ESI profile is typically determined by replacing the holey cladding with a uniform material that possesses the same effective refractive index ($n_{clad} \equiv n_{FSM}$) and approximating the holey fibre core by a circular region of pure silica. Due to the fact that no clearly defined boundary between core and cladding region exists in a holey fibre, the core diameter of an ESI fibre must be chosen arbitrarily. In most cases, the core radius is defined to be 0.625Λ, which is found empirically via comparison with results obtained using a more rigourous plane-wave technique [18]. Unfortunately, this choice is only valid over a fairly limited range of fibre parameters and wavelengths, and as such cannot be used to accurately model the modal properties of holey fibres. However, this simple ESI approach can be used to provide useful insight into holey fibre operation. Indeed, in order to gain an understanding of the basic modal properties of a holey fibre, the effective index approach is

ideal as it enables these novel fibres to be evaluated using familiar terminology. Here, this ESI approach is used to explain endlessly single-mode guidance.

The number of modes supported by a conventional fibre is related to the V-parameter, which is defined as

$$\mathrm{V} = \frac{2\pi a}{\lambda}\mathrm{NA}, \tag{1.1}$$

where a is the core radius and the numerical aperture, NA= $\sqrt{{\mathrm{n_{core}}}^2 - {\mathrm{n_{clad}}}^2}$. A step-index fibre is single-mode for V < 2.405. In a conventional fibre, both $\mathrm{n_{core}}$ and$\mathrm{n_{clad}}$ depend only weakly on wavelength, and so the V-parameter, and hence the number of modes, increases rapidly towards short wavelengths. However, in a holey fibre, the cladding index is strongly wavelength dependent and acts to lower the NA towards short wavelengths. This functionality balances the wavelength dependence of the V-parameter, resulting in a nearly constant value of V over a large wavelength range. Indeed, if the cladding holes are small enough, the NA can be low enough at all wavelengths to result in *endlessly* single-mode guidance. This phenomenon is illustrated in Fig. 1.4, in which the effective V-parameter (V_{eff}) is plotted for holey fibres with $\Lambda = 7.5$ μm and increasing values of d/Λ. These values of (V_{eff}) are calculated using the values of $\mathrm{n_{FSM}}$ plotted in Fig. 1.3 and assume a core radius of $= 0.625\Lambda$ in the ESI fibre (as previously discussed) [18]. The dashed line in Fig. 1.3 indicates the V=2.405 single-mode cut-off. Fig. 1.4 clearly shows how the effective V-parameter rises to a constant value as the wavelength decreases in a holey fibre. Furthermore, it can be seen that when the holes are small enough, the V-parameter stays below 2.405 at all wavelengths, resulting in a fibre that is endlessly single-mode [4]. Note that the effective index approach used here (incorrectly) predicts that the endlessly single-mode condition occurs for $d/\Lambda \lesssim 0.36$. Note that more accurate numerical techniques predict that this condition occurs for $d/\Lambda \lesssim 0.40$ for n=1.444 [19].

The property of endlessly single-mode guidance is one of the many novel properties exhibited by holey fibres. However, to explain these properties in detail it is useful to first give an outline of the basic holey fibre fabrication techniques, as presented in Section 1.2.4. A basic understanding of these techniques facilitates the description of the many and varied holey fibre structures and associated modal properties reported to date, as discussed in Sections 1.2.5, 1.2.6 and 1.2.7.

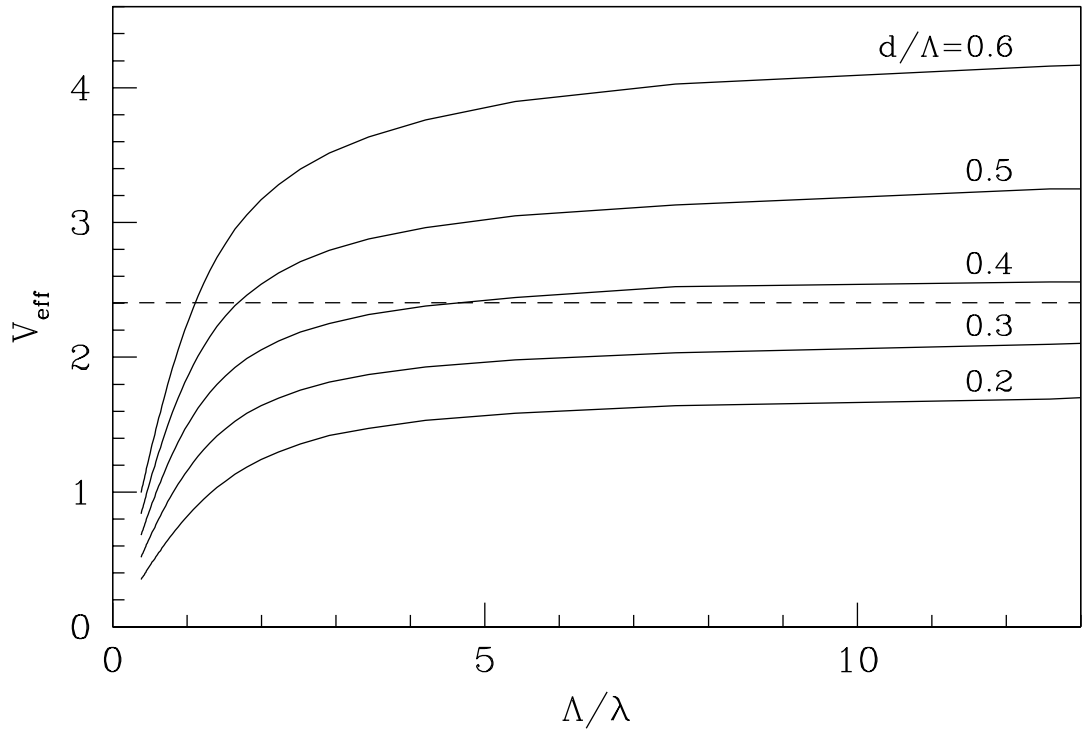

Figure 1.4: The effective V-parameter (V_{eff}) for holey fibres with $\Lambda = 7.5$ μm and $d/\Lambda = 0.2$, 0.3, 0.4, 0.5 and 0.6, plotted as a function of Λ/λ. The dashed line indicates the single-mode cut-off point given by $V_{\text{eff}} = 2.405$. The effective V-parameter is calculated using the values of n_{FSM} obtained from the method in Ref. [15], and the refractive index of silica is assumed to be constant, with a value of 1.444.

1.2.4 Fabrication

Holey fibres are typically fabricated by heating and pulling a preform into fibre using a conventional fibre drawing tower. The fibre preform is typically constructed by stacking many silica capillaries around a central, solid silica rod. In a typical holey fibre, all the capillaries in the preform share the same dimensions and the central solid rod is of equal diameter. In the final fibre, the central solid rod forms the core, and the surrounding glass capillaries form the microstructured cladding. An idealised sketch of a typical holey fibre preform and final fibre are shown in Fig. 1.5 (a) and (b) respectively. Note that small silica rods are often used to fill in the gaps around the outside of the capillary stack to prevent large air holes forming in this region in the final fibre.

The parameters of the final fibre depend both on the dimensions of the stacking elements used in the preform and on the specific drawing conditions. The hole-to-hole spacing, Λ, can be controlled during manufacture via the outer diameter of the final fibre, while the hole size depends on many factors during fabrication. For example, if the ends of each capillary

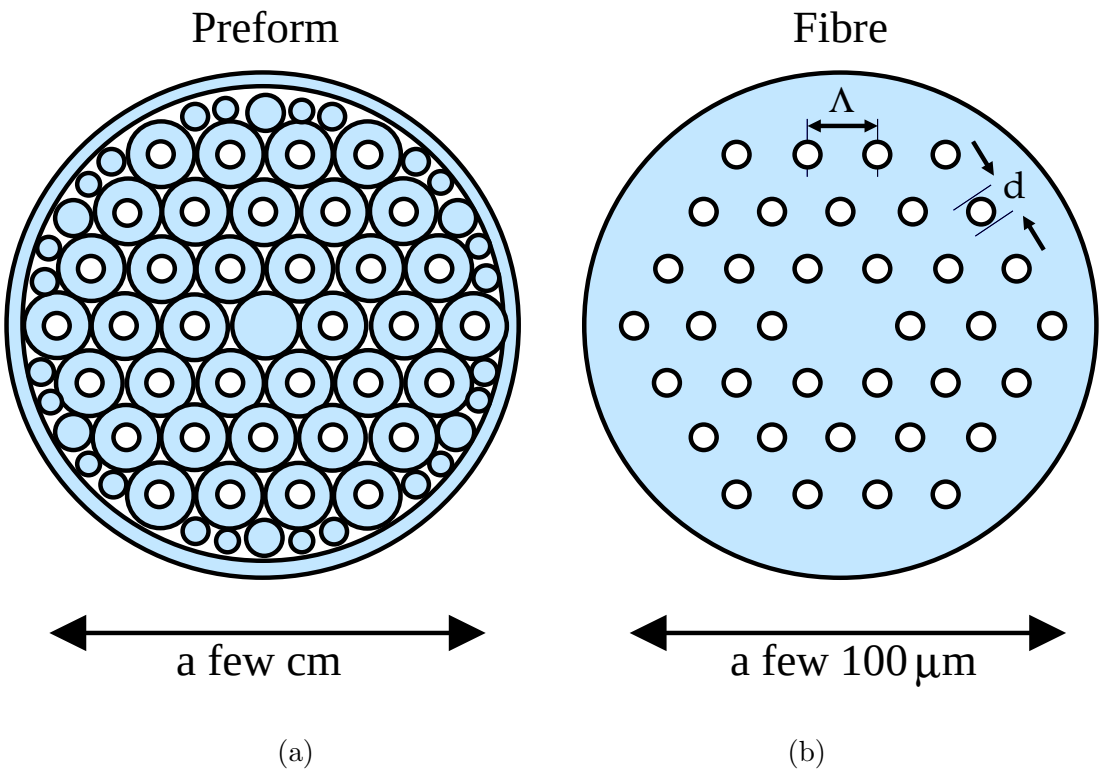

Figure 1.5: Idealised sketches of (a) a typical holey fibre preform and (b) the final holey fibre

in the preform are not sealed, the relative size of the air holes in the final fibre can be made to be much smaller than those in the original preform by taking advantage of the fact that surface tension effects act to collapse the capillaries as the fibre is drawn. However, this can result in a run-away process that completely closes the air holes, resulting in a useless fibre (note that this is especially true when small air holes are present, as in large-mode-area holey fibres). To prevent this, the top of each capillary in the preform is often sealed. As the air within the preform heats and expands, a pressure differential is obtained between the air inside and outside the fibre, which counterbalances surface tension effects. As the fibre is drawn, the volume of air remaining in the preform typically becomes less than that inside the pulled fibre. This causes the pressure differential to decrease as the fibre is drawn, resulting in smaller holes towards the end of the pull. By adjusting drawing conditions, such as the pull/feed speed, the change in the pressure differential can be compensated for to some extent. In this way, holey fibres with uniform cladding geometries can be reliably fabricated in lengths of a few hundred metres. Conversely, the hole size can be radically altered during the fabrication process by changing the drawing conditions, allowing many different fibre structures to be created from the one preform. However, for a specific fibre design it is generally considered best practice to start with capillary dimensions in the

preform that, when scaled down, best match the target fibre parameters.

The finite extent of the cladding region in a holey fibre results in an intrinsically leaky structure due to the fact that the core index is the same as that of the surrounding glass (Note that this is discussed in more detail in Sections 1.2.5, 5.4 and 7.3). Consequently, no true bound modes exist and only leaky modes are guided, each of which has an associated confinement loss. However, these losses can be reduced to negligible values if a sufficient number of rings of holes are used. Typically, six to seven rings of holes are required to achieve negligible confinement losses in the fundamental mode of the fibre, which corresponds to around 130 to 170 stacking elements respectively. Other propagation losses in the final fibre result from the Rayleigh scattering and infrared absorption intrinsic to the glass used to make the fibre. For silica glass these losses can be as low as 0.14 dB/km [20]. However, the propagation losses of early holey fibres were typically a few dB/km and result from imperfections, such as scratches or surface roughness in the stacking elements used to construct the preform, and also from OH contamination. In order to minimise these sources of propagation loss, the stacking elements are usually made from high quality silica with a low OH content (The fibres considered in detail within this thesis are made from F300 synthetic silica glass from Heraeus Tenevo AG), and are carefully polished, cleaned and dehydrated to ensure smooth, contamination free surfaces in the preform. The lowest propagation losses reported in a holey fibre to date are ≈ 0.28 dB/km at 1550 nm [21], which compare favourably with the propagation losses of conventional step-index single-mode fibre (losses of Corning SMF-28 are ≈ 0.2 dB/km at 1500 nm).

To date, most work on holey fibres has focussed solely on silica glass. However, holey fibres have also been made from non-silica glasses, such as tellurite and chalcogenide glasses, which offer optical properties not available in silica, such as mid-IR transmission and high values of refractive index and non-linearity [22, 23, 24, 25, 26]. These so called soft-glasses possess lower melting points than silica glass and can, as a result, be extruded to form a preform in one step. This not only simplifies fabrication, but also enables the fabrication of small-core holey fibres with high air filling fractions that are ideally suited for exploring nonlinear effects. An example of this fibre type is shown in Fig. 1.6 (c) and is discussed in detail in the following section.

The fabrication techniques described here have great flexibility and allow many different types of holey fibre to be created by varying the type of elements used to construct the preform and by varying the structure scale of the final fibre. A selection of holey fibres

made at the ORC are shown in Fig. 1.6, which serves to illustrate the many different holey fibre types that can be fabricated using the techniques described above. These fibres are described briefly in the figure caption and are also used to illustrate the numerous optical properties exhibited by the wide range of holey fibres in the following sections. This description is divided into three categories: (1) Large-core holey fibres, (2) Small-core holey fibres and (3) Non-silica holey fibres.

1.2.5 (1) Large core holey fibres

Large-mode-area single-mode holey fibres

The flexibility of holey fibre fabrication techniques can be used to create extremely large-mode-areas, simply by creating fibres with large values of Λ. Such holey fibres can also be fabricated with very small and very large values of NA, depending on the relative hole size. Large-mode-area holey fibres with relatively small air holes can be endlessly single-mode, which has obvious advantages for broadband applications, but also offers a unique way of creating large-mode-area, single-mode fibres [30]. Large-mode-area fibres are required in high power applications, for both passive and active devices, where the large mode size is used to minimise nonlinear effects and increase the maximum power level that can be tolerated without incurring damage. For many of these applications, good beam quality and hence single-mode operation is also an essential requirement. In large-mode-area step-index fibres, the single-mode condition ($V<2.405$) is met by lowering the dopant concentration in the core or cladding glass as the core size is increased (recall that $V=f2\pi a\mathrm{NA}/\lambda$). The largest mode area reported in a single-mode conventional fibre to date is $\approx 400\ \mu\mathrm{m}^2$ at 1550 nm [31]. In a holey fibre, the condition for endlessly single-mode guidance is defined by $d/\Lambda \lesssim 0.40$, and is independent of the absolute value of Λ or λ. Since Λ defines the core size, and hence the mode area, these novel fibres seemingly offer a simple route towards unlimited mode-areas in the single-mode regime.

However, light guided in any waveguide is subject to bending losses, which, in general, increase with mode size and decreasing NA and thus represent the fundamental limiting factor on practical mode areas. In both conventional and holey fibres, the bending losses increase towards long wavelengths as the modal field extends further into the cladding, resulting in a larger and more weakly guided mode that is more susceptible to bend induced loss. However, in holey fibres, bending losses also increase towards short wavelengths as a direct consequence of their novel cladding structure [4]. The additional short wavelength

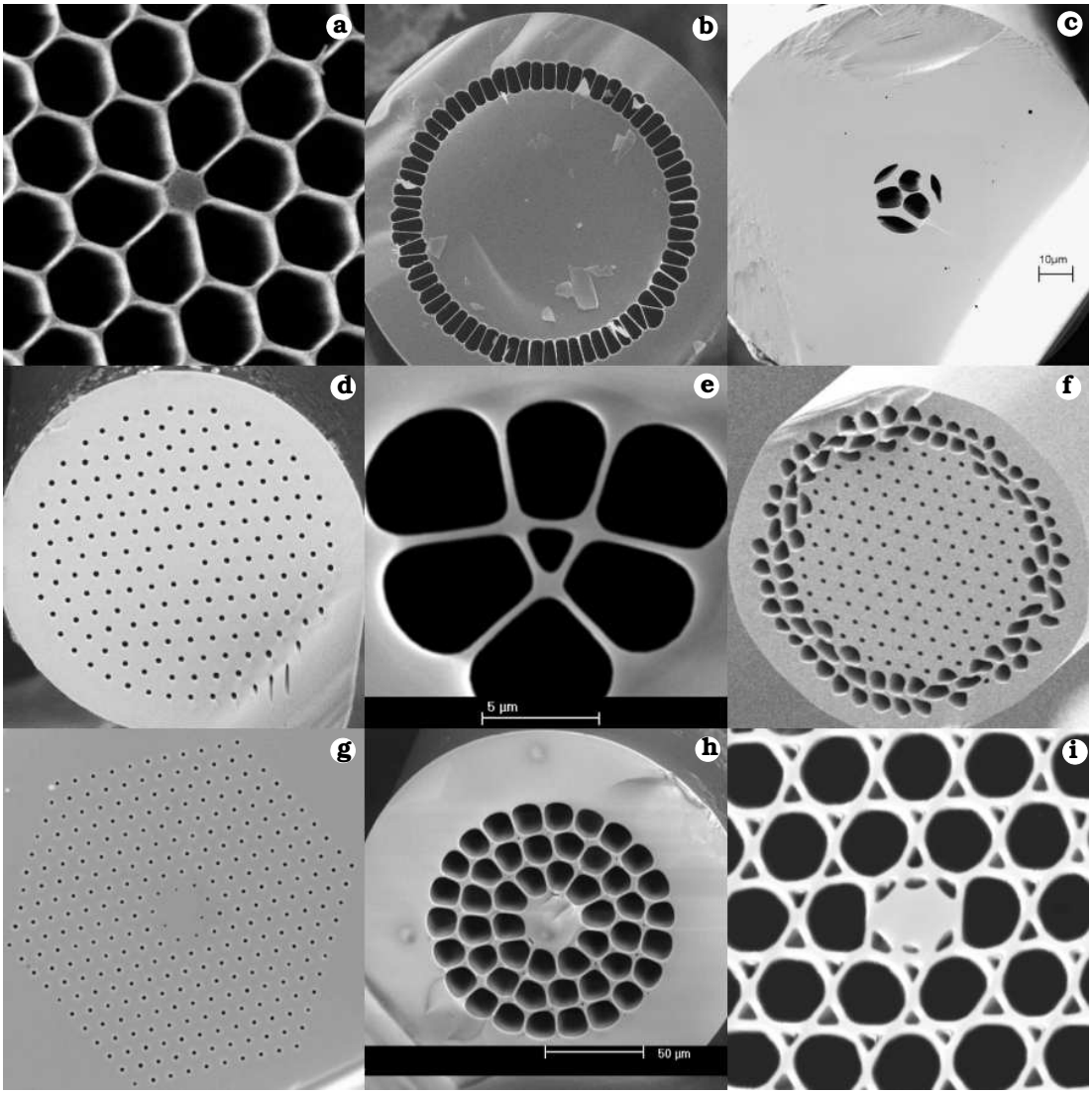

Figure 1.6: A selection of holey fibres made at the ORC: (a) a pure silica, small-core holey fibre with a core diameter of ≈ 1.2 μm and $d/\Lambda \approx 0.95$; (b) a pure silica, highly multi-mode, large-core holey fibre with a core diameter of ≈ 200 μm; (c) a small-core, non-silica holey fibre from Refs [23, 24], in which the core (diameter ≈ 2 μm) is suspended by three 2 μm-long supports that are less than 400 nm thick; (d) a pure silica, large-mode-area, endlessly single-mode holey fibre with $\Lambda \approx 11$ μm, $d/\Lambda \approx 0.24$. Note that the core is formed by one solid rod in the preform; (e) a pure silica holey fibre with three similarly sized small cores (diameter ≈ 1 μm), that are suspended by 2 μm long supports that are ≈ 200 nm thick; (f) a double-clad Ytterbium doped holey fibre from Ref. [27]. The inner cladding is defined by the small, periodically arranged air holes ($\Lambda \approx 10$ μm, $d/\Lambda = 0.3$) and the outer cladding is defined by the double layer of large air holes; (g) a pure silica, large-mode-area holey fibre with a triangular core that is formed by using three adjacent rods in the preform. Fibre parameters: $\Lambda \approx 11$ μm, $d/\Lambda \approx 0.2$; (h) a hybrid holey fibre from Ref. [28], which is a Ytterbium doped, cladding-pumped fibre laser with a conventional step-index central region (inner cladding diameter is 28 μm) and a holey outer cladding; (i) a small-core, highly birefringent silica holey fibre laser with an elliptically shaped, Ytterbium doped core that is 2.6×1.5 μm in size [29].

bend loss edge exhibited by holey fibres results directly from the fact that the NA falls as the wavelength decreases. As such, the bending losses of holey fibres not only define the bandwidth of useful operation for a given fibre, but also define the upper limit on practical mode size for a given wavelength. It has been shown empirically that the mid-point in wavelength between the long and short bend loss edges in holey fibres is approximately given by $\Lambda/2$ [32]. For large-mode-area holey fibres, in which $5\,\mu\text{m} < \Lambda < 25\,\mu\text{m}$, all wavelengths of light that are transparent in silica ($\approx 0.3 - 2\ \mu$m, see Section C.2 for more details) lie on the short-wavelength side of this mid-point. As such, the bending losses of large-mode-area silica holey fibres are expected to decrease with wavelength, for all wavelengths of interest, and the maximum permissible mode area for single-mode operation will thus increase with wavelength. Note that the maximum permissible mode size for this fibre type is explored in Chapter 5 and 7 of this thesis, and that more details on bend loss in holey fibres can be found in Section 2.3.

An example of a large-mode-area single-mode holey fibre is shown in Fig. 1.6 (d). Such fibres are typically fabricated using a one-step stack-and-draw capillary approach as described in Section 1.2.4, in which one solid rod is used in the preform to form the core and typical fibre parameters are $5\,\mu\text{m} < \Lambda < 25\,\mu\text{m}$ and $0.2 < d/\Lambda < 0.5$. The largest mode area in a single-mode holey fibre with practical bending losses reported to date is $\text{A}_{\text{eff}}^{\text{FM}} = 600\,\mu\text{m}^2$ at 1550 nm [10]. As mentioned above, large mode areas are required to minimise nonlinear effects for transmission and high power applications. The effective fibre nonlinearity is defined as $\gamma = 2\pi n_2/\lambda \text{A}_{\text{eff}}^{\text{FM}}$, where n_2 is the nonlinear index coefficient. The typical value of n_2 for silica is $2.6{\times}10^{-20}\text{m}^2\text{W}^{-1}$. In conventional single-mode step-index fibre (Corning SMF-28), this equates to $\gamma \approx 1\ \text{W}^{-1}\text{km}^{-1}$. In contrast, the holey fibre with $\text{A}_{\text{eff}}^{\text{FM}} = 600\,\mu\text{m}^2$ at 1550 nm has an effective nonlinearity of $\approx 0.16\ \text{W}^{-1}\text{km}^{-1}$ [10], which is almost an order of magnitude less than that of a conventional step-index fibre.

Note that although the condition for endlessly single-mode guidance is defined for $d/\Lambda \lesssim 0.4$, in practice, broadband single-mode guidance can be observed in large-mode-area fibres with values of d/Λ up to ≈ 0.5 (see Sections 5.3 and 5.4 and 7.3). This arises from the fact that all modes of a holey fibre are leaky. In practice, the extent of the cladding region in any holey fibre is finite and results in an intrinsically leaky structure due to the fact that the core index is the same as that of the surrounding glass. In such a fibre no true bound modes exist and only leaky modes are guided, each of which has an associated confinement loss. The confinement losses are related to the size, spacing and number of

rings of holes in a fibre. For large-mode-area, single-mode fibres, the confinement losses of the fundamental mode can be reduced to negligible values by using at least 5-7 rings of holes in the fibre[1]. However, the confinement losses of the higher-order modes are greater than those of the fundamental. If a fibre is close to cut-off, the confinement losses of the higher-order modes can be great enough to ensure that these modes are only observed in a few cm of fibre. In this way, only the fundamental mode is observed for significant lengths of fibre, and the fibre is defined as *effectively* single-mode. This is explored in detail in Sections 5.3 and 5.4 and 7.3.

Large-mode-area multi-mode holey fibres

In addition to offering an attractive route towards single-mode fibres, holey fibre technology also offers a simple way of creating fibres with large numerical apertures by taking advantage of the large index contrast between air and glass. For example, by using large values of Λ and values of $d/\Lambda \gg 0.5$, multi-mode fibres with large-mode-areas can be created. This route has advantages over conventional techniques, in which large dopant concentrations are required in order to create large values of NA (since large dopant concentrations may reduce the power handling capabilities of the fibre). This type of fibre has applications in high power delivery where beam quality is not a critical issue. However, note that even for large values of d/Λ, a holey fibre will support only a finite number of modes towards short wavelengths due to the fact that the effective V-parameter remains constant over a large wavelength range, as shown in Figure 1.4. In addition, highly multi-mode large-core fibres can also be fabricated by creating a preform from one large solid rod that is surrounded by many thin-walled capillaries. When pulled to fibre, this type of preform creates an all silica, high NA fibre like the one shown in Fig. 1.6 (b), which has a core diameter of ≈ 200 μm. Such fibres have applications in extremely high power transmission where beam quality is not an issue, and in 'light pipes' for endoscopy applications.

Multiple-rod holey fibres

The fabrication techniques described in Section 1.2.4 can be easily extended to produce multiple core structures by replacing cladding capillaries in the preform with solid rods [33]. This has advantages over the conventional techniques used to produce multiple core fibres,

[1]For example, in a typical large-mode-area holey fibre with $\Lambda = 12.0$ μm and $d/\Lambda = 0.4$, the confinement losses of the fundamental mode fall from ≈ 0.7 dB/m to $\approx 5 \times 10^{-8}$ dB/m as the number of rings is increased from 2 to 5 at 1064 nm.

which involve drilling or fusing standard single core preforms together. In contrast to these conventional methods, a multiple core holey fibre can be made in a simple one-step process to a standard outer diameter, with each core accurately identifiable along the entire length of fibre. This multiple-rod approach can also be used to create large-mode-area holey fibres by using three, as shown in Fig. 1.6 (g), or even seven adjacent rods in the preform [34, 35, 36, 37]. Using seven adjacent rods in the preform to create the fibre core, an effective area of $\approx 1000\ \mu\text{m}^2$ has been fabricated [37], which represents the largest mode area reported in a single-mode fibre to date. However, the bending losses of this fibre, which would determine its practicality, have not been reported. This multiple-rod approach to large core fibres is explored in Chapter 6.

Active holey fibres

Although holey fibres are typically made from a single material and do not rely on dopants for guidance, doped regions can be incorporated simply by using stacking elements made from doped glass to create active fibre devices [38]. For example in Fig. 1.6 (i), an Ytterbium doped rod extracted from a conventional doped fibre preform was used to create an active, small-core holey fibre, in which mode-locked lasing was demonstrated [29]. Another advantage of the holey fibre fabrication technique is that it is simple to create different hole sizes within the cladding by using different sized capillaries in the preform. This method can be used to create double-clad holey fibre lasers, in which a secondary, high air-filling fraction cladding is created using large, thin walled capillaries in the preform [27, 39, 35, 36]. An example of this fibre type is shown in Fig. 1.6 (f) [27], in which the inner cladding is defined by the small, periodically arranged air holes ($\Lambda \approx 10\ \mu$m, $d/\Lambda = 0.3$) and the outer cladding is defined by the double layer of large air holes. Due to the high refractive index contrast between air and silica, this technique can be used to create high NAs in the inner cladding region, allowing a greater acceptance angle for the typically highly multi-mode pump light. Indeed, using this approach, NAs as high as 0.8 have been reported [39]. The main drawback to this double-clad approach in a holey fibre is that the secondary cladding with a high air-fill fraction can act as a thermal insulation layer, interrupting heat dissipation from the inner cladding to the outside of the fibre. Numerical work using a finite-element technique to model heat flow in a double-clad holey fibre has shown that this problem can be minimised by increasing the number and the width of the silica bridges that connect the inner cladding to the outer portion of the fibre and have shown that by careful

design, the temperature profile can be comparable to that of a conventional double-clad fibre. [36]. Indeed, a cladding-pumped holey fibre laser in which three adjacent (doped) rods form the core has been used to demonstrate a single-mode power output of 260 W with 73% efficiency without any thermo-optical problems, reduction in beam quality or degradation of the fibre coating [36]. This power level corresponds to a power per fibre length of 65 W/m, which is in the same order of magnitude as some of the highest values reported for conventional double-clad fibre lasers [40, 41, 42].

These techniques can also be extended to create hybrid fibre devices in which guidance is achieved by means of a conventional fibre core and a microstructured region is included to enhance the optical properties. For example, double-clad fibre lasers with conventional fibre cores and inner cladding regions with high NAs have been created in this way [43, 28]. An example of this hybrid fibre laser type is shown in Fig . 1.6 (h) which is a Ytterbium doped, cladding-pumped fibre laser with a conventional step-index central region (inner cladding diameter is 28 μm) and a holey outer cladding [28]. In addition, 'hole assisted' designs have been used to tailor the dispersion properties in a fibre with a conventional step-index core [44].

1.2.6 (2) Small core holey fibres

Highly nonlinear holey fibres

While the large-mode-area holey fibres discussed above are typically pulled from preform to fibre in one step, smaller scale structures are generally achieved via a two-step process. In the two step-process, a cm-sized preform is first pulled into a cane a few mm thick, which is inserted inside a thick walled capillary. This second stage preform can then be drawn into fibre with micron scale cladding features. Note that for small scale structures ($\Lambda/\lambda \approx 1$), holey fibres can be single-mode for quite high values of d/Λ (see Fig. 1.4). For example, for $\Lambda = 1.0$ μm, a holey fibre is single-mode for $d/\Lambda \lesssim 0.9$ at 1550 nm [19]. When the air-filling fraction in these small scale structures is high, as shown in Fig. 1.6 (a), (c) and (i), these fibres can exhibit highly nonlinear effects. Even though silica glass does not possess an intrinsically high nonlinearity, the combination of small core sizes and high NA in these fibres leads to tight mode confinement and high optical sensitivities even for modest powers. As mentioned above, the effective fibre nonlinearity is defined as $\gamma = 2\pi n_2/\lambda A_{\text{eff}}^{\text{FM}}$, and in conventional single-mode step-index fibres $\gamma \approx 1$ W^{-1}km^{-1}. In conventional step-index fibres this value has been increased to ≈ 20 W^{-1}km^{-1} [45] by decreasing the core size and

increasing the germanium concentration in the core (which acts to increase n_2). In a holey fibre, however, the effective fibre nonlinearity can be greatly increased simply by decreasing the core size. To date, silica holey fibres with $A_{\text{eff}}^{\text{FM}}$ as small as 1.5 μm^2 at 1550 nm [46] have been created. This equates to an effective fibre nonlinearity ≈ 70 W^{-1}km^{-1}, which is 3.5 times greater than the highest reported nonlinearity in conventional fibres.

In addition, holey fibres can also be made from non-silica glasses, such as tellurite and chalcogenide glasses, which can offer intrinsically high values of nonlinearity [22, 23, 24, 25, 26]. These so called soft-glasses possess lower melting points than silica glass and can, as a result, be extruded to form a preform in one step. This simplifies fabrication, especially in the small core, high NA regime. An example of this fibre type is shown in Fig. 1.6 (c), which is fabricated via an extrusion process from SF57; a commercially available highly nonlinear silicate glass with a high lead oxide content (available from Schott glass) [24, 23]. The effective nonlinearity for this fibre is measured at ≈ 640 W^{-1}km^{-1}, which is more than an order of magnitude greater than the highest nonlinearity ever reported in a silica fibre. Furthermore, recent results from a similar fibre have exceeded 1000 W^{-1}km^{-1} [47]. Such fibres offer access to nonlinear effects at remarkably low powers and short device lengths.

As mentioned in Section 1.2.2, the wavelength dependent cladding index can be tailored via the cladding parameters d and Λ to create a range of unique dispersive properties, such as extremely high values of anomalous and normal dispersion at 1550 nm [5], anomalous dispersion at short wavelengths [6, 7], broadband dispersion-flattening [8] and multiple zero-dispersion wavelengths [48]. These unusual properties can be utilised in a variety of ways. For example, anomalous dispersion at short wavelengths has made solitons at visible and near IR wavelengths possible [49]. In addition, many nonlinear effects are highly sensitive to the dispersive properties of the fibre, and so the ability to tailor dispersion, combined with the extremely small mode areas that can be created in holey fibres, leads to the possibility of realising highly efficient nonlinear processes such as supercontinuum generation. Supercontinuum generation is the conversion of a single wavelength into a broad spectrum as a result of complex interplay between a whole host of nonlinear effects [50, 51]. By tailoring the dispersion to optimise nonlinear effects for a given pump wavelength, this cascade process can be used to generate a broad flat continuum spanning from the UV to IR wavelengths [52].

However, it should be noted that there is a minimum possible effective area that is possible to achieve in a holey fibre. If Λ is smaller than the wavelength of light, the

fibre core becomes too small to confine light and the mode area broadens. In the most extreme case, a holey fibre with a high air-filling fraction can be approximated by a solid rod suspended in air. Using this analogy, the minimum possible mode area in a silica holey fibre can be approximated as 1.5 μm^2 at 1550 nm, which occurs for a rod of radius 1.2 μm (calculated using the exact solutions for a step-index fibre, assuming an air cladding [53]). Note also that in these small core designs, the confinement losses can be high due to the fact that the extent of the cladding, even with many rings of air holes, is not large. For 6 rings of holes with $\Lambda = 1.0$ μm and $d/\Lambda = 0.9$, typical confinement losses at 1550 nm are 0.2 dB/km. However, for nonlinear applications, only short lengths of fibre are required and loss values up to ≈ 1 dB/km can be tolerated. (The confinement losses quoted in this section are calculated by Vittoria Finazzi using the multipole method [54], as outlined in Section 1.4.)

Birefringence in holey fibres

For certain applications, such as device and sensor applications, highly birefringent structures are required as a way of discriminating or isolating particular fibre modes. Small core holey fibres offer a way of creating highly birefringent fibres via asymmetric core/cladding structures. This type of birefringence is known as form birefringence and can be large if the index contrast between core and cladding regions is high and if the core and cladding features are similar in scale to the wavelength of light. Various asymmetric cladding geometries have been successfully used to create highly birefringent small core holey fibres [55, 56, 57]. For example, a fibre of this type is shown in Fig. 1.6 (i), which has a small elliptically shaped core (2.6×1.5 μm) and a cladding region with a high air-filling fraction. A figure of merit often used to quantify birefringence is the beat length, which is simply $2\pi/\Delta\beta$, where $\Delta\beta$ is the intrinsic birefringence. The beat length in the fibre shown in Fig. 1.6 (i) has been measured to be 0.3 mm at 1550 nm, which represents the most highly birefringent single-mode fibre reported to date [29]. However, due to the fact that even quite minor imperfections in the fibre structure can lead to high values of form birefringence in holey fibres of this type, it can be difficult to avoid such effects in these small scale structures. Conversely, due to the fact that this effect decreases as the fibre core increases and as the hole size decreases, form birefringence is typically low in large-mode-area, single-mode fibres with minor imperfections, with beat lengths of order 3-5 m at 1064 nm [58]. Indeed, this means that asymmetry cannot be used effectively to create birefringence in larger core

holey fibres. However, for large-mode-area fibres, conventional approaches can be used to create highly birefringent structures [59]. This has been demonstrated by the addition of stress-applying rods into single-mode holey fibres with $\Lambda = 3.2 - 6.0$ and $d/\Lambda = 0.48$ to create a relatively wavelength independent birefringence of the order of $1.5{\times}10^{-4}$. However, note that in applications such as data transmission, it is necessary to minimise the effects of mode splitting that arise from birefringence. In conventional fibres this can be achieved by spinning the fibre to average out any imperfections in the structure that would otherwise lead to form birefringence. This has recently been demonstrated in holey fibres, where significant reduction in the polarisation mode dispersion is reported in large-mode-area structures [58].

Sensing

Another interesting property of holey fibres arises directly from the presence of air holes close to the core. Although the modal field decays exponentially within the air holes, for fibres with a small hole-to-hole spacing and a large air fill fraction, like the fibre shown in Fig. 1.6 (a), up to 50% of the modal field can be located within the air holes [60]. This overlap can be exploited for efficient evanescent sensing applications. For example, the holes can be filled with gases or liquids, enabling the light to interact with the fluid over a long path length, which can be coiled compactly. A short length of holey fibre similar to the one shown in Fig. 1.6 (a), with a core diameter of 1.7 μm and $d/\Lambda \approx 0.9$ (modal overlap is $\approx 17\%$) has been filled with acetylene gas in a demonstration of this principle [61], and has enabled the gas diffusion constant to be evaluated by monitoring the fibre attenuation as a function of time. [62].

Another type of small core holey fibre is shown in Fig. 1.6 (e), which possesses three small, near air-suspended cores of similar size. This type of fibre is fabricated by using large, thin-walled capillaries within the preform. In this case, small cores can form at the points where adjacent cladding capillaries meet due to surface tension effects that arise as the preform is heated and drawn into fibre. In this type of fibre core, $\approx 20\%$ of the guided mode can be located in the air [63]. While this overlap is less than can be achieved in small-core fibres of the type shown in Fig. 1.6 (a), it would be far easier to fill the large air holes in the type of fibre shown in Fig. 1.6 (e) with gases or liquids to create a sensing device.

1.2.7 (3) Non-silica holey fibres

Non-silica glass holey fibres

Nearly all non-silica fibres fabricated to date have small cores of a few μm in diameter designed to exploit the large non-linearities of these novel glasses [23, 24, 25, 26]. However, non-silica glasses also offer advantages in terms of transmission wavelengths, enabling access to the mid-IR. For transmission applications, the ideal fibre is single-mode and possesses low nonlinear effects. The nonlinearities of non-silica glasses are typically high, but can be reduced by increasing the mode area. However, the fabrication of large-mode-area, single-mode non-silica fibres has, until recently, proven problematic. Extrusion techniques are not suited to fabricating this type of structure in a single step, due to the many small holes that are required in such a structure. In addition, previous attempts at stacking non-silica glass capillaries have met with poor results due to glass fragility. However, recent results suggest that by using only rods, the stack-and-pull approach may offer a practical route towards large mode areas [64]. Furthermore, although extrusion techniques are not suited to fabricating many-hole fibre structures in one step, this technique could still be used to fabricate more complex stacking elements, which would minimise the number of elements required in the preform.

Polymer holey fibres

Holey fibres have also been made from polymers [65, 66], which offer even greater flexibility in design: in addition to capillary stacking, polymer holey fibres can also be fabricated using techniques such as extrusion, drilling or injection moulding. This flexibility means that it becomes straightforward to obtain arbitrary hole sizes, shapes and arrangements within the preform. In this way, single-mode, highly birefringent, twin-core, graded-index and hollow core band-gap structures have been demonstrated [66]. Due to the ease of fabrication and the wide variety of fibre structures that can be created, polymer holey fibres offer significant advantages over conventional plastic fibres. However, as a result of the fact that the intrinsic attenuation losses of polymers is much higher than that of silica glass, (typical polymer optical fibres have losses of a few 100 dB/km [67]), these fibres are unlikely to rival holey fibres for applications that require more than a few metres of fibre. However, in hollow core band-gap fibres, the light can be guided in the air, and the fibre losses need not reflect the intrinsic material losses of the fibre [12, 68]. In this regime, microstructured polymer fibres may offer significant advantages due to ease of fabrication.

Band-gap fibres are discussed in more detail in Section 1.3.

Solid holey fibres

As mentioned in Section 1.2.4, fabricating long lengths of uniform holey fibre can be challenging due to the interaction between air pressure and surface tension within the fibre. Indeed, in air/glass holey fibres drawn down to small dimensions, the cladding air holes can be significantly distorted from their original circular geometry, as shown in Fig. 1.6 (a). This is not a problem in conventional solid optical fibres, and km-long lengths of fibre with the parameters of the preform can be simply fabricated. However, the novel optical properties of a holey fibre, which arise from the wavelength scale air holes in the cladding, are not restricted to air/glass structures. In theory, two uniform solid materials could be used to create a solid microstructured fibre with similarly unusual optical properties if the refractive index contrast between the two materials is sufficiently high. The most challenging aspect of realising this type of microstructured fibre is finding two solid materials that are both thermally and chemically compatible, and that also possess a sufficiently large refractive index difference. A solid microstructured fibre made from two lead-silicate glasses with refractive indices of 1.53 and 1.76 has recently been fabricated [69]. In this solid holey (SOHO) fibre, the cladding is defined by a hexagonal arrangement of circular low-index glass regions and the fibre geometry is shown to be essentially unchanged during fibre drawing. Indeed, the relative size, shape and position of the low index regions are shown to remain virtually identical even when the fibre dimensions are reduced such that micron scale features are achieved in the cladding. In addition, solid microstructured fibres possess several practical advantages in terms of polishing, angle cleaving and splicing.

Another type of solid microstructured fibre has been proposed in which angularly alternating segments of high and low refractive index glass define the cladding region [70, 71]. Using an approximate effective index approach the authors show that this fibre type has the potential to create large-mode-area fibres that are single-mode over broad wavelength regions. However, the authors do not discuss what benefits this fibre type would offer over more traditional air/glass designs (other than fabrication uniformity as discussed above).

Increased functionality

Previously in this section, the subject of filling the air holes inside traditional holey fibres with gases or liquids was discussed. In this context, the emphasis was on exploiting the

evanescent fields present in the holes to create efficient and compact sensing devices [60, 61, 62]. However, the air holes in holey fibres can also be filled with other materials to increase fibre functionality in other applications. For example, a holey fibre in which a long period fibre grating has been written is shown to exhibit temperature sensitive wavelength shifts in the core/cladding resonances when the air holes in the fibre are filled with a temperature sensitive polymer [72]. In addition, liquid crystals have been infused into short lengths of holey fibre, in which thermally controlled optical switching behaviour is demonstrated [73, 74, 75]. Note that liquid crystal infused holey fibres have also been shown to demonstrate photonic band-gap effects that are highly temperature dependent.

1.3 Band-gap fibres

1.3.1 Introduction

In the sections below, recent progress in the field of photonic band-gap fibres is reviewed. However, note that this is a brief summary intended only to give context to the holey fibre work presented here.

1.3.2 Recent progress

Progress in the field of band-gap fibres, while rapid, has not matched the explosive activity of holey fibre research. This is due in part to the necessarily high tolerances on fabrication for these fibres, but also results from the challenges of accurately modelling modal properties, which is an essential requirement in fibre design. Unlike holey fibres, in which relatively simple scalar models can be used to evaluate modal properties (see Section 1.4), a full vectorial representation of the electromagnetic fields is essential for band-gap fibres. The techniques used to model the modal properties of band-gap fibres are not discussed in any detail within this thesis. However, techniques based on a fully vectorial version of the plane-wave technique outlined in Section 1.4.3 are capable of accurately modelling photonic band-gap fibres and have been used to explore guidance within these structures [76]. These techniques show that for a triangular hole arrangement, the mid-point of the band-gap is defined by Λ and the spectral width of the band-gap is defined by the air-filling fraction (the higher the air-fill, the wider the band-gap [77]). As a result, the majority of band-gap fibres fabricated to date, which are designed for IR wavelengths, have Λ in the range of $\approx 2-5$ μm, with a high air-filling fraction of $\approx 85-95\%$ [78, 79, 80]. An example of

this fibre type is shown in Fig. 1.1 (b), which has $\Lambda \approx 5$ μm, with an air-filling fraction of $\approx 90\%$. This type of fibre is generally fabricated in a two-step process; the fibre preform is typically formed by hexagonally-packed, thin-walled capillaries and a large air core is formed by removing 7 or 19 central capillaries [78, 80]. (Supporting rods at either end of the preform maintain this otherwise unstable structure). The preform is pulled into cane, which is then jacketed inside a thick walled capillary, and re-drawn to fibre dimensions.

Note that the fabrication of perfectly periodic high air-fill structures is challenging, and the first band-gap fibres were instead based on a 'honeycomb' arrangement of holes formed by the gaps between hexagonally packed rods, [81], in which full two-dimensional band-gaps can arise for air-filling fractions of only a few percent [82]. In this fibre type, the core is created by substituting a capillary for a central rod in the preform, which forms a low-index defect in the two-dimensional photonic crystal. However, both characterisation and modelling has shown that the modes of these fibres are localised in the solid regions of the fibre core and are typically non-Gaussian in shape [81, 82]. In contrast, band-gap fibres with a triangular arrangement of large, closely spaced air holes in the cladding can support Gaussian-like modes in a large hollow core. As a result, this type of band-gap fibre is favoured despite the additional fabrication challenges.

Whilst losses in air-guided photonic band-gap fibres have the potential to be very low, until recently reported losses were typically of the order of 100-200 dB/km, with fibres manufactured in lengths typically no longer than ≈ 100 m. Attenuation losses in photonic band-gap fibres can arise from the finite extent of the cladding and from imperfections within the cladding structure. However, coupling between surface and core modes of the structure has been identified as the most significant contributor to transmission loss in hollow-core photonic band-gap fibres [79, 83, 84]. In recent months the transmission losses of hollow-core band-gap fibres have been drastically reduced to a record low of 1.7 dB/km at 1550 nm, measured over 800 m of fibre [85]. However, while this value represents great improvements on the losses of the early fibres, it is still an order of magnitude greater than the losses of conventional fibres, and much work is required before photonic band-gap fibres can be considered to be truly low-loss waveguides suitable for long-haul transmission and high power applications. In addition, while preliminary results suggest that photonic band-gap fibres are far less sensitive to bend induced loss than either holey or conventional fibres [80], which is an obvious advantage in large-mode-area high-power applications, no comparative work has been presented in which the modal area of the fibre is considered.

Whilst the damage threshold of an air-core fibre can potentially be high, large-mode-areas would still be required in order to optimise coupling to large-mode-area sources and also to minimise air-breakdown and nonlinear effects for pulsed sources.

1.3.3 Non-silica band-gap fibres

Another way of creating photonic band-gap air-core fibres has been recently demonstrated. These so called 'Omniguide' or hollow multilayer photonic band-gap fibres guide light in a large hollow core that is surrounded by concentric circles of alternating media [68]. An example of this fibre type is shown in Fig. 1.7. The concentric circles are made of alternating layers of high refractive index glass (n $\approx$ 2.8) and low refractive index polymer (n $\approx$ 1.55) that are 5-10 μm thick. These layers are deposited onto a flat substrate, which is rolled up into a hollow pipe and then drawn into fibre. The transmission windows of these fibres can be scaled from 0.75 to 10.6 μm via the cladding layer dimensions. At 10.6 μm (CO_2 laser light) losses are determined to be < 0.1 dB/m, which is many orders of magnitude below that of the intrinsic fibre material, demonstrating that photonic band-gap materials need not be selected for transparency at the guide wavelengths. However, the large core dimensions (diameter > 300 μm) mean that these fibres are highly multi-mode and although the observed fibre output is indicative of less than 10 excited modes, the fibre output is consequently a sensitive function of the bend radius.

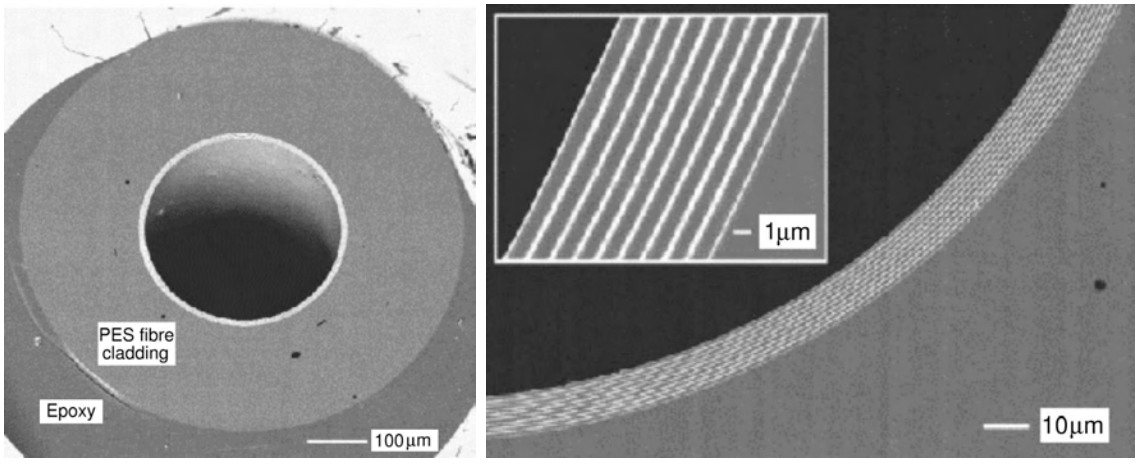

(a) (b)

Figure 1.7: (a) and (b) show SEM images of a hollow-core photonic band-gap fibre with a multilayer cladding consisting of alternating layers of high index polymer and low index glass. The hollow core appears black, the polymer (PES) regions, grey, and the glass layers (As_2Se_3) white. Figures taken from Ref. [68]

The fact that transmission losses in a band-gap fibre need not reflect the intrinsic

material losses of the fibre material offers potential for low loss transmission in band-gap fibres made from other materials, such as non-silica glasses and polymers. Microstructured fibres with band-gap structures have been recently demonstrated in polymer, which offers significant advantages in terms of ease of fabrication, as discussed in Section 1.2.7. In addition, non-silica glasses, which have been proposed for low-loss band-gap fibres at mid-IR wavelengths [77], may offer potential for larger band-gaps at a variety of other wavelengths due to the typically high refractive indices of these glasses. Initial studies have shown that increasing the refractive index can increase the width of the band-gap for low air-filling fractions, but that it does not necessarily result in wider band-gaps for higher air-filling fractions [77].

1.4 Modelling holey fibres

1.4.1 Introduction

The transverse refractive index profile of a typical holey fibre is complex. As a result, the many tools that have been developed to aid understanding of conventional fibres are not directly transferrable. However, in recent years, several techniques have emerged that are capable of evaluating the modal properties of holey fibres. In this section, a selection of these techniques are summarised. The techniques in this selection include those that are most widely used and those that are most applicable to the large-mode-area holey fibres considered within the study presented in the main body of this thesis. In general, a combination of the techniques presented here is usually necessary to form a complete picture of the modal properties of any given holey fibre. Note that modelling bend loss is discussed separately in Chapter 2.

For holey fibres with small values of d/Λ, the weakly-guiding approximation is found to produce accurate results despite the high index contrast between the air/glass regions in the cladding [86]. (See Section 3.2.6 for more details). However, when the air-filling fraction of a holey fibre becomes large ($d/\Lambda \gtrsim 0.5$), the effective index contrast between core and cladding regions becomes sufficiently large to require the use of fully vectorial methods.

1.4.2 The effective index approach

In the effective index approach, developed by Birks *et al.* in 1997 [4], the complex refractive index profile of a holey fibre is replaced by an *equivalent* step-index (ESI) fibre, whose modal

properties can then be evaluated using well established techniques. The ESI profile is determined by replacing the microstructured cladding with a uniform material that possesses the same effective refractive index and approximating the holey fibre core by a circular region of pure silica. The effective cladding index of a holey fibre, n_{FSM}, is evaluated by calculating the propagation constant, $\beta_{FSM} = n_{FSM}k$, of the lowest-order cladding mode, often referred to as the fundamental space filling mode (FSM). Note that this quantity is strongly wavelength dependent and must be reassessed for each wavelength at which the holey fibre is to be modelled. A simple analytical method of evaluating n_{FSM} was discussed in Section 1.2.2. In this approach, n_{FSM} is calculated by solving the wave equation for a single hexagonal unit cell centred on an air hole, by approximating the hexagonal boundary by a circular one of radius $\Lambda/2$ [16, 15]. Although more accurate methods of evaluating n_{FSM} exist (as described in the rest of this section), this simple analytical approach is typically used in an ESI approximation due to the fact that the definition of core radius generally represents a far larger source of error, as discussed in the following.

Due to the fact that no clearly defined boundary between the core and cladding region exists in a holey fibre, the core diameter of an ESI fibre must be chosen arbitrarily. In most cases, the core radius is defined to be 0.625Λ [18]. This value was determined as the best choice for a holey fibre via comparison of results with those obtained using a more rigourous plane-wave technique. However, this choice is valid for a fairly limited range of fibre parameters and wavelengths. Indeed, it has been shown that both the core and cladding regions of a holey fibre have effective indices that vary with wavelength and that the effective index approach cannot be used to accurately model the modal properties of holey fibres, especially properties such as dispersion or birefringence, which are sensitive functions of the cladding geometry [87, 88, 89]. To accurately model the optical properties of holey fibres it is important to consider the full complex refractive index profile, and some of the techniques that have been developed to do this are discussed in the rest of this section.

Despite these inaccuracies, this technique can offer many useful insights into the modal properties of holey fibres. For example, properties such as the effective mode area can be approximately evaluated, due to the fact that the modal field can be reasonably well approximated by a Gaussian field [17]. In addition, as shown in Section 1.2.3, the effective index approach correctly predicts the phenomenon of endlessly single-mode guidance for fibres with relatively small holes. Furthermore, this approach can be used to demonstrate

that bending losses increase towards both short and long wavelengths in a holey fibre, as discussed in Section 2.3 [4, 16], although it cannot be used to examine the magnitude of loss with any accuracy.

1.4.3 Expansion methods

Plane wave expansion

The modal properties of a holey fibre can also be modelled using an adaptation of the full-vector technique developed by Silvestre *et al.* [90]. In this technique, the modal fields and the refractive index profile are represented by a Fourier decomposition (i.e. plane waves). The refractive index profile is defined over a restricted region and periodic boundary conditions are used to extend the structure over all space. The wave equation can then be solved to find the modes of the fibre and their associated propagation constants. Since this technique accounts for the full complex refractive index profile of a holey fibre, it is capable of accurately modelling the modal properties of holey fibres [91, 92, 14]. However, in order to incorporate the fibre core adequately, the repeated region, called a supercell, must be much larger than the guided mode such that each core within the repeated structure is independent of one another. The larger the supercell required, the more inefficient this approach becomes. In addition, an accurate description of the modal properties is only possible when a sufficient number of terms are used in the expansions of the refractive index and the modal fields. A plane wave expansion is an efficient way of representing the typically periodic index profile of a holey fibre, but is not an efficient way of representing the fibre modes of interest, i.e. those that are localised in the fibre core. Consequently, many terms are required to form an accurate representation of the core modes and, as a result, this method can be computationally intensive.

However, this method is an accurate and efficient way of calculating the modal fields of an infinite, periodic cladding [91, 14]. For various reasons it is often necessary to have knowledge of the fundamental space filling mode (FSM). This quantity is required in the effective index approximation, as described above and is also needed in the methods used here to calculate bend loss (see Section 3.5.1). Whilst this technique can be computationally intensive for the large supercells required to accurately model the core defect, only a single unit cell is necessary in order to calculate the properties of an infinite cladding structure composed of a perfectly regular lattice. In addition, since the modal fields of a holey fibre cladding are non-localised, a plane-wave expansion represents an efficient description of

both the refractive index and the modal fields in this case.

Note that any optical fibre in which the refractive index profile is perfectly symmetric with higher than 2-fold symmetry does not exhibit form birefringence [93]. However, due to the fact that in this technique the transverse refractive index profile is typically defined on a Cartesian grid, some small degree of (artificial) birefringence is always predicted. This can be reduced (but not eliminated) by increasing the grid resolution.

Localised function expansion

In an alternative approach developed by Mogilevtsev *et al.* [88, 89] the refractive index profile and the modal fields of a holey fibre are decomposed into a series of localised Hermite-Gaussian functions. By describing the modal field in terms of localised functions, this quantity can be accurately represented without requiring the use of too many terms. However, Hermite-Gaussians provide a poor description of the non-localised transverse refractive index profile in holey fibres. Consequently this approach cannot represent the index profile of a holey fibre in an efficient way, which severely limits the applicability of this approach.

Orthogonal function method

A hybrid approach that incorporates the best features from the plane-wave and localised function expansion techniques described above has been developed by Monro *et al.* in Refs [13, 86, 94, 95], in which both scalar and vector forms of this model are described. In this approach, the functions used to describe the transverse refractive index and modal fields of a holey fibre are chosen carefully to suit. In Refs [86, 94] the air-hole lattice is decomposed using a series of plane-waves and the fibre core and the modal fields are described using a series of localised Hermite-Gaussian functions. In this way, both the transverse refractive index profile and the modal fields of a holey fibre can be accurately represented without requiring the use of too many terms in each expansion. This allows for an efficient description of the relevant modal properties.

This hybrid approach is particularly efficient for idealised periodic fibre structures, since only symmetric terms are required in each expansion in order to accurately model the fundamental mode. However, by using the complete basis set in each expansion (i.e. even and odd terms), higher-order modes and holey fibres with asymmetric index profiles can also be efficiently modelled using this technique [13]. Note that for more complex index structures it becomes more efficient to describe the entire refractive index profile in terms

of a plane-wave expansion. This implementation can be used to predict the properties of actual holey fibres by using SEM images to define the index profile [96]. Note that this method is not suited to calculations of the cladding modes of a holey fibre, as a direct result of the fact that localised functions are used in the modal expansion.

1.4.4 Beam propagation methods

Techniques based on beam propagation methods (BPM) are capable of accurate representations of the modal properties of arbitrary index waveguides and as such are applicable to holey fibres [97]. In a BPM technique, the modes of a fibre are calculated indirectly by propagating light step-by-step through a full three-dimensional refractive index profile. Such techniques have the advantage that non-periodic boundary conditions can be used allowing the full complex propagation constant to be calculated, from which properties such as confinement and bending losses can be directly extracted. However, these techniques are typically computationally intensive. Indeed, this is further exacerbated by the high grid resolution that is required in order to accurately represent the relatively small scale features present in a holey fibre. Note that this technique also predicts some small degree of (artificial) birefringence due to the cartesian grid onto which the index profile is typically defined, as discussed in Section 1.4.3.

1.4.5 The finite element method

The finite element method can also be used to provide an accurate vector analysis of the modal properties of holey fibres as this is also applicable to arbitrary index profiles [98]. In the finite element method, the transverse refractive index profile is split into distinct homogeneous subspaces. This involves dividing the index profile into a mesh of triangles and quadrilaterals (the finite elements), which decrease in size towards the centre of the fibre. The classical Maxwell differential equations are then solved for these elementary subspaces, taking into account the conditions of continuity of the fields. The Maxwell equations are discretised for each element, which leads to a set of elementary matrices. These elemental matrices are then combined to create a global matrix system for the entire structure. This method can be used to evaluate the full, complex propagation constants of the modal fields (and hence the confinement losses) of a finite structure, and is capable of producing reliable numerical solutions, but is computationally intensive [98].

1.4.6 The multipole method

In the multipole approach [99], the transverse refractive index profile of the fibre is approximated by non-overlapping circular holes of arbitrary, but uniform refractive index. For most holey fibres, in which an array of circular air holes define the cladding region, this represents an excellent approximation. The modal fields and their associated complex propagation constants are then calculated using decompositions based on cylindrical harmonic functions localised in each of the circular air holes. Note that this method is also capable of calculating accurate, complex values of the effective cladding index (n_{FSM}) of a finite cladding, by considering a structure without a core. This technique has one key advantage over the other methods described in the section above: since the refractive index profile is not defined on a cartesian grid, false birefringence is avoided, allowing an accurate description of the modal symmetries. However, this method can be computationally intensive due to the fact that it is necessary to consider the entire extent of the fibre in this approach. Furthermore, it is not possible to consider an arbitrary refractive index profile.

1.5 Motivation and outline of thesis

Large-mode-area optical fibres are required in high power applications, for both passive and active devices, where the large mode size is used to minimise nonlinear effects and increase the maximum power level that can be tolerated without incurring damage. For many of these applications, good spatial beam quality is also a critical issue and single-mode operation is, therefore, desirable.

At the start of this project (July 2000), holey fibres had recently been identified as an alternative route towards large-mode-area fibres, with the publication of a single paper detailing the fabrication and characterisation of a holey fibre with $\Lambda \approx 10$ μm and $d/\Lambda \approx 0.12$ [30]. Characterisation of this fibre validated the prediction that the property of endlessly single-mode guidance is essentially scale invariant. This demonstrated the huge potential that holey fibres could offer in the large-mode-area single-mode regime.

However, while bending losses were understood to be the largest single limiting factor on the maximum mode size that could be tolerated in practice, little was known about the factors that influenced bend loss in a holey fibre. Indeed, although basic theoretical models could be used to illustrate that the bending losses of holey fibres were radically different from those of conventional fibres, increasing towards both long and short wavelengths, no theoretical model had been developed that could accurately model even the most basic aspects of bend loss in a holey fibre. As a result, little knowledge existed about the magnitude of bend loss that one may expect for a given mode area in a holey fibre, or how sensitive these losses were to the structural parameters and the wavelength of operation. The ability to predict the bending losses of holey fibres is essential both for future fibre design and for assessing what benefits holey fibres may offer over their conventional counterparts in the large-mode-area, single-mode regime. Furthermore, in order to gain a good understanding of the parameters that influence bend loss in holey fibres it is essential to develop a method of accurately predicting bend loss that can take into account the full complex refractive index profile of a holey fibre. The aims of the study presented here are thus threefold: (1) to develop methods of accurately predicting bend loss that can be applied to both holey and conventional fibres, (2) to use these techniques to explore the potential offered by holey fibres in the large-mode-area, single-mode regime, and (3) to place their performance in context against conventional step-index fibres. In order to fulfil these aims, it is also essential to be able to accurately predict the effective mode area and modedness (i.e. whether a given fibre is single-mode or multi-mode) of both fibre types.

Furthermore, reliable methods of characterising the bend loss, the effective mode area and the bending losses of holey and conventional fibres are also essential to enable comparative studies and also to validate the theoretical techniques developed here.

In the following chapter, an introduction into bend loss is presented that details the mechanisms responsible for loss in a curved optical waveguide and introduces the common terminology used in conventional fibres. The ways in which the bending losses of holey fibres differ from those of conventional fibres and the models that have been developed to model these losses are also discussed within this chapter. Finally, the requirements of the model developed here to study bending losses in large-mode-area holey fibres is outlined.

The numerical models and experimental techniques that have been developed as part of this study to characterise large-mode-area holey and conventional fibres are described in detail in Chapter 3 and Chapter 4 respectively. Validation of the numerical models used here via comparison with experimental results is presented within Chapter 4, 5, 6 and 7. In Chapter 5, the modal properties of holey fibres are explored at 1064 nm, which is one of the most widely used wavelengths in laser applications. The range of structural parameters that give rise to single-mode, large-mode-area holey fibres with practical levels of bend loss are evaluated numerically using the techniques from Chapter 3. The maximum tolerable effective mode area in a single-mode holey fibre at 1064 nm is also investigated in this chapter, and a comparative study of conventional fibres that aims to explore how these two fibre types compare at this wavelength is also presented. Throughout this chapter, experimental results from holey fibres fabricated as part of this study are used to validate the numerical methods. In Chapter 6, the possibility of improving bend loss in holey fibres at 1064 nm, by using different arrangement of holes in the cladding is explored numerically. Experimental results are also presented. In Chapter 7 the spectral dependence on mode area and bend loss in holey fibres is considered both numerically and experimentally. Within this chapter, the maximum tolerable mode area is investigated as a function of wavelength and the spectral behaviour of holey fibres is compared with those of equivalent conventional fibres. Within this chapter, non-silica holey fibres made from Gallium Lanthanum Sulphide (GLS) glass for mid-IR transmission applications are also briefly investigated in terms of bend loss and nonlinearity.

Chapter 2

Introduction to bend loss

2.1 Introduction

The focus of the work presented within this thesis is large-mode-area holey fibres. The aims of this thesis are discussed in detail in Section 1.5, but are essentially to assess the potential benefit offered by holey fibres in the large-mode-area, single-mode regime. Since the fundamental limiting factor for mode size in any optical waveguide is bend loss, understanding the mechanisms responsible for bend loss is essential to the aims of this thesis. A brief overview of the mechanisms responsible for bend loss in conventional optical waveguides, and the classifications typically used are presented in Section 2.2.1. The differences between the bending losses of holey and conventional fibres are discussed in Section 2.3.

At the time of this study (July 2000 - Dec 2003), there were no reported techniques that could accurately model even the most basic aspects of bend loss in a holey fibre. As a result, one of the first aims was to formulate a theoretical model capable of accurately predicting bend loss in holey fibres. In addition, it was decided that any model should be capable of including the full complex refractive index profile of a holey fibre in order to gain a complete understanding of the factors that influence bend loss in these novel fibres. Although the many techniques developed for conventional fibres are not directly transferable to holey fibres due to the complex nature of the refractive index profile, it may be possible to combine certain elements of these conventional techniques with models developed for modelling straight holey fibres, as summarised in Section 1.4. Consequently, a brief summary of some of the methods used to predict bend loss in conventional fibres and waveguides is presented in Section 2.2. This summary also serves to illustrate some of the bend loss characteristics observed in conventional fibres. This is followed by a discussion

of some of the ways in which these techniques have been adapted to holey fibres via an effective index approximation in Section 2.3.2. Finally, the techniques developed here to model the bend losses of holey fibres are outlined. Note that these techniques are explained in detail in Sections 3.4 and 3.5.

2.2 Conventional waveguides and fibres

2.2.1 Bend loss mechanisms and classifications

As light encounters a bend in an optical waveguide, the modal field distorts outward in the direction of curvature to a degree that is related to the severity of the bend. The distorted modal field propagates along the length of the curved section until returning to the straight waveguide, where the modal field reverts back into that of the straight waveguide. During this process, power is lost from the waveguide as a result of bend induced coupling from the core mode(s) to any or all of leaky higher-order, cladding, radiation and backward propagating modes. The interaction between all modes within a bent waveguide is complex, and in conventional waveguide and fibre theory the mechanisms responsible for bend loss are typically represented by two distinct components: *Transition loss* and *Pure bend loss*, which can be considered separately. Transition loss, which is also referred to as mode-conversion loss, is a one-off loss that results from the modal distortion induced by the change in curvature at the beginning and end of a bend. The magnitude of this loss component is directly related to the rate of change of curvature; for example, if the curvature changes over a sufficiently long length scale, the mode shape can change adiabatically and no power is lost from the mode. However, in most situations, the curvature changes over a short length scale and this component of bend loss is often approximated as a conversion loss between different waveguide sections, by evaluating the overlap between the modal fields of straight and bent waveguide sections [100, 101, 102]. Pure bend loss is defined as the continual loss of power that occurs as the distorted mode propagates along the curved waveguide section. This component of bend loss is often considered in terms of the radiative loss from the tails of the mode: as the mode propagates around the curved waveguide, the tails of the modal field on the outside of the bend must travel faster than the rest of the mode to maintain a flat phase front [103]. At some distance from the centre of the mode, the velocity required to maintain a flat phase front will exceed the local speed of light. The power in the tails of the mode beyond this point is thus unable to 'keep pace' with the rest

of the mode and is lost as radiation. The magnitude of loss, for both transition and pure bend loss components, increases towards long wavelengths, for decreasing values of NA and increasing mode size.

Although this distinction between transition and pure bend loss may seem somewhat artificial at first sight, this approach is frequently, and successfully, employed in studies of both slab waveguides and optical fibres [100, 104, 101, 105, 106, 107, 108, 109, 110]. Indeed, by considering different types of bend, we can see that these components represent relevant physical quantities. For example, bend loss in long lengths of spooled fibre will be dominated by pure bend loss, while in lengths of fibre with many separate macro-bends, the multiple transition regions can contribute significantly to the overall bend loss.

In addition to the transition and pure bend loss components described above, bend loss is also traditionally separated into *macro-bend* and *micro-bend* regimes depending on the relative scale of the bend [111]. Macro-bending losses result from long length bends that are significantly greater in scale than the waveguide core, while micro-bending losses occur for small-scale bends, along which the mode distorts continuously. In conventional fibres and waveguides, macro-bend losses are found to be dominated by pure bend loss and micro-bend losses are found to be dominated by transition losses. In conventional optical fibres, micro-bends generally result from the processes of coating, cabling, packaging and installation and can thus be reduced by refining these procedures. In addition, the magnitude of loss attributed to micro-bends in conventional cabled fibre such as SMF-28 is typically negligible [112]. In contrast, the macro-bend losses of a fibre are a fundamental factor in defining its practicality and in this study we consider macro-bend losses only.

2.2.2 Modelling bend loss in conventional waveguides and fibres

Introduction

Over the years, numerous different approaches for calculating the modal fields and the losses associated with bent waveguides and fibres have emerged. In the following, a brief summary of some of these techniques is presented, which also serves to illustrate some of the bend loss characteristics of conventional fibres. Note that single-mode fibres are the focus of this study and macro-bend loss is considered to represent the major limiting factor for practical mode areas in this regime (see Section 2.2.1). Consequently, all the approaches described below deal only with macro-bend losses in single-mode waveguides and, unless otherwise indicated, rely on analytical solutions to the wave equation with a weak guidance

approximation. Within these approaches, transition loss is most often ignored due to the fact that pure bend loss is found to dominate in the macro-bend regime. Furthermore, the effect of field deformation is often ignored completely in the calculation of pure bend loss in conventional fibres and waveguides in order to simplify the descriptions of the modal fields. This approach is approximately valid for gentle bends, in which the field of the bent waveguide is not greatly different from that of the straight waveguide, but does, obviously, lead to some degree of inaccuracy in the predictions of bend loss.

Summary of theoretical approaches

The separation of macro-bend loss in an optical waveguide into the two components described above was first proposed in Ref. [113], where these components are described as: (1) A dissipative loss along the curved waveguide section (referred to in later literature as pure bend loss), which results from the inability of the tails of the modal field to negotiate the bend, and (2) A mode conversion loss (also referred to as transition loss), incurred by the modal field on entering and leaving the bend, which is related to the fact that the modal field distorts radially outwards in a bent waveguide. Approximate formulas to predict the contribution from both of these bend loss components are calculated using analytical solutions to Maxwell's equations for slab waveguides. The pure bend loss is calculated by evaluating the fraction of the guided mode that cannot travel fast enough around the bend to keep phase with the rest of the mode and the transition loss is calculated via a generalised coupled wave approach. However, in this approach, the field deformation induced by the curved waveguide is ignored in the model of pure bend loss and the modal fields are approximated by those of the straight waveguide.

One popular method of defining the modal fields of a bent waveguide is to transform the refractive index of the straight waveguide such that it mimics the modal properties of the bent waveguide. This approach is called conformal transformation and was first proposed as a solution to this problem in 1975 [100]. In this conformal transformation approach, a curved waveguide is approximately represented by a straight waveguide with an effective refractive index distribution by expressing the wave equation in terms of a local coordinate system that follows the curvature of the waveguide. Once defined, the transformed index profile can then be used to evaluate the modal fields and the attenuation of the bent structure using a variety of techniques. This technique was first applied to slab waveguides, where the modal fields and complex propagation constants are found by breaking the transformed

index profile into a series of constant index steps and applying a Wentzel-Kramer-Brillouin (WKB) approach [100]. The pure bend loss is then obtained from the imaginary part of the propagation constant and the transition loss via an overlap integral used to calculate the mode mismatch between straight and bent waveguide sections. Although no comparison was made to experimental results in this first study, results from another report in which the same technique was used showed excellent agreement with experimental results [101], demonstrating the validity of the conformal transformation.

This conformal transformation technique can also be applied to optical fibres for which the weak guidance approximation is valid [114], and was first implemented to calculate the modal fields of bent step-index fibres in 1976 [115]. The effective refractive index distribution for a bent optical fibre is given by Eq. 3.9, and essentially acts to superimpose a gradient on the refractive index profile of the fibre, rising in the direction of the bend. The full derivation for the conformal transformation for an optical fibre is given in Ref. [114], and is discussed in detail in Section 3.3.1. A conformal transformation is a popular first step to modelling the modal properties of bent step-index fibres and some of the various approaches that can evaluate both pure bend and transition losses in this way are explored in the following [111, 106, 108, 109, 116, 117, 114, 102].

For example, a simple approach to model the transition losses of step-index fibre is proposed in Ref. [102]. In this technique, a first order perturbation method is used to find approximate analytical expressions for the modal fields of the transformed refractive index profile. The transition loss is then calculated as a splice loss using an overlap integral that calculates the modal overlap between the mode of the straight and bent fibre. In another method, coupled mode theory is used to evaluate the losses incurred due to mode coupling within the transition region of a step-index fibre via the energy in, and interaction between, the fundamental core mode and the lowest-order radiation mode as a function of distance along the bend [118]. Using this model, the authors show that the power lost in the transition region of a bend in an optical fibre oscillates as a function of distance and that radiation is emitted in discrete beams in this region. This behaviour had previously been observed experimentally for bent fibres immersed in index-matching liquid [119]. In a following paper [120], oscillations in bend loss as a function of bend radius are studied with the same technique, showing reasonable agreement with experimental results in terms of peak positions. Note that various other approaches have also been used to successfully predict the oscillations in bend loss that occur as a function of wavelength, which have

been shown to arise from the wavelength dependent coupling between core and cladding modes [121, 122].

A couple-mode technique together with a conformal transformation is also employed in Ref. [111], to demonstrate how the rate of change of curvature in the transition regions can influence the bend loss. In this technique, the power in the radiation field is calculated from integrating the Poynting vector over the appropriate solid angle for a step-index fibre with an infinite cladding. The authors demonstrate that the contribution from transition losses to the overall bend loss decreases as the change in curvature becomes less abrupt.

Other techniques apply beam propagation methods (BPM) to model the bending losses in both step-index and parabolic-index fibres [108, 106, 123]. Using BPM techniques, the pure bend loss is evaluated via the imaginary part of the propagation constant of the fundamental mode and the transition losses can be calculated by considering coupling to the radiation modes of the bent fibre and the associated attenuation coefficients. In Refs [108] offsetting the core and/or introducing a dip in the refractive index profile along the outside of the bend are shown to considerably improve the losses. A similar approach to improving bending losses in step-index fibres and waveguides is also proposed in Ref. [123], where BPM techniques are used to show that introducing both depressed and increased index regions on the outside of the core can reduce bend losses beyond that achievable with the presence of a depressed region alone. Note that in Ref. [106], the authors show that an equivalent step-index (ESI) approach is not an accurate method of assessing bending losses in a graded-index fibres due to the arbitrary nature in which certain parameters, such as the core radius of the ESI parameter, must be defined.

Other approaches towards modelling pure bending losses involve Fourier decompositions of the modal field. In ref. [124] the fields near and far from the core are assumed to be unperturbed, and the modal field between these two regions are expanded into a Fourier series containing Airy functions. The coefficients of the backward propagating field are determined by matching boundary conditions and the attenuation coefficient for pure bend loss is then derived from the amplitude of the backward propagating field. In Ref. [125] a model including the finite coating and cladding of a step-index fibre is developed, which is essentially an extension of [124] and this approach shows reasonable comparison with experimental results. Ref. [116] extends the theory in [125] so that the expansion includes the whole of the cladding. In Ref. [117] a more generalised theory based on the same approach is developed, which shows excellent agreement with experimental results.

Approaches that do not use a conformal transformation typically ignore the modal distortion in the bent fibre altogether. As mentioned before, this approach is approximately valid for gentle bends, in which the field of the bent waveguide is not greatly different from that of the straight waveguide, but does, obviously, lead to some degree of inaccuracy in the predictions of bend loss. However, this approximation enables the problem of calculating the bend loss to be greatly simplified and permits simple analytical models of bend loss to be derived. For example, in Ref. [126], a loss formula for the fundamental mode of infinitely clad step-index fibres is derived for weakly-guiding fibres. In this derivation, the loss coefficient is determined by calculating the power outflow from the field in the cladding, which is expressed in terms of a superposition of cylindrical outgoing waves. This technique was later adapted to include the field deformation via conformal mapping [115]. However, a comparison of results from these two techniques show that for single-mode fibres, the effect of the field-deformation has a minimal effect on the predicted loss. Comparison with experimental results shows that both techniques overestimate the bend loss in optical fibre, although they do predict the correct parametric dependencies [127]. The approach of Ref. [126] is also used in Ref. [128] in which an analytical expression for bend loss in optical fibres with axially symmetric refractive index profiles is evaluated by approximating the index profile by a staircase function and expressing the fields in a matrix representation. A simplified version of this approach is also presented in Ref. [129].

One novel method uses a surface current analogy to determine pure bend loss in a step-index fibre by replacing the effect of the core with fictitious currents on its surface [130]. The formula for the attenuation coefficient derived using this technique is remarkably similar to those derived using more conventional techniques [126], although the predicted losses are significantly overestimated.

2.3 Bending losses in holey fibres

2.3.1 Differences between bend loss in holey and conventional fibres

The bending losses of holey fibres differ qualitatively from those of conventional step-index fibres. Like conventional fibres, holey fibres exhibit a bend loss edge at long wavelengths due to the fact that the mode extends further into the cladding, resulting in a more weakly guided mode that will suffer a greater perturbation in response to bending. Holey fibres also possess an additional bend loss edge at short wavelengths as a direct consequence of

their novel cladding structure [4]. In a holey fibre the effective cladding index is strongly wavelength dependent and increases towards short wavelengths (see Section 1.2.2). This acts to decrease the NA towards short wavelengths, resulting in a more weakly guided mode that becomes more susceptible to bend induced distortion and loss. This explanation is sufficient to explain this phenomenon, however, since bending losses in holey fibres represent the main focus of the work presented here, these losses are explained in a little more detail in the following.

In a bent fibre, power is lost as a result of bend induced coupling from the core mode(s) to any or all of leaky higher-order, cladding, radiation and backward propagating modes. The amount of power lost in a bent fibre is dependent on the severity of the bend, the fibre structure, and the wavelength of light, each of which influence the strength of coupling between the modes present. To first approximation, the strength of coupling between two modes can be gauged from the effective index difference of those modes: the closer they are in effective index the more power is coupled from one to the other. Here this approximation is used to illustrate the spectral dependence of bend loss in holey and conventional fibres. To keep matters simple, we consider the coupling between the fundamental core mode and the lowest-order cladding mode only. Note that in a step-index fibre the effective index of the lowest-order cladding mode is taken to be the refractive index of the solid cladding, n_{clad}, and in a holey fibre is defined as the effective cladding index of the microstructured region, n_{FSM}. The relative change in bend loss with respect to wavelength can thus be evaluated by considering the relative spacing of the cladding index (n_{clad} or n_{FSM}) and the effective index of the fundamental core mode, n_{FM}. This is illustrated in Figs 2.1 (a) and (b), in which sketches of n_{FM} and the cladding index are shown as a function of wavelength for a holey and conventional fibre respectively. A sketch of the bend loss is shown as a function of wavelength for these two fibre types in Figs 2.1 (c) and (d) respectively. These graphs are explained in the following.

As can be seen in Figs 2.1 (a) and (b), in both fibre types, the effective index of the core mode decreases towards long wavelengths as the mode extends further into the lower index cladding, and tends asymptotically towards the refractive index of the core towards short wavelengths. The differences in bend loss between the two fibre types arise from the fact that the cladding indices in these two fibre types have different functionalities. In a conventional fibre, the cladding index is weakly dependent on wavelength and can be considered to be constant. The difference between the effective index of the core mode

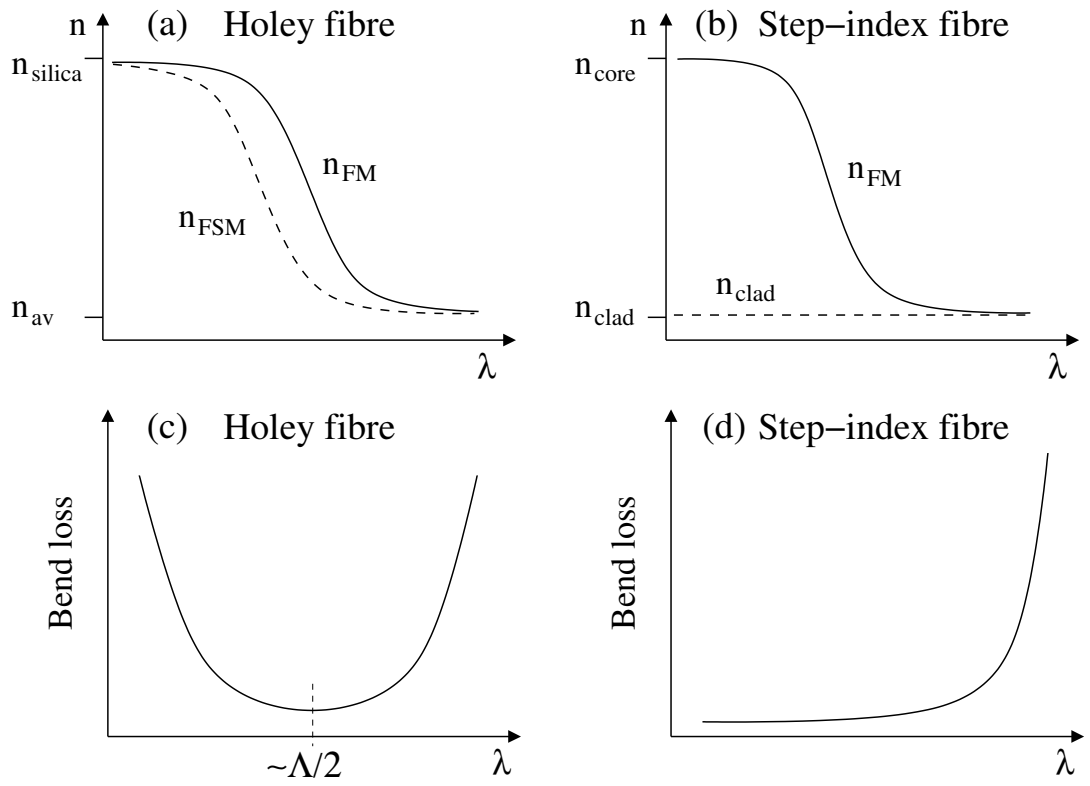

Figure 2.1: Schematic of the effective index for the fundamental core mode and the lowest-order cladding mode in (a) a holey fibre and (b) a conventional step-index fibre. Here, n_{silica} is the refractive index of silica glass, n_{av} represents the volume average index of a holey fibre cladding and n_{core} and n_{clad} are the core and cladding indices of a step-index fibre respectively. n_{FM} is the effective index of the fundamental core mode and n_{FSM} is the effective refractive index of a holey fibre cladding, which is also referred to as the effective index of the fundamental space filling mode (FSM) of the cladding. A sketch of the bend loss is shown in (c) and (d) for holey and conventional fibres respectively.

and the cladding index thus only ever decreases towards long wavelengths, and thus the bending losses only ever increase with wavelength, as shown in Fig. 2.1 (d). In a holey fibre, the fundamental core mode and the fundamental cladding mode share the same parametric dependency on wavelength. For both of these modes, the effective index increases towards short wavelengths as the mode becomes more confined to the silica regions, and decreases towards long wavelengths as the light samples more of the air holes. The bending losses therefore increase towards both long and short wavelengths, as shown in Fig. 2.1 (c).

Consequently, although a holey fibre can be single-mode at all wavelengths, the two bend loss edges limit the bandwidth of useful operation and thus define the maximum practical mode size for each wavelength in that range. It has been shown empirically that the mid-point in wavelength between the long and short bend loss edges in holey fibres with a

triangular arrangement of air holes is approximately given by $\Lambda/2$ [32]. For large-mode-area holey fibres, in which $5\,\mu\text{m} < \Lambda < 25\,\mu\text{m}$, all wavelengths of light that are transparent in silica lie on the short-wavelength side of this mid-point. As such, the bending losses of large-mode-area silica holey fibres are expected to decrease with wavelength, for all wavelengths of interest. This is in direct contrast to conventional fibres, in which bending losses increase towards long wavelengths only. As such, it is not obvious to see how these two fibre types will compare in the large-mode-area single-mode regime. Consequently, the ability to accurately predict these losses is essential in order to assess the potential offered by holey fibres, relative to conventional fibres. In addition, another important difference between conventional and holey fibres is the angular symmetry of the index profile. Conventional fibres are typically circularly symmetric, whereas holey fibres are not. Holey fibres usually possess a six fold symmetry, and this may be reflected in the bending losses. As a result, it is important that any model of bending losses in holey fibres can incorporate the effect of the complex refractive index profile.

In the following section, some of the models that have been developed to evaluate bending losses in holey fibres are discussed. These models are all based on analogy with conventional single-mode fibres and the limitations associated with this are explored. The requirements for an accurate model of bend loss in a holey fibre is also outlined.

2.3.2 Modelling bend loss in holey fibres

Background

Predicting the bending losses of holey fibres is a challenging problem. Most of the methods developed for conventional fibres (as summarised in Section 2.2) assume a circularly symmetric index profile and cannot be applied to holey fibres without first replacing the complex refractive index profile with that of an equivalent step-index (ESI) fibre. This approach has been used in a few studies on the modal properties of holey fibres with mixed results. In Refs. [4, 16], the authors demonstrate that the short wavelength bend loss edge in a holey fibre can be qualitatively described using an effective index approach together with the conventional formula for predicting pure bend loss from Ref. [128]. In another study, an ESI-based calculation of pure bend loss is shown to yield good agreement with experimental data for a fibre with $\Lambda = 7.8$ μm and $d/\Lambda = 0.30$, but not for a fibre with $\Lambda = 10$ μm and $d/\Lambda = 0.55$ [32, 131]. This poor agreement is due in part to the difficulties in choosing certain ESI parameters, such as core radius, that are required to assign an

appropriate ESI profile [87].

In recent months, a different method based on a step-index analogy was proposed [132]. In this approach, an approximate formula for pure bend loss, developed for step-index single-mode fibres, is expressed solely in terms of A_{eff}^{FM}, R_o, n_{FM} and n_{FSM}, where n_{FM} is the effective index of the fundamental core mode and n_{FSM} is the effective index of the fundamental cladding mode [129]. In this way, the conventional loss formula can be evaluated for a holey fibre without having to define an ESI profile. However, the modal properties A_{eff}^{FM}, n_{FM} and n_{FSM} of the holey fibre still need to be evaluated. Various methods for calculating these properties in a holey fibre are discussed in Section 1.4. In general, these methods involve numerical solutions to the wave equation and are all fairly computationally intensive. The key to the simplicity of the method proposed in Ref. [132] is that the authors use approximate formulas to define A_{eff}^{FM} and $\sqrt{{n_{FM}}^2 - {n_{FSM}}^2}$ in terms of λ, Λ and d/Λ only. The approximate definitions are based on functions fitted to data generated for infinite, perfectly periodic triangular lattice structures using a plane-wave approach. Where n_{FM} appears on its own in the approximate loss formula, the assumption $n_{FM} = n_{glass}$ is made, resulting in a bend loss dependent only on n_{glass}, λ, Λ and d/Λ. The results presented within Ref. [132] show good agreement with experimental data for the fibres considered. However, the assumption of $n_{FM} = n_{glass}$ is only valid for large values of Λ/λ and d/Λ. These approximations lead to increasing inaccuracy as d/Λ decreases in the large-mode-area regime, as demonstrated in Section A.2, and also means that this method cannot be used to predict any properties of the long wavelength bend loss edge, which occur in holey fibres for $\Lambda/\lambda \ll 1$. In addition, this simple method is restricted solely to holey fibres with a perfect triangular arrangement of air holes in which the core is formed by the omission of a single hole due to the way in which the parameters A_{eff}^{FM} and $\sqrt{{n_{FM}}^2 - {n_{FSM}}^2}$ are defined. This is a significant disadvantage since holey fibre geometry can vary significantly from this basic design, as illustrated in Fig. 1.6 in Section 1.2.4, including different air/glass geometries in addition to hybrid and solid microstructured fibre types. Furthermore, this method ignores the symmetry differences between holey and step-index fibres: holey fibres typically possess a 6-fold symmetric cladding geometry, but can be more complex, such as the case of a triangular core formed by three adjacent rods in the preform [34]. This may have an important influence on the bending losses of these novel fibres and needs to be considered. Also, since this technique is based on a formula derived for single-mode step-index fibres it cannot be used to evaluate the bending losses associated with higher-order

modes. However, this method has the virtues of being both quick and simple to evaluate and is accurate enough to gauge the practicalities of large-mode-area fibre design for simple triangular lattice geometries. Note that the model presented in Ref. [132] is discussed in more detail in Section A.2.

Bend loss model developed here

As mentioned in the introduction to this chapter, at the start of this project, there were no theoretical techniques that could be used to accurately model even the most basic aspects of bend loss in a holey fibre. Simple models based on the step-index analogy were in existence and could be used to show that the bending losses increase towards both long and short wavelengths in a holey fibre [4, 16], but were incapable of accurately assessing the magnitude of these losses. (Note that in recent months, one model has emerged that can be used to assess the magnitude of loss in large-mode-area holey fibres with large air holes, but this method has several limitations, as discussed above [132]). Since the ability to accurately predict bend loss in a holey fibre is essential to the aims of this thesis, the first step was to develop such a model. Furthermore, due to the fact that models based on approximating the holey fibre index profile by an equivalent step-index (ESI) fibre had so far proved unreliable, it was decided that the model developed here should avoid all such ESI approximations, and instead use the full geometrically complex refractive index profile of a holey fibre in all calculations. This approach would remove any inaccuracy resulting from a circularly symmetric representation of the transverse index profile, enabling the real mode shape to be considered and allowing the angular orientation of the bend to be considered in any calculation. The necessity for this is supported by experimental observations of bend loss, in which a dependence on the angular orientation of the fibre has been observed (see Section 4.5).

In addition, in the few studies of bend loss in holey fibres reported at the time of this study [4, 16, 32], the contribution from transition loss is ignored, and calculations based solely on the pure bend loss component are used to evaluate macro-bending losses. This may seem perfectly reasonable, since in studies of macro-bending losses in conventional fibres, pure bend loss is generally assumed to be dominant and transition loss is only considered to be an important contribution for very short lengths of curved fibre [105, 133]. Indeed, the effect of mode distortion is often ignored completely in the macro-bend regime [126, 128]. However, the relative contributions of these two components may well be different in a

Acknowledgements

Firstly, I would like to thank my supervisors; Tanya Monro and David Richardson; Tanya, thank you for your guidance and support, and for your contagious enthusiasm; and Dave, thank you for your advice, support and perspective throughout my PhD. It has been a pleasure to work with both of you.

I would also like to express my appreciation to Kentaro Furusawa, Marco Petrovich and John Hayes, who fabricated the beautiful holey fibers reported in this research. I would like to thank Vittoria Finazzi for her contributions to the theoretical work presented here and for the times spent puzzling over various numerical problems with me. I am also grateful to Matteo Fuocci, who carried out some of the experimental work presented here. My thanks go also to Elanor Tarbox for proof reading my thesis and to Arthur Longhurst, Dave Oliver and David Monro for their computer support and unfailing ability to make my computer well again. I would also like to thank the following people from the ORC for their time and help: Simon Butler, Chris Nash, Heather spencer, Christine stoner, and Eve Smith.

My thanks also go to my friends and fellow PhD students: Ami, for being a wonderful source of perspective, support, friendship and yummy Swedish recipes; to Anoma, for all those long lunches and pep talks and also to Ian and Malcolm; you all listened to me complain, you celebrated my small victories and you made me laugh when I needed to. Thank you. I would also like thank to Vir for her support, to Carla for the much appreciated Maltesers when writing up, to Jim for his assurances that the write-up will be over soon (it is!), to Mell for her understanding and willingness to listen to me rant, and to Heather and Marianne for the wonderful breaks in snowy Switzerland and sunny Dorset.

I am also deeply grateful to my parents and to my sister Ali, for their love and support. You are my best friends and I simply can't thank you enough for everything you have done for both myself and Stu during our PhDs. I would also like to express my thanks to Anne and Bill for your support over these (many) years of student-dom.

And finally, my thanks go to Stu, for far more reasons than I can write here. Thank you. Now we are Drs together!

holey fibre. Indeed, mode distortion may play a more important part in the bend loss of a holey fibre due to the fact that there is no well defined boundary between core and cladding regions. Consequently, the core mode is free to distort out in the gaps between air holes, and this may result in a higher level of mode distortion than in conventional fibres. As a result, the model of bend loss developed here considers the contribution from both transition and pure bend loss components in a holey fibre. The techniques developed to predict these components of loss within a holey fibres are described in Chapter 3, within Sections 3.1, 3.4 and 3.5.

Part II

Numerical and experimental methods

2.4 Overview

As mentioned in Section 1.5, the aims of the study presented here are threefold: (1) to develop methods of accurately predicting bend loss that can be applied to both holey and conventional fibres, (2) to use these techniques to explore the potential offered by holey fibres in the large-mode-area, single-mode regime, and (3) to place their performance in context against conventional step-index fibres. In order to fulfil these aims, it is also essential to be able to accurately predict the effective mode area and modedness of both fibre types. Furthermore, reliable methods of characterising the bend loss, the effective mode area and the bending losses of holey and conventional fibres are also essential to enable comparative studies and also to validate the theoretical techniques developed here.

The chapters in this part describe these experimental and numerical techniques. In Chapter 3 the numerical techniques used here to calculate the effective mode area, the bending losses and to assess the modedness of both holey and conventional fibres are described. Chapter 4 details the procedures that have been developed here to measure these modal properties in large-mode-area fibres. The numerical techniques presented here are also validated via comparison with the experimental results presented in Chapter 4. Note that the experimental and numerical techniques described in the following have been purposefully designed to be suitable for both holey and conventional fibres, to enable direct comparisons to be drawn between the two fibre types.

Chapter 3

Modelling fibres

3.1 Introduction

As discussed in Section 2.4, in order to explore the potential offered by large-mode-area single-mode holey fibres, and to place their performance in context against conventional step-index fibres, methods of predicting the effective area, the modedness and the bending losses of both holey and conventional fibre types are required. The numerical techniques used here to model these three key properties are described in the following.

As discussed in Section 2.3.2, it was decided that the method of modelling bend loss developed here should ideally avoid any ESI approximation, and should instead use the full geometrically complex refractive index profile of a holey fibre in all calculations. In addition, since little was known about the bending losses of holey fibres at the time of this research, it was also decided that the model of bend loss developed here should consider the contribution from both transition and pure bend loss components in a holey fibre. In order to develop methods of predicting transition loss and pure bend loss in a holey fibre, we look back to the methods that have been developed for conventional waveguides and extract elements of these approaches that do not make any assumptions regarding the nature of the modal fields. If we then assume that the modal fields and propagation constants of the straight and bent holey fibres can be evaluated (as is discussed below), the components of bend loss can be evaluated in the following manner: the transition loss can be approximated as a splice loss between two different fibres, after the methods presented in Refs [100, 101, 102], and the pure bend loss can be evaluated by calculating the fraction of the modal field that cannot travel fast enough around the bend to maintain phase with the rest of the mode, after the method presented in Ref. [113]. The methods

from Refs [100, 101, 102, 113] are discussed in Section 2.2, and their adaptation to holey fibres is presented in detail in Sections 3.4 and 3.5.

The biggest challenge with the above approaches to modelling bend loss is therefore the calculation of the modal fields and propagation constants of the straight and bent holey fibre. A selection of techniques capable of modelling the modal fields of straight holey fibres and their associated propagation constants was presented in Section 1.4. However, the method chosen here must also be capable of modelling the modal properties of the bent fibre. In their current form, only methods based on a BPM approach would be capable of this, as all other approaches start from a two-dimensional representation of the transverse refractive index profile, which is assumed to be invariant in the direction of propagation. As mentioned in Section 1.4, BPM approaches are extremely computationally intensive. However, in conventional fibres and waveguides, a conformal transformation is often used to alter the refractive index profile of the straight guide to create an index profile that is invariant in the direction of propagation and that accurately mimics the modal properties of the bent waveguide [114]. This process is described in more detail in Sections 2.2 and 3.3, but essentially involves superimposing a gradient onto the refractive index profile of the straight waveguide. In studies on conventional waveguides, the transformed structure can then be used to evaluate the modal properties of the bent waveguide using a variety of techniques. However, holey fibres possess a complex transverse structure, and the additional gradient present in a refractive index profile transformed in this way precludes the use of many models. For example, the multipole method is only capable of considering circular regions of uniform index embedded in a uniform background material. Techniques that are capable of modelling such a complex structure include those based on beam propagation, finite-element and expansion techniques, all of which are outlined in Section 1.4. However, bend loss is a sensitive function of the refractive index profile, which in a holey fibre contains many wavelength scale features. As such, it is necessary to use a high level of resolution in the numerical grid onto which the index profile is defined. Consequently, techniques based on beam propagation, finite-element and plane-wave methods can become prohibitively computationally intensive. Fortunately, the orthogonal function method described in Section 1.4.3 takes advantage of the fact that the core mode(s) of a fibre are localised to improve the efficiency of the calculations [86, 94, 95]. This technique is similar to the plane-wave approach, in which the modal fields and the refractive index profile are decomposed into plane waves. However, by using localised functions in the decomposition

of the modal fields, this method requires far fewer terms to form an accurate description and as a result can be computationally efficient. Since the modes of the bent fibre are localised for all bend radii of practical interest, this method is chosen here to model the modal fields and propagation constants of both straight and bent holey fibres, as discussed in Sections 3.2 and 3.3.

Of course, the bending losses are not the only modal properties that require evaluation in this study. In order to place any meaningful interpretation on the bending losses, knowledge of the mode area and the modedness of the straight fibre is also required. The mode area can be quite simply extracted from the modal field of the straight fibre via numerical integration, as explained in Section 3.2. However, evaluating the modedness of a holey fibre can be more complicated. Although the orthogonal function method calculates a spectrum of modes in any given fibre, it is necessary to determine the effective index of the holey fibre cladding (n_{FSM}) in order to evaluate which of these modes are actually guided in the core. Since the orthogonal function technique uses localised functions, it is not capable of evaluating the effective index of the (extended) fundamental cladding mode, and another technique must be employed. Here, a commercial plane-wave method is chosen, which can be both accurate and efficient since only a single-unit cell of the cladding microstructure needs to be considered in this case (as explained in Sections 1.4 and 3.5.1) [134]. However, this combination of orthogonal function and plane-wave techniques is not sufficiently accurate for fibres close to cut-off. In this situation it becomes necessary to consider a single method to evaluate the effective indices of both core and cladding modes and the Multipole approach is used instead. Note that all calculations using this technique presented within this thesis are performed by Vittoria Finazzi at the ORC [54], and that the issue of determining modedness is discussed further in Section 3.6. The multipole approach has the added advantage of being able to calculate the confinement losses of all modes present in a holey fibre, something which the orthogonal function technique cannot perform, due to the periodic boundary conditions used. The confinement losses of higher-order modes can be high enough to render a fibre effectively single-mode, which is considered in Section 5.13.

In summary, three different methods of modelling the modal properties of holey fibres are used within this thesis: (1) The orthogonal function technique is used to model the modal fields and propagation constants of both straight and bent holey fibres, with the addition of a conformal transformation in the case of the bent fibre. (2) A commercially available

plane-wave method is used to evaluate n_{FSM} of the straight fibre, which is used to determine the modedness of holey fibres far from cut-off and is also required in the description of pure bend loss (see Section 3.5). (3) The multipole method (via Vittoria Finazzi) is used to evaluate the modedness of holey fibres close to cut-off and to model confinement losses. These techniques are described in the rest of this chapter. The orthogonal function method, developed by Tanya Monro at the ORC [86, 94, 95] is modified slightly here for the study of large-mode-area holey fibres, as described in Section 3.2. However, this description is only designed to be sufficient to explain the basic principles of this technique. For more detail please refer to Refs [86, 94, 95]. The extension of this technique to the bent fibre via a conformal transformation is discussed in Section 3.3. The techniques used to model the transition losses and pure bend losses are then described in Sections 3.4 and 3.5. The various techniques used to determine the modedness of a holey fibre are discussed in Section 3.6. For comparison purposes, conventional large-mode-area step-index fibres are also considered in this study and the methods used to evaluate the parameters of equivalent structures and to model the modal properties of these fibres are also described here, within Sections 3.7.

Note that the holey fibres studied here are typically large core structures with relatively small holes and the scalar approximation is found to be suitable in most cases (see Sections 3.2.6 and 3.3.4). However, note that the fully vectorial version of the orthogonal function technique outlined in Section 3.2 is used to study the effect of polarisation in the bent fibre in Section 4.5.5.

3.2 Modelling the modal properties of straight holey fibres

3.2.1 Introduction

The model developed in Refs [86, 94, 95] is adapted here to calculate the modal properties of straight and bent large-mode-area holey fibres. In this model, the transverse refractive index profile and the modal fields are decomposed using carefully chosen orthogonal functions, which enable the wave equation to be reduced to an eigenvalue equation that can be solved to find the modes of the fibre and their corresponding propagation constants. The transverse refractive index profile is described using a Fourier decomposition and the modal electric field is described using Hermite Gaussian functions. Since the refractive index profile of a holey fibre is typically periodic in nature and the modal field is localised in the centre of the fibre, these functions are a natural choice allowing each quantity to be represented accurately without requiring the use of too many terms. In the following sections, a full vector version of the orthogonal function method is described.

3.2.2 Background

It is assumed that the holey fibre is uniform in the propagation (z) direction, and so the modal electric field can be written as

$$\mathbf{E}_j(x,y,z) = (\mathbf{e}_j^{\mathbf{t}}(x,y) + e_j^z(x,y)\hat{\mathbf{z}})\,\exp(i\beta_j z) \tag{3.1}$$

where β_j is the propagation constant of the jth mode, and $\mathbf{e}^{\mathbf{t}} = e_x\hat{\mathbf{x}} + e_y\hat{\mathbf{y}}$ and e_j^z are the transverse and longitudinal components of the modal electric field, respectively. Inserting this ansatz into the full vector wave equation, the following pair of coupled equations for the transverse modal electric field components $e_x(x,y)$ and $e_y(x,y)$ is obtained:

$$\left[\frac{\nabla^2}{k^2} - \frac{\beta^2}{k^2} + n^2\right] e_y = \frac{-1}{k^2}\frac{\partial}{\partial y}\left(e_x\frac{\partial \ln n^2}{\partial x} + e_y\frac{\partial \ln n^2}{\partial y}\right) \tag{3.2}$$

$$\left[\frac{\nabla^2}{k^2} - \frac{\beta^2}{k^2} + n^2\right] e_x = \frac{-1}{k^2}\frac{\partial}{\partial x}\left(e_x\frac{\partial \ln n^2}{\partial x} + e_y\frac{\partial \ln n^2}{\partial y}\right) \tag{3.3}$$

where $k = 2\pi/\lambda$ is the wavenumber, $n = n(x,y)$ is the transverse refractive index profile and the subscript labelling the mode number (j) has been dropped for brevity [103]. To solve Eqs 3.2 and 3.3, the transverse refractive index profile and the modal electric field are decomposed using orthogonal functions. The choice of functions is crucial in making this method efficient and accurate, as discussed in Sections 3.2.3 and 3.2.4. Note that it is necessary to use both odd and even functions in these decompositions in order to accurately model the asymmetric modes of the bent fibre.

3.2.3 Transverse refractive index profile

The transverse refractive index profile, is described using a Fourier decomposition with $4P$ terms performed over the entire fibre profile.

$$n^2 = \sum_{a,b=0}^{P-1} p_{ab} \cos\mathcal{X} \cos\mathcal{Y} + \sum_{a,b=0}^{P-1} q_{ab} \sin\mathcal{X} \cos\mathcal{Y} + \sum_{a,b=0}^{P-1} r_{ab} \cos\mathcal{X} \sin\mathcal{Y} + \sum_{a,b=0}^{P-1} s_{ab} \sin\mathcal{X} \sin\mathcal{Y} \tag{3.4}$$

where

$$\mathcal{X} = \frac{2a\pi x}{l}, \quad \mathcal{Y} = \frac{2b\pi y}{l} \tag{3.5}$$

and l is the transverse extent of the structure. In all the calculations reported here, $l = 10\Lambda$, which is determined by evaluating the convergence of the propagation constant as a function of l. For any given holey fibre structure, the coefficients p_{ab}, q_{ab}, r_{ab} and s_{ab} are evaluated by performing overlap integrals and need only to be calculated once for any structure. (Please refer to Ref. [94] for more details).

Fig. 3.1 shows the reconstructed index profile for a fibre with $\Lambda = 12.2$ μm and $d/\Lambda = 0.4$ for increasing values of P (i.e. for an increasing number of terms in the Fourier expansion). Figs 3.1 (a-f) correspond to cross-sections along $x = 0$ through the reconstructed index profile for $P = 50$ to 350. The exact refractive index profile is shown by the dashed line in each plot. These figures show that the refractive index profile can be represented quite accurately using relatively few terms and that the reconstruction can be improved by increasing the number of terms used. Note that the number of terms (P) required to describe the refractive index profile accurately increases towards small values of d/Λ due to the fact that the higher frequency sine and cosine functions are needed to describe the small air holes [86]. For the large-mode-area fibres considered here, with values of d/Λ ranging from 0.2 to 0.5, $P = 200$ is found to be sufficient. This value is determined by evaluating the convergence of the propagation constant (β) as a function of P. Note that the number of points across the computational box used in all the calculations presented here is 2801×2801 (also determined by evaluating the convergence of β).

Note that due to the fact that the transverse refractive index profile of a holey fibre is a discontinuous function, an oscillatory behaviour known as the Gibbs phenomenon is observed in the reconstructed refractive index profile. This artefact can be improved by using more terms in the expansion, but as P increases, these oscillations do not decrease significantly in amplitude. Instead, they increase in frequency, compressing in location towards the edge of each air hole. It is not possible to gauge the impact of these oscillations

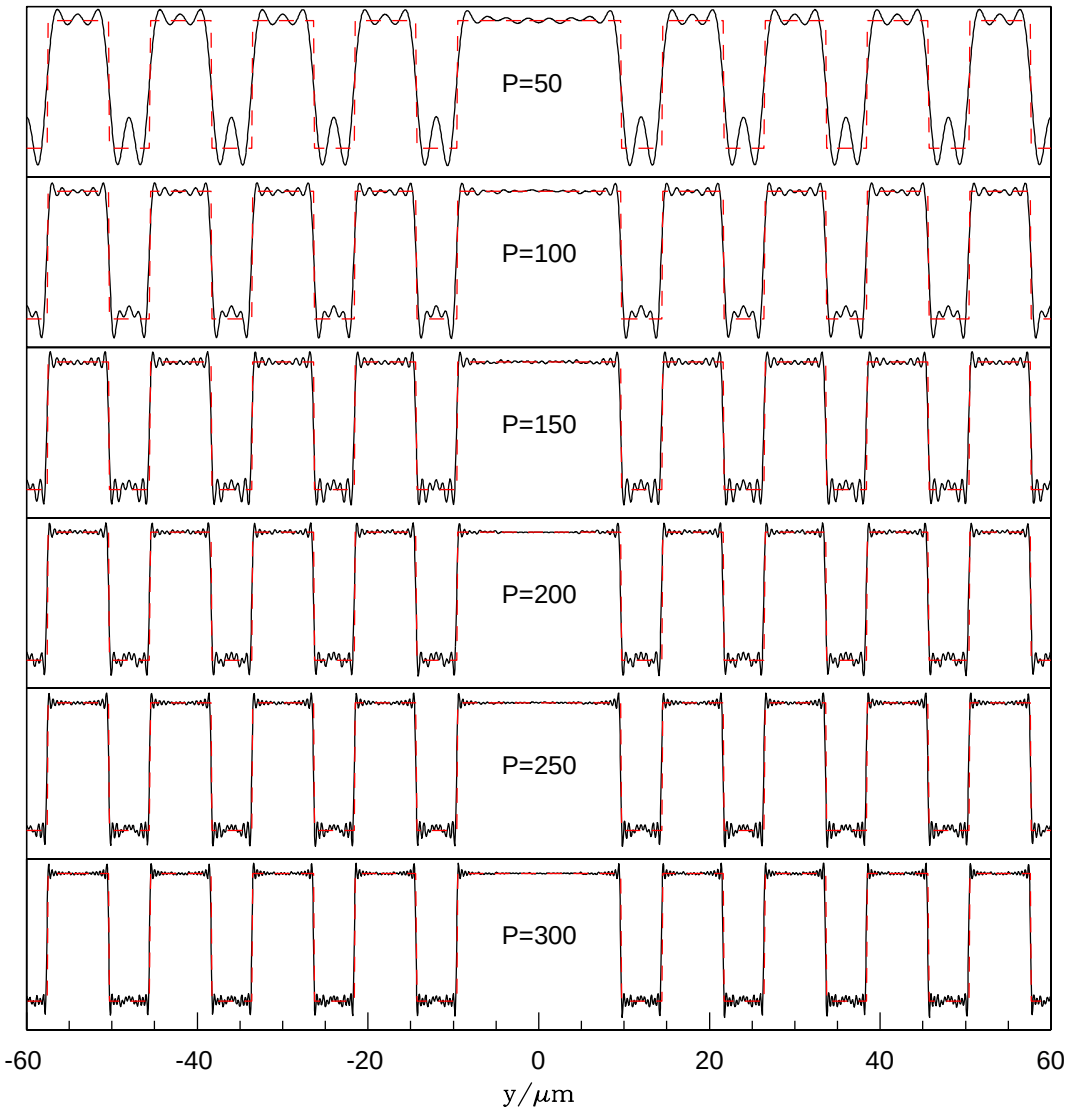

Figure 3.1: (a) Cross-sections along $x = 0$ of the reconstructed refractive index profile for a holey fibre with $\Lambda = 12$ μm and $d/\Lambda = 0.4$) for different numbers of terms used in the decomposition: (a) $P = 50$, (b) $P = 100$, (c) $P = 150$, (d) $P = 200$, (e) $P = 250$, (f) $P = 300$. The exact refractive index profile is shown by the dashed line in each plot and ranges from 1.0 (air) to 1.449631 (silica at 1064 nm).

since they cannot be removed and it is therefore difficult to state what effect they may have on the overall result. However, the frequency of these oscillations is small relative to the wavelength of light and the refractive index fluctuations 'seen' by the light field will therefore be averaged out. Further evidence that the effect of the Gibbs phenomenon on the overall result is small is the excellent agreement between theoretical predictions and measured quantities achieved using this approach [86].

As periodic basis functions are used to describe the refractive index profile here, this method is most efficient for periodic structures. However, this is not a restriction and

non-periodic refractive index profiles can also be accurately represented [13].

3.2.4 Modal electric field

The modal electric field from Eq. 3.1 is expanded as

$$\mathbf{e}^t(x,y) = \sum_{a,b=0}^{F-1} (\varepsilon_{ab}^x \psi_a(x)\psi_b(y)\hat{\mathbf{x}} + \varepsilon_{ab}^y \psi_a(x)\psi_b(y)\hat{\mathbf{y}}) \tag{3.6}$$

where F is the number of terms in the expansion and the ψ_a and ψ_b are elements of the following orthonormal set of Hermite-Gaussian basis functions which have a characteristic width ($w_m = m_w\Lambda$) and are centred on the fibre core ($x = y = 0$):

$$\psi_i(x) = \frac{2^{-i/2}}{\sqrt[4]{\pi}\sqrt{i!w_m}}\ exp\left(\frac{-x^2}{2w_m^2}\right) H_i\left(\frac{x}{w_m}\right) \tag{3.7}$$

Here, H_i is the Hermite polynomial of order i. Note that the same functions can be used for both x and y components in the expansion of the modal field in Eq. 3.6 because the Hermite Gaussians are a complete basis set. Furthermore, due to the fact that the modal fields of the fibres investigated here are typically symmetric structures (and the level of asymmetry in the bent mode is not great) there is no compelling reason to choose different functions for the x and y components in the field expansion.

3.2.5 Solving the wave equation

By substituting the decompositions for the refractive index profile and the modal fields into the vector wave equation, the latter can be reduced to an eigenvalue problem by making use of the orthonormality of the Hermite-Gaussian basis functions. This process is discussed in detail in Ref. [86] and [94] for the case where only even functions are used in both of the decompositions. In this case, the x and y-components of the wave equation (Eqs 3.2 and 3.3) decouple and the eigenvalue problem thus consists of two eigenvalue equations, representing the x and y-components of the modal field and associated propagation constants. For the case described here, the x and y-components of the wave equation are coupled and after substitution with each decomposition, reduce to a single, more complex, eigenvalue equation. By numerically solving this eigenvalue equation at a particular wavelength, the real part of the propagation constant(s) (β_x and β_y) and the coefficients in the field expansion (ε_{ab}^x and ε_{ab}^y) can be calculated for the x and y-components of each mode present in the fibre at that wavelength. The coefficients in the field expansion can then be used to construct the modal fields of the fibre. The solution to the eigenvalue equation produces $2F^2$

eigenvalue/eigenvector pairs for each wavelength considered. However, only a few of these pairs (or two for the case of a single-mode fibre) correspond to guided modes of the fibre for each wavelength considered. The guided modes can be distinguished by extracting the eigenvalues (β_i^2/k^2) that fall within the range allowed by the structure. These are given by $\mathrm{n_{FSM}} < \beta^2/\mathrm{k}^2 < \mathrm{n_{glass}}$, where $\mathrm{n_{glass}}$ is the refractive index of glass (i.e. the core) and $\mathrm{n_{FSM}}$ is the effective index of the cladding region. Methods for evaluating $\mathrm{n_{FSM}}$ are discussed in Section 3.5.1.

Since the Hermite Gaussian functions used to describe the modal fields form a complete basis set, the characteristic width ($w_m = m_w\Lambda$) can be chosen arbitrarily. However, if a value of w_m is chosen to suit the particular fibre geometry and operation wavelength, the number of Hermite-Gaussian functions (F) required to form an accurate description can be minimised. For $\Lambda \approx 2\ \mu$m at a wavelength of 1550 nm, a characteristic width of 0.5Λ was found to be optimal [86]. This seems physically reasonable, as the effective mode area should be approximately that of the core. For holey fibres in which Λ is sub-wavelength, however, the effective mode area can be considerably larger than the core size and w_m must be larger than 0.5Λ. By a similar argument, w_m should ideally be smaller than 0.5Λ for holey fibres with a large Λ. For the large-mode-area fibres considered here, with $7\,\mu\mathrm{m} < \Lambda < 20\,\mu\mathrm{m}$ and $0.2 < d/\Lambda < 0.6$, a characteristic width of 0.32Λ has been found to be optimal in the wavelength range $308 - 1600$ nm. For this value of w_m, 12 Hermite-Gaussians are then sufficient to produce a good description of the mode. However, the method of calculating bend loss used here (described in Section 3.5) is extremely sensitive to the exact shape of the mode and so the accuracy of the modal representation is particularly important. As a result, 32 Hermite-Gaussians are used to describe the modal field in this implementation. As before, these optimum values are determined by evaluating the convergence of the modal effective index. (Note that for the triangular core fibres discussed in Chapter 6, the optimum value of m_w is found to be 0.31 and that for conventional step-index fibres, $w_m = 0.52\Lambda$ is optimal.) Typical graphs of the effective modal index (shown for the x-polarised mode) as a function of F and m_w are shown in Figs 3.2 (a) and (b) respectively. Note that the difference in the predicted values of $\mathrm{R_c^{FM}}$ for the large-mode-area holey fibres considered here at 1550 nm is typically less than 1% for calculations of the bent modal field made with $F = 32$ and $F = 34$, and $m_w = 0.32$ and $m_w = 0.34$.

Once the modal field has been constructed, the effective area ($\mathrm{A_{eff}}$) can be calculated

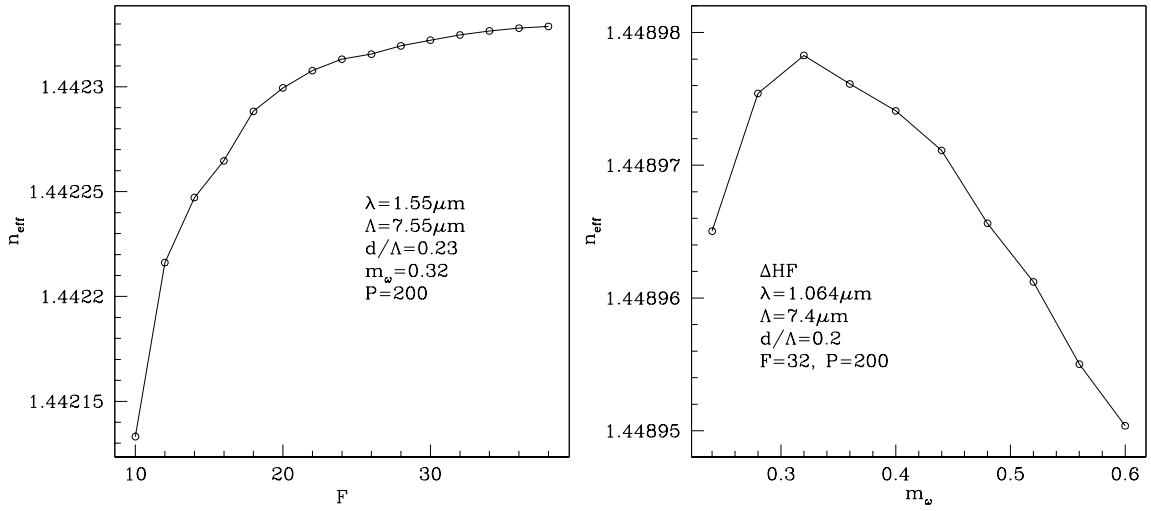

(a) (b)

Figure 3.2: (a) Effective modal index (for the x-polarised mode) for a holey fibre with $\Lambda = 7.55$ μm and $d/\Lambda = 0.23$) at 1550 nm. (b) Effective modal index (for the x-polarised mode) for a triangular core holey fibre with $\Lambda = 7.4$ μm and $d/\Lambda = 0.2$) at 1064 nm.

via numerical integration using the following expression from Ref. [135]:

$$\mathrm{A_{eff}} = \frac{(\int_{-\infty}^{\infty}\int_{-\infty}^{\infty}|E(x,y)|^2 dxdy)^2}{\int_{-\infty}^{\infty}\int_{-\infty}^{\infty}|E(x,y)|^4 dxdy} \tag{3.8}$$

Note that only the effective area of the fundamental mode (FM) is considered within this study and is referred to by $\mathrm{A_{eff}^{FM}}$.

3.2.6 Discussion

Although the full vectorial version is outlined in the above description, the scalar approximation is found to be suitable for calculations of the straight mode for all the fibres considered in this study, which possess low values of NA. For all fibres considered in this study there is negligible difference between scalar and vector calculations of the fundamental mode of the straight fibre. For example, for a fibre with $\Lambda = 15.0$ μm and $d/\Lambda = 0.63$, which represents the most highly multi-mode structure considered within this thesis, the propagation constant for the x-polarised mode differs only in the 10^{th} significant figure between scalar and vector calculations at 1064 nm. Furthermore, the scalar version is also found to be suitable for calculating the modes of the bent fibre, with similarly small differences in β observed between scalar and vector calculations. As a result, the full vector model is only used here when considering the effects of polarisation in detail. This is discussed further in Section 3.3.4. Unless otherwise stated, all results presented here have been calculated

using the scalar version of the modal model above.

3.2.7 Example calculation

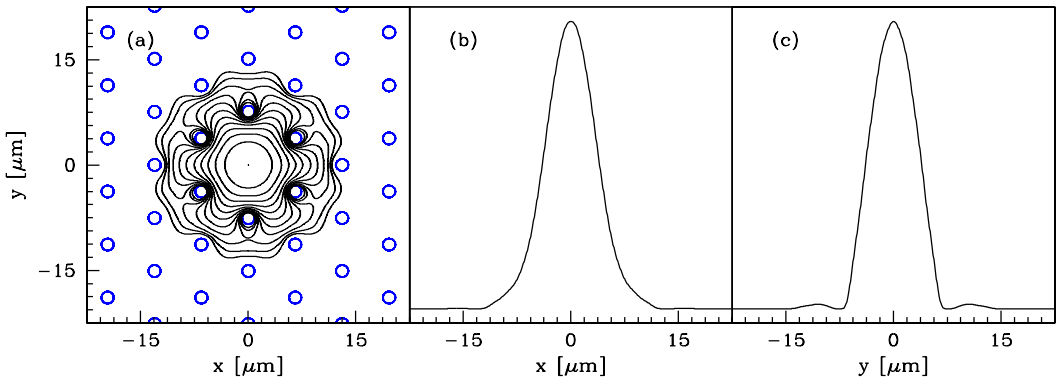

Figure 3.3: (a) Contour plot of the calculated modal intensity for holey fibre HF_1 at 1550 nm. Contours are spaced by 2 dB. (b) and (c) show cross-sections of this modal intensity profile in the x and y directions respectively (the y-axis for (b) and (c) has arbitrary units). In this calculation, 200 functions have been used in the Fourier decomposition of the refractive index profile (P) and 32 Hermite-Gaussians (F) have been used in the modal field expansion (each with a characteristic width (m_w) of 0.32).

As an example, Fig. 3.3 shows the calculated intensity profile for the fundamental core mode of the single-mode holey fibre HF_1 ($\Lambda = 7.55$ μm and $d = 1.71$ μm) at 1550 nm. Fig. 3.3 (a) shows a contour plot of the modal intensity profile and Figs 3.3 (a) and (b) show cross-sections of the modal intensity in the x and y directions respectively. This fibre has an effective area (A_{eff}^{FM}) of 130 μm^2 and an effective index (n_{FM}) of 1.44233 (Note that only the central region of the structure used in the calculation is shown). For all predicted values, the effective area is calculated using the definition in Ref. [135].

3.3 Modelling the modal properties of bent holey fibres

3.3.1 Representing the bent fibre

To model the modal fields of a bent holey fibre, the above method is used together with a conformal transformation [114]. The conformal transformation is used to replace the bent fibre with a straight fibre that has an equivalent refractive index profile and is performed before the mode calculation. The equivalent refractive index profile is found by expressing the scalar wave equation in terms of a local coordinate system that follows the curvature of the fibre [114]. (The scalar approximation is valid for the fibres considered here as discussed

in Sections 4.5.3 and 4.5.5.) A fibre, bent in the y direction for example, can be represented by a straight fibre with an effective refractive index distribution of

$$n_b{}^2(x,y) = n^2(x,y)(1 + 2y/R_o) \tag{3.9}$$

where R_o is the radius of curvature and $n(x,y)$ is the refractive index profile of the straight fibre. Thus, by applying the transform in Eq. 3.9 to the refractive index profile of a straight holey fibre, an index profile that mimics the modal properties of a bent holey fibre can be defined. For example, the refractive index profile of holey fibre HF_1, shown in Figs 3.4 (a) and (b), is transformed using Eq. 3.9 for a bend radius of 14.5 mm, as shown in Fig. 3.4 (c). (Note that only the central region of the structure is shown).

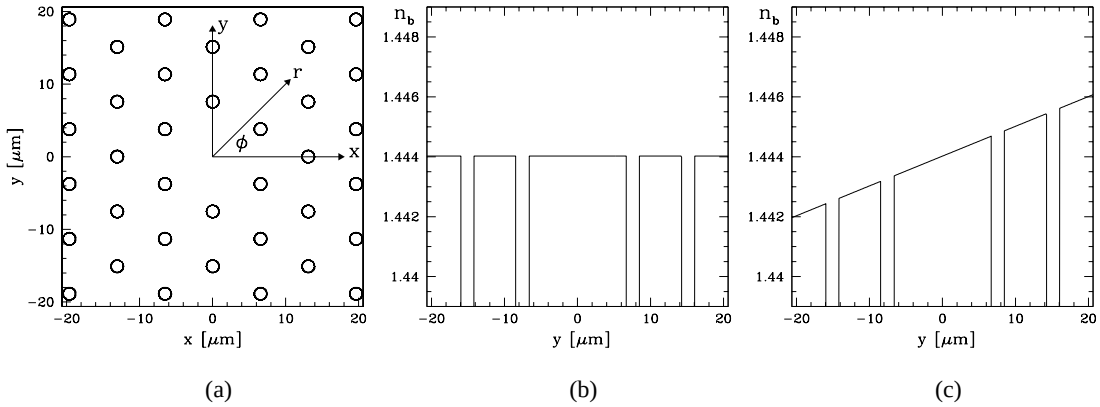

Figure 3.4: (a) Cross-section through centre of holey fibre HF_1. (b) Transverse slice along $x = 0$ through (a), (c) Transverse slice along $x = 0$ for the refractive index profile in (a) transformed using Eq. 3.9 for a bend in the y direction, $R_o = 14.5$ mm.

These figures show clearly that the transform in Eq. 3.9 superimposes a gradient onto the refractive index of the straight fibre in the direction of the bend. One can see, intuitively, that the mode will distort outwards in the direction of the bend, towards the region of higher refractive index. Furthermore, since the gradient is, by definition, proportional to the severity of the bend, one can see that the mode will become increasingly distorted towards tighter bend radii. This can be seen in Fig. 3.6, which is discussed in Section 3.3.3.

3.3.2 Calculating modal properties

Once the equivalent index profile has been determined, the modal calculation is performed as for a straight holey fibre, with the refractive index profile described using the Fourier decomposition in 3.4. As for the straight holey fibres, P=200 in the Fourier decomposition is sufficient to produce an accurate description. Figs 3.5 (a) and (b) show cross-sections

through reconstructed index profiles using $P = 200$ for a holey fibre with $\Lambda = 12$ μm and $d/\Lambda = 0.4$. Fig. 3.5 (a) shows the reconstructed index profile for the straight fibre and Fig. 3.5 (b) shows the reconstruction of the same index profile that has been transformed using Eq. 3.9 for a bend radius of $R_o = 4.4$ cm in the y direction. Although these profiles look almost identical at first sight, the gradient imposed in (b) can be seen to be accurately represented in the index decomposition by dividing (b) by (b), as shown in Fig. 3.5 (c).

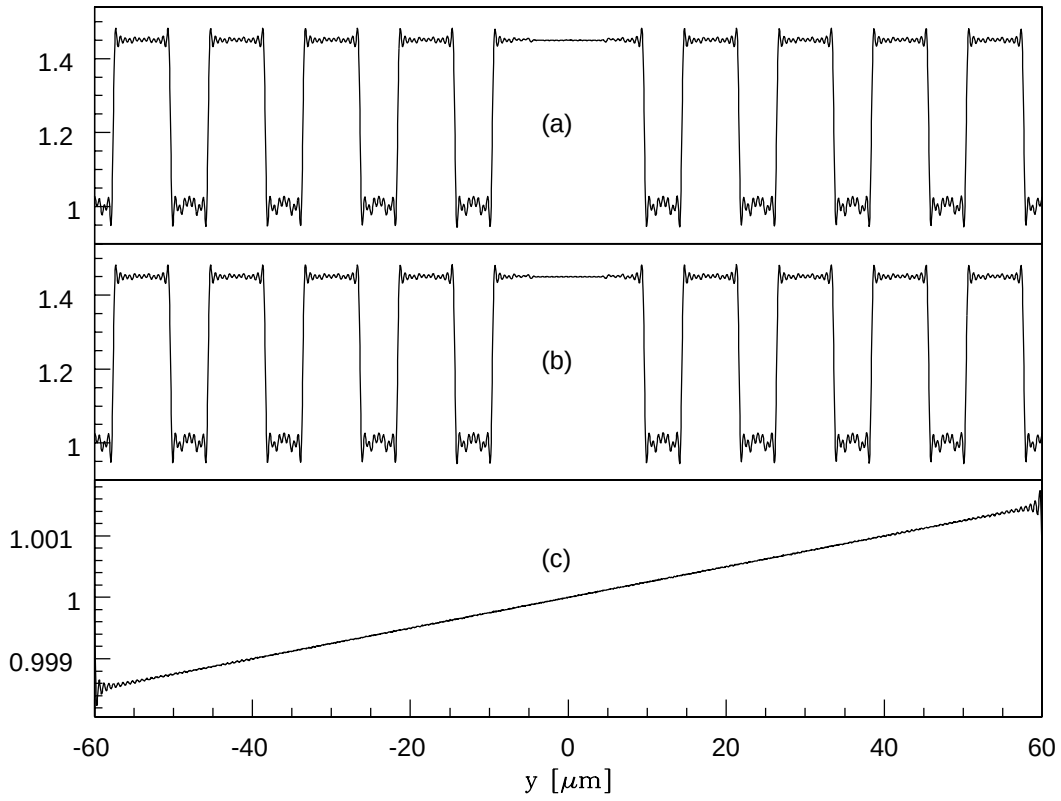

Figure 3.5: Cross-sections along $x = 0$ of the reconstructed index profile for a holey fibre with $\Lambda = 12$ μm, $d/\Lambda = 0.4$ for (a) straight fibre and (b) bent fibre, with a bend of $R_o = 4.0$ mm in the y direction. In both calculations $P = 200$. (c) The ratio of (b)/(a).

3.3.3 Example calculations

Example modal profiles for bent fibres are shown in Fig. 3.6 for fibre HF_1 ($\Lambda = 7.55$ μm and $d/\Lambda = 0.23$). Figs 3.6 (a) and (b) show the intensity distribution at 1550 nm for bends in the x direction of radius 25 mm and 19 mm respectively. Fig. 3.6 (c) shows slices in the x direction; the solid line corresponds to the mode of the straight fibre (shown in Fig. 3.3), the dotted line to the mode in Fig. 3.6 (a) and the dashed line to the mode in Fig. 3.6 (b). Similarly, Figs 3.6 (c) and (d) show the intensity distribution at 1550 nm for bends in

the y direction of radius 25 mm and 19 mm respectively. Fig. 3.6 (e) shows slices in the y direction; as before the solid line corresponds to the mode of the straight fibre (shown in Fig. 3.3), the dotted line corresponds to the mode in Fig. 3.6 (c) and the dashed line corresponds to the mode in Fig. 3.6 (d).

These figures show clearly that, as is expected, the mode of the bent fibre is asymmetric in shape and shifts away from the centre of the fibre towards the outside of the bend. We can also see that the mode extends further into the cladding and becomes increasingly distorted with decreasing bend radius. The asymmetry in the position and shape of the mode means that the odd terms in the Hermite-Gaussian expansion (odd values of a and b in Eq. 3.6) become essential in forming an accurate description due to the fact that Hermite Gaussian functions used to describe the modal field (Eq. 3.6) are centred on the fibre core. Indeed, the values stated previously ($F = 32$ and $m_w = 0.32$) were chosen to represent the modal field sufficiently accurately for our bend loss calculations.

Using this approach, the pure bend loss can also be studied as a function of wavelength. As mentioned previously, holey fibres possess a short wavelength bend loss edge in addition to a more conventional long wavelength loss edge. The increase in loss towards short wavelengths results from the fact that the numerical aperture decreases strongly with wavelength, causing the mode to suffer a greater perturbation in response to bending. This is illustrated in the predicted mode profiles shown in Figs 3.6 (g) and (h), calculated for fibre HF_1 at 633 nm, bent in the x direction for $R_o = 80$ mm and $R_o = 70$ mm respectively. Indeed, from the transverse cross-sections shown in Fig. 3.6 (i) for the bends at 633 nm, and in Fig. 3.6 (c) for bends in the same direction at 1550 nm, it can be seen that the overall degree of mode distortion is similar for the two wavelengths despite the fact that the bend radii are significantly larger for the examples shown at 633 nm.

The modal model outlined here can consider arbitrary index profiles and the exact refractive index profile of a real holey fibre can be extracted from a SEM to calculate the modal fields. However, an idealised index profile is typically used for simplicity, in which measurements of Λ and d are extracted directly from a scanning electron microscope image of the real fibre. This is generally a fair assumption for large-mode-area fibres, in which circular air holes are typically arranged on an almost perfectly regular triangular lattice. Indeed, in these calculations it is possible to take further advantage of this symmetry by considering only one half of the fibre, since even in the bent fibre the refractive index profile possesses a two-fold symmetry. However, the model implemented here has been kept

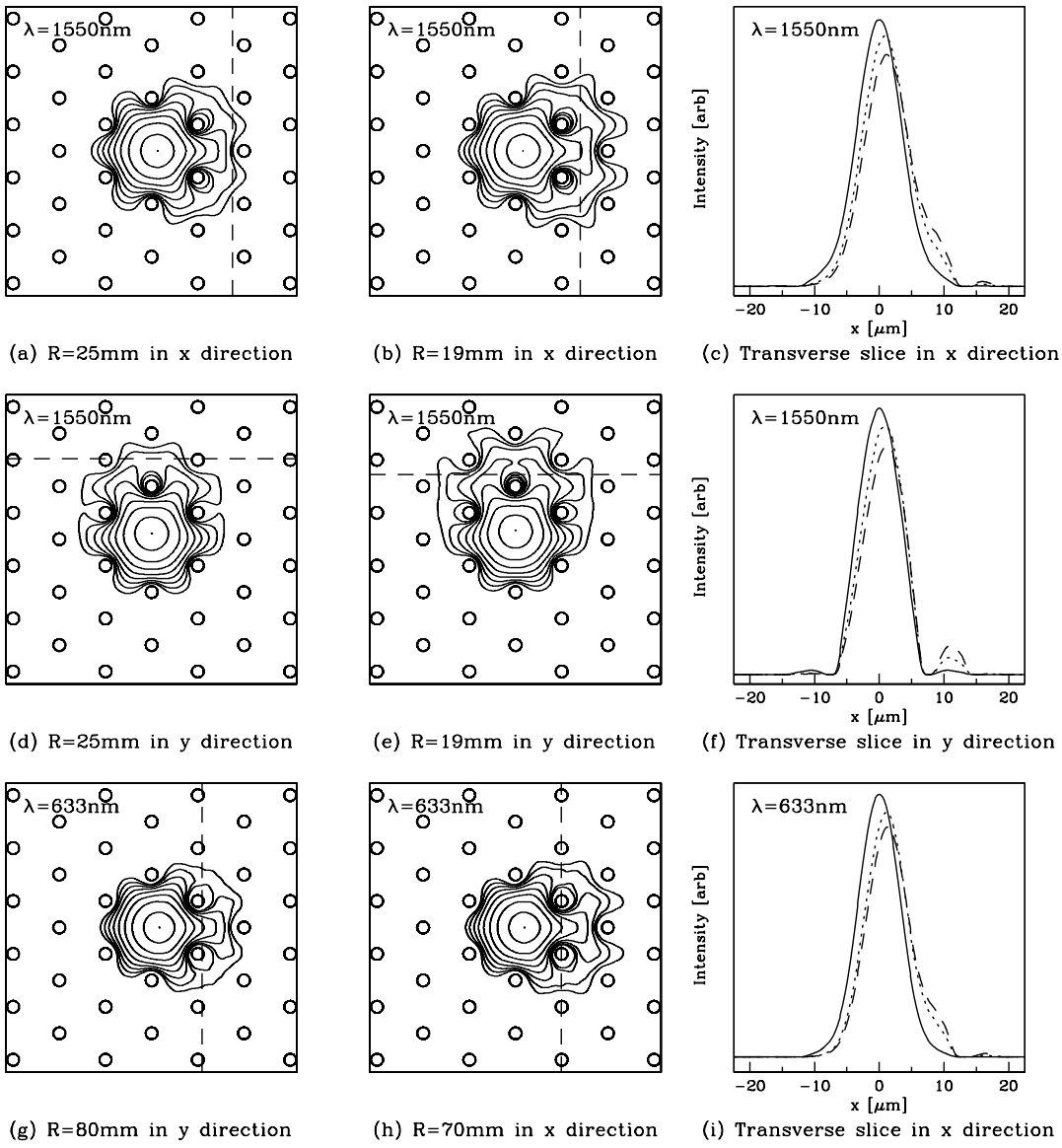

Figure 3.6: Parts (a), (b), (d), (e), (g) and (h) show calculated modal intensities for HF_1. The contours are spaced by 2 dB. The dashed line on each mode profile corresponds to the distance x_r in our model of pure bend loss, defined in Section 3.5. Figs (c) and (f) each show three transverse slices along the x and y direction respectively. The solid line in each case corresponds to the mode of the straight fibre at 1550 nm (shown in Fig. 3.3), the dotted line corresponds to the mode in (a) and (d) respectively ($R_o = 25$ mm) and the dashed line corresponds to the mode in (b) and (e) respectively ($R_o = 19$ mm). Fig. (i) shows three transverse slices along the x direction where the solid line corresponds to the mode of the straight fibre at 633 nm (not shown), the dotted line corresponds to the mode in (g) ($R_o = 80$ mm) and the dashed line corresponds to the mode in (h) ($R_o = 70$ mm).

as general as possible to enable more complex fibre geometries to be considered. (However, note that within this thesis, only results from idealised index profiles with at least a two-fold symmetry are considered). Note also that the refractive index of silica is calculated using

the Sellmeier Equation [135], which is given in Section C.

3.3.4 Discussion

Recall that the conformal transformation used to represent the transverse refractive index profile of the bent fibre, as described in Section 3.3.1, is defined using the assumption that the bend radius (R_o) is within the macro-bend regime, in which $R_o \gg a$, where a is the core radius. Consequently, one may assume that the predicted modal properties of the bent fibre, calculated using this conformal transformation, are valid for all bend radii that satisfy the condition $R_o \gg a$, which represents all bend radii considered here. However, we find that the macro-bend assumptions in the conformal transformation cause the calculated effective modal indices to become non-physical at bend radii that are defined as macro-bends, i.e. for $R_o \gg a$. This non-physical results occurs for the following reasons: as the fibre is progressively bent, the gradient imposed on the refractive index profile by the conformal transformation increases. This has a direct result on the effective modal index of the fundamental core mode, causing it to increase as the bend radii is reduced. At some radii, the effective index of the fundamental core mode thus becomes larger than the index of silica, which is non-physical. However, for all the fibres considered here, we find this non-physical result occurs at bend radii that are much smaller than the critical bend radius (R_c), which is defined as the radius at which the bend loss of the fundamental mode is equal to 3 dB per loop. Since $R_o = R_c$ is typically used to mark the radius at which a given fibre is no longer useful for transmission applications, the regime of $R_o \ll R_c$ is of no interest in this study and none of the results presented within this thesis are significantly affected by the macro-bend assumption within the conformal transformation.

Furthermore, we find that the scalar approximation can be applied to the bent fibre for all the fibres considered in this study, which possess low values of NA and are only considered in the macro-bend regime. Indeed, for the holey fibre with the largest core and highest NA studied here ($\Lambda = 15$ μm and $d/\Lambda = 0.63$) there is less than 5% difference between the critical bend radius of the fundamental mode calculated using the scalar and vector version of the model presented above (see also Sections 4.5.3 and 4.5.5). This is advantageous since 32 Hermite-Gaussians are used in the expansion of the modal field and the numerical simulations are a approximately 6 times faster for the scalar approximation than those for the fully vectorial approach (typical computation time for the scalar version is ≈ 5 hours, compared to ≈ 30 hours for the fully vectorial version). However, the full

vector version is used for studying the effects of the polarisation of the mode in detail in Section 4.5.5.

3.4 Modelling transition loss

Transition losses occur where the curvature of the fibre changes suddenly, such as at the beginning and end of a macro-bend. As light travels into the curved fibre, the modal field distorts radially outwards, evolving over some length scale into the mode of the bent fibre. Power is lost in this transition if the length scale is too short for an adiabatic change in mode shape to take place. In this model, a worst case scenario of an abrupt change of curvature from $R = \infty$ to $R = R_o$ is considered with the assumption that all power is lost instantaneously to radiation. In this approximation, the transition loss is analogous to a splice loss between the mode of the straight fibre and the mode of the bent fibre, and so the transition loss (in dB) is;

$$\mathrm{TL} = -10\log_{10}(\sigma) \tag{3.10}$$

where

$$\sigma = \left(\frac{|\iint E_o \cdot E_b^* \; dx\, dy|^2}{\iint E_o \cdot E_o^* \; dx\, dy \iint E_b \cdot E_b^* \; dx\, dy} \right) \tag{3.11}$$

where $E_o = E_o(x, y)$ is the field distribution of the straight fibre and $E_b = E_b(x, y)$ is the field distribution of the bent fibre and $\int$ implies integration from $-\infty$ to $+\infty$ [102].

The assumption that all power is lost as radiation, instantaneously, and the fact that mode coupling is ignored, results in overestimated losses. In reality, power is lost through coupling to higher-order, cladding, radiation and backward propagating modes, which is neither an instantaneous or one way process as power can be coupled back into the core mode(s). Despite this overestimation, this method can be used to gauge the order of magnitude of this component of bend loss and to predict trends relating to the fibre design. In addition, since the transition loss is calculated directly from the distorted modal field of the bent fibre, this method can also be used to study the effect of the angular orientation of the fibre in the bend.

3.5 Modelling pure bend loss

Pure bend loss is defined as the continual loss of radiation that occurs along any curved section of fibre and is related to the inability of the tails of the mode to successfully navigate the bend. The method used here to model the pure bend loss of a holey fibre is based on a method developed for predicting the pure bend loss of slab waveguides [113]. Fig. 3.7 depicts a guided mode propagating in the z direction around a bend in the x plane that has a radius of curvature R_o. For the mode to propagate along a curved trajectory without

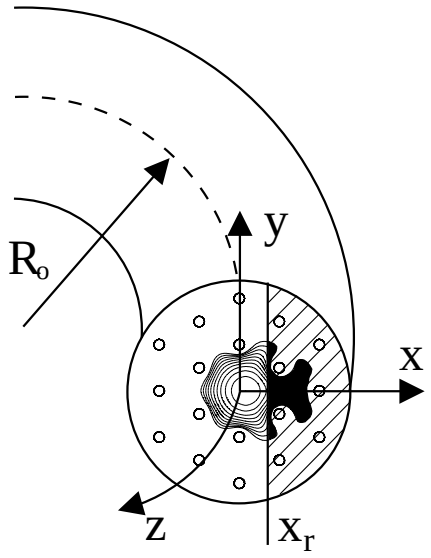

Figure 3.7: Mode propagating in the z direction around a bend of radius R_o in the x direction.

suffering loss, the local velocity along the phase fronts of the mode must decrease on the inside of the bend and increase on the outside of the bend in order to maintain a constant angular velocity across the mode. At some distance towards the outer tails of the mode (defined as $x = x_r$), the required phase velocity will exceed the local speed of light. Since the tails of the mode propagate in the cladding of the fibre, this maximum speed is given by $\mathrm{c}/\mathrm{n_{clad}}$, where c is the speed of light in a vacuum and $\mathrm{n_{clad}}$ is the refractive index of the cladding region. In a holey fibre, the cladding index is assumed to be equal to the effective index of the fundamental space filling mode ($\mathrm{n_{clad}} = \mathrm{n_{FSM}}$). Note that only the $\mathrm{n_{FSM}}$ of the straight fibre is required in this calculation since it is this quantity that represents the maximum (effective) local speed in the microstructured cladding region. As such, the distance from the centre of the fibre at which the phase fronts of the mode are required to travel faster than the local speed of light is given by;

$$x_r = \left(\frac{\beta_b}{\beta_{\mathrm{FSM}}} - 1\right) R_o \tag{3.12}$$

where β_b is the propagation constant of the mode of the bent fibre and $\beta_{\mathrm{FSM}} = \mathrm{n_{FSM}k}$, is the propagation constant of the fundamental mode of the cladding structure, where $k = 2\pi/\lambda$. Note that the derivation for x_r is shown in Section A.1. We then assume that the fraction of power in the guided mode at $x > x_r$ (f_o) is lost as radiation over some length scale (L), with a power decay rate of;

$$P = P_o e^{-2\alpha z} \tag{3.13}$$

where P_o is the power in the guided mode before the bend, P is the power in the guided mode at the end of the bend, z is the length of the curved section, and α is the pure bend loss in units of Np/m (1 Np $= -0.5ln(P_{in}/P_{out})$). At $z = L$, the remaining power in the modal field is given by $P = P_o - f_o$. If this expression is substituted into Eq. 3.13, then the attenuation constant is defined as $\alpha = (f_o/P_o)/(2L)$, where f_o/P_o is the fraction of modal power lost and is given by;

$$\frac{f_o}{P_o} = \frac{\int_{-\infty}^{\infty}\int_{x_r}^{\infty} E_b \cdot E_b^* \, dx\, dy}{\int_{-\infty}^{\infty}\int_{-\infty}^{\infty} E_b \cdot E_b^* \, dx\, dy} \tag{3.14}$$

for a bend in the x direction, where $E_b = E_b(x, y)$ is the modal field of the fibre in the bend. The pure bend loss in units of dB/m is then given by:

$$\text{PBL} = \frac{4.343}{L}\frac{f_o}{P_o} \tag{3.15}$$

In Ref. [113], it was assumed that the length scale, L, was equal to one Rayleigh range ($L = Z_R$). However, from detailed calculations, this choice of L is found to produce an non-physical dependency on mode size. For any waveguide, an increase in the NA results in tighter mode confinement and hence lower bend loss. However, the Rayleigh range decreases so rapidly with mode size that for $L = Z_R$, small increases in NA (and hence small decreases in mode size) can actually result in a larger value of predicted bend loss, which is non-physical. Instead, an alternative length scale is proposed, which is based on a simplified ray approach as described in the following. Fig. 3.8 shows a section of fibre with a radius of curvature R_o. The propagation axis (z) is shown by a solid line and the dashed line traces the position of $x = x_r$ around the fibre. D is the distance from the centre of the core to the outermost hole in the cladding. The fraction of the modal field beyond $x > x_r$ is assumed to be no longer guided by the fibre and instead travels along the tangent to x at $x = x_r$, leaving the fibre completely at the outer boundary of the micro-structured cladding. The length scale, L, over which this occurs is then given by:

$$L = \sqrt{((R_o + D)^2 - (R_o + x_r)^2)} \approx \sqrt{2R_o(D - x_r)} \tag{3.16}$$

Using this approximate ray approach, the predicted bend loss decreases with increasing NA as expected. For all holey fibres in this study, 7 rings of holes are assumed, and D is taken to be $7\Lambda + 0.5d$.

Due to the fact that all mode coupling is ignored in this model of pure bend loss, the magnitude of the loss is overestimated, as expected. However, via comparison with

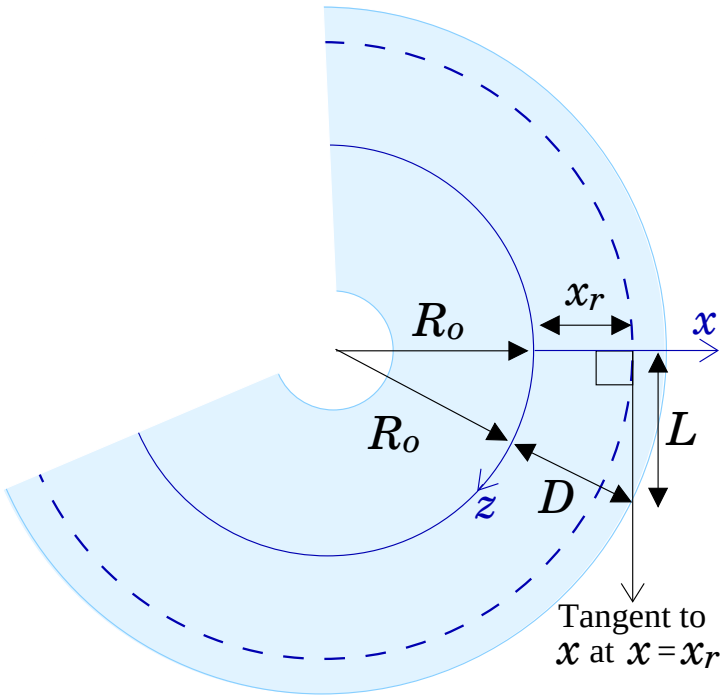

Figure 3.8: Section of curved fibre with radius of curvature R_o in the x direction.

experimental results (see Section 4.5), this inaccuracy can be remedied by introducing a simple constant of proportionality (τ) into the definition of L:

$$L = \tau\sqrt{2R_o(D - x_r)} \tag{3.17}$$

The constant of proportionality, τ, thus represents a first order correction to account for mode coupling, which is otherwise ignored in this simplified model. Here τ is determined via comparison with a series of experiential results from different fibres, as discussed in Section 4.5.

3.5.1 Evaluating the effective cladding index of a holey fibre

In the following section, various methods for evaluating the effective cladding index, also known as the fundamental space-filling mode (FSM), of a holey fibre are discussed. This value is required in the modal model outlined in Section 3.2 to determine the solutions that represent guided modes and is also required in Eq. 3.12 above ($\beta_{\mathrm{FSM}} = \mathrm{n_{FSM}k}$, where $k = 2\pi/\lambda$). In order to accurately predict the bending losses, knowledge of β_{FSM} is required correct to at least 7 significant figures. (Numerical results show that changes in the 8 $^{\mathrm{th}}$ significant figure of β_{FSM} produces changes in the 4 $^{\mathrm{th}}$ significant figure of the pure bend loss, while changes in the 7 $^{\mathrm{th}}$ significant figure of β_{FSM} can lead to changes in the 2 $^{\mathrm{nd}}$ significant

figure of the pure bend loss.) A simple, full vector analytical method of calculating β_{FSM} is proposed in Ref. [15], in which the microstructured cladding is approximated by a unit cell with circular boundaries and periodic boundary conditions. In this study, results for a holey fibre with $\Lambda = 2.3$ μm and $d/\Lambda = 0.26$ show good agreement with Ref. [91]. However, this analytical approach returns values of β_{FSM} that are in agreement with those calculated using a more accurate plane-wave method to only 3-4 significant figures for a range of fibre structures [134]. While this gives a good approximation for β_{FSM}, the level of accuracy is well below that required in the calculation of bend loss using the approach outlined here.

A better approach is to model the holey fibre cladding directly by considering a structure in which there is no core. One method that can be used to do this is the multipole approach [99], in which the modal fields are calculated using decompositions based on cylindrical harmonic functions localised in each of the cladding holes. This method is capable of producing accurate, complex values of β_{FSM} for a finite cladding structure. However, it is necessary to consider the entire extent of the fibre in this approach and it is, as a result, computationally intensive. The plane-wave method, as discussed briefly in Section 1.4.3, is also capable of producing accurate values of β_{FSM} [91, 14]. Whilst this technique can be computationally intensive, only a single unit cell is required in the calculation for an infinite cladding structure composed of a perfectly regular lattice. In this way, β_{FSM} for an infinite cladding can be calculated in an efficient and accurate way. In the study presented here, a commercially available software package called BandSOLVE$^{\mathrm{TM}}$, which is based on a plane wave approach, is used to calculate β_{FSM} [134].

3.5.2 Example calculations and other insights

In Fig. 3.6 example modal profiles for fibre HF_1 ($\Lambda = 7.55$ μm and $d/\Lambda = 0.23$) are shown for various bend radii and directions at 1550 nm and 633 nm. In this section, the pure bend loss calculations are described for some of the cases shown in Fig. 3.6, which highlight some of the main trends predicted by our model of pure bend loss. The critical point (x_r) beyond which all power is lost as radiation is defined in Eq. 3.12 and depends only on the propagation constant of the mode of the bent fibre (β_b), the propagation constant of the FSM of the straight fibre (β_{FSM}) and the bend radius (R_o). The location of x_r is indicated on each plot in Fig. 3.6 by a dashed line. For HF_1 at 1550 nm, $\beta_{\mathrm{FSM}} = 5.844182 \times 10^6$. For a bend of $R_o = 25$ mm in the $\phi = 0^{\mathrm{o}}$ direction (Fig. 3.6 (a)), $\beta_b = 5.846873 \times 10^6$ and so $x_r = 11.5$ μm, which equates to 3% of the mode lost as radiation. For a bend of $R_o = 19$ mm

in the $\phi = 0^{o}$ direction (Fig. 3.6 (b)), $\beta_b = 5.847015 \times 10^6$ and $x_r = 9.2$ μm, which equates to 10% of the mode lost as radiation. These results demonstrate that the predicted bend loss increases with decreasing bend radius as expected. This method can also be used to show that the bend loss at 633 nm is worse than the bend loss at 1550 nm, offering confirmation of the presence of the short wavelength loss edge. For example, Figs 3.6 (g) and (h) show the predicted modal intensity profiles for fibre HF_1 at 633 nm for bend radii of 80 mm and 70 mm respectively. Although these bend radii are much larger than the 25 and 19 mm previously considered at 1550 nm (shown in Figs 3.6 (a), (b), (d) and (e)), the fraction of mode lost as radiation is larger for this shorter wavelength. At 633 nm, 9% of the mode is lost as radiation for a bend radius of 80 mm and 15% of the mode is lost for a bend radius of 70 mm. Since the bend loss increases with decreasing bend radius, it can be seen that for similar values of R_o, the overall loss at 633 nm will be much greater than that at 1550 nm for fibre HF_1, demonstrating that the bend loss increases towards short wavelengths as expected.

3.6 Determining the presence of higher-order modes

There are several approaches that can be used to determine the modedness of a holey fibre, as discussed briefly in Sections 1.4 and 3.1. In this study, three approaches are used to determine if a holey fibre is single-mode. The simplest of these takes advantage of the way in which the modal fields and propagation constants of each of the holey fibres considered here are calculated. The technique used here is the orthogonal function method (OFM), and is described in Section 3.2. In this method, the wave equation is reduced to an eigenvalue problem, requiring the solution of a $2F^2 \times 2F^2$ matrix (where F is the number of Hermite Gaussian functions used in the decomposition of the modal electric fields). The solutions of this eigenvalue equation thus correspond to $2F^2$ eigenvalue/eigenvector pairs for each wavelength considered (please refer to section 3.2 and references therein for more details). The particular solutions that correspond to guided modes of the fibre can be distinguished by determining the eigenvalues that lie within the range $n_{FSM} < \beta^2/k^2 < n_{glass}$, where n_{glass} is the refractive index of glass and n_{FSM} is the effective index of the cladding region. In order to determine how many modes are guided by the fibre, n_{FSM} must therefore be calculated for each wavelength of interest. However, the Hermite Gaussians used to describe the modal fields in this model are localised functions. As such, the cladding modes are not accurately represented and the effective index of the first cladding mode, (n_{FSM}), must be calculated

via another approach. Here a commercially available plane-wave approach is chosen (see Section 3.3) [134]. While plane-wave techniques are, in general, computationally intensive, only a single-unit cell needs to be considered in the calculation of n_{FSM} (as explained in Sections 1.4 and 3.5.1), making this an efficient method in this example. However, while the orthogonal function and plane-wave techniques are both accurate methods, they contain different assumptions, and are thus not entirely equivalent. This is only an issue for fibres close to the single-mode cut-off, where the fundamental cladding mode and the (potential) first higher order mode are close in effective index. In this situation it becomes necessary to consider a single method to evaluate the effective indices of both core and cladding modes and in this case, the multipole method (MM) is used. As mentioned previously, using the multipole method it is possible to accurately determine the modal properties of holey fibres with finite cladding structures. By considering fibre structures in which there is no core, the cladding modes can also be accurately calculated. The multipole method also has the advantage that it is possible to extract the confinement losses of any higher-order modes present within the fibre. All calculations made using the multipole method presented in this thesis have been performed by Vittoria Finazzi [54]. Another simple approach is to evaluate the modedness of an equivalent step-index (ESI) fibre, the parameters of which can be determined from the modal properties of the holey fibre, as discussed in Section 3.7.1. The holey fibre is thus defined to be single-mode if the V-number of the ESI fibre, defined as $V = 2\pi a \mathrm{NA}/\lambda$, is less than 2.405. However, due to the arbitrary way in which certain ESI parameters are chosen, we find that this method is also not sufficiently accurate for holey fibres close to the single-mode cut-off, as demonstrated in the following.

Example calculations to determine the modedness of two fibres at 1064 nm, made using the three methods described above, are shown in Fig. 3.9. Here the modal indices are plotted for two fibres with effective areas of 190 μm^2 at 1064 nm, one with $\Lambda = 12.2$ μm and $d/\Lambda = 0.42$ and another with $\Lambda = 12.7$ μm and $d/\Lambda = 0.45$. For both fibres, three sets of effective modal indices are plotted for the fundamental core mode, the first higher-order core mode and the fundamental cladding mode (see figure caption for legend). Three sets of calculations are presented for the three techniques described above, indicated on the graph by the letters OFM, ESI and MM (note that here OFM indicates the combination of orthogonal function and plane-wave techniques). We see that the OFM technique predicts that both fibres are single-mode, while the ESI approach predicts that both fibres are few-moded. However, the (more accurate) multipole approach shows that the fibre with

$d/\Lambda = 0.42$ is single-mode, whilst the fibre with $d/\Lambda = 0.45$ is few-moded. In fact, the confinement loss of the higher-order mode, calculated using the multipole technique is found to be 0.46 dB/m, demonstrating that this mode would be observed in practice. Note that at 1064 nm, the ESI approach predicts that the onset of higher-order modes occurs at $d/\Lambda > 0.41$, the OFM predicts that this occurs at $d/\Lambda > 0.48$, while the multipole approach predicts that higher-order modes appear for $d/\Lambda > 0.43$.

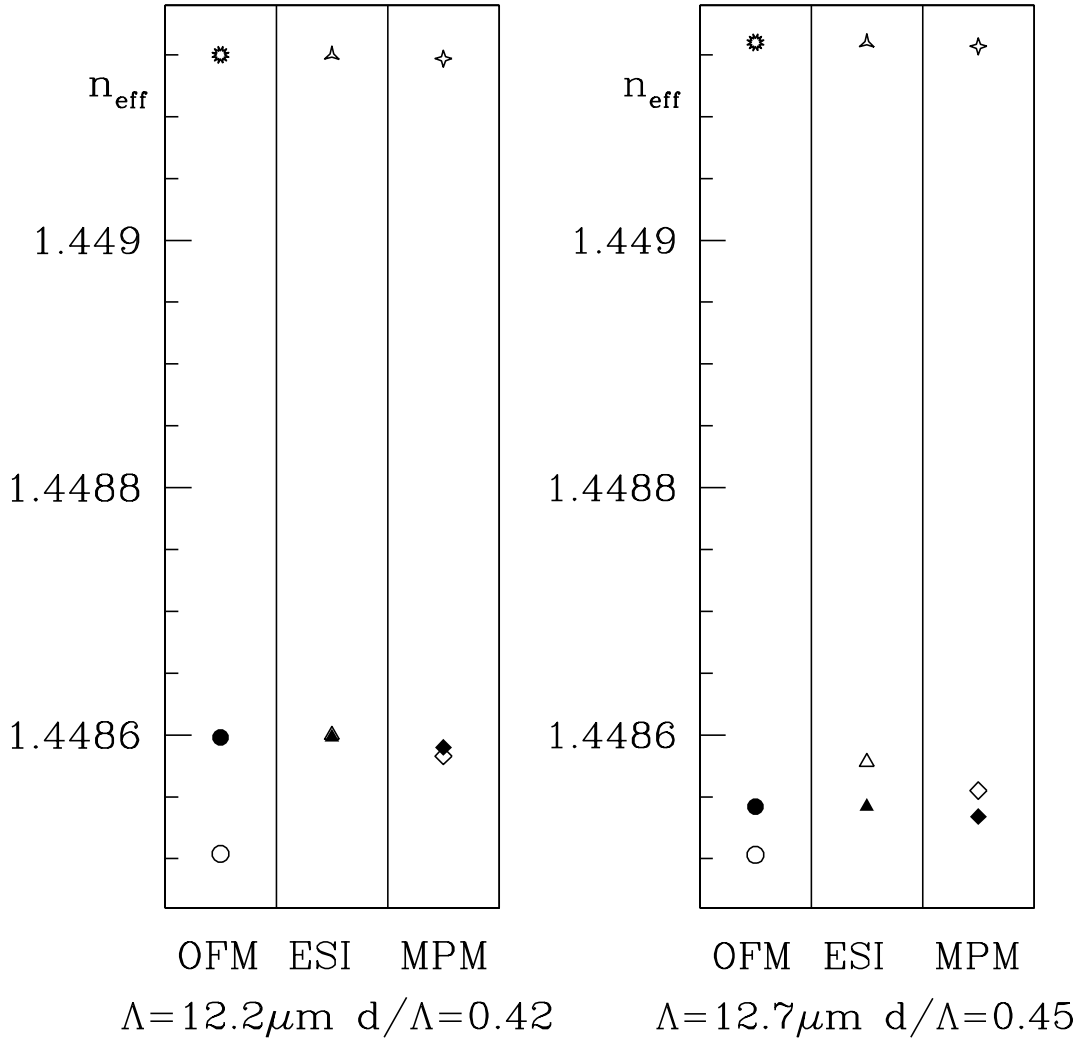

Figure 3.9: Effective indices for the modes of two fibres calculated using the orthogonal function method (OFM) for the infinite structure, using exact solution for the ESI fibre, using the multipole method (MM) for a structure with 6 rings of holes. The fancy open shapes represent the fundamental core mode, the filled shapes represent the fundamental cladding mode and the smooth open shapes represent the first higher-order core mode.

3.7 Comparison step-index fibres

3.7.1 Choosing step-index parameters

In this study, the bending losses of several step-index fibres are evaluated theoretically in order to benchmark the performance of the holey fibres considered here. The parameters of the comparison fibres are chosen by finding an *equivalent* step-index fibre that best matches the modal properties of the holey fibre for a given wavelength. The parameters of each equivalent step-index (ESI) are determined using a similar approach to the ones in Refs [4, 87], in which the core index of the ESI fibre is that of pure silica and the cladding index is taken to be the effective cladding index of the holey fibre. Using this approach, the core radius is defined empirically to be 0.625Λ. However, since the modal properties of the corresponding holey fibre are already known, we are not restricted to this arbitrary definition of core radius. Instead we choose to define the core radius of the ESI fibre by matching the effective mode area of the holey fibre. (It has been shown in Section 4.1 that the fundamental mode of a holey fibre can be well approximated by a Gaussian function.) In this way, we can define a step-index fibre that is equivalent in effective area and numerical aperture, which are the most important factors in determining the bend loss. This approach is applied in Section 5.7, in which a comparative study between the bending losses of large-mode-area holey and step-index fibres is presented at 1064 nm, and also in Section 7.2.2, where the spectral dependency of bend loss is investigated for both fibre types.

3.7.2 Modelling modal properties and bending losses

Obviously the most efficient way to model the modal properties of straight step-index fibres is to solve the exact solutions, such as those in Ref. [53]. There are also many reported techniques that can be used to model the modal properties of the bent fibre and/or the associated bend loss, as discussed in Section 2.2 and references therein. However, in order to allow comparisons to be drawn between the bending losses of holey and conventional fibres, we choose to apply the same methods to the step-index fibres as for the holey fibres where applicable. As mentioned previously, the method developed here to calculate the modal properties of holey fibres can be applied to almost any fibre profile, including step-index fibres. By using the same approach as for the holey fibres, which contain the same set of assumptions, we are able to make direct comparisons between the two fibre types. The method followed for step-index fibres is identical to that outlined for the holey fibres above,

with the exception of the characteristic width of the Hermite Gaussian functions w_m used in the decomposition of the modal field in Eq. 3.7. For step-index fibres $w_m = 0.52a$, where a is the core radius, is found to be optimal. Note that the same value for the cladding extent (D), required in the definition of L in Eq. 3.16, is used for each pair of holey and ESI fibres. However, when accurate values of bend loss are not required, for example, in Section 5.7.3 a quicker and more approximate approach is used. This is outlined in Section 5.7.3.

3.8 Summary and conclusion

The aims of this thesis, which are discussed more fully in Section 1.5, are essentially to explore the potential offered by large-mode-area single-mode holey fibres, and to place their performance in context against conventional step-index fibres. In order to do this, methods of predicting the effective area, the modedness and the bending losses of both holey and conventional fibre types are required. At the time of this study no suitable techniques existed to model the bending losses of holey fibres, and so the first step was to develop such a method. In addition, since little was known about the bending losses of holey fibres in general, it was also decided that any model of bend loss should include contributions from both transition and pure bend loss components. The methods that have successfully been developed to model both of these components of bend loss in holey fibres are outlined in the above sections of this chapter. Note that these techniques are also suitable for conventional fibre types.

The models of transition loss and pure bend loss presented in this chapter have been constructed by combining elements from methods developed for conventional waveguides with established techniques that have been developed for modelling the modal properties of straight holey fibres. Transition loss is modelled by approximating the mode conversion at points of changing curvature as a splice loss between the straight and bent fibre [100, 101, 102], as described in Section 3.4. The modal fields required in this calculation are evaluated using the orthogonal function technique developed by Tanya Monro [13, 86, 94, 95], with the addition of a conformal transformation in the case of the bent fibre (see Sections 2.2 and 3.3). A description of this technique is presented in Section 3.2, and the adaption to bent holey fibres is discussed in Section 3.3. This approach to modelling the modal field of the bent fibre is also employed in the model of pure bend loss developed here. This method is described in Section 3.5 and is based on the method presented in Ref. [113], in which the bend loss is evaluated by calculating the fraction of the modal field that cannot travel

fast enough around the bend to maintain phase with the rest of the mode. The effective cladding index of the straight fibre is required in this calculation and this is evaluated using a commercially available plane-wave technique [134].

The methods of modelling bend loss developed here involve several assumptions. The assumptions inherent to the conformal transformation routinely used in conventional fibres restricts modal calculations to bend radii in the macro-bend regime. The macro-bend regime is defined for bend radii that are much larger than the core radius of the fibre. However, via inspection of calculations, we find that this model breaks down within the macro-bend regime. Fortunately, this break-down occurs at bend radii that are far smaller than any required to evaluate the critical bend radius for all of the fibres considered here (see Section 3.3.4). Furthermore, in the method developed for modelling transition loss, the loss due to mode conversion is assumed to take place instantaneously, when in reality, the mode changes shape over a finite length scale. In addition, mode coupling is ignored in both the model of transition and pure bend loss. These assumptions mean that both components of bend loss will be overestimated. For the case of transition loss, the model presented here serves as an estimate of the maximum possible loss that can be attributed to this component of loss. Indeed, as it turns out, this contribution is small and can be neglected, as demonstrated experimentally in Section 4.5. In addition, we find that the overestimation in the method of pure bend loss can be compensated for by introducing a scaling factor. This is discussed in more detail in Sections 3.5 and 4.5.

For reasons of simplicity and computational efficiency it is preferable to use a scalar version of the orthogonal function method to evaluate the modal fields and propagation constants of holey fibres. However, the refractive index profile in a holey fibre contains features with a large refractive index contrast and the conformal transformation, used to model a bent structure, imposes an asymmetry on this profile. However, for large-mode-area holey fibres with reasonably small holes, the effective cladding index creates a low NA fibre and, in the macro-bend regime, the asymmetric distortion imposed by the conformal transformation represents only a slight perturbation. As a result, we find that the scalar version of the orthogonal function technique can indeed be used to model the modal properties of both straight and bent holey fibres with large-mode-areas. For example, for a fibre with $\Lambda = 15.0$ μm and $d/\Lambda = 0.63$, which represents the most highly multi-mode structure considered within this thesis, the propagation constant for the x-polarised mode differs only in the 10^{th} significant figure between scalar and vector calculations at

1064 nm. In addition, there is less than 5% difference between the critical bend radius of the fundamental mode for this fibre calculated using the scalar and vector version of the model presented above at 1064 nm (see also Sections 4.5.3 and 4.5.5). However, the fully vectorial version of the orthogonal function technique outlined in Section 3.2 is used to study the effect of polarisation in the bent fibre in Section 4.5.5.

As mentioned above, the bending losses are not the only modal properties that require evaluation in this study. In order to place any meaningful interpretation on the bending losses, knowledge of the mode area and the modedness of the fibre is also required. The mode area can be quite simply extracted from the modal field of the straight fibre via numerical integration, as explained in Section 3.2. In Section 3.6, the three methods used here to evaluate the modedness of holey fibres are discussed: (1) The orthogonal function technique can be used in conjunction with the calculation of the effective cladding index n_{FSM} using a plane-wave technique, (2) The V-parameter of an equivalent step-index (ESI) fibre can be determined, and (3) the multipole method can be used. This last approach is by far the most accurate and is used when considering fibres that are close to cut-off. Note that all multipole calculations included in this thesis are performed by Vittoria Finazzi [54].

In conclusion, the methods listed in the above sections of this chapter can be used to model mode area, pure bend loss, transition loss, and modedness, in both holey and conventional fibres. In the next chapter, the experimental techniques developed to measure these properties are presented, together with a comparative study between experimental and numerically derived values that are used to validate these numerical models.

Chapter 4

Experimental methods

4.1 Introduction

As discussed in Section 2.4, in order to explore the potential offered by large-mode area single-mode holey fibres, methods of characterising the effective area, the modedness and the bending losses of both holey and conventional fibre types are required. Experiments designed to measure these three key properties are described in the following.

As discussed briefly in Section 1.4.2, the effective mode area of holey fibres can be reasonably well approximated by an equivalent step-index fibre at a given wavelength due to the fact that the modal field can be approximated by a Gaussian function [17]. Indeed, all the fibres considered in this thesis, which have $7\,\mu\text{m} \lesssim \Lambda \lesssim 20\mu\text{m}$ and $0.2 \lesssim d/\Lambda \lesssim 0.5$, have an overlap with a Gaussian function of optimum width that is greater than 95% in the wavelength range of 300 to 1600 nm (this overlap is defined in Eq. 3.11, in which E_b is replaced by a Gaussian function). As a result, we find that conventional methods for measuring effective mode area can be adapted for the large-mode-area holey fibres considered in this study, as described in Section 4.3. However, we have found that conventional techniques for measuring bending losses are not transferable to holey fibres. In part, this is due to the fact that most reports of bend loss are vague in their description, but also results from the fact that these measurements are designed for conventional fibres with mode areas less than approximately 100 μm^2 at telecommunications wavelengths. For such fibres, the critical bend radii are typically less than 1 cm and the majority of techniques induce tension on the fibre to ensure that the bent fibre describes a perfect circle [127, 136, 137, 122]. We have found that using tension on large-mode-area fibres is not only unnecessary, since the bend radii of interest are typically large, but that it can result in non-repeatable results

for holey fibres. We suspect that this non-repeatability for the case of holey fibres results from the fact that they are more sensitive to strain than their conventional counterparts. Indeed, we have observed that the strain induced by the small magnets traditionally used to hold the fibre in a V-groove can severely distort the modal field. However, it should be noted that the holey fibres studied here have been shown to possess comparable levels of mechanical strength to conventional solid fibres [138]. In addition, since step-index fibres are typically circularly symmetric, conventional bend loss measurements do not consider the effect of the angular orientation of the fibre. In contrast, holey fibres typically possess a six fold symmetry, and this may influence the bend loss. In response to these requirements, we have developed several techniques to measure the bending losses of large-mode-area holey fibres as a function of bend radius and the angular orientation of the fibre that ensure minimal strain and tension on the fibre. In the following sections detailed descriptions are presented for the experiments designed to study the following (1) the bend loss as a function of bend radius, (2) the bend loss as a function of wavelength, (3) the relative impact of transition loss and pure bend loss and (4) the effect of the fibre geometry on the bend loss. Note that these experiments are also suitable for conventional fibres, enabling comparative measurements.

Whilst the general procedures for each experiment are identical for both fibre types, some basic experimental techniques such as fibre end preparation and measurements of the refractive index profile must be approached differently for holey fibres. The details of these basic techniques are briefly discussed in Section 4.2. A brief outline of the methods used to launch light into the fibres studied here is also included in this section.

4.2 Basic experimental techniques

4.2.1 Measurement of the refractive index profile

For the conventional fibres considered here, the refractive index profile is measured directly from the preform. However, as discussed in Section 1.2.4, the transverse structure of a holey fibre can differ greatly from the preform. As a result, the refractive index profile is determined via a scanning electron microscope (SEM) image of the fibre cross-section. At the ORC, this technique has been found to be capable of resolving sub 100 nm features. Note that a crude measurement of the refractive index profile of a holey fibre can be made using an optical microscope. Although this is an invaluable technique for initial characterisation,

diffraction effects mean that the hole size cannot be accurately determined in this way.

4.2.2 End preparation

The large-mode-area fibres considered here typically have outer diameters of between 150-300 μm. As a result, the polymer coating is removed from the ends of the fibre using solvent instead of a standard mechanical stripper. (Here a 50:50 mix of dichloromethane and butanone is used). For holey fibres it is important to ensure that the fibre tip does not come into contact with the solvent, since the liquid would be drawn up into the fibre via capillary effects. This would significantly change the refractive index profile and hence the guidance properties of the fibre. Once the polymer coating has been removed, the bare fibre ends can then be cleaved using a suitable commercial fibre cleaver, or by hand with a ceramic fibre tile. Note that small cracks or splits can form on the cleaved surface of holey fibres, which can distort the mode shape [139]. However, we have found that this problem can be eliminated by careful cleaving.

4.2.3 Launching light into large-mode-area fibres

In most cases, the bare fibres ends are mounted in front of the launch and detection optics using standard V-grooves. If it is necessary to control the angular orientation of the fibre end, a fibre chuck mounted in a fibre chuck rotator is used instead. When using a collimated laser as a light source, a typical launch arrangement comprises 2 mirrors, to align the collimated beam, and an aspheric lens to couple the light into the fibre. The choice of focal length of this lens depends on the size of fibre mode and the numerical aperture of the fibre. For the large-mode-area fibres used in this study, we find that Gel tech's aspheric lenses with focal lengths between $8-15$ mm produce good coupling for wavelengths in the range $1-1.55$ μm. For visible light sources we find that a x 10 microscope objective can be used to achieve good coupling efficiency. The launch arrangement is similar for fibre based sources, with a collimating lens used in place of the two mirrors. For a white light source, we find that the best coupling is achieved with a x 10 microscope objective placed as close to the light bulb as possible. More details of the process of coupling light into a fibre using a white light source are given in Section 4.4.3.

In some of the experiments described below, it is necessary to rotate the fibre between measurements. To do this, the fibre is removed from the detector and is replaced after the fibre chuck has been rotated at the launch. By imaging the fibre ends in situ, we have found

that the entire fibre maintains the orientation set at the launch, for fibre lengths ≤ 2 m.

4.3 Experiment 1: Effective area measurement

4.3.1 Introduction

The effective area of each fibre in this study is extracted directly from measurements of the far-field divergence, obtained via a scanning knife-edge technique [140]. In this approach, the far-field angle of divergence θ, shown in Fig. 4.1, is determined by measuring the width of the diverging beam (w) as a function of the distance from the end of the fibre (z). If we assume that the modal field can be approximated by a Gaussian function, the effective area of the fibre mode can be extracted from the well known expressions for the propagation of a Gaussian beam in free space [141] (see below for details). At first sight, it may seem that a Gaussian mode profile is not an assumption appropriate to holey fibres, since the transverse modal fields are somewhat hexagonal in shape. However, for the types of holey fibre considered here, the hole size is small relative to the hole-to-hole spacing (d/Λ typically $\lesssim 0.5$) and the hole-to-hole spacing is much larger than the wavelength ($\lambda/\Lambda \approx 0.1$). In this regime, the hexagonal nature of the cladding structure is only subtly reflected in the shape of the mode. Indeed, numerical calculations show that the fundamental mode of every holey fibre studied in detail here has an overlap with a Gaussian function greater than 95%.

4.3.2 Experimental set-up

The experimental set-up for this measurement is shown in Fig. 4.1. Both ends of a length of fibre are stripped of coating and cleaved (as described in Section 4.2.2). Light is launched into one end of the fibre and the other end is firmly secured at one end of a long translation rail in a rotating fibre chuck. The fibre is positioned so that the centre of the beam diverging from the end of the fibre is aligned parallel to the translation rail. It is important that the fibre remains in the same orientation for the duration of the measurement. It is also essential that the cleaved bare fibre end is of excellent quality to ensure that the far-field image is representative of the fibre mode. A rotating optical chopper is mounted on the translation rail and is positioned so that the blades cut the diverging beam at 90^{o}. The distance between the centre of the chopper and the centre of the beam, x, (shown in the insert in Fig. 4.1) is recorded. The light that passes through the optical chopper is then focused onto a large area photo-diode using a large diameter lens (diameter ≈ 10 cm). This lens must

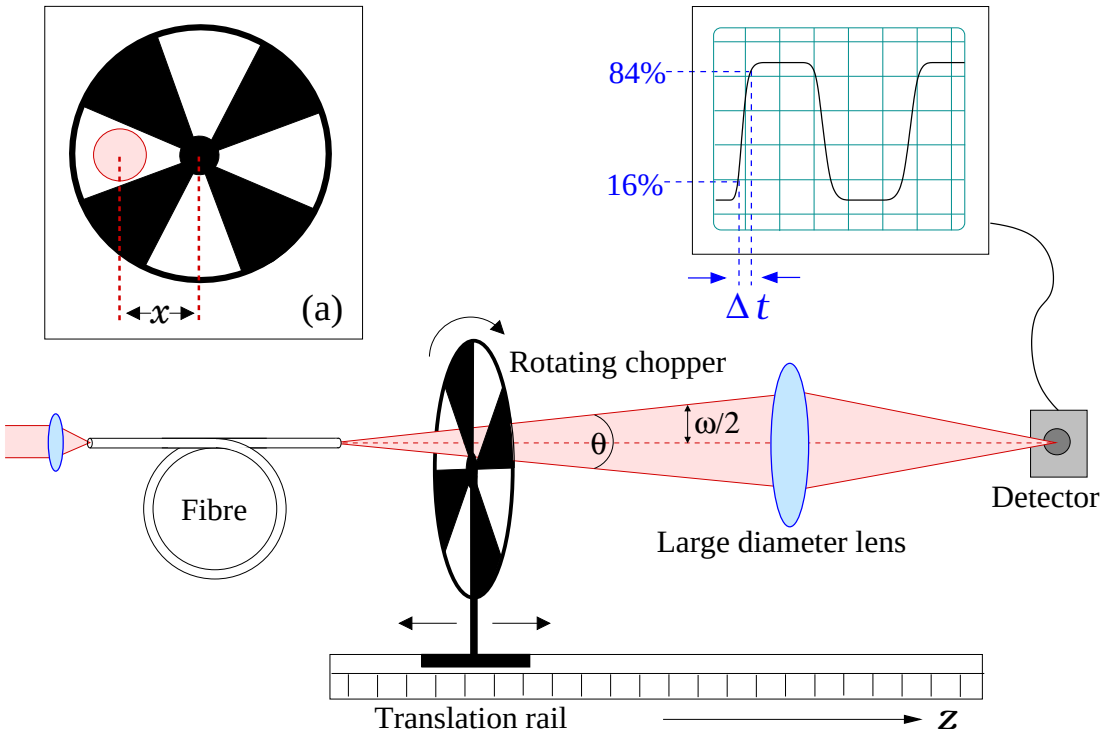

Figure 4.1: Experimental set-up to measure mode field diameter

be far enough away from the end of the fibre to ensure that the optical chopper has at least 5 cm of translation, but it must also be close enough to the end of the fibre to ensure that the tails of the far-field light emitted by the fibre are captured by the lens. Similarly, the gaps between the blades of the optical chopper must be sufficiently large to allow the beam to pass unhindered in the 'on' state of the chopper.

An oscilloscope connected to the photo-diode displays a (nearly) square wave, the sides of which are slightly rounded due to the time taken for the chopper blade to cut through the beam (See Fig. 4.1). It is this transit time that we wish to record. We define the beam width, w, as the distance between the peak intensity (shown as I_o on Fig. 4.2) and the point at which the intensity drops to $1/e^2$ of its maximum. Here we choose to measure this distance between the points $-w/2$ and $w/2$ across the beam, which corresponds to intensity levels of $I_o/\sqrt{e}$ either side of the maximum intensity, I_o, as shown in Fig. 4.2.

If we then define t_1 and t_2 to be the times at which the leading edge of the chopper blade is at a position of $r = -w/2$ and $r = w/2$ respectively, then the time taken for the blade to cut through the width of the beam, w, is given by $\Delta t = t_2 - t_1$. At times t_1 and t_2, 84 and 16% of the total power in the beam is incident on the photo-diode, respectively.

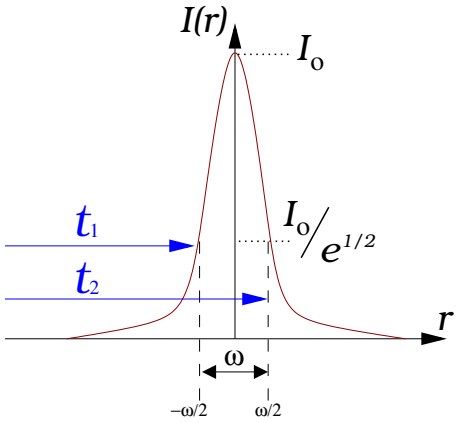

Figure 4.2: Experimental set-up to measure mode field diameter

These percentages are given by:

$$\frac{\int_{-w/2}^{\infty} I(r)dr}{\int_{-\infty}^{\infty} I(r)dr} = 0.84 \qquad \frac{\int_{w/2}^{\infty} I(r)dr}{\int_{-\infty}^{\infty} I(r)dr} = 0.16 \tag{4.1}$$

By setting the low and high clip levels on the oscilloscope to these percentages, the rise time of the signal equals the time taken for the blade to cut through the beam (Δt).

The width of the beam w (defined as the $1/e^2$ width, or the distance between $I = -I_o/\sqrt{e}$ and $I = I_o/\sqrt{e}$) is then given by $\Delta t \times v$, where v is the speed of the chopper at the centre of the beam and is given by:

$$v = \frac{2\pi x f}{n}, \tag{4.2}$$

where x is the distance between the centre of the chopper and the centre of the beam, f is the frequency of the chopper and n is the number of gaps in the chopper (In Fig. 4.1 $n = 4$). Although this assumes that the speed of the chopper blade is a constant value across the width of the beam, the error introduced by this assumption is small. By recording Δt and hence w, as a function of distance from the fibre end (z), the far-field angle of divergence $\theta \approx dw/dz$ is determined by the gradient of w graphed against z. A sample set of data from the measurement of one of our holey fibres at 1064 nm is shown in Fig. 4.3. The angle of divergence is ≈ 0.047 radians, which corresponds to an A_{eff}^{FM} of 170 μm^2. Note that in order to determine the far-field divergence it is not necessary to know the distance from the fibre end to the chopper, only the relative distance between each width measurement is required. Ideally, somewhere between $5 - 10$ measurements of the beam width should be taken, separated by approximately $0.5 - 1$ cm depending on the level of divergence. Assuming that the fibre orientation remains the same, a variation of $\approx 1\%$ in the beam

width is observed for repeat measurements. This corresponds to a variation of $\approx 2-3\%$ in the final A_{eff}^{FM} for repeat measurements.

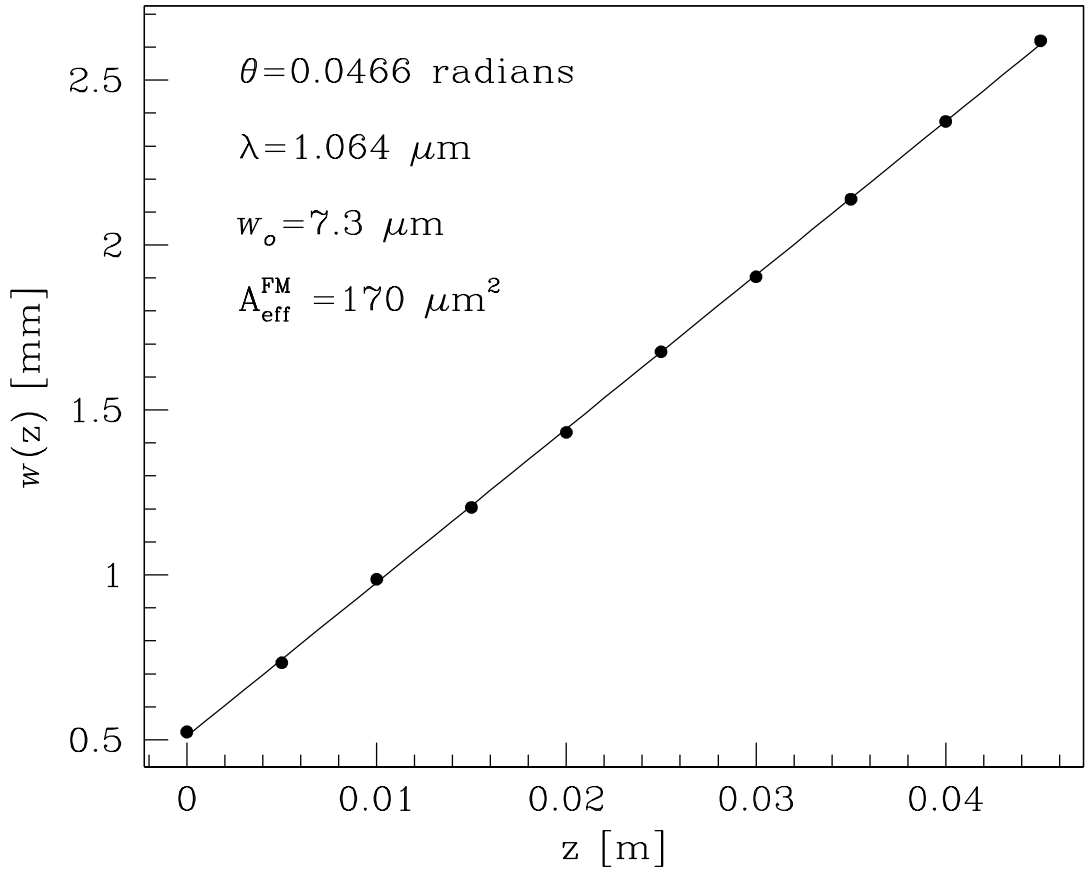

Figure 4.3: Example data from a MFD measurement of a large-mode-area holey fibre

Once the far-field divergence of the fibre has been determined, the spot-size of the fibre mode, $w_o = w(z = 0)$, can be calculated using the following equations. For a Gaussian beam there is a simple relationship between θ and w_o. This is given by:

$$w(z) = \frac{\lambda\ z}{\pi\ w_o} \tag{4.3}$$

$$\theta = \frac{d\ w(z)}{dz} = \frac{\lambda}{\pi\ w_o} \tag{4.4}$$

$$w_o = \frac{\lambda}{\pi\ \theta} \tag{4.5}$$

For a circularly-symmetric Gaussian modal field, the effective area defined in [135] reduces to:

$$A_{eff}^{FM} = \pi\ w_o^2, \tag{4.6}$$

which is used here for all measured values. As mentioned above, this is a simplification for the holey fibres considered here, which have slightly hexagonal-shaped modes, but both theoretical calculations and direct measurements of the near-field mode profile show this to be a reasonable approximation. In fact, theoretical modelling shows that the spot size varies by $\approx 5-10\%$ in different angular directions and by averaging repeated measurements taken for several different angular orientations of the fibre, we find that a more representative value of effective area can be obtained. Including all sources of error, such as those arising from imperfect cleaves and alignment, in addition to that mentioned above, we estimate at most a 5% variation in repeat effective area measurements for a given fibre.

4.3.3 Discussion

The method described here is best suited to large-mode-area fibres, which possess small angles of divergence (limited by the diameter of the lens and the aperture size of the optical chopper as discussed above) and is restricted to single-mode fibres in which the field profile can be well approximated by a Gaussian function. This requirement means that it is important to ensure that no cladding or higher-order modes are present at the measurement end of the fibre. Any cladding modes will act to offset the zero level of the transverse intensity profile, making the mode appear smaller. The presence of higher-order modes will also cause the effective area measurement to be underestimated by introducing a much higher angle of divergence. Indeed, we have found that even a very low level presence of a higher-order mode can greatly perturb the measurement. Cladding modes can be stripped from the fibre trivially, since they are typically very sensitive to bending and can be completely removed with quite a gentle bend. Bending the fibre can also be used to filter out higher-order modes, if there is a sufficient differential between the bend loss of the fundamental and the first higher-order mode.

4.4 Bend loss Measurements

4.4.1 Introduction

This section describes in detail the experiments that we have used to characterise the bend loss of the fibres considered in this study. The experiments shown here allow us to measure bend loss as a function of bend radius and wavelength, to investigate the contributions made by transition loss and pure bend loss to the overall bend loss and also to study the

effect of the cladding geometry on the bend loss.

In any bend loss measurement it is important to ensure that any change in fibre curvature is well defined and to ensure that the fibre lays flat along its entire length. These precautions ensure that the measured loss can be attributed purely to the regions of curvature that are deliberately imposed along the length of fibre and not from any other minor perturbations in the straight fibre regions, ensuring a robust and repeatable method of measurement. The bend loss is defined as the ratio between the power transmitted through the straight fibre and the bent fibre, expressed in dB.

4.4.2 Experiment 2: Bend loss as a function of radius

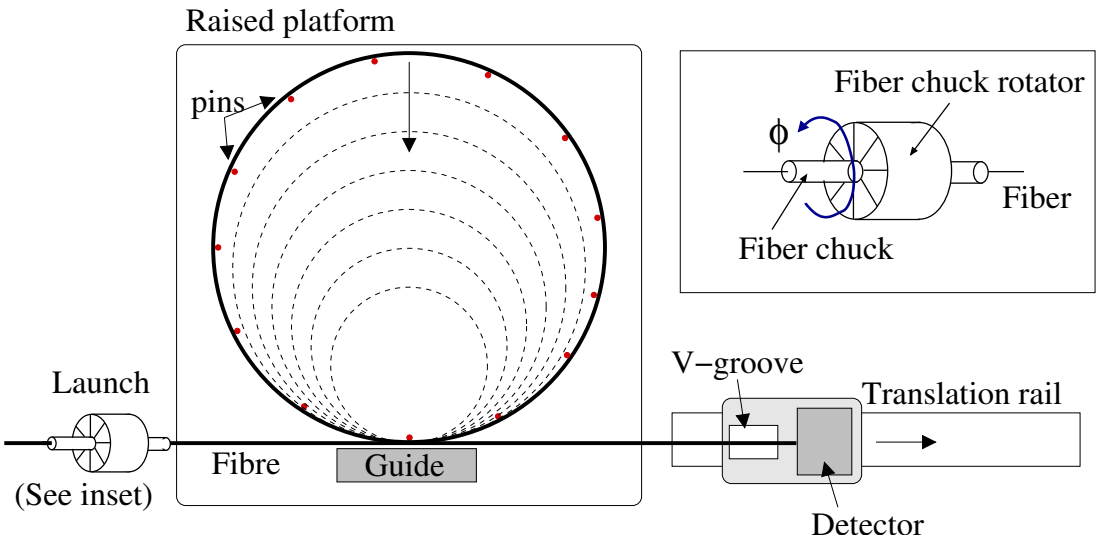

Figure 4.4: Experimental set-up to measure loss incurred due to one loop of radius R_o.

The experimental set-up for measuring bend loss as a function of radius for a single wavelength is shown in Fig. 4.4. Both ends of a section of fibre approximately 2 m in length are prepared as described in Section 4.2.2. One end of the fibre is secured at the launch in either a fibre chuck, as shown, or onto a standard V-groove. The free end of the fibre is mounted in a V-groove attached to a power detector, which is in turn mounted on the translation rail so that the fibre end and the detector move as one. After the power transmitted through the straight fibre has been recorded, the fibre is bent into a single loop on the raised platform that holds the fibre at the same height as the launch and detection optics to ensure that the fibre lays flat along its entire length.

Each bend radius is defined by a circle drawn on the surface of the raised platform, which is comprised of stiff foam with an upper layer of thick cardboard. A straight edged

guide at the beginning and end of the loop, together with a series of pins pushed into the raised platform inside the bend, hold the fibre in place and ensure that the transition from straight to bent fibre is sharply defined. The bend radius is decreased by moving the pins into the next circle on the platform and translating the detector to take up any slack in the fibre, with care taken to ensure that no strain is placed on the fibre. To extract the critical bend radius, which is defined as the radius at which the loss is equal to 3 dB (50%) for one loop of fibre, this measurement should be performed for about 5-10 different radii, spaced by 0.5-1 cm in radius.

Note that in addition to the critical bend radius, this measurement can also yield information regarding the number of modes present in the fibre. Higher-order modes experience greater attenuation than the fundamental mode for a given bend radius, and the critical bend radius is therefore larger for higher-order modes. If higher-order modes are present to any significant degree, bend loss as a function of radius becomes step-like, instead of a smooth curve, with each step representing the loss of one or more higher-modes. This is discussed in more detail in Sections 5.13 and 5.4.

4.4.3 Experiment 3: White light bend loss measurements

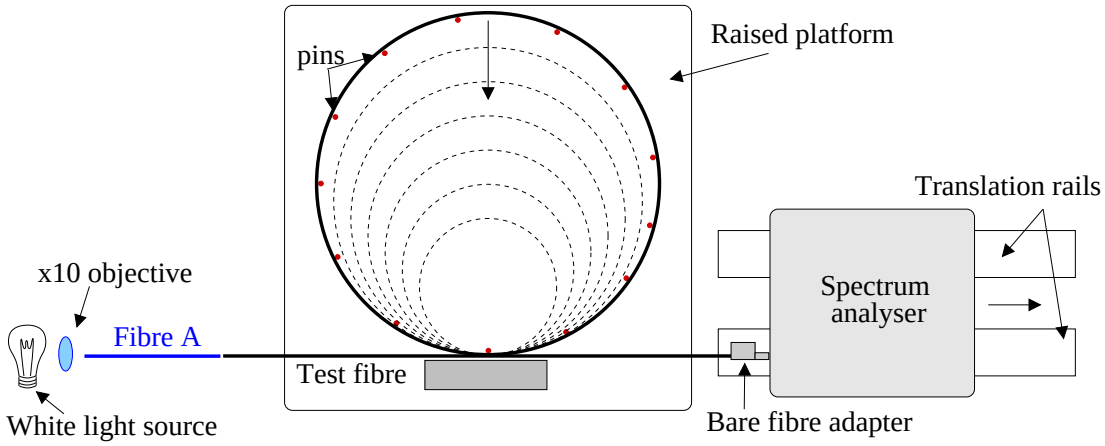

Figure 4.5: Experimental set-up to measure loss incurred due to one loop of radius R

The measurement described in Experiment 2 for measuring the bend loss as a function of radius for a single wavelength can be adapted for a white light source as in Fig. 4.5. Using a x 10 microscope objective, white light is focussed into fibre A, which is an endlessly single-mode holey fibre with an effective area of around 300 μm^2. Fibre A is then butt-coupled to the fibre under characterisation. Fibre A is used here to reduce the spot-size incident on the test fibre in order to avoid exciting the cladding modes. The rest of the

experimental details are identical to the single wavelength example described above, except for the power detector. In place of the power detector, a spectrum analyser is used in conjunction with a bare fibre adaptor to record power levels in the wavelength range 350 to 1700 nm. Note that because the spectrum analyser is significantly bigger than the power metre, two translation rails are used in place of the previous one.

As before, the data from this experiment can also be interpreted to reveal information about the modedness of the fibre, as is described in Sections 7.3.2.

4.4.4 Experiment 4: Distinguishing transition loss and pure bend loss

As mentioned in Section 2.2.1, bend loss in any waveguide can be separated into two components; *transition loss* and *pure bend loss*. Transition loss, which is also referred to as mode-conversion loss, results from the modal distortion induced by the abrupt change in curvature at the beginning and end of a bend. Pure bend loss is defined as the continual loss of radiation from the distorted mode that occurs along any curved section of fibre. As discussed in Section 2.2.1 it is essential to have knowledge of the contribution from these two components in order to formulate a theoretical model of bend loss in a holey fibre. In response to this requirement, the experiment described here was designed to determine the relative contributions of transition loss and pure bend loss to the overall bend loss of the fibre.

The experiment shown in Fig. 4.6 (a) was designed in Ref. [105] to distinguish transition and pure bend loss in conventional step-index fibres. Both ends of a section of fibre approximately 2 m in length are prepared as described in Section 4.2.2. One end of the fibre is mounted at the launch in either the fibre chuck and fibre chuck rotator, as shown, or in a V-groove. The other end is mounted in a V-groove attached to a power detector, which is in turn mounted on a rotating rail. The length of fibre is then progressively wrapped around a drum of radius R_o by rotating the rail carrying the detector about the centre of curvature. The fibre is carefully supported at points A and B with straight guides to produce a sharp change in curvature without inducing any unwanted stresses on the fibre. The guide at point A remains fixed and it is extremely important for the guide at B to reproduce the same sharp change in curvature as the fibre is wrapped around the drum.

Fig. 4.6 (b) shows a sketch of typical results. Transition losses occur at the points A and B where there is a sharp change in curvature from $R = \infty$ to $R = R_o$ and back again. These transition losses (TL) take place over a finite length of fibre, as shown by the curved section

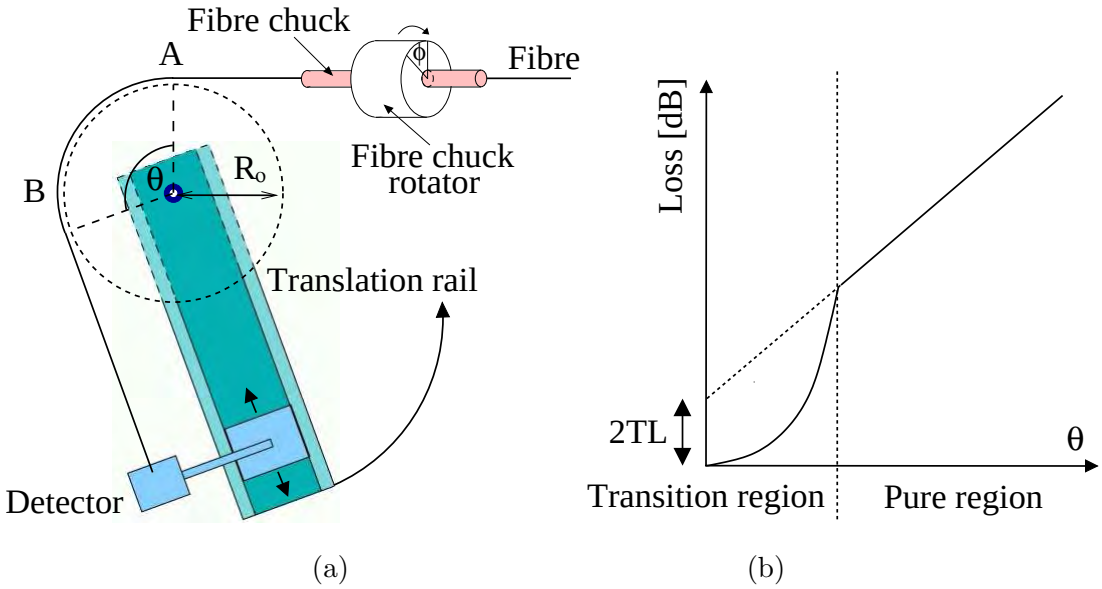

Figure 4.6: (a) Experimental set-up to observe transition loss and pure bend loss in a bent optical fibre. Loss is measured as the fibre is progressively wrapped around a drum of radius R_o (The wrap-around angle = θ). The fibre chuck and rotator are used to control the angular orientation (ϕ) of the fibre in the bend. (b) Schematic of results.

in graph Fig. 4.6 (b). The length of fibre between points A and B is of constant curvature and suffers a continuous pure bend loss along its entire length. As the wrap-around angle (θ) is increased, the length of the curved section of fibre (and the pure bend loss) increases linearly. The pure bend loss can be extracted from the gradient of the straight line section of the graph in Fig. 4.6 (b), which is offset by the two transition losses at the beginning and end of the bend. The transition loss can then be extrapolated from the graph as sketched in Fig. 4.6 (b).

4.4.5 Experiment 5: Bend loss as a function of angular orientation

As mentioned in Section 4.2.3, the fibre chuck and rotator can be used to control the angular orientation (ϕ) of the fibre in the bend. Using the set-up in experiment 4, with the wrap around angle set such that the majority of loss can be attributed to pure bend loss without the overall loss value being too severe, we can study the effect of the geometry of the cladding structure on the bend loss in detail. Although the effect of angular orientation of the fibre in the bend can be studied with all of the bend loss experiments described here, we choose the set-up in experiment 4 to study this in detail since this experiment can be performed for a partial loop of fibre. This is advantageous as we can study the loss for bend radii where the mode is significantly distorted into the cladding region, with losses

low enough to be recorded accurately. (It is also easier to change the angular orientation of the fibre in this set-up.) The results from this experiment are presented in Section 4.5.

4.5 Experimental validation

4.5.1 Overview

In this section results are presented from an experimental study of bend loss in holey fibres at 1550 nm together with theoretical predictions where appropriate. The aim of this section is to demonstrate the effectiveness of the experimental techniques described in the above sections of this chapter and to validate the theoretical methods described previously in Chapter 3.

In the following sections, bend loss as a function of the radius of curvature, the relative contributions of transition and pure bend loss, and the effect of the angular orientation of the fibre in the bend are considered. Unless otherwise stated, all values of pure bend loss are calculated using the scalar version of the modal model described in Section 3.2.

4.5.2 The fibres

In this section, results are presented for four large mode holey fibres (HF_1, HF_2, HF_3 and HF_4) and one conventional fibre (C_1), which I have characterised in terms of effective area and bend loss. All of the holey fibres in this chapter were drawn from the same preform and the smallest fibre, HF_1, is shown in Fig. 4.7. In each of these fibres, the core is offset from the centre of the fibre by one period. This offset was introduced because the same cladding configuration was used to make a cladding pumped holey fibre laser, in which the offset is used to enhance the modal overlap between the core and cladding modes [29]. Note that the four holey fibres considered within this section are made entirely from silica glass, but that a lower grade (higher OH content) glass was used for the outer jacketing tube in the preform of these fibres.

The measured effective mode areas, extracted from divergence measurements as described in Section 4.3, are listed in Table 4.1 for each fibre included in this chapter. The effective mode areas range from 130 μm^2 to 230 μm^2 at 1550 nm. For comparison, conventional Corning SMF-28 telecommunications fibre has a mode area of approximately 85 μm^2 at 1550 nm [112], and the largest mode area (of a single-mode fibre) achieved with conventional technology is around 400 μm^2 at 1550 nm [31]. Although endlessly single-mode holey fibres have been demonstrated with effective areas as large as 1000 μm^2 [37], here we choose to study holey fibres with more conservative mode areas, which possess reasonably low bending losses. However, this work is extended to larger mode area holey fibres in

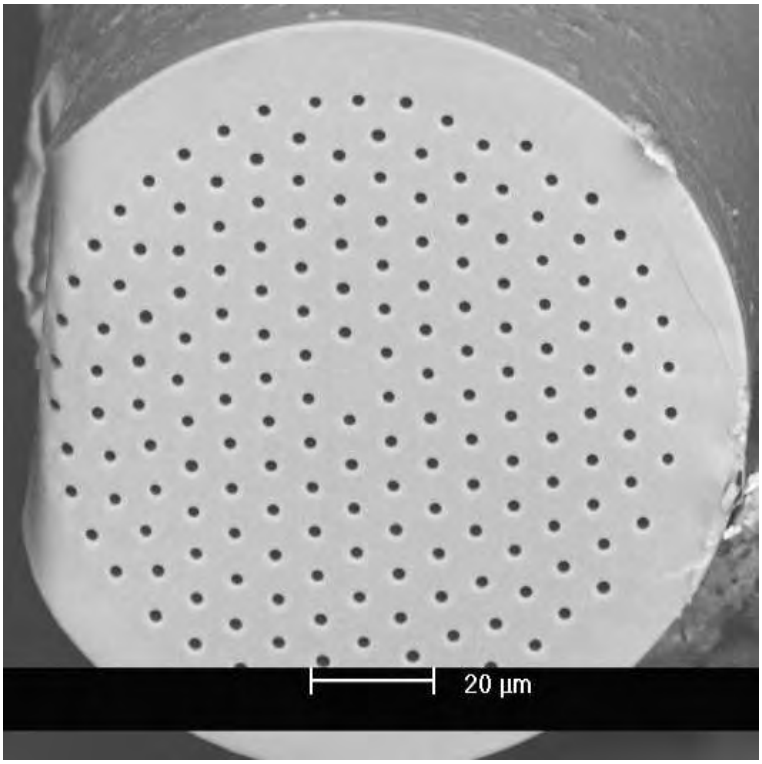

Figure 4.7: Holey fibre HF_1: the hole-to-hole spacing (Λ) is 7.55 μm and the hole diameter (d) is 1.71 μm.

further sections (see Chapter 5).

4.5.3 Bend loss as a function of radius of curvature

Loss was measured at 1550 nm as a function of the bend radius for fibres HF_1, HF_2 and HF_3 using the experiment described in Section 4.4 . These measurements were repeated for several random angular orientations of the fibre and are shown in Figs 4.8 (a), (b) and (c), by the open shapes. Superimposed on each graph is a curve fitted to all the experimental data for each fibre. This enables us to average over the different angular orientations and thus extract an average value for the critical bend radius, R_c. Note that the fibres considered in this section are endlessly single-mode and that $R_c \equiv \mathrm{R_c^{FM}}$, where $\mathrm{R_c^{FM}}$ is the critical bend radius of the fundamental mode. This critical radius is found to be 21 mm, 46 mm and 66 mm for holey fibres HF_1, HF_2 and HF_3 respectively, which increases with mode size as expected.

In order to understand the relative contributions that transition loss and pure bend loss make to the net observed loss, these results are compared to theoretical predictions. For one full loop of fibre, there are two transition regions, one at the beginning of the bend and another at the end of the bend, which result in two transition losses. Figs 4.9 (a), (b) and

Table 4.1: Fundamental mode area (A_{eff}^{FM}) for holey fibres $HF_1 - HF_4$ and the conventional step-index fibre C_1. The holey fibre parameters are extracted from scanning electron microscope images.

fibre	NA	a [μm]	A_{eff}^{FM} [μm^2] @ 1.55 μm
C_1	0.11	4.0	126

fibre	Λ [μm]	d/Λ	A_{eff}^{FM} [μm^2]	
			@ 1.55 μm	@ 633 nm
HF_1	7.6	0.23	130	72
HF_2	9.7	0.23	215	100
HF_3	11.3	0.24	230	103
HF_4	9.5	0.25	180	98

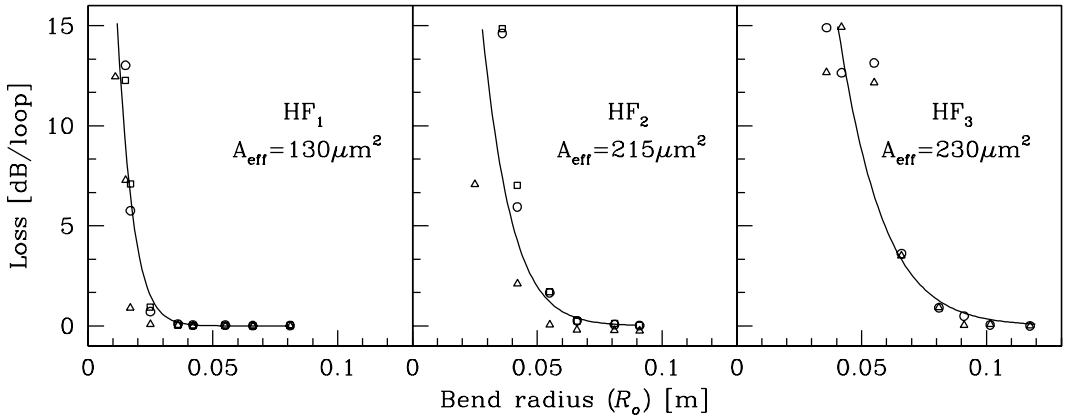

Figure 4.8: Loss for one loop of fibre as a function of bend radius. Open shapes represent measured bend loss for (a) HF_1, (b) HF_2 and (c) HF_3 for different random angular orientations of the fibre. The solid line in each graph corresponds to the fitted curve from which the critical radius is extracted.

(c) show the measured bend loss for fibres HF_1, HF_2 and HF_3, as in the previous graph, together with predicted values for the transition loss and pure bend loss. The dotted lines in Figs 4.9 (a), (b) and (c) show the predicted transition loss for one full loop of fibre bent in the $\phi = 0^o$, 45^o and 90^o directions for HF_1, HF_2 and HF_3 respectively. These predicted values clearly show that transition loss is a small overall contribution to bend loss for these holey fibres in the macro-bend regime at 1550 nm and implies that the majority of loss must be attributed to pure bend loss.

The predicted pure bend loss is shown for each fibre by the solid lines in Figs 4.9 (a), (b) and (c) for bends in the $\phi = 0^o$, 45^o and 90^o directions. Recall that in the model of pure bend loss described in Section 3.5, a constant of proportionality (τ) was introduced

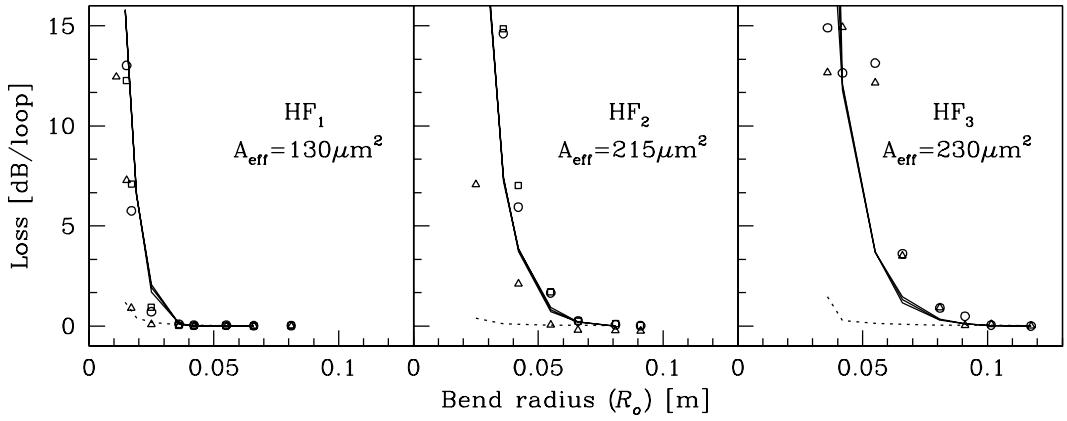

Figure 4.9: Loss as a function of bend radius. Open shapes represent measured bend loss for (a) HF_1, (b) HF_2 and (c) HF_3 for different random angular orientations of the fibre, while the predicted pure bend loss is shown by solid lines for bends in the $\phi = 0^o$, 45^o and 90^o direction. The predicted transition loss is shown by dotted lines for bends in the $\phi = 0^o$, 45^o and 90^o direction.

in Eq. 3.16. Since the transition loss is a small contribution to the overall loss (Fig. 4.9), this factor can be found by fitting the predicted curves to the experimental data. We find that by choosing $\tau = 6$, we achieve excellent agreement with experimental data for all three fibres, as can be seen in Figs 4.9 (a), (b) and (c). For example, using our scalar model, the critical bend radius of the fundamental mode (R_c^{FM}), is predicted to be 23 mm, 44 mm and 58 mm for holey fibres HF_1, HF_2 and HF_3 respectively. This compares well with experimental values of R_c^{FM} (given above) of 21 mm, 46 mm and 66 mm for holey fibres HF_1, HF_2 and HF_3 respectively.

As mentioned above, the holey fibres considered within this chapter (HF_1, HF_2, HF_3 and HF_4) are not made from a single grade of silica. A lower grade (higher OH content) silica glass was used for the outer jacketing tube in the preform of these fibres. In addition, we find that the bend losses of these fibres are lower than those fibres made from a single grade of silica. This may result from the fact that the refractive index of this lower grade silica is slightly less than the silica used in the rest of the fibre. As a result, the lower index region acts as a secondary cladding and, when the fibre is bent, may act to confine the bent mode to the inner cladding more effectively, enabling the cladding modes to couple back into the core mode more efficiently, resulting in lower bending losses. Consequently, we find that the fitting factor τ is actually greater for these fibres than other holey fibres that have been made entirely from a single, high grade of silica. For all other fibres considered in this thesis, $\tau = 2.0$ is found to produce the best agreement with experiment. For example see Sections 5.4, 5.6, 6.2.4, and 7.3.3.

4.5.4 Distinguishing transition loss and pure bend loss experimentally

In this section, we present results from the experiment designed to separate the relative contributions of transition loss and pure bend loss, shown in Fig. 4.5.4. This experiment was performed for the conventional fibre C_1 ($A_{eff}^{FM} = 126\ \mu m^2$ at 1550 nm) and the similarly sized holey fibre HF_1 ($A_{eff}^{FM} = 130\ \mu m^2$ at 1550 nm) to enable comparisons to be drawn between the two fibre types. For each fibre, the loss was measured as a function of θ for a fixed radius of curvature. A radius of 14.5 mm was chosen to ensure that the loss due to mode deformation was sufficiently large for the transition region to be clearly visible.

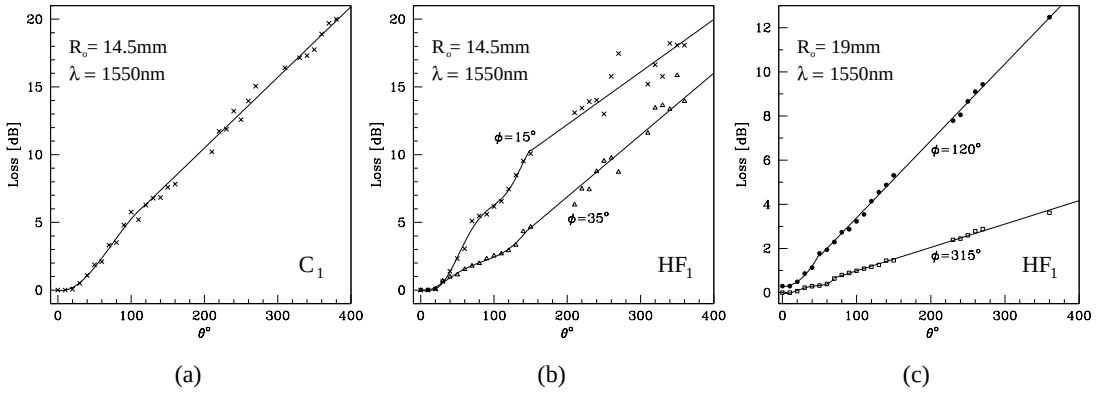

Figure 4.10: Results from experiment shown in Fig. 4.6 for $\lambda = 1550$ nm (a) conventional fibre C_1, $R_o = 14.5$ mm, (b) holey fibre HF_1, $R_o = 14.5$ mm, (c) holey fibre HF_1, $R_o = 19$ mm.

Figs 4.10 (a) and (b) show the measured loss at 1550 nm for $R_o = 14.5$ mm as a function of angle for the conventional fibre C_1 and holey fibre HF_1 respectively, together with fitted curves drawn to guide the eye. Unsurprisingly, we find that the overall loss values for HF_1 are similar in magnitude to those of the similarly sized conventional fibre C_1. In addition, we find that, for both fibre types, two regions of loss can be distinguished: the curved section at small values of θ is the transition region, while pure bend loss dominates as the length of the bent fibre is increased. As expected, we find that a linear fit can be used to describe the pure bend loss region. For the case of holey fibre HF_1, data sets are shown that correspond to two different angular orientations of the fibre relative to the bend (see Fig. 4.10 (b)). These two data sets demonstrate that both the transition loss and the pure bend loss depend strongly on the orientation of the holey fibre relative to the bend. Notice also that the shape of the curve in the transition region for holey fibre HF_1 is more complex than that of the conventional fibre, which may reflect the more complex spatial modal field distribution of a bent holey fibre

The pure bend loss for one loop of fibre, extracted from the slope of the linear fit to the pure bend loss regions in Figs 4.10 (a) and (b), is found to be 19.4 dB for the conventional fibre C_1 and 14.0 dB and 16.6 dB for the different orientations of holey fibre HF_1 for $R_o = 14.5$ mm. The range of values measured here for HF_1 compare well with predicted values of pure bend loss, which range between 13.9 dB and 16.8 dB depending on the angular orientation of the fibre and the polarisation of the mode. (The variation in bend loss as a function of angular orientation and polarisation is discussed in more detail in Section 4.5.5.)

The transition loss for $R_o = 14.5$ mm, extracted from the y intercept of the straight line fit, is found to be approximately 0.06 dB for the conventional fibre C_1 and 4.5 dB and -2.2 dB for the different orientations of the holey fibre HF_1. This latter, apparently non-physical, result may arise from the assumption that the pure bend loss is constant within the transition regions at the beginning and end of the bend. This is true only if the mode of the straight fibre transforms into the mode of the bent fibre instantaneously. From the width of the transition region in Figs 4.10 (a) and (b) we can see that this is not the case. As mentioned previously, on entering the bend, the modal field evolves, over some length scale, into the mode of the bent fibre, which extends further into the cladding in the direction of the bend. In the initial stages of distortion, the pure bend loss will thus be less than for the fully distorted mode. By assuming a constant value of pure bend loss within the transition region, we underestimate the transition loss from the intercept of the straight line fit to the pure bend loss region. From this argument, we can see that the y intercept of the straight line fit to the pure bend loss region may be negative, if the mode distortion is significant. For fibre HF_1 at 1550 nm, with a bend radius of 14.5 mm, the overall predicted transition loss is equal to 2 dB, which is approximately consistent with the experimentally derived values. Although this value is still small when compared to the pure bend loss, it is significantly higher than the measured transition loss for the similarly sized conventional fibre C_1 for $R_o = 14.5$ mm.

Results for $R_o = 19$ mm for fibre HF_1 at 1550 nm are shown in Fig. 4.10 (c) and demonstrate that for this larger bend radius and lower overall loss, the transition region is relatively less pronounced. The two data sets shown here were chosen to correspond with the maximum and minimum observed loss orientations. The pure bend loss for one loop of fibre, extracted from the slope of the linear fit to the pure bend loss regions in Fig. 4.10 (c) are 4.0 dB and 12.6 dB for the different orientations of holey fibre HF_1. Again, this

shows good agreement with our predicted values for pure bend loss, which are found to be between 6.6 dB and 7.7 dB for one loop of fibre, depending on the angular orientation of the fibre and the polarisation of the mode.

The effect of the short wavelength loss edge was also briefly investigated. Since the midpoint between the long and short wavelength loss edges has empirically been shown to be $\Lambda/2$ [32], we expect that the bend loss for all wavelengths below 1550 nm should increase, despite the fact that the mode size decreases ($A_{\text{eff}}^{\text{FM}} = 130\ \mu\text{m}^2$ at 1550 nm and $A_{\text{eff}}^{\text{FM}} = 70\ \mu\text{m}^2$ at 633 nm). This was confirmed experimentally by measuring the bend loss of fibre HF_1 at 633 nm, using the set-up shown in Fig. 4.6 for the two angular orientations shown in Fig. 4.10 (b) ($R_o = 14.5$ mm, data not shown here for reasons of brevity). As expected, we find that the losses at 633 nm are considerably higher than for this same bend radius at 1550 nm, shown in Fig. 4.10 (b). The components of loss, extracted from a straight line fit to the pure bend loss region, yield values of 9 dB for two transition losses and 50 dB for one full loop of fibre. Although the transition loss is still a small overall contribution to the overall loss, it is relatively higher than for the same fibre and bend radius at 1550 nm. In addition, we also find that there is no significant difference in the bending losses for the two angular orientations of fibre, which correspond to the maximum and minimum loss orientations found at 1550 nm. Recall that our predictions show that for a given bend radius, the modal field suffers a greater distortion at 633 nm relative to 1550 nm, increasing the modal field intensity close to the boundary of the microstructured cladding. As a result, we may expect the variation in loss as a function of angular orientation to increase at 633 nm relative to 1550 nm. This is something that obviously warrants further investigation, but is not considered in any more detail here.

In the next section, we investigate the effect of the geometry of the cladding structure on the bend loss characteristics at 1550 nm in more detail.

4.5.5 Bending losses in holey fibres as a function of angular orientation

For the holey fibres considered in this chapter, we have shown that the measured bend loss varies as a function of the angular orientation of the fibre in the bend (see for example Fig. 4.10). In this section we look at this in more detail using both experimental and theoretical techniques.

In Fig. 4.11 the predicted pure bend loss is shown for holey fibre HF_1 as a function of bend radius. For each bend radius, the loss is shown for bend directions of $\phi = 0^{\text{o}}$, 45^{o} and

90°, calculated using both the scalar and vector version of the modal model described in Section 3.2. The relationship between the bend loss, the bend direction and the polarisation of the mode is complex, and for simplicity we highlight the main trends shown in Fig. 4.11. We can clearly see that the variation in bend loss for any given bend radius increases as the bend becomes tighter. In addition, we find that for those bends that are tighter than the critical radius, the variation in loss can be mainly attributed to the different polarisations of the mode. (In addition, we also find that the degree of variation is most pronounced for the y-polarised mode in this regime). Conversely, for those bends that are larger than the critical radius, the loss variation is greatest for the different bend directions, and the influence of the mode polarisation is small. Note also that while the results calculated using the scalar version of the modal model in Section 3.2 predict a smaller variation in loss with respect to the angular orientation of the fibre in the bend, the average loss values agree well, demonstrating that the scalar version is perfectly adequate for a practical estimation of R_c^{FM}.

From previous experiments we have seen that the observed variation in loss agrees well with predicted values for pure bend loss. However, in the results presented in Section 4.5.4 only a few angular orientations of the fibre were considered. To evaluate the relationship between bend loss and the angular orientation of the fibre in a more systematic manner, we used the experimental set-up shown in Fig. 4.6. The wrap-around angle θ was fixed at 130° and the loss was measured as a function of angular orientation (ϕ) for holey fibre HF_1 for a fixed bend radius of 14.5 mm and 19 mm at 1550 nm. A wrap-around angle of 130° was chosen so that the majority of loss could be attributed to pure bend loss without the overall loss value being too severe. The resulting loss curve for $R_o = 14.5$ mm (not shown here for brevity) shows a variation in loss with angular orientation that is equivalent to a loss of 41.5 dB in one full loop of fibre, with a minimum loss of 5.5 dB and an average loss approximately equal to 19 dB for one loop. This value, averaged over 160 equally spaced angular orientations, agrees well with our predicted values of pure bend loss, which range between 13.9 dB and 16.8 dB depending on the angular orientation of the fibre and the polarisation of the mode (from Fig. 4.11). However, the observed variation in loss per loop is far greater than predicted by theory; 41.5 dB compared to the predicted value of 2.9 dB.

Similarly, we find that for a bend radius of 19 mm, the average observed loss values agree well with predictions, but the degree of variation does not. Measured values of bend loss vary between 4.0 dB and 12.6 dB, with an average value (averaged for 11 equally spaced

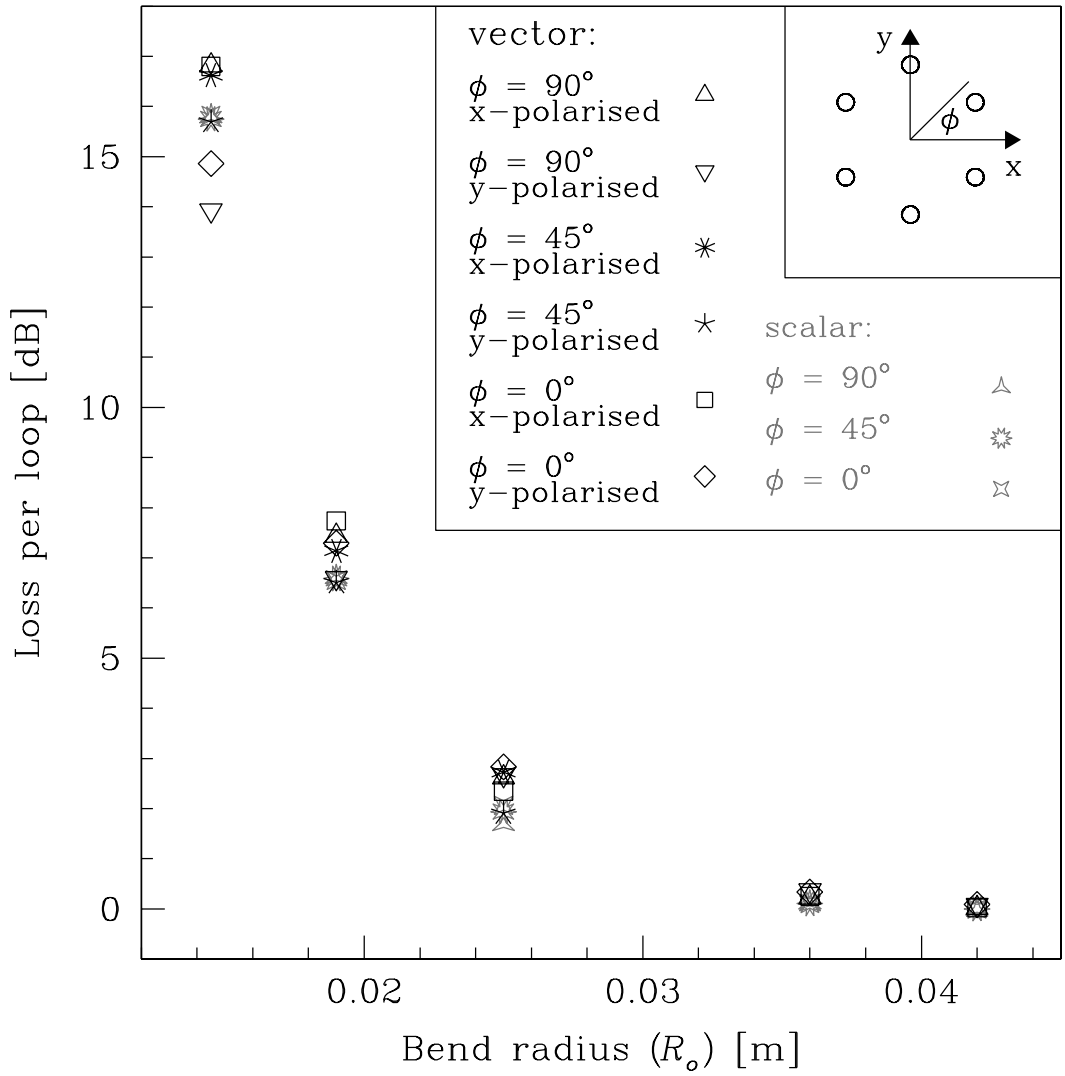

Figure 4.11: Predicted pure bend loss as a function of bend radius for HF_1 at 1550 nm for different bend directions (ϕ) and polarisation states as indicated on the figure.

values of ϕ) of 8.7 dB for one loop of fibre, while predicted values vary from 6.6 dB to 7.7 dB for one loop of fibre.

In order to understand this apparent discrepancy between the observed variation in loss and our theoretically derived values, we investigated how the cladding structure of the fibres used here differs from the idealised fibre profile used in our theoretical calculations. One obvious difference is the slightly irregular nature of the outer boundary of the microstructured cladding, which results from the fact that the positions of the air holes deviate from the perfect lattice in the 3 outermost rings of holes. Furthermore, in all of the fibres used here, the core is offset from a central position by one lattice point and results in the fact that the extent of the cladding (D) varies from seven to eight rings of holes around the

core. Unfortunately, the loss curves for HF_1 as a function of angular orientation at 14.5 mm and 19 mm (both not shown here) have a complex shape, and it is difficult to correlate the measured loss values with any of the features discussed above. However, we find that by increasing the bend radius and thus decreasing the overall loss values, it becomes easier to distinguish the effects of some of the cladding features.

The bend loss was measured as a function of the angular orientation of the fibre for holey fibre HF_4, which is larger in scale than HF_1 (parameters shown in Table 4.1), but has an almost identical cladding configuration. A bend radius of 30.5 mm was chosen for this fibre to achieve low overall bending losses so that the effects of the cladding might be more clearly distinguished. Fig. 4.12 (a) shows loss as a function of angular orientation for HF_4 for a wrap-around angle of 130^o and a bend radius of 30.5 mm at 1550 nm. Fig. 4.12 (b) shows $1/D$ as a function of angular orientation, where D is defined as the distance from the centre of the core to the centre of the outermost hole in the cladding. We can see that these two graphs are strongly correlated, with the region of minimum loss coinciding with the direction in which the extent of the cladding is greatest and the maximum region of loss coinciding with direction in which the outermost hole is closest to the core. Indeed, these results show that for this radius, one additional ring of holes in the cladding can reduce the loss by approximately 1.5 dB for a wrap-around angle of 130^o, which is equivalent to a reduction of 20 dB/m. In addition to the overall shape of the two curves, we can also see that some of the sharp features in the shape of the cladding boundary are reflected in the loss curve. For example, around 140^o and between 200^o and 230^o sharp increases in loss can be seen to correspond to holes in the outermost cladding that are closer to the core than their neighbours. This demonstrates that both the overall extent of the cladding and the shape of the boundary are important factors in determining the bend loss and must be considered in the design of future holey fibres.

4.6 Discussion and conclusion

The theoretical approaches to bend loss presented in Chapter 3 are validated via comparison with experimental results in the above sections. Results from an experiment designed to separate the components of bend loss is presented in Section 4.5.4. The results from this experiment, which was performed for several different bend radii and at different wavelengths, show, unsurprisingly, that both components of bend loss increase as the bend radius is reduced. In addition, by comparing results for different wavelengths it can be seen that

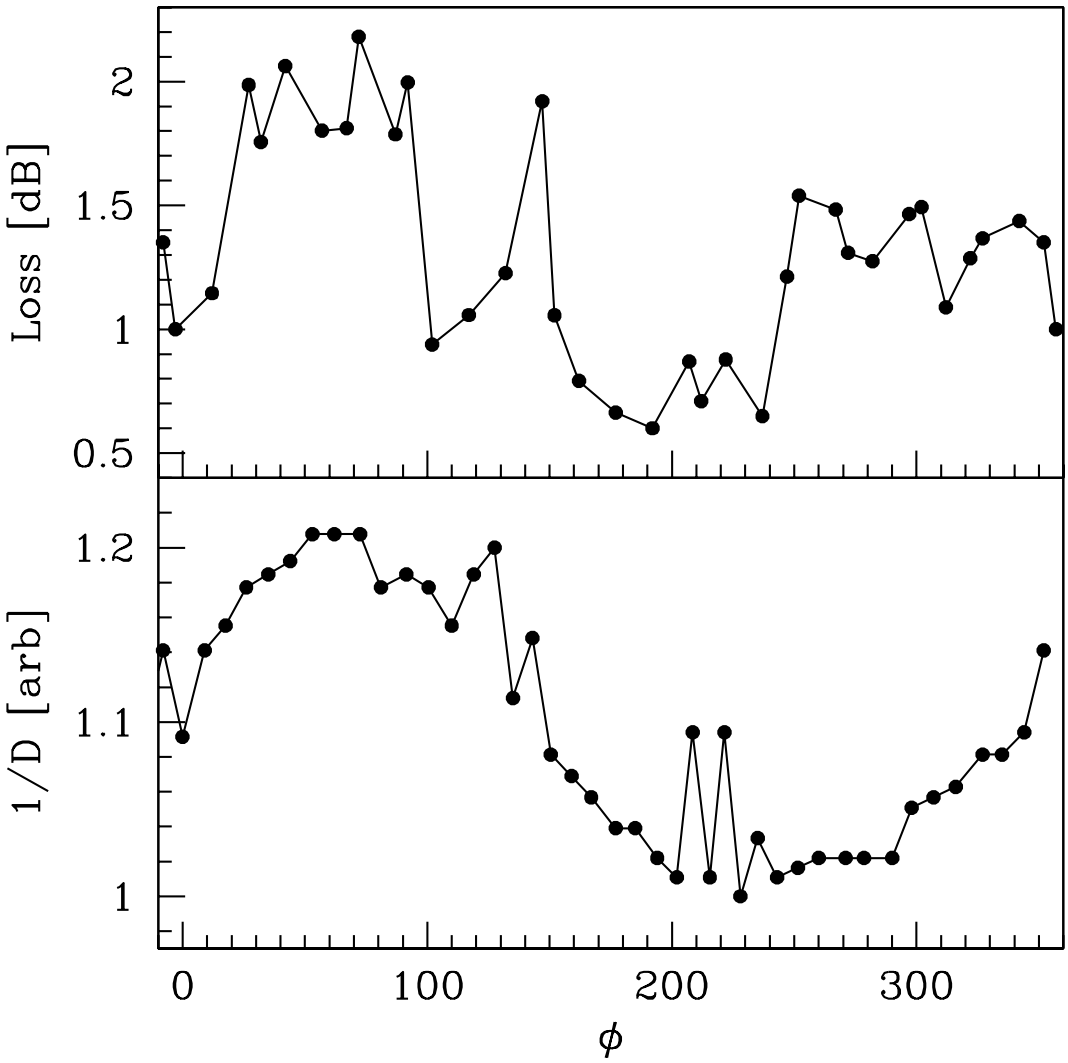

Figure 4.12: (a) Loss as a function of angular orientation for holey fibre HF_4 $R_o = 30.5$ mm (b) $1/D$ as a function of angular orientation for holey fibre HF_4 where D = distance from the centre of the core to the outermost hole in the cladding.

both the transition loss and the pure bend loss increase towards short wavelengths, despite the fact that the mode area decreases, demonstrating the presence of the short wavelength bend loss edge. These relationships are correctly predicted by the models for transition loss and pure bend loss described in Sections 3.4 and 3.5, and show that the mode of the bent fibre becomes increasingly distorted with decreasing bend radii and wavelength. In addition, both experimental observations and theoretical predictions show that the transition loss is a small overall contribution to macro-bend loss in the holey fibres considered here and that the bend loss for one full loop of fibre can be well approximated by pure bending losses only, as in conventional fibres. Recall that in the model of pure bend loss

described in Section 3.5, a constant of proportionality (τ) was introduced in Eq. 3.16. Since the transition loss is a small contribution to the overall loss (Fig. 4.9), this factor can be found by fitting the predicted curves to the experimental data. We find that by choosing $\tau = 6$, we achieve excellent agreement with experimental data for all three fibres, as can be seen in Figs 4.9 (a), (b) and (c). Indeed, the model of pure bend loss proposed here predicts the critical radius to within 4-12% of the observed value for the three fibres considered in this chapter.

As mentioned previously, an important difference between conventional and holey fibres is the complex nature of the transverse refractive index profile. Previous work on bending losses in holey fibres has ignored the effect of the complex fibre structure for simplicity. However, a strong variation in loss is observed as a function of angular orientation in the holey fibres considered in this section, as demonstrated in Section 4.5.4. Calculations of pure bend loss made using the full vectorial version of the orthogonal function method (as described in Section 3.2), demonstrate that the bend loss does vary as a function of the angular orientation of the fibre in the bend and also that the different polarisations experience different losses. These calculations, which are presented in Section 4.5.5, show that the variation in the predicted pure bend loss with respect to angular orientation and polarisation increases as the bend is tightened. However, the maximum predicted variation in loss with respect to different bend directions and different polarisation is an order of magnitude less than the variation observed experimentally and thus the inner fibre geometry cannot be responsible. Instead, it is found that the variation in bend loss with respect to the fibre orientation is directly related to the extent of the cladding and, more specifically, to the distance from the centre of the core to the outermost hole (for the fibres considered here, the core is offset by one lattice point), as shown in Section 4.5.5. The fact that this relatively subtle deviation from a perfect structure is so strongly reflected in the bend loss indicates that the structure of the outer cladding is an important consideration in large-mode-area holey fibre design. This variation in bend loss results from the fact that the confinement of the bent mode is strongly dependent on the extent of the cladding. Due to the fact that the model used here to calculate the modal fields of the bent fibre uses periodic boundary conditions, we are not able to model the confinement losses of the distorted mode that are associated with a finite holey cladding. Methods that could be used to study these effects in holey fibres include the multipole approach and various BPM or finite element techniques. However, BPM and finite element techniques are typically computationally

intensive and the multipole approach is not capable of modelling the mode of a bent holey fibre using the transformation in Eq.3.9, since it assumes a constant background refractive index [99].

As mentioned in Section 4.8, the four holey fibres considered within this section are not made from a single grade of silica and possess a lower refractive index region in their outermost cladding layer due to the fact that a lower grade silica glass was used for the outer jacketing tube in the preform of these fibres. Consequently, we find that the fitting factor of $\tau = 6.0$ is too high for other fibres that are made entirely from a single grade of silica. For all other fibres considered in this thesis, which are made entirely from a high grade silica, $\tau = 2.0$ is found to produce excellent agreement with experimental results. (For examples please refer to Sections 5.4, 5.6, 6.2.4, and 7.3.3).

Note that the decrease in τ from 6.0 to 2.0 corresponds to a 3-fold increase in bend loss, and values of R_c^{FM} that are between 5 and 20% larger, depending on the particular fibre structure. These results suggest that a second, lower-index cladding region may be an effective way to reduce bending losses in large-mode-area holey fibres. This improvement in bend loss may result from the fact that the lower index region confines the cladding modes and couples power back into the core mode more efficiently, resulting in lower bending losses. However, this is not pursed here for several reasons. The methods developed here to predict bend loss in holey fibres are capable of modelling arbitrary index profiles, and so can include a low index region in the outer cladding. However, initial calculations made using the techniques described in Chapter 3 for structures with low index regions in the outer cladding show minimal improvement in bend loss. This is thought to result from the fact that coupling effects are ignored in the model of bend loss developed here. Moreover, the main aim of the work presented here is to gain a good understanding of the way in which the basic fibre parameters d and Λ influence the mode area, the bend loss and the modedness of the fibre, which represent the three key fibre properties for large-mode-area design. This study is presented in the following chapter, in which the trade-offs between mode area and bend loss are investigated in the single-mode regime as a function of fibre structure at a wavelength of 1064 nm. The way in which more complex cladding designs can be used to improve bend loss in a holey fibre is discussed in more detail in Chapter 6.

Part III

Numerical and experimental results

Chapter 5

Large-mode-area, single-mode holey fibres at 1064 nm

5.1 Introduction

The aim of this chapter is to determine the maximum practical mode size that can be achieved in a holey fibre for single-mode operation at 1064 nm. As with any fibre, the maximum mode size that can be tolerated in practice is determined by the bending losses. The upper limit for tolerable bend loss is defined here as a critical bend radius (R_c) of 15 cm, where R_c is defined as the radius at which the bend loss is equal to 3 dB for one loop of fibre. This value is based on observations of the behaviour of various large-mode-area fibres during experimental characterisations. I have found that fibres with a critical bend radius greater than $\approx$ 15 cm become extremely sensitive to low level vibrations and air-currents in the laboratory environment, and exhibit rapidly fluctuating power levels. Of course, the definition of a tolerable bend radius will differ greatly depending on the application and the way in which the fibre is packaged. For example, some applications may require short lengths of near straight fibre that could be packaged in a robust and rigid outer tube to protect from perturbations. In this case the maximum tolerable mode area will obviously be greater than that predicted here, but for most applications, which require coiled lengths of fibre in order to minimise device size, a bend radius of <15 cm may be more practical. For comparison, the minimum recommended bend radius for conventional single-mode step-index fibre with $A_{eff}^{FM} \approx 80\ \mu m^2$ at 1550 nm is typically < 2 cm.

In order to predict the maximum practical mode size in a single-mode holey fibre at 1064 nm it is therefore necessary to understand the relationships between the structural

parameters d and Λ, the mode size, the bend loss and the number of modes present in the fibre. This task is undertaken here using the theoretical techniques described in Chapter 3 and is broken down into three calculation stages. Initially, the effective mode area of the fundamental mode (A_{eff}^{FM}) is calculated for a range of fibre structures at 1064 nm in order to map out the range of fibre parameters that produce large-mode-areas (defined as any mode area greater than 80 μm^2, which is approximately that of standard conventional step-index fibre). Once an appropriate range of structures has been identified, the critical bend radius of the fundamental mode, R_c^{FM}, is then calculated for each structure within this range. The third and final set of calculations determines which fibres within this range are single-mode. In this way, it is possible to determine the subset of structures within the parameter space studied that are both single-mode and possess practical bending losses. This three-step process is split across two sections within this thesis. In an initial study, presented in Section 5.2, fibres with A_{eff}^{FM} up to ≈ 400 μm^2 are considered. In Section 5.5.2, this work is extended to include structures with A_{eff}^{FM} up to ≈ 800 μm^2 in order to determine the largest practical mode size attainable in holey fibres at 1064 nm. Unless otherwise indicated, all values of R_c presented within this chapter have been calculated for a bend in the x direction.

The calculations presented in Section 5.2 provide the basis for a more detailed study into the effect of the fibre structure on modal properties for $A_{eff}^{FM} = 190$ μm^2, which is presented in Section 5.3. By focussing on a fixed value of A_{eff}^{FM} it is possible to look at the relationship between the fibre structure and the modal properties for fibre close to cut-off in more detail. Experimental results are presented in Section 5.4 and 5.6 for a selection of holey fibres that were fabricated as part of this study. These experimental results illustrate the effectiveness of the numerical techniques used here and demonstrate that the large-mode-area structures considered here can be fabricated. In order to understand how holey fibres compare with conventional step-index fibres in this large-mode-area, single-mode regime, a similar study is also undertaken for conventional fibres and the results of this are presented in Section 5.7.

5.2 Defining the range of practical structures (1)

5.2.1 Effective mode area

In this section we investigate how the structural parameters Λ and d/Λ influence the effective area of the fundamental mode of holey fibres at 1064 nm. In the first of these studies presented here, the range of fibre parameters evaluated is chosen with the aim of

encompassing single-mode structures with 80 $\mu m^2 \lesssim A_{eff}^{FM} \lesssim 400\ \mu m^2$, that are also practical to fabricate. (The fabrication of holey fibres is discussed in Section 1.2.4.)

The minimum value of d/Λ is chosen to be 0.2 due to the fact that the modal properties of large-mode-area holey fibres, such as A_{eff}^{FM}, become increasingly sensitive to the fibre structure towards small values of d/Λ and this reduces tolerances during fabrication [31]. Moreover, we find that values of $d/\Lambda < 0.2$ result in impractically large bending losses (see Section 5.1.) The maximum value of d/Λ is determined by considering the upper limit on single-mode operation. Although there is much debate over how to determine the number of modes present in a holey fibre, with the cut-off for single-mode operation quoted for values of d/Λ ranging from 0.4 to 0.45 [142, 17, 143, 144, 145, 146, 147], all reports agree that holey fibres are multi-mode for values of $d/\Lambda > 0.5$ at 1064 nm. As a result, structures with $0.2 < d/\Lambda < 0.5$ are studied here. The range of values for Λ is then determined only by the range of effective areas required. In this section I choose $7\mu m < \Lambda < 14\mu m$ to take a first look at the range of effective mode sizes this creates.

Fig. 5.1 shows a plot of effective mode area for the fundamental mode (A_{eff}^{FM}) at 1064 nm as a function of Λ, for $7\,\mu m < \Lambda < 14\,\mu m$ for 4 values of d/Λ: 0.2, 0.3, 0.4 and 0.5 at 1064 nm. For the range of structures considered here, A_{eff}^{FM} ranges from 56 to 410 μm^2. This plot shows that the mode size can be enlarged by increasing Λ, which acts to increase the core size, or by using smaller holes, which acts to lower the numerical aperture. Note that different fibre structures can result in the same values of A_{eff}^{FM}. For example, an effective mode area of 155 μm^2 can be achieved with $\Lambda = 8.0\ \mu m$, $d/\Lambda = 0.2$ and with $\Lambda = 12.0\ \mu m$, $d/\Lambda = 0.5$, as shown in Fig. 5.1. The intensity profile of the fundamental mode for these two fibres is shown in Fig. 5.2 (a) and (b) respectively. These modal profiles show clearly that while these two fibres share the same value of effective mode area, the mode shapes are significantly different, reflecting the geometry of each fibre. In Fig. 5.2 (a), the mode extends past the first ring of air holes and as a result is filamented in shape. In contrast, the mode in Fig. 5.2 (b) is well confined to the core and presents a neater, more Gaussian-like mode shape. These differences arise from the different value of the effective cladding index (n_{FSM}) in each fibres. For the fibre in Fig. 5.2 (a) $n_{FSM} = 1.448697$, and for the fibre in Fig. 5.2 (b) $n_{FSM} = 1.448135$ (see Fig. 6.1 (b) in Chapter 6), which corresponds to a numerical aperture (NA) of 0.052 and 0.066 respectively. (the refractive index of silica is taken from the Sellmeier equation to be 1.449631, as described in Section C). In the fibre in Fig. 5.2 (a), the low NA allows the light to penetrate further into the cladding region

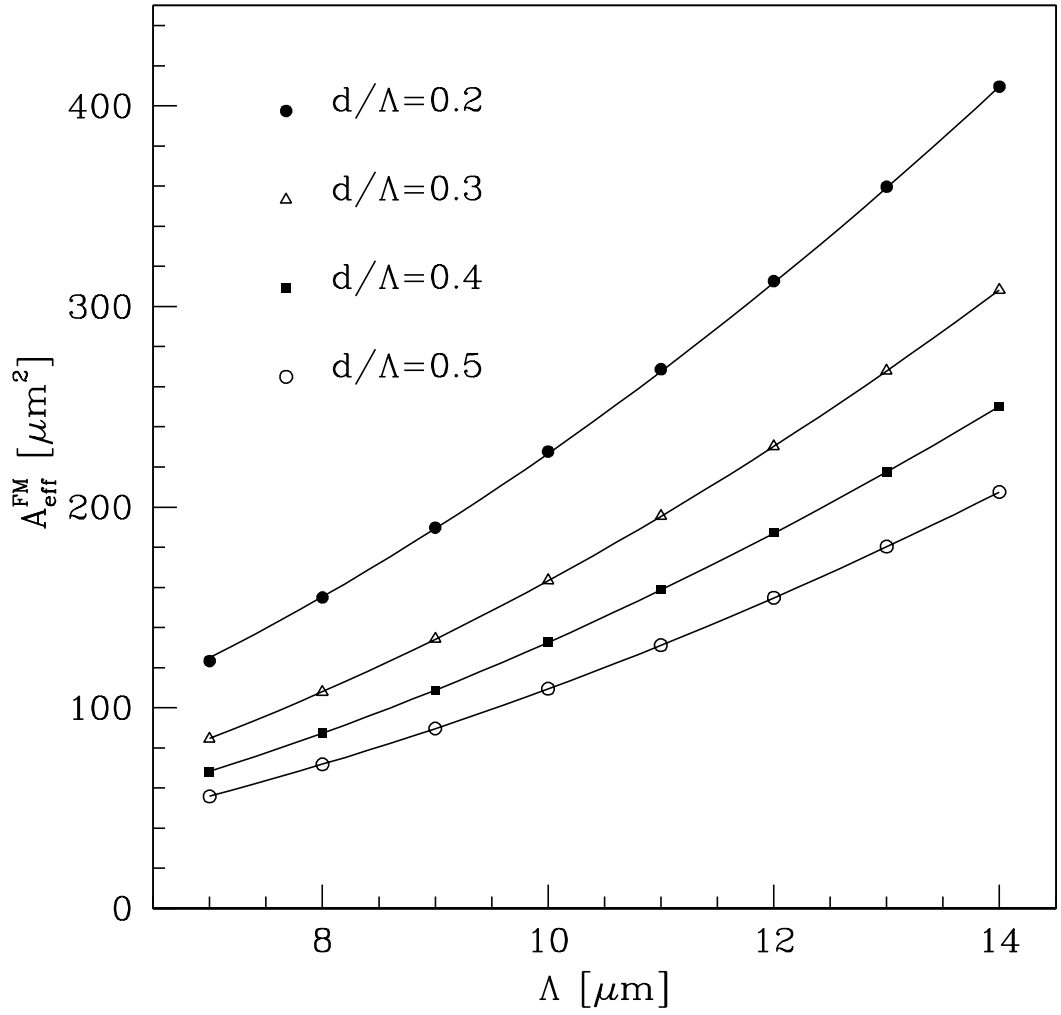

Figure 5.1: Points show the predicted effective mode area of the fundamental mode (A_{eff}^{FM}) as a function of the hole-to-hole spacing, 7 μm $< \Lambda <$ 14 μm, for a range of relative hole sizes: $0.2 < d/\Lambda < 0.5$ at 1064 nm. The solid line for each value of d/Λ is a fitted curve of the form $y = ax^3 + bx^2 + c$ drawn to guide the eye.

than in the fibre in Fig. 5.2 (b), which has a higher NA. As a result, the mode areas of the fibres are equal, despite the fact that the region of silica inside the inner ring of holes (i.e. the core) is smaller for the fibre in Fig. 5.2 (a) than in Fig. 5.2 (b).

In order to better visualise the relationship between the fibre structure and the mode size of the fundamental mode, I have used the data in Fig. 5.1 to create a contour plot of A_{eff}^{FM} as a function of Λ and d/Λ, which is shown in Fig. 5.3. (Note that the accuracy in the fit used to construct this contour plot is $\approx 2 - 3\%$). This plot shows how the mode area increases with increasing values of Λ and decreasing values of d/Λ. It can also be seen that the mode area increases more rapidly with decreasing d/Λ towards smaller values of d/Λ.

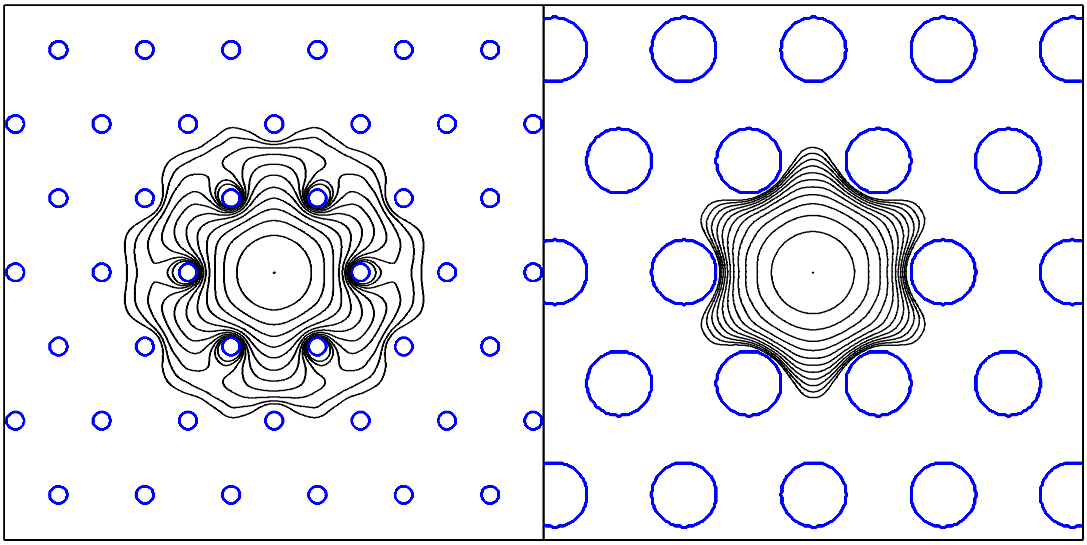

(a) (b)

Figure 5.2: Modal intensity profile at 1064 nm for a holey fibre with (a) $\Lambda = 8.0$ μm, $d/\Lambda = 0.2$ and (b) $\Lambda = 12.0$ μm, $d/\Lambda = 0.5$. Contours are separated by 2 dB.

This results from the fact that the modal field becomes less affected by each individual hole as d/Λ decreases, allowing the modal field to penetrate further into the cladding. By tracing the path of any given contour line on this plot it can also be clearly seen that a wide range of structures can be used to create fibres with the same mode area. However, as demonstrated by the above examples (shown in Fig. 5.2 (a) and (b)), each different structure that results in the same mode area will correspond to a fibre with a different mode shape and a different NA. (The effect of the fibre structure on mode shape, bend loss and modedness is studied in detail for $A_{eff}^{FM} = 190$ μm^2 in Section 5.3). The differences in mode shape and NA may influence both the number of modes guided by the fibre and the associated bending losses. The next step in this study must therefore be to determine the bend loss and the modedness of each of the structures considered here in order to determine the best way of creating single-mode fibres with the lowest bending losses for a given mode area.

5.2.2 Bend loss

In this section, the critical bend radius of the fundamental mode (R_c^{FM}) is calculated for each of the fibres in Fig. 5.1 using the numerical techniques described in Chapter 3. The results of these calculations are plotted in Fig. 5.4. As described in Section 4.5, R_c^{FM} is evaluated for each fibre considered by calculating the bend loss for several values of bend

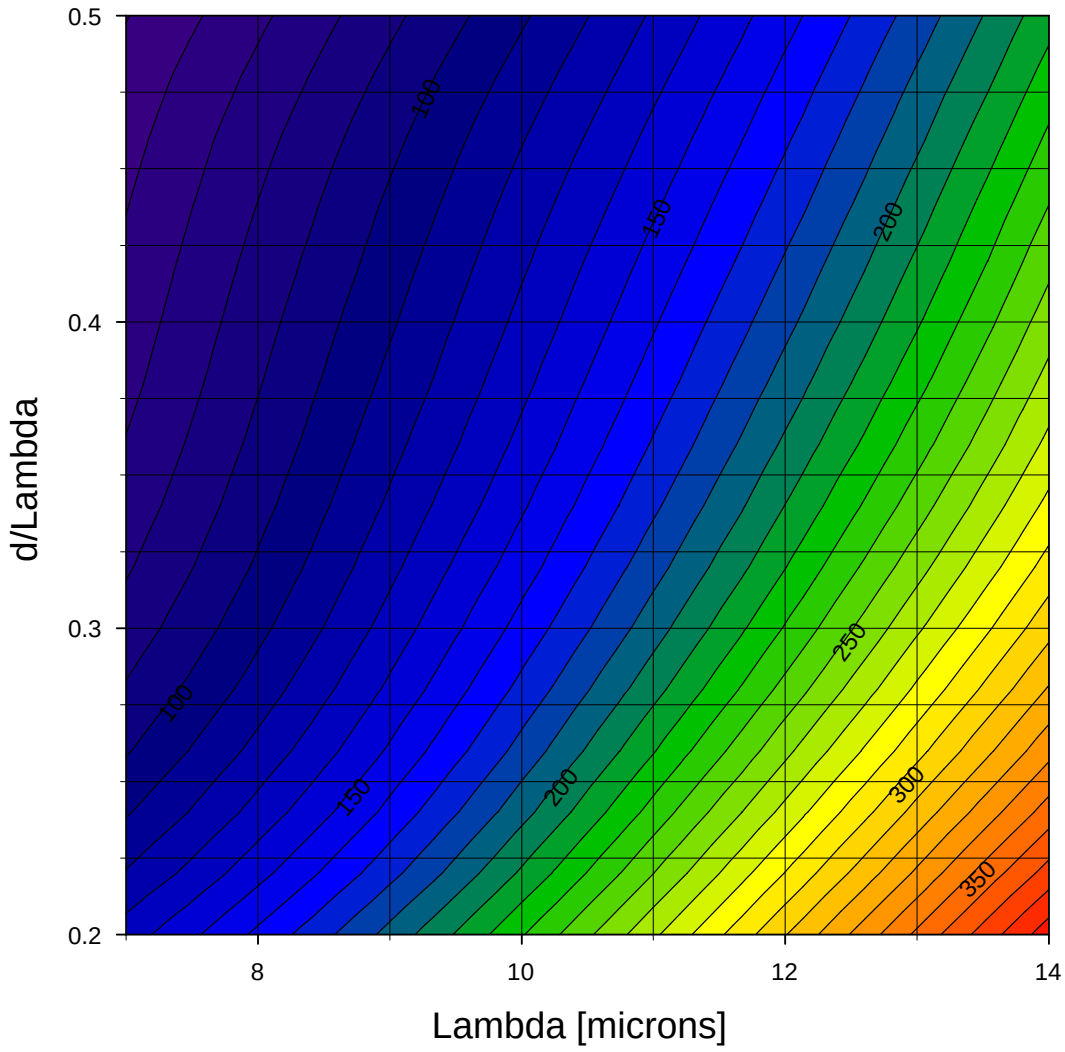

Figure 5.3: Contour plot generated from the data in (a) showing effective mode area in μm^2 as a function of Λ and d/Λ.

radius above and below R_c^{FM}. The value of R_c^{FM} is then extracted by fitting a curve through these points, as demonstrated in Section 4.5.3. The number of calculations performed for any given fibre thus depends on the number of points required to ensure that a fitted curve is representative, which is usually somewhere between 4-6. However, towards small values of Λ and large values of d/Λ, the bend loss becomes a sharp function of bend radius and a greater number of points are required to accurately determine R_c^{FM} (This is discussed further in Section 5.3). Note that in Fig. 5.4, the critical bend radii of the smallest mode area fibres with $d/\Lambda = 0.5$ are not shown. These calculations have been omitted for two reasons: (1) the calculation of R_c^{FM} is time consuming for these fibres as described above and (2) the critical bend radii of these fibres are small, each less than 2 cm, and so the

bend loss is not a concern from a practical standpoint.

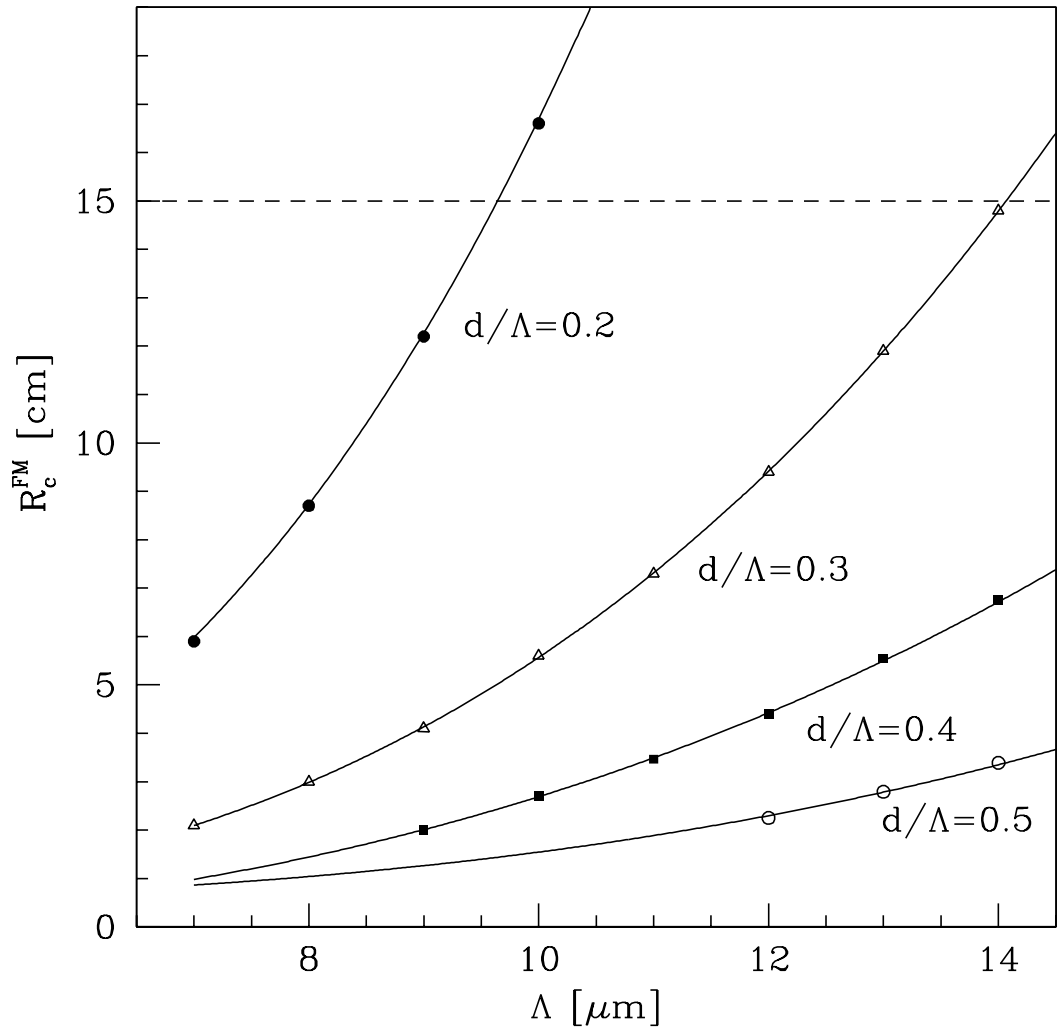

Figure 5.4: Points show predicted values of the critical bend radius of the fundamental mode (R_c^{FM}) as a function of the hole-to-hole spacing, Λ, for a range of holes sizes: $0.2 < d/\Lambda < 0.5$ at 1064 nm. The solid line for each value of d/Λ is a fitted curve of the form $y = ax^3 + b$, drawn to guide the eye. The dotted line marks the position of $R_c^{FM} = 15$ cm.

Fig. 5.4 shows R_c^{FM} for a selection of the fibres considered here at 1064 nm, which range in A_{eff}^{FM} from 56 to 410 μm^2. For the entire range of fibres, R_c^{FM} ranges from below 2 cm to as high as 45 cm. However, only those fibres with practical levels of bend loss ($R_c^{FM} < 15$ cm) are indicated on Fig. 5.4. This plot shows that the bend loss improves (i.e. R_c^{FM} decreases) with decreasing Λ and increasing d/Λ. These facts demonstrate that the relationship between bend loss and the fibre structure in holey fibres is similar to that of conventional fibres, in which the bend loss can be improved by decreasing the core size

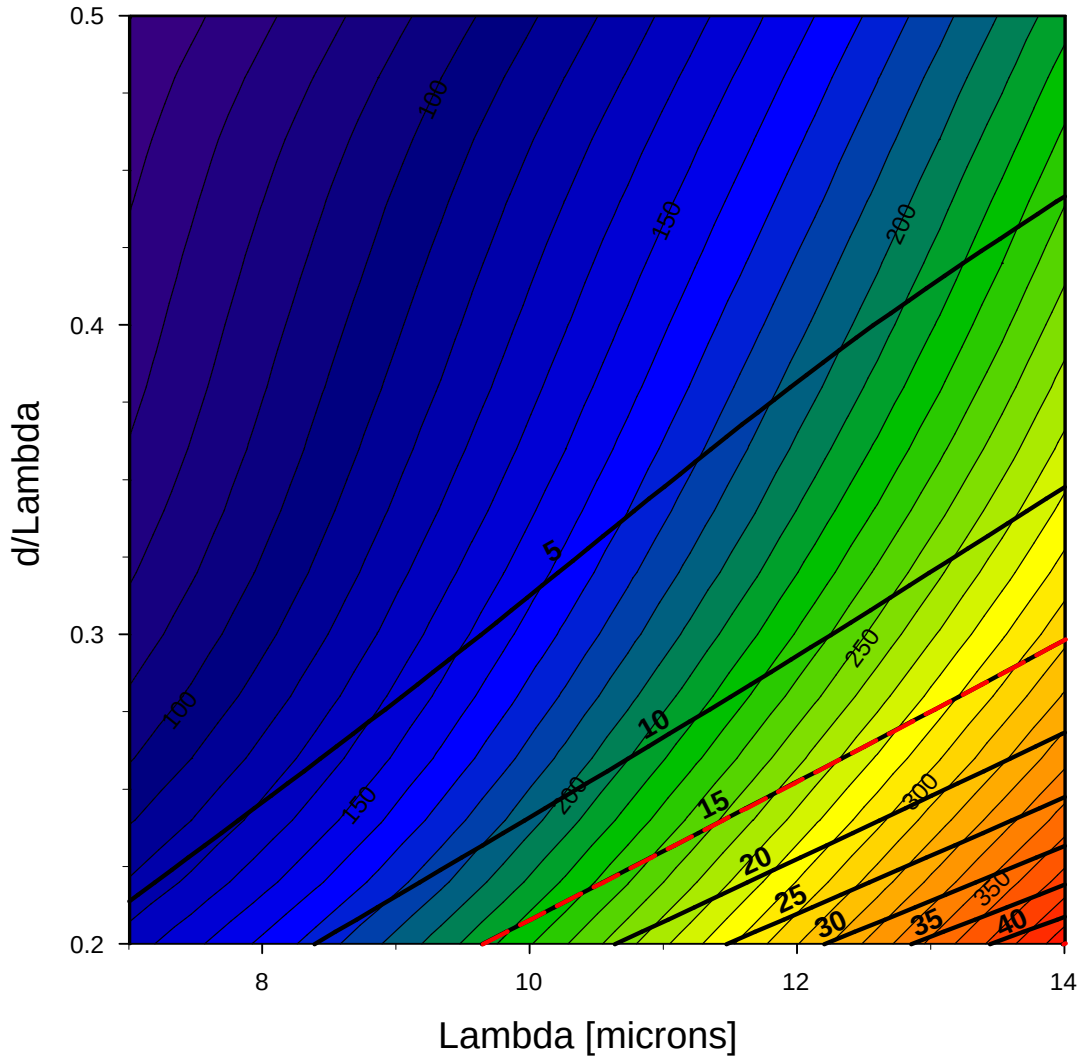

Figure 5.5: Thick black lines show contours of the critical bend radius of the fundamental mode (R_c^{FM}) in cm (generated from the data in Fig. 5.4) as a function of Λ and d/Λ. The dashed red and black line indicates the $R_c^{FM} = 15$ cm contour line. The graded colour contours correspond to A_{eff}^{FM} in μm^2, repeated from Fig. 5.3.

and/or increasing the numerical aperture. This is further discussed in Section 5.7, in which the bending losses of holey and conventional fibres at 1064 nm are compared in detail.

As before, a contour plot of R_c^{FM} as a function of Λ and d/Λ is constructed in order to better visualise the relationship between the fibre structure and the bend loss (note that the accuracy of the fit that is used to construct this contour plot is $\approx 2-3\%$). Contour lines of R_c^{FM} in cm are shown by the thick black lines in Fig. 5.5, which are superimposed onto the contour plot of A_{eff}^{FM}, repeated from Fig. 5.3. As in Fig. 5.4, this contour plot demonstrates that the bending losses increase towards larger values of Λ and decrease for larger values of d/Λ. By plotting the A_{eff}^{FM} and R_c^{FM} together in this way it becomes easy to visualise

how the A_{eff}^{FM} and R_c^{FM} both change with respect to the structural parameters. For example, Fig. 5.5 demonstrates that for a given value of d/Λ, both A_{eff}^{FM} and R_c^{FM} increase with Λ. Similarly, for a fixed value of Λ we see that both A_{eff}^{FM} and R_c^{FM} decrease as the relative hole size is increased. Recall that in Section 5.1 the upper limit for tolerable bend loss was defined as a critical bend radius of 15 cm (shown on Fig. 5.3 by the dashed red and black contour line). By using this definition, the range of fibres that possess tolerable levels of bend loss are located above the R_c^{FM}=15 cm contour line in Fig. 5.5. The largest mode area fibre in this range has $A_{eff}^{FM} \approx 320\ \mu m^2$. However, it can be seen that for any given value of A_{eff}^{FM}, the bending losses improve as the relative hole size increases. This demonstrates that the optimum way of creating large-mode-area holey fibres at 1064 nm, with low values of bend loss, is to use large values of Λ and d/Λ. (This is intuitive, since it is equivalent to using a large core and a high NA in a conventional fibre.) If this relationship holds true for $\Lambda > 14\ \mu m$, one can imagine following the contour lines of $A_{eff}^{FM} > 320\ \mu m^2$, across and up to larger values of Λ and d/Λ, into a region of parameter space where $R_c^{FM} < 15$ cm. However, as discussed in Chapter 1, the number of modes supported by a holey fibre increase with increasing d/Λ. It is therefore essential to know the position of the boundary between single-mode and multi-mode guidance on Fig. 5.5 before additional structures are considered. This is explored in the following section.

5.2.3 Modedness

In the previous two sections, the effective mode area and bending losses of the fundamental mode for a selection of holey fibres with structural parameters in the range $0.2 < d/\Lambda < 0.5$ and $7\ \mu m < \Lambda < 14\ \mu m$ have been evaluated and the range of practical structures has been determined. However, as mentioned in Section 1.5, in this study, I wish only to consider single-mode structures. In order to assess the subset of structures in Fig. 5.5 that are single-mode, I choose to use a simple analytical formula from Ref. [19] that is extrapolated from numerical calculations made using a multipole technique. In Ref. [19], the modedness is determined by evaluating the effective area of the first mode above the fundamental mode in effective index, herein referred to as the second mode. The second mode is defined to be a higher-order mode of the fibre if it is confined to the core region. If the second mode is instead localised within the cladding, it is defined to be a cladding mode. At the boundary between single and dual-mode guidance the effective area of the second mode expands rapidly as the mode changes from being tightly confined to the core to filling the

entire cladding region. As a result, the position of the single/dual-mode boundary can be calculated by evaluating the effective area of the second mode for a range of structural parameters. A fit to the numerical data yields the equation below that describes the parameter subspace over which holey fibres are single-mode:

$$\lambda/\Lambda = \alpha(d/\Lambda - 0.406)^{\gamma} \tag{5.1}$$

where $\alpha = 2.80 \pm 0.12$ and $\gamma = 0.89 \pm 0.02$. The value of 0.406 represents the predicted value of d/Λ for which a holey fibre is endlessly single-mode. This equation provides a quick and simple way of evaluating the position of the single-mode/multi-mode boundary for a wide range of fibre structures. The calculations within Ref. [19] are performed for a wavelength of 1550 nm and the refractive index of silica is taken to be 1.444024. Compared with the value of 1.449631 used here for calculations at 1064 nm, this corresponds to a difference of less than 0.4% in index. Based on comparisons of $(d/\Lambda)_c$ made using a different technique in Section 5.3, we deduce that this small difference in refractive index does not seem to influence the predicted position of the single-mode/multi-mode boundary in any significant way.

Eq. 5.1 can be rearranged to give an equation that defines the value of d/Λ at which higher-order modes appear in holey fibres as a function of the structural parameters d and Λ:

$$(d/\Lambda)_c = \frac{\sqrt[\gamma]{\lambda/\Lambda}}{\alpha} + 0.406 \tag{5.2}$$

The value of $(d/\Lambda)_c$ for $\lambda = 1064$ nm is indicated on Fig. 5.6 by the solid red line. Note that $(d/\Lambda)_c$ flattens to an asymptotic value of 0.406 towards large values of Λ. This results from the fact that the effective cladding index in a holey fibre asymptotically approaches the refractive index of glass towards large values of Λ. The subset of fibres within the range studied here that are both single-mode and that possess practical levels of bend loss are therefore bounded by the solid red line and the dashed red and black $R_c^{FM} = 15$ cm contour line on the contour plot of A_{eff}^{FM} in Fig. 5.6. The largest practical mode area in a single-mode holey fibre at 1064 nm will thus be located at the point where the single-mode/dual-mode boundary line and the $R_c^{FM} = 15$ cm contour line in Fig. 5.6 meet. It can be seen that this will occur at somewhere in the range $0.3 \lesssim d/\Lambda \lesssim 0.42$ and $\Lambda > 14$ μm and is further explored in Section 5.5.2.

In the next section, I present the results from a more detailed study of mode shape, bend loss and modedness for a selection of fibres that lie along the 190 μm^2 contour line of A_{eff}^{FM}.

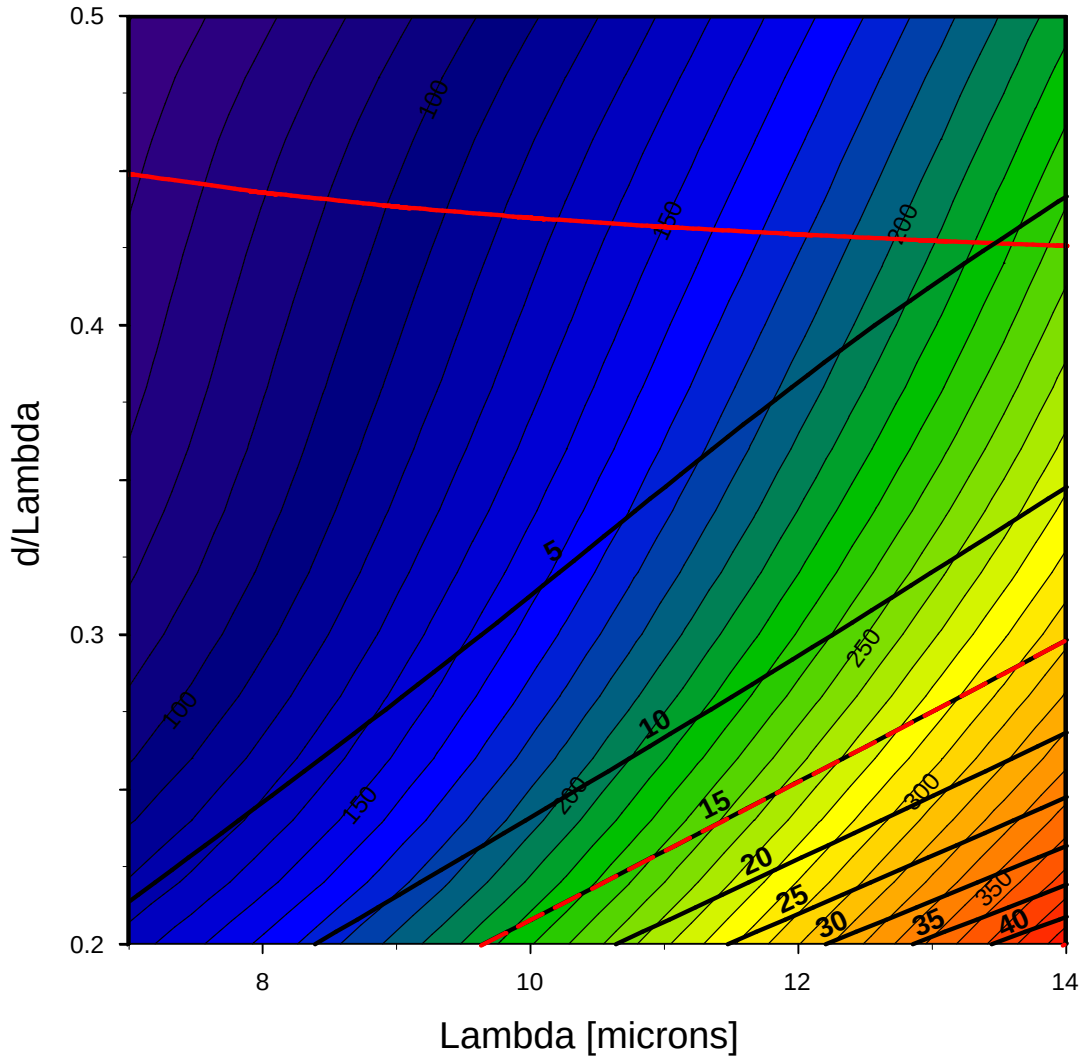

Figure 5.6: Thick black lines show contours of the critical bend radius of the fundamental mode (R_c^{FM}) in cm (generated from the data in Fig. 5.4) as a function of Λ and d/Λ. The dashed red and black line indicates the $R_c^{FM} = 15$ cm contour line. The graded colour contours correspond to A_{eff}^{FM} in μm^2, repeated from Fig. 5.3. The solid red line indicates the value of $(d/\Lambda)_c$ from Eq.5.2

5.3 Numerical study of holey fibres with $A_{eff}^{FM} = 190\ \mu m^2$

5.3.1 Introduction

In this section, results are presented from a detailed numerical study of the modal properties of a selection of fibres with different structural parameters that all possess $A_{eff}^{FM} \approx 190\ \mu m^2$. An A_{eff}^{FM} of 190 μm^2 was chosen as this represents a reasonably large-mode-area for which all fibres with $d/\Lambda > 0.2$ are practical in terms of their bending losses ($R_c^{FM} < 15$ cm), as shown in Fig. 5.6. This range of structures thus encompasses both single-mode and multi-mode fibres. The aim of this study is to evaluate how the modes of these fibres

and their associated losses change as the relative hole size increases. By choosing a range of fibres with the same A_{eff}^{FM} it is possible to make valid comparisons in terms of bending losses. These results are also used to validate the use of Eq. 5.2 to determine the position of the single-mode/multi-mode boundary shown in Fig. 5.6 and to help illustrate some of the key findings in the above sections. This numerical study is complemented by the experimental results presented in Section 5.4, which demonstrate the effectiveness of the modelling techniques used here to predict the modal properties of large-mode-area holey fibres.

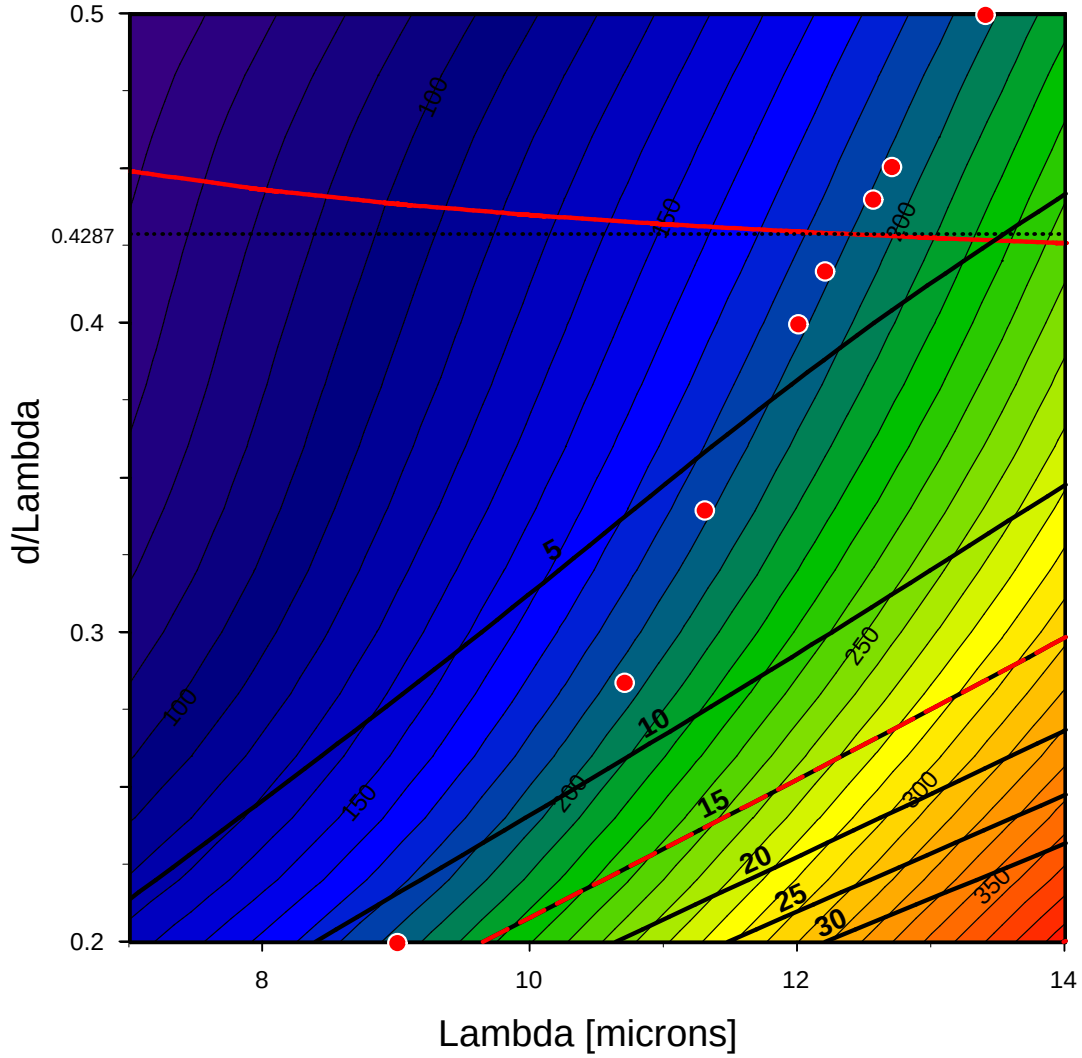

Figure 5.7: The effective area contour plot from Fig. 5.3 (b) is repeated here. The solid black lines represent the R_c^{FM} lines, the dashed red and black line indicates the R_c^{FM} = 15 cm contour line and the solid red line represents the value of $(d/\Lambda)_c$ from Eq.5.2. The dotted black line marks the value of d/Λ where the A_{eff}^{FM} = 190 μm^2 contour line intercepts the solid red line. The red dots show the structural parameters of some holey fibres listed in Table 5.1.

Table 5.1 lists the structural parameters and calculated modal properties for a selection of holey fibres that possess $A_{eff}^{FM} = 190\ \mu m^2$ at 1064 nm. d/Λ ranges from 0.2 to 0.63 and Λ ranges from 9.0 to 15.0 μm. The values of A_{eff}^{FM} and R_c^{FM} listed in Table 5.1 have once again been calculated using the numerical methods described in Chapter 3. The parameters of these holey fibres are shown by the red dots on the contour plot of A_{eff}^{FM} in Fig. 5.7. Note that the slight deviation in the position of each red dot from the 190 μm^2 line in Fig. 5.7 is in part due to the accuracy of the contour plot itself (fitted curves used to construct contour lines accurate to $\approx 2-3\%$) and also results from the fact that the effective area of each fibre is only approximately equal to 190 μm^2 in each case (see Table 5.1). However, for the purposes of this study, the effective areas of each fibre are similar enough to be considered identical.

5.3.2 Modedness

Table 5.1: Calculated modal properties for a range of holey fibre structures. SM stands for single-mode, MM stands for multi-mode. FM refers to a property of the fundamental mode.

Fibre	Λ [μm]	d [μm]	d/Λ	A_{eff}^{FM} [μm^2]	R_c^{FM} [cm]	Modes
HF_A	9.00	1.80	0.20	190	12.2	SM
HF_B	10.70	3.04	0.28	190	7.7	SM
HF_C	11.30	3.84	0.34	190	5.9	SM
HF_D	12.00	4.80	0.40	188	4.4	SM
HF_E	12.20	5.09	0.42	187	4.0	SM
HF_F	12.56	5.53	0.44	189	3.7	MM
HF_G	12.70	5.73	0.45	188	3.6	MM
HF_H	13.40	6.70	0.50	190	3.0	MM
HF_I	15.00	9.46	0.63	189	1.8	MM

Also included in Table 5.1 are predictions for the modedness of each fibre, in which SM indicates a single-mode fibre and MM indicates a multi-mode fibre. This property has been determined by Vittoria Finazzi from the ORC using a multipole approach [54] (this approach is outlined briefly in Section 1.4). Note that this technique differs slightly from the approach in Ref. [19] from which Eq. 5.2, used in the above calculation of modedness

for a large range of structures, is taken. While both techniques make use of the multipole approach to calculate the modal properties of a holey fibre, they differ in the way in which the modedness of a fibre is determined. As mentioned in Section 5.2.3, in Ref. [19], the modedness is defined by evaluating the localisation of the second mode. For the calculations reported in this section, the modedness of a fibre is determined by comparing the effective indices of the second mode and the fundamental cladding mode (also known as the fundamental space filling mode), which is calculated by considering the fibre structure without a defect (i.e. no core). The fibre is defined to be single-mode if the effective index of the second mode is lower than the effective index of the cladding as the second mode is thus a cladding mode. In Fig. 5.8, the effective modal indices for the second mode (HOM) and the fundamental space filling mode (FSM) are plotted as a function of d/Λ for the fibres in Table 5.1 that are close to cut-off. The value of d/Λ at which the two curves meet thus corresponds to cut-off for $A_{eff}^{FM} \approx 190\ \mu m^2$ at 1064 nm. In Fig. 5.8, the curves of effective modal index for the second mode and the fundamental space filling mode cross at $d/\Lambda = 0.4316$ (shown by the dashed line). This cut-off value is in excellent agreement with the value of 0.4287 given by Eq. 5.2 for $A_{eff}^{FM} = 190\ \mu m^2$, as shown in Fig. 5.7, which demonstrates that Eq. 5.2 can be used to accurately define the single-mode/multi-mode cut-off in holey fibres at 1064 nm.

5.3.3 Modal properties (1): Fundamental mode

Some of the information presented in Table 5.1 is also presented graphically in Fig. 5.9. The main plot in Fig. 5.9 shows the critical bend radius of the fundamental mode (R_c^{FM}) as a function of d/Λ at 1064 nm. The dots represent the calculated values of R_c^{FM} for each of the fibres listed in Table 5.1. The red line is a fit to the values of R_c^{FM} of the form $y = a/(x^2 + b) + c$, which is drawn to guide the eye. This plot demonstrates that for a fixed mode area, the critical bend radius of the fundamental mode decreases as the values of Λ and d/Λ increase and once again confirms that the optimum route towards large-mode-area fibres with low bending losses is to use large values of d/Λ. The vertical dashed line in Fig. 5.9 marks the cut-off value of d/Λ ($(d/\Lambda)_c = 0.43$) at which the fibres change from being single-mode (SM) into multi-mode (MM) as predicted by both of the multipole methods described above. The four insets on the right hand side of the main plot in Fig. 5.9 show the modal intensity profiles for fibres HF_A, HF_B, HF_E and HF_I from Table 5.1. As seen previously in Section 5.1, these profiles illustrate how the shape of the mode changes

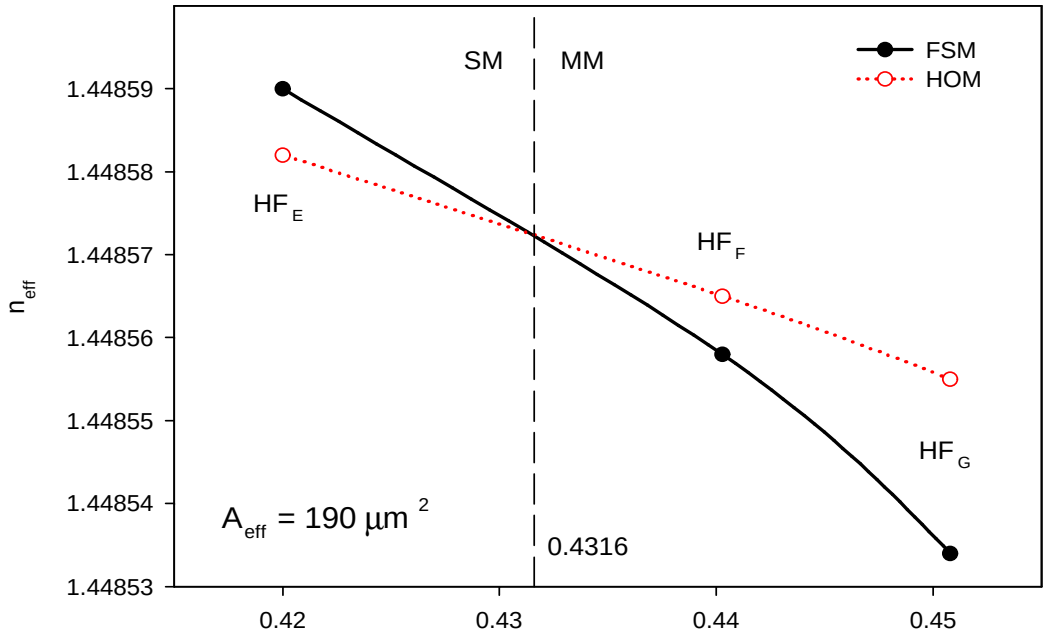

Figure 5.8: Effective modal index as a function of d/Λ for fibres HF_E, HF_F and HF_G at 1064nm. The closed circles and solid line corresponds to the fundamental space filling mode (FSM), while the open circles and dotted line corresponds to the second mode (HOM). The fibre parameters are shown in Table 5.1. The dashed line shows the value of d/Λ at which the two curves of effective index cross.

as the relative hole size increases, with the modal field becoming more confined to the core and less filamented in shape.

The effect of the relative hole size on the shape of the bent mode is illustrated in Fig. 5.10, in which modal intensity profiles for 1064 nm are shown for a range of bend radii for fibres HF_A, HF_B, HF_E and HF_I from Table 5.1. These four fibres have $A_{eff}^{FM} \approx 190\ \mu m^2$ at 1064 nm and values of $d/\Lambda = 0.20, 0.28, 0.42$ and 0.63 respectively. For each fibre, the first plot in the series shows the modal intensity profile for the straight fibre and the last plot in the series represents a bend radius that is close or equal to R_c^{FM} (see figure caption for details). As expected, these modes demonstrate that the mode of the bent fibre deforms outward in the direction of the bend, with the degree of deformation increasing as the bend becomes tighter. In addition, these modal profiles illustrate how the nature of the mode deformation changes depending on the relative hole size. For fibre HF_A, in which $d/\Lambda = 0.20$, significant mode deformation (and hence bend loss) occurs for bend radii that are large relative to R_c^{FM}. For example, for $R_o = 15$ cm (shown in Fig. 5.10 (b)), which is 23% larger than R_c^{FM}, the bend loss is ≈ 0.5 dB per loop (≈ 0.5 dB/m). Note that the bend loss of each fibre considered in Fig. 5.10 is shown as a function of bend radius in Fig. 5.11.

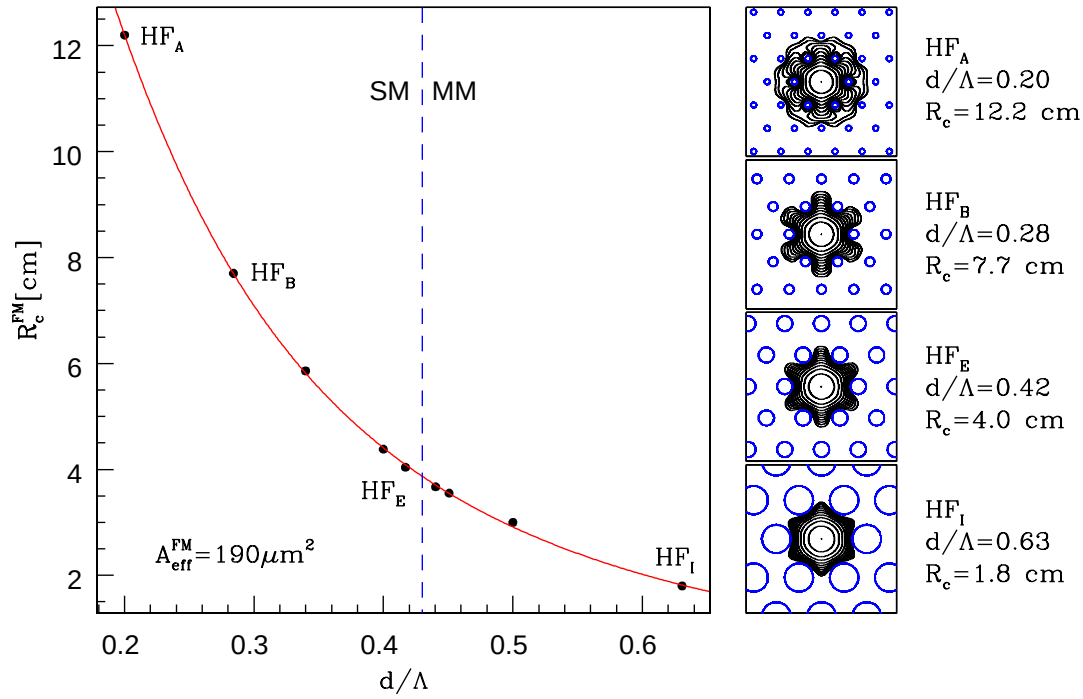

Figure 5.9: Main plot: Critical bend radius of the fundamental mode (R_c^{FM}) as a function of d/Λ at 1064 nm. The black dots represent the values of R_c^{FM} for the fibres listed in Table 5.1, all of which possess $A_{eff}^{FM} = 190 \approx \mu m^2$. The red line is a fit to these values of R_c^{FM} of the form $y = a/(x^2 + b) + c$, drawn to guide the eye. The vertical dashed line marks the cut-off position at which the fibres change from being single-mode (SM) into multi-mode (MM). The four insets on the right hand side of the main plot show modal intensity profiles of the fundamental mode for the straight fibre for four of the holey fibres studied. The fibre parameters are shown adjacent to mode profiles. Contour lines are separated by 2 dB

The mode profiles in Fig. 5.10 (b), (c) and (d) and the corresponding bend loss curve in Fig. 5.11 show that for fibre HF_A, the mode deforms in a gradual manner as the bend is tightened, steadily extending further into the cladding region and experiencing greater loss. In contrast, for fibre HF_I, which possesses considerably larger holes ($d/\Lambda = 0.63$), the mode is well confined to the core even at bend radii close to R_c^{FM}. For this fibre, the mode first extends past the first ring of holes for $R_o \approx R_c^{FM}$. As a result, the bend loss occurs suddenly and increases sharply. This is illustrated by the shape of the bend loss curve in Fig. 5.11 and by the mode profiles shown in Figs 5.10 (o) and (p), which represent bend radii of 1.9 cm and 1.8 cm respectively. Despite the fact that the bend radius depicted in Fig. 5.10 (o) is only 6% larger than R_c^{FM}, the mode is still confined within the first ring of holes and experiences losses of only ≈ 0.06 dB per loop (≈ 0.5 dB/m). In comparison, for fibre HF_A, the fibre experiences a loss of ≈ 2 dB per loop (≈ 2.4 dB/m) for a bend radius that is 6% larger than R_c^{FM}. The sudden deformation of the bent mode in fibre HF_I occurs

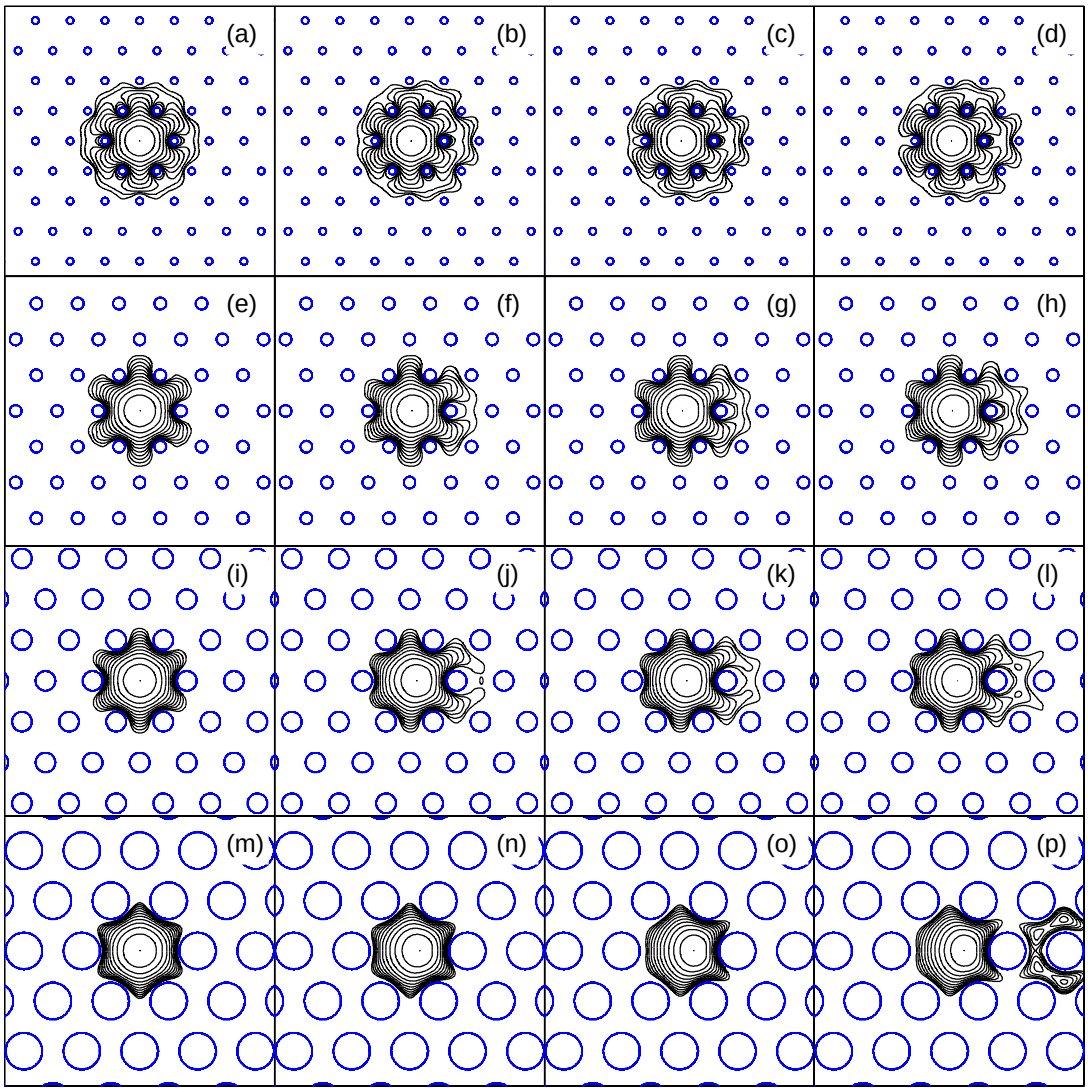

Figure 5.10: Modal intensity profiles of the bent fibre for four of the holey fibres listed in Table 5.1: (a)-(d) fibre HF_A; (a) straight fibre, (b) $R_o = 15$ cm, (c) $R_o = 14$ cm and (d) $R_o = 12$ cm. (e)-(h) fibre HF_B; (e) straight fibre, (f) $R_o = 9.4$ cm, (g) $R_o = 8.4$ cm and (h) $R_o = 7.4$ cm. (i)-(l) fibre HF_E; (i) straight fibre, (j) $R_o = 4.4$ cm, (k) $R_o = 4.2$ cm and (l) $R_o = 4.0$ cm. (m)-(p) fibre HF_I; (m) straight fibre, (n) $R_o = 2.0$ cm, (o) $R_o = 1.9$ cm and (p) $R_o = 1.8$ cm. Contours are spaced by 2 dB.

as the bend radius is decreased from 1.8 cm to 1.9 cm, as in Fig. 5.10 (p), where the mode becomes significantly deformed, extending well past the first ring of holes and experiencing losses of ≈ 2.4 dB per loop (> 20 dB/m). The bent modes for fibres HF_B and HF_E, also shown in Fig. 5.10, possess $d/\Lambda = 0.28$ and 0.42 respectively and demonstrate that the way in which the mode deforms with respect to decreasing bend radius changes gradually as the relative size of the holes within the fibre increases.

In summary, Fig. 5.10 and Fig. 5.11 together demonstrate that for a given mode area, the bend loss improves as d/Λ increases and that the improvement in bend loss towards

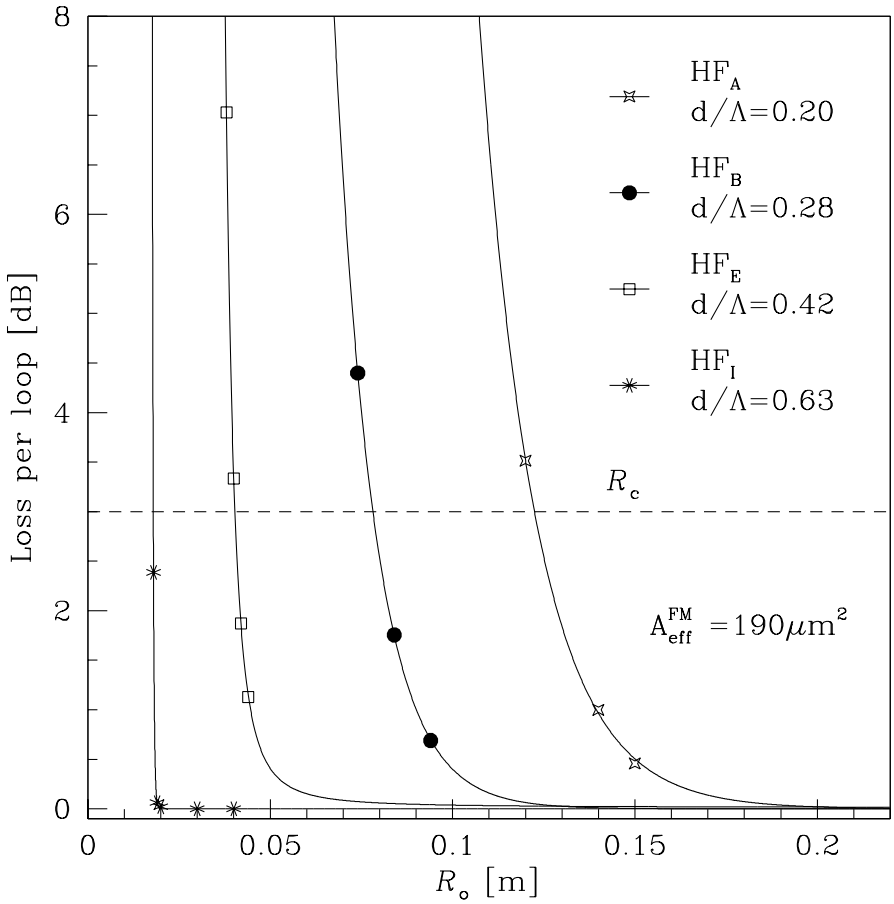

Figure 5.11: Points show bend loss for one loop in dB as a function of bend radius (R_o) for four of the holey fibres listed in Table 5.1. The solid curves are drawn to guide the eye. The dashed line indicates the 3 dB loss level, which is defined as R_c.

larger values of d/Λ is reflected not only in the absolute value of R_c^{FM}, but also in the shape of the bend loss curve. Fig. 5.11 shows clearly that the onset of bend loss in response to decreasing curvature becomes much sharper as d/Λ increases. This demonstrates that it is possible to operate close to R_c^{FM} without incurring significant bend losses in fibres with large values of d/Λ. However, it should be noted that for radii at which bend losses are low, the mode deformation can still significantly alter the mode shape and mode area. This is most notable for fibre HF_I in Figs 5.10 (m)-(p). For example, in Fig. 5.10 (o), the mode is well confined to the core, and the bending losses are low. However, the mode is significantly deformed, and is squashed against the inner ring of holes in the direction of the bend. This reduces A_{eff}^{FM} by $\approx 15\%$ to ≈ 160 μm^2.

This effect is illustrated in Fig. 5.12, in which the relative change in mode area (defined as $A_{eff}^{bent}/A_{eff}^{FM}$, where A_{eff}^{bent} is the effective mode area of the fundamental mode in the bent fibre) for the fundamental mode is plotted as a function of bend radius for each of the

holey fibres listed in Table 5.1. This graph illustrates that small values of d/Λ offer little resistance to mode deformation. For small values of d/Λ, the mode of the bent fibre is pushed gradually out into the cladding region as the bend radius is tightened, increasing the mode area, but creating a more complex mode shape (as can be see in Figs 5.10 (a)-(d)). From Fig. 5.12, it can be seen that this pattern of mode deformation holds for fibres HF_A, HF_B and probably HF_C, in which $d/\Lambda = 0.20, 0.28$ and 0.34 respectively. For these fibres, A_{eff}^{FM} has increased by $\approx 5\%$ to $\approx 220\ \mu m^2$ at $R_o = R_c^{FM}$.

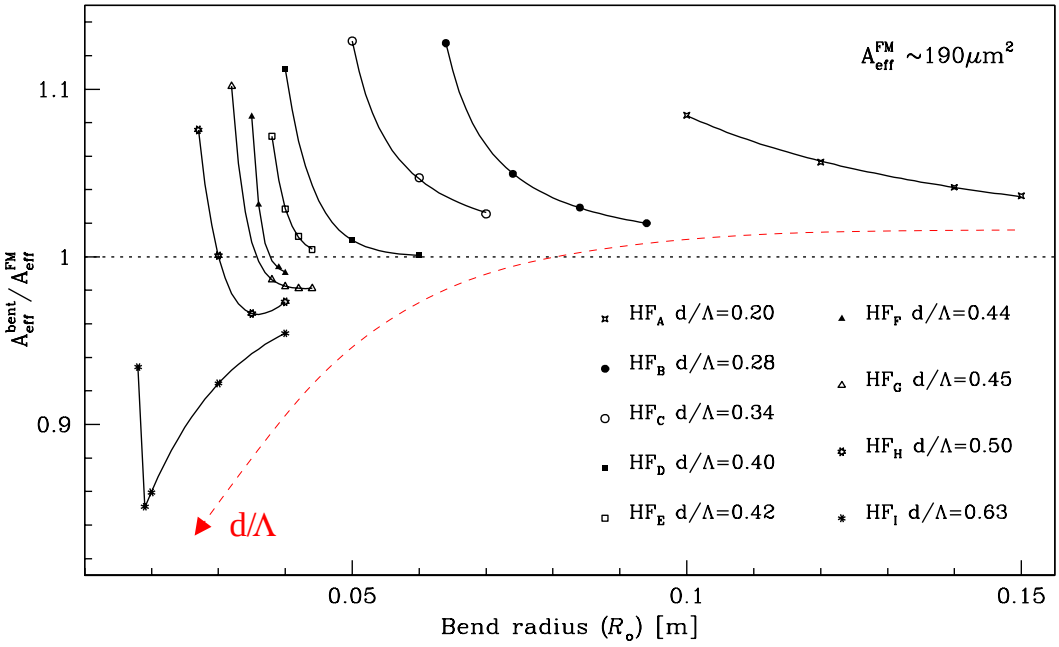

Figure 5.12: Relative change in effective mode area ($A_{eff}^{FM}/A_{eff}^{bent}$) as a function of bend radius (R_o) for the holey fibres listed in Table 5.1. The dashed red line indicates the direction in which the value of d/Λ increases in this plot.

For each of the fibres with $d/\Lambda \geq 0.42$ however, we see that for some range of bend radii, the effective area of the bent mode drops below that of the straight fibre. As mentioned above and illustrated by Fig. 5.10 (o), this reduction in mode area results from the fact that the large holes strongly confine the mode to the core. Instead of extending into the cladding region as the fibre is bent, the mode is squashed against the inner ring of holes. However, Fig. 5.12 shows that as the bend radii is further reduced, the mode area of the bent fibre reaches a minimum and then begins to increase. This turning point represents the radius at which the mode starts to extend past the inner ring of holes as in Fig. 5.10 (p). For all fibres except HF_I, the mode area of the bent fibre is either greater than or equal to that of the straight fibre at $R_o = R_c^{FM}$. For fibre HF_I, A_{eff}^{FM} at $R_o = R_c^{FM}$ is $\approx 6\%$ smaller than

the mode of the straight fibre at $\approx 180\ \mu m^2$, with a minimum value of $\approx 160\ \mu m^2$ ($\approx 15\%$ smaller than the mode of the straight fibre) at $R_o = 1.9$ cm. Although the reduction in A_{eff}^{FM} is only significant for the fibres considered here at relatively small bend radii, it may become a consideration at larger radii in larger mode area fibres.

5.3.4 Modal properties (2): Higher-order modes

As described in Section 1.4, the multipole method is capable of accurately calculating the confinement losses of the modes of a holey fibre. The confinement losses for the first higher-order mode present in the multi-mode fibres included in this study have been calculated by Vittoria Finazzi at the ORC and are listed in Table 5.2 for 6 rings of holes [54]. It has been shown that in holey fibres with a six-fold symmetric cladding, the fibre modes can be classified in an analogous way to the symmetry based classification used for the modes in a step-index fibre [148]. As such, the first higher-order multiplet in a holey fibre is a linear combination of modes that are equivalent to the TE_{01}, the TM_{01} and the two degenerate HE_{21} modes of a step-index fibre. In the large core, low NA regime, these four modes are near-degenerate and possess similar levels of confinement losses. Here the confinement losses are calculated for 6 rings of holes for the first higher-order mode with the highest effective index, which represents the higher-order mode with the strongest level of confinement. The modal intensity profiles for the first higher-order mode guided in each fibre are shown in Fig. 5.13 (a), (b), (c) and (d). Transverse cross sections of these intensity profiles in the x direction are shown in (e), (f), (g) and (h), and transverse cross sections of the intensity profile in the x direction are shown in (i), (j), (k) and (l) respectively. Note that the higher-order mode for the multi-mode fibre with the smallest holes (HF_F, $d/\Lambda = 0.44$), is broad, extending well into the cladding region. As d/Λ increases, the modal field of the HOM becomes smaller and more confined to the core. This change in mode size is reflected in the confinement losses of the HOM, which reduce dramatically with increasing values of d/Λ. For the fibres shown here, the confinement losses of the HOM decreases from 3.4 dB/m to less than 1×10^{-8} dB/m as the relative hole size is increased from 0.44 to 0.63 (both values of confinement loss quoted for 6 rings of holes). The high value of confinement loss for the higher-order mode in fibre HF_F ($C_{loss}^{HOM} = 3.4$ dB/m for 6 rings of holes), means that it is unlikely that this mode would be observed in lengths of fibre greater than a few 10's of cm. As as result, we define this fibre to be *effectively* single-mode and thus extend the range of d/Λ that results in single-mode guidance in practice. The fact that fibres with values

of $d/\Lambda > (d/\Lambda)_c$ can be effectively single-mode is confirmed by the experimental results presented in Section 5.4.

Table 5.2: Calculated modal properties for a range of holey fibre structures. Note that SM stands for single-mode, MM stands for multi-mode, FM refers to a property of the fundamental mode, and HOM refers to a property of the first higher-order mode.

Fibre	Λ [μm]	d [μm]	d/Λ	A_{eff}^{FM} [μm^2]	R_c^{FM} [cm]	Modes	C_{loss}^{HOM} for 6 rings of holes [dB/m]	R_c^{HOM} [cm]
HF_F	12.56	5.53	0.44	189	3.7	MM	3.40	> 14.5
HF_G	12.70	5.73	0.45	188	3.6	MM	0.46	> 14.5
HF_H	13.40	6.70	0.50	190	3.0	MM	1.75×10^{-5}	14.5 -17.1
HF_I	15.00	9.46	0.63	189	1.8	MM	negligible	2.7 - 2.8

For fibres HF_G, HF_H, HF_I listed in Table 5.2, the confinement losses of the higher-order modes are low enough to ensure that these modes would be observed in lengths of straight fibre of a few metres at least. However, it may still be possible to selectively guide only the fundamental mode by exploiting the fact that the fundamental mode is the least sensitive to bend induced loss and that the bend loss is exponentially dependent on the radius of curvature. If the higher-order modes suffer a sufficiently greater bend loss than the fundamental mode, it may be possible to selectively remove these modes by bending the fibre. The technique of removing unwanted higher-order modes by bending the fibre is well known in conventional fibres [149, 150] and can be evaluated by calculating the bending losses of the first higher-order mode, since all other higher-order modes present in a fibre will be less bend resistant. Whether this is also possible in holey fibres can be determined by using the numerical methods outlined in Chapter 3, which are capable of calculating the modal properties of higher-order modes. In the scalar version of the orthogonal function method outlined in Section 3.2, the second and third solutions of the eigenvalue equation approximate to the linearly polarised LP_{11}^x and LP_{11}^y modes, examples of which can be seen in Figs 5.14 (b) and (c) for fibre HF_H.

Unfortunately, whilst the method of calculating bend loss used here is applicable to higher-order modes, it cannot be used for fibres HF_F and HF_G due to the fact that they are so close to cut-off. As mentioned in Section 3.6, the modedness of a holey fibre is most accurately determined by the multipole approach. However, the multipole approach

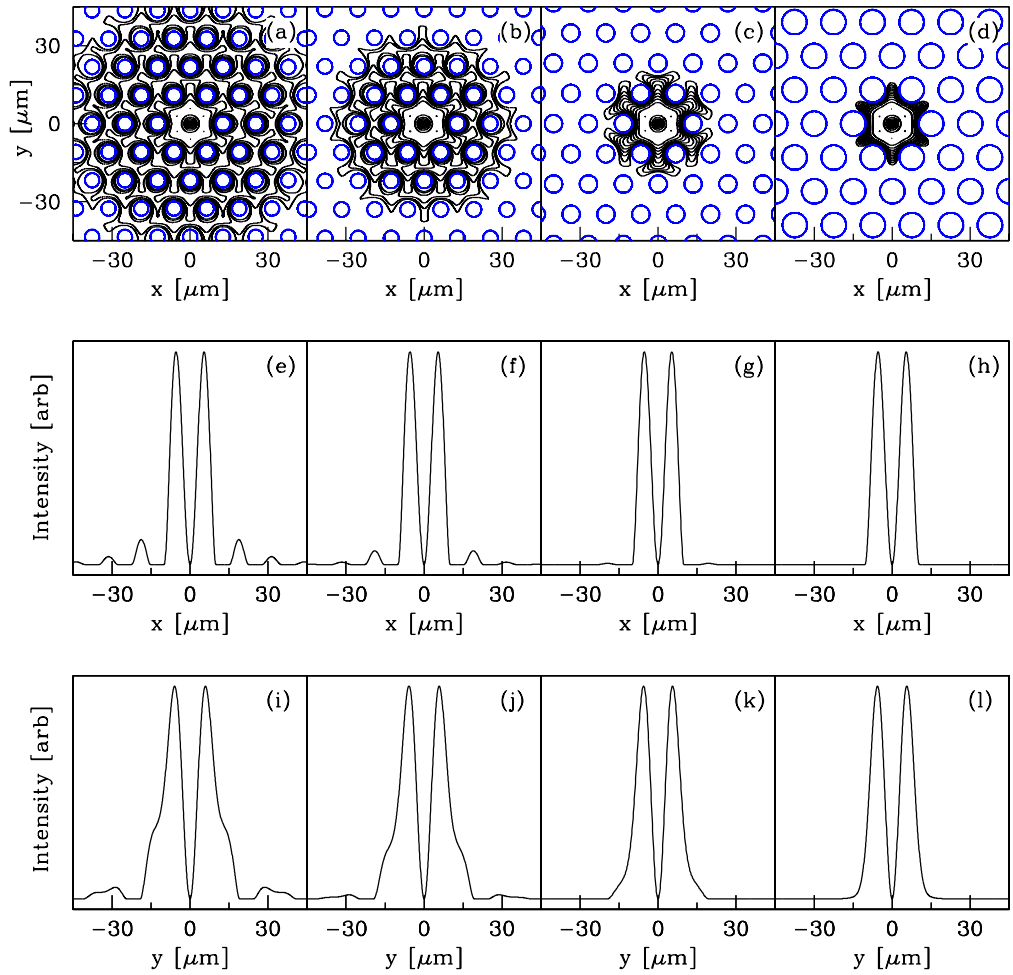

Figure 5.13: Contour plots of intensity for the first higher-order mode in fibres (a) HF_F, (b) HF_G, (c) HF_H and (d) HF_I. The contour lines are separated by 2 dB. Transverse cross sections of the intensity profile in the x direction are shown in (e), (f), (g) and (h), and transverse cross sections of the intensity profile in the x direction are shown in (i), (j), (k) and (l) respectively. The fibre parameters are listed in Table 5.1.

is incapable of considering the graded index profile that is required to generate the modes of a bent fibre. Here we use an orthogonal function method to calculate the modes of the bent fibre, which systematically produces modal effective indices that are slightly lower than those calculated by the multipole method (also discussed in Section 3.6). As a result, the orthogonal function method (incorrectly) predicts that fibres HF_F and HF_G are single-mode at 1064 nm. The bend loss for the higher-order modes cannot be calculated in this instance due to the fact that the point at which all radiation is lost from the fibre, defined as $x_r = R_o(\frac{\beta_b}{\beta_{FSM}} - 1)$ in Eq. 3.12, is a negative value for $\beta_b < \beta_{FSM}$, where β_b and β_{FSM}

are the propagation constant of the bent fibre mode and the fundamental cladding mode respectively. However, since the higher-order modes for fibres HF_F and HF_G, as calculated by the multipole approach and shown in Fig. 5.13, have higher confinement losses and extend further into the cladding region than those in fibre HF_H, it is reasonable to assume that the bending losses of the higher-order modes in fibres HF_F and HF_G will be greater than those in HF_H. Consequently, by calculating the bend losses for fibres HF_H, a lower bound can be placed on the critical bend radius for the higher-order modes of fibres HF_F and HF_G.

The LP_{11}^x and LP_{11}^y modes, calculated for fibre HF_H using the orthogonal function method, are shown in Figs 5.14 (b) and (c) respectively together with the fundamental mode for the same fibre, shown in Fig. 5.14 (a). The effective indices of the modes in Figs 5.14 (a), (b) and (c) are 1.449167 1.448540 and 1.448538 respectively. The same modes for the bent fibre are shown in Figs 5.15 (a), (b) and (c) for $R_o = 15$ cm. The bending losses associated with the LP_{11}^x and LP_{11}^y modes for the four multi-mode holey fibres listed in Table 5.1 are evaluated below.

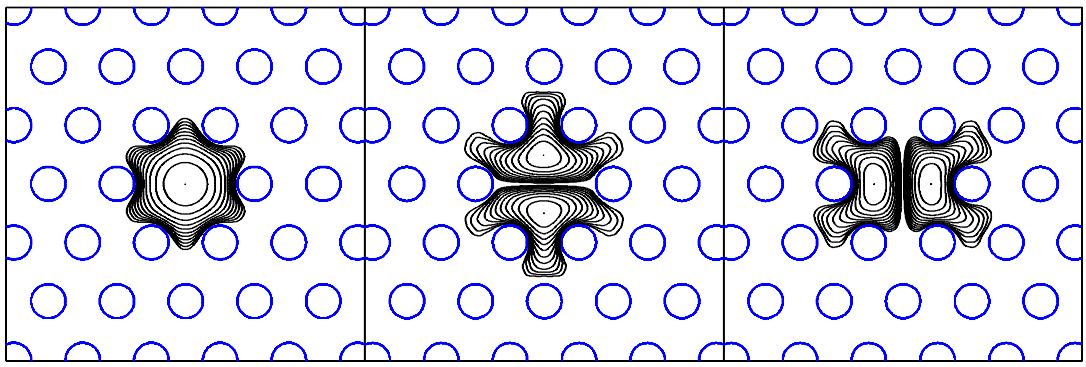

(a) (b) (c)

Figure 5.14: Modal intensity profile for (a) the fundamental mode, (b) the LP_{11}^x and (c) LP_{11}^y for holey fibre HF_H, $\Lambda = 13.4$ μm, $d/\Lambda = 0.5$ at 1064 nm. Contours are separated by 2 dB.

The bend loss for each of the modes present in fibre HF_H is shown in Fig. 5.16 (a) as a function of bend radius. The solid line represents the bend loss of the fundamental mode and the dotted and dashed lines represent the bend loss of the LP_{11}^x and LP_{11}^y respectively. The critical bend radius for the LP_{11}^x and LP_{11}^y modes is extracted as 14.5 and 17.1 cm respectively. The smallest of these is still ≈ 5 times larger than the critical bend radius for the fundamental mode (3.0 cm), demonstrating that the LP_{11} modes can be stripped without perturbing the fundamental mode. In Fig. 5.16 (b), the sum of the bend loss from

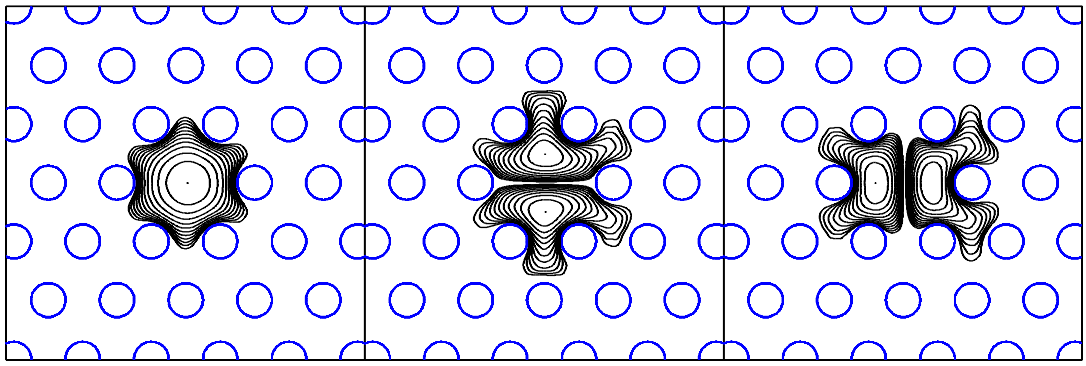

(a) (b) (c)

Figure 5.15: Modal intensity profile for (a) the fundamental mode, (b) the LP_{11}^{x} mode and (c) the LP_{11}^{y} mode, for $R_o = 15.0$ cm for holey fibre HF_H, $\Lambda = 13.4$ μm, $d/\Lambda = 0.5$ at 1064 nm. Contours are separated by 2 dB.

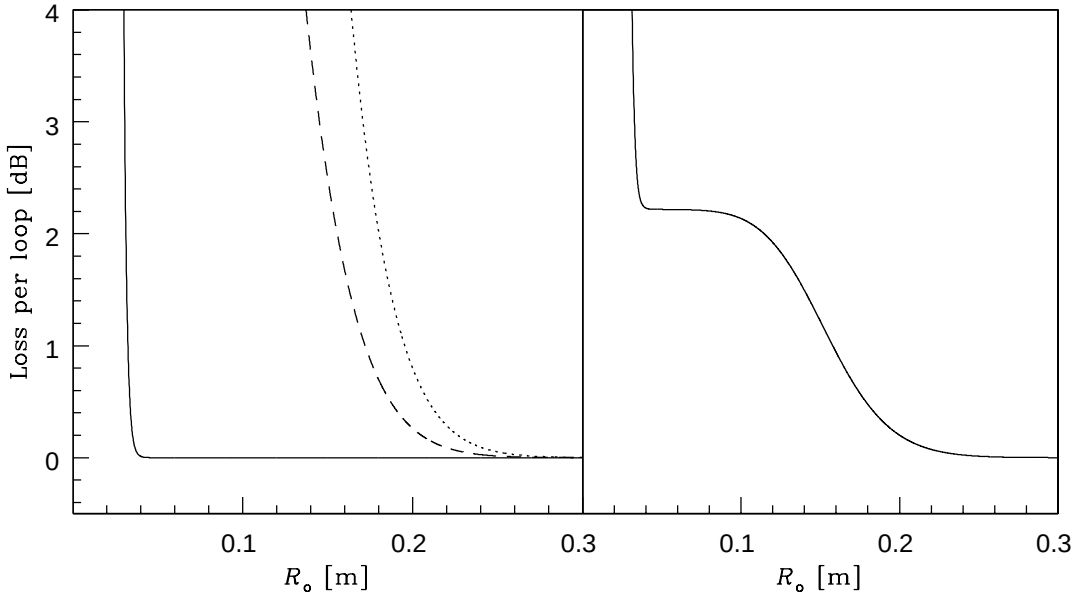

(a) (b)

Figure 5.16: (a) Pure bend loss as a function of bend radius for the fundamental mode (solid line) and the LP_{11}^{x} and LP_{11}^{y} modes in fibre HF_H (dotted and dashed lines respectively) ($\Lambda = 13.4$ μm, $d/\Lambda = 0.5$). (b) The sum of the loss from the fundamental and the two higher-order modes shown in (a), assuming a ratio of 3:1:1 respectively.

the fundamental mode and the LP_{11}^{x} and LP_{11}^{y} modes is plotted as a function of bend radius assuming a ratio of 3:1:1 respectively. This ratio is purely chosen to produce a graph of total bend loss that best matches with some experimental results presented in the next section. As such, the first rise in loss in Fig. 5.16 (b) represents loss from the LP_{11}^{x} and LP_{11}^{y} modes and the second, sharper rise in loss corresponds to the loss from the fundamental mode.

Note that the loss from the LP_{11}^{x} and LP_{11}^{y} modes appears as a single curve in Fig. 5.16 (b) due to the fact that the bending losses of the two modes are similar compared with the fundamental mode. This plot of total bend loss for fibre HF_H demonstrates that the LP^{11} modes can be stripped from the fibre using a few turns with a bend radius of $\approx 10-15$ cm or a single loop of ≈ 8 cm, without suffering loss from the fundamental mode. Indeed, as can be seen from Fig. 5.15 (a), the fundamental mode is not perturbed to any significant degree for $R_o = 15$ cm. However, approximately 2 dB of power is lost from the fibre in this process, which is less than ideal from a power handling perspective.

The numerical results presented above demonstrate that it is possible to remove higher-order modes by introducing a bend in a holey fibres for $d/\Lambda = 0.5$. In the following, a similar evaluation is performed for fibre HF_I, in which $d/\Lambda = 0.63$, and hence possesses lower overall bend loss, in order to determine the upper limit in which this approach can be successfully used to eliminate higher-order modes. The LP_{11}^{x} and LP_{11}^{y} modes calculated for fibre HF_I using the orthogonal function method are shown in Figs 5.17 (b) and (c) respectively together with the fundamental mode for the same fibre, shown in Fig. 5.17 (a). The same modes for the bent fibre are shown in Figs 5.18 (a), (b) and (c) for $R_o = 3.0$ cm. The bending losses associated with the LP_{11}^{x} and LP_{11}^{y} modes for the fibre HF_I are evaluated below.

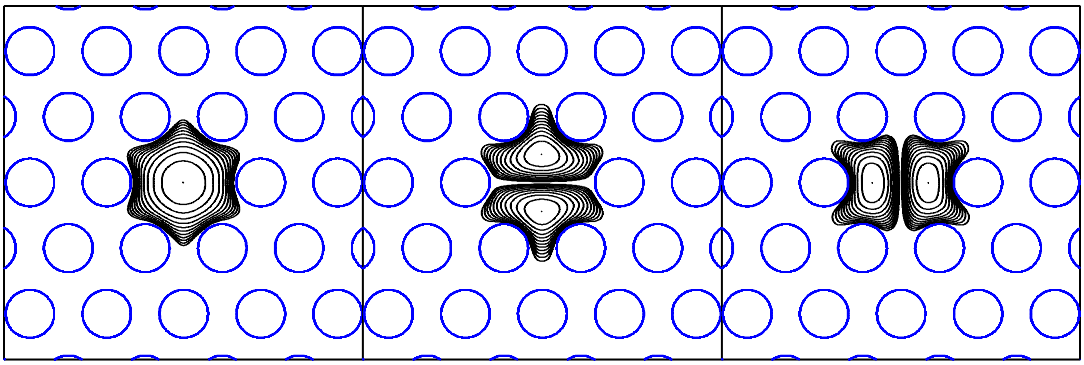

(a) (b) (c)

Figure 5.17: Modal intensity profile for (a) the fundamental mode, (b) the LP_{11}^{x} and (c) LP_{11}^{y} for holey fibre HF_I, $\Lambda = 15.0$ μm, $d/\Lambda = 0.63$ at 1064 nm. Contours are separated by 2 dB.

The calculated bending losses for the first three modes present in fibre HF_I are plotted as a function of bend radius in Fig. 5.19 (a). The solid line represents the bend loss of the fundamental mode and the dotted and dashed lines represent the bend loss of the LP_{11}^{x} and LP_{11}^{y} respectively. In contrast to the loss curve of the fundamental mode, in which

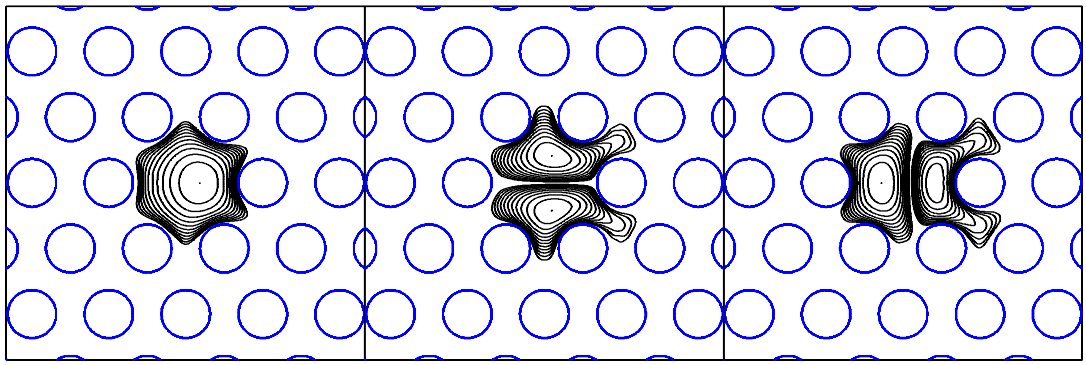

(a) (b) (c)

Figure 5.18: Modal intensity profile for (a) the fundamental mode, (b) the LP_{11}^{x} mode and (c) the LP_{11}^{y} mode, for $R_o = 3.0$ cm for holey fibre HF_I, $\Lambda = 15.0$ μm, $d/\Lambda = 0.63$ at 1064 nm. Contours are separated by 2 dB.

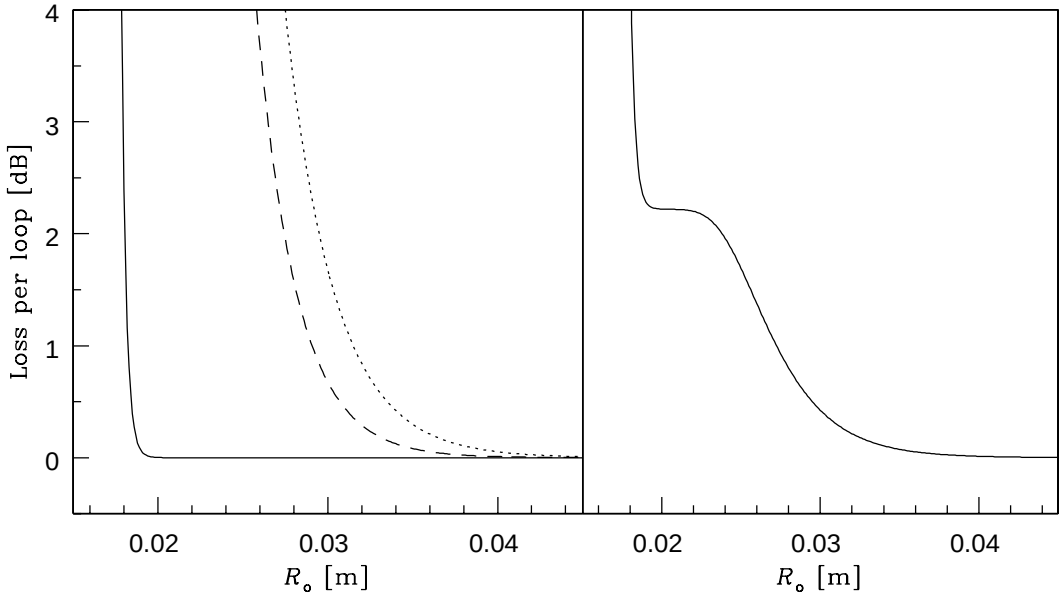

(a) (b)

Figure 5.19: (a) Bend loss as a function of bend radius for the fundamental mode (solid line) and the LP_{11}^{x} and LP_{11}^{y} modes in fibre HF_I (dotted and dashed lines respectively) ($\Lambda = 15.0$ μm, $d/\Lambda = 0.63$). (b) The sum of the loss from the fundamental and the two higher-order modes shown in (a), assuming a ratio of 3:1:1 respectively.

the loss begins sharply at $R_o \approx R_c^{FM}$, the bend loss for the higher-order modes increases more gradually as function of bend radius, reflecting the fact that the modes are not so well confined to the core. The fact that the higher-order modes become more distorted than the fundamental mode for the same bend radius can be seen in Fig. 5.18 and Fig. 5.19. The critical bend radius for the LP_{11}^{x} and LP_{11}^{y} modes is extracted as 2.7 and 2.8 cm respectively.

Once again, the sum of the bend loss from the fundamental mode and the LP_{11}^{x} and LP_{11}^{y} modes is plotted as a function of bend radius assuming a ratio of 3:1:1 respectively in Fig. 5.19 (b). The critical bend radii for the LP_{11} modes are ≈ 1.5 larger than the critical bend radius of the fundamental mode, which is equal to 1.8 cm. From Fig. 5.19 (b) it can be seen that the higher-order modes can be stripped from the fibre using several turns of fibre with a bend radius of $\approx 2.5 - 3.0$ cm or a single loop of ≈ 2 cm. However, although the bend loss for the fundamental mode is not significant for $R_o = 2 - 3$ cm, the modal distortion does affect the mode area of the fundamental mode in this range. As shown above in Fig. 5.10 (n) for $R_o = 2.0$ cm and in Fig. 5.18 (a) for 3.0 cm, the fundamental mode is somewhat squashed. For these radii, A_{eff}^{bent} of fibre HF_I reduces to $\approx 96\%$ and 85% of that of the straight fibre, reducing the power handling capabilities of the fibre. As such, these results suggest that for the mode area of $\approx 190\ \mu m^2$ considered here, fibre HF_I with $d/\Lambda = 0.63$, probably represents the upper limit in d/Λ in which the higher-order modes can be successfully stripped by bending the fibre, without significantly perturbing the fundamental mode.

5.3.5 Conclusion

In conclusion, the numerical work presented in this section explores, in detail, the effect of the fibre structure on the bending losses and modedness of large-mode-area holey fibres at 1064 nm. Using the numerical techniques described in Chapter 3, the modal properties of a selection of fibres in which the fundamental mode has an effective area of $\approx 190\ \mu m^2$ are evaluated. The fibres considered here possess values of Λ ranging from 9.0 to 15.0 μm and values of d/Λ ranging from 0.2 to 0.63, which includes both single-mode and multi-mode structures. The results from this study confirm that, for a given mode area, the bend loss reduces as the relative hole size increases and that the onset of higher-order modes can be accurately predicted by Eq. 5.1. Furthermore, by evaluating the bending losses of the fundamental mode and the confinement and bending losses of the first higher-order modes (when present), four regions of guidance are established: (1) True single-mode guidance for $d/\Lambda \lesssim 0.43$, in which only the lowest-order mode is guided within the fibre. (2) *Effective* single-mode guidance for $0.43 \lesssim d/\Lambda \lesssim 0.45$, in which higher-order modes are guided by the fibre, but possess such high confinement losses that they would not be observed in practice for lengths of fibre greater than a few 10's of cms. (3) *Selective* single-mode guidance for $0.45 \lesssim d/\Lambda \lesssim 0.63$, whereby higher-order modes that possess low confinement losses can be

selectively stripped from the fibre by bending the fibre (without perturbing the fundamental mode), if the critical bend radius of the first higher-order mode is sufficiently larger than the critical bend radius of the fundamental mode. (4) Robust multi-mode guidance for $d/\Lambda \gtrsim 0.63$, in which higher-order modes are present in the fibre and possess low values of confinement and bend loss. Note that the defining ranges of d/Λ given in each case refer only to fibres in which the fundamental mode has an effective area of $\approx 190\ \mu\text{m}^2$ at 1064 nm. For smaller effective areas, these boundaries shift towards larger values of d/Λ due to the fact that the smaller regions of solid silica that make up the holey fibre core permit larger values of numerical aperture for true single-mode guidance. Towards larger mode areas, the reverse is true and the boundaries for each region of guidance shift towards smaller values of d/Λ. The boundary values of d/Λ quoted above therefore represent upper limits for larger mode area fibres. The theoretical predictions summarised above are now validated experimentally in the following section.

5.4 Experimental study (1): $\text{A}_{\text{eff}}^{\text{FM}} \approx 200\ \mu\text{m}^2$

5.4.1 Introduction

Within this section, results are presented from an experimental study into the modal properties of four holey fibres with effective areas of $\approx 200\ \mu\text{m}^2$ that have different structural parameters, with $\mu\text{m}\ 11.7 < \Lambda < 13.8\,\mu\text{m}$ and $0.33 < d/\Lambda < 0.51$. The fibres in this selection include both single-mode and multi-mode structures that have been characterised in terms of mode area, mode shape and bend loss at 1064 nm. Note that unless otherwise indicated the experimental results presented in this section correspond to measurements made using a single-mode CW laser with a wavelength of 1064 nm as the source illumination. These measurements are used to demonstrate the validity of the numerical predictions made in Sections 5.2 and 5.3. Note that all the numerical predictions presented within this section are calculated using the scalar version of the model presented in Section 3.2, and that the constant of proportionality, τ, defined in Eq.3.17, is taken to be 2.0 (see also Section 4.5.3). Note that I have chosen this value of τ via comparison between numerical predictions and experimental results for a large selection of holey fibres. Furthermore, this choice is found to result in excellent agreement with experimentally measured values for every pure silica holey fibre considered in this study and is the only free parameter in the model of bend loss developed here.

5.4.2 The fibres

In Table 5.3 the properties of some fibres that were fabricated and characterised as part of this study are listed. The structural parameters of these fibres are also indicated by the green dots on the contour plot in Fig. 5.20, which is repeated from Fig. 5.7. The red dots on this figure refer to the fibre parameters studied in Section 5.1. Please refer to the figure caption for more details. Fibres F334Zeop, F334Zsop and F334Ysop derive from the same preform and were fabricated by John Hayes at the ORC. Fibre F200B2 was fabricated by Kentaro Furusawa, also at the ORC. All of these fibres are made entirely from pure silica rods and tubes of F300 synthetic silica glass from Heraeus Tenevo AG. SEM images of these four fibres are shown in Fig. 5.21.

Table 5.3: Measured (^{m}) and predicted (^{p}) modal properties for a range of holey fibres (predicted values correspond to the fundamental mode only). * fibre is effectively single-mode at 1064 nm. ** fibre is selectively single-mode for $R_o \lesssim 7$ cm (i.e. higher-order modes can be removed for $R_o \lesssim 7$ cm).

Fibre	Λ [μm]	d [μm]	d/Λ	$A^m{}_{\text{eff}}$ [μm^2]	$A^p{}_{\text{eff}}$ [μm^2]	R_c^m [cm]	R_c^p [cm]	Modes
F334Zeop	11.74	3.84	0.33	200	210	7.1	7.2	SM
F334Zsop	11.93	5.39	0.45	165	170	3.3	-	MM*
F334Ysop	12.63	6.48	0.51	165	170	< 2	-	MM*
F200B2	13.80	7.04	0.51	195	210	< 2	-	MM**

5.4.3 Results and discussion

The measured values of $A_{\text{eff}}^{\text{FM}}$ for these four fibres range from 165 to 200 μm^2. The measured values of $A_{\text{eff}}^{\text{FM}}$ agree with theoretical predictions to $\approx \pm$3-5%, which is consistent with the estimated error of $\approx \pm 5\%$ in the method of measuring the $A_{\text{eff}}^{\text{FM}}$, as described in Section 4.3. SEM images of the fibres listed in Table 5.3 are shown in Fig. 5.21. Note that the innermost ring of holes in the F334 fibres (shown in Figs 5.21 (a), (b) and (c)) are elliptical in shape, as shown in Fig. 5.21. Fortunately, the nature of this ellipticity does not break the 6-fold symmetry of the fibre and so it is reasonable to assume that it will not induce any significant level of birefringence. As mentioned in Section 3.2, the method used here to model the modal properties of holey fibres is capable of considering an arbitrary profile, and the exact holey fibre structure from an SEM can be used in this calculation. However,

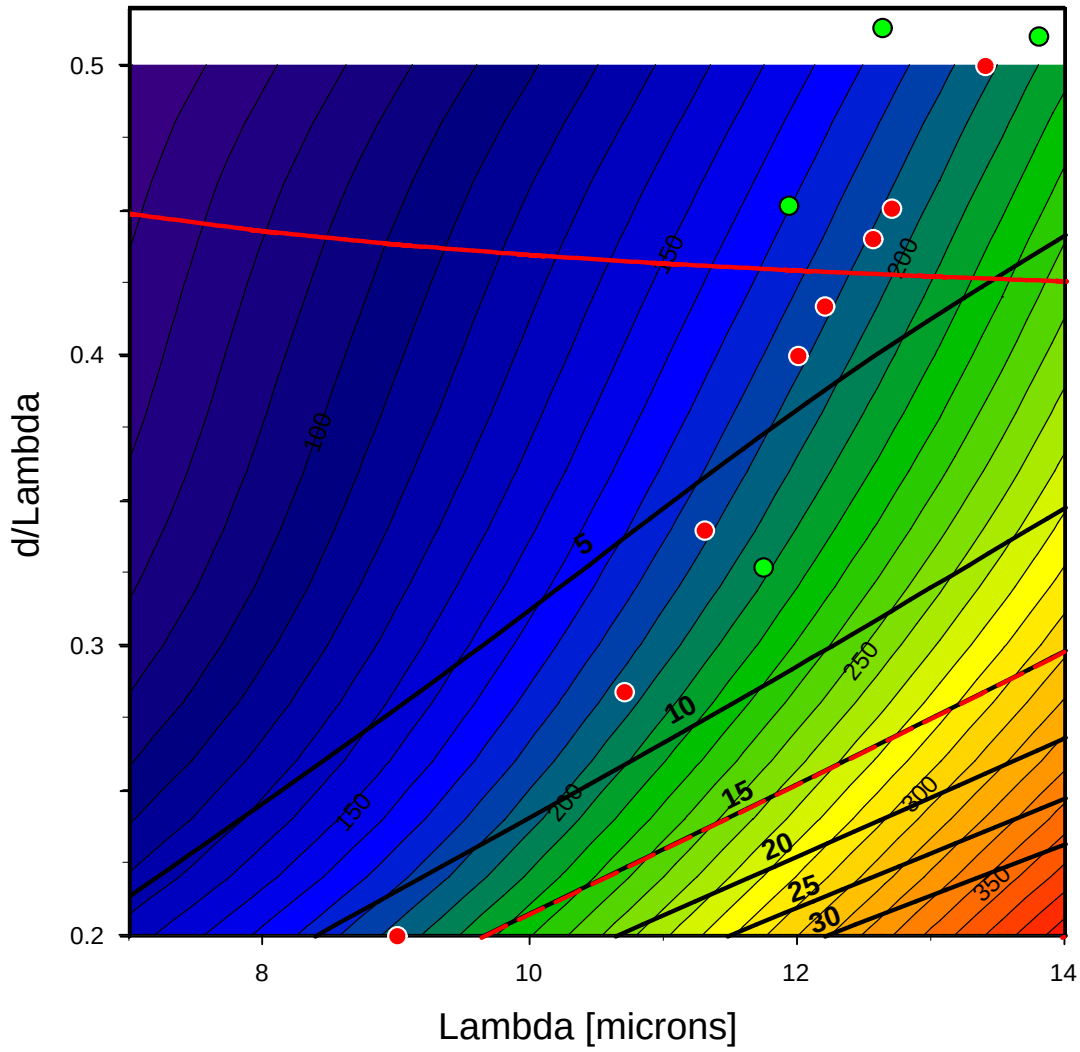

Figure 5.20: The effective area contour plot from Fig. 5.7 is repeated here. The solid black lines represent R_c^{FM} contour lines, the dashed read and black line shows the position of the R_c^{FM} = 15 cm contour line and the solid red line indicates the value of $(d/\Lambda)_c$ from Eq. 5.2. The red dots show the structural parameters of the holey fibres listed in Table 5.1, the green dots show the parameters of holey fibres characterised in this section. Note that the y axis scale is increased to 0.52, in order to include fibres F334Ysop and F200B2.

in general, the refractive index profile of a real holey fibre can be well approximated by an idealised refractive index profile with perfectly circular holes, and this approach is typically used for simplicity. Whilst the ellipticity in the innermost ring of holes in the F334 fibres means that the refractive index distribution deviates from the idealised profile, the level of ellipticity (ratio of axis of ellipse $\approx$ 1.0 : 1.2) is not sufficient to radically alter the fibre properties, and we find that it can be adequately compensated for by defining an ideal fibre structure that has an equivalent air filling fraction to the real fibre. Note that the F334 fibre parameters quoted in Table 5.3 refer to the equivalent, idealised, profiles used

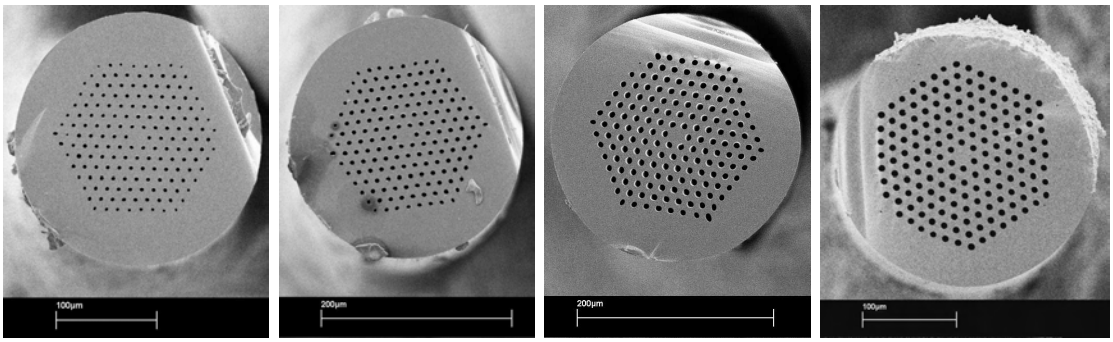

(a) (b) (c) (d)

Figure 5.21: SEM images of four holey fibres, (a) F334Zeop, (b) F334Zsop (c) F334Ysop and (d) F200B2. The fibre parameters are shown in Table 5.3 and are also indicated on the figure.

in numerical calculations. The success of this representation is illustrated by the excellent agreement between the measured and predicted values of R_c^{FM} for fibre F334Zeop, shown in Table 5.3 and in Fig. 5.22 for 1064 nm. In Fig. 5.22 the bend loss for one loop of fibre is plotted as a function of bend radius for fibre F334Zeop at 1064 nm. The experimental data is shown by open circles and the theoretical predictions are shown by the closed circles and the solid line. The predicted mode profile together with the idealised refractive index profile used in these calculations are shown in the insert. This plot demonstrates the ability of the numerical techniques to accurately predict the bend loss in holey fibres.

The excellent agreement between measured and calculated modal properties is further illustrated in Fig. 5.23, in which the near field mode profile of fibre F334Zeop at 1064 nm is shown at 1064 nm for: (a) the actual fibre and (b) the numerical simulation. In Fig. 5.23 (a), the near field is imaged by focussing the far field output from the fibre onto a COHU 7512 CCD camera. The contour levels are indicated on each plot. The contour lines in Fig. 5.23 (b) have been chosen to match some of the camera levels from Fig. 5.23 (a) to aid comparison. In both Fig. 5.23 (a) and (b), cross-sections of the modal intensity in the horizontal and vertical directions, which are indicated by the dashed lines, are plotted along the bottom and left hand side of each figure respectively. These two figures demonstrate that the orthogonal function method (as described in Section 3.2) is capable of accurately predicting the fundamental mode of a holey fibre.

As described in Section 5.3.4, the fundamental mode is the least sensitive to bend induced loss and the bend loss for each mode is exponentially dependent on the radius of curvature. When higher-order modes are present within a fibre, the loss as a function of bend radius becomes staggered, with each step in loss representing a different mode, as

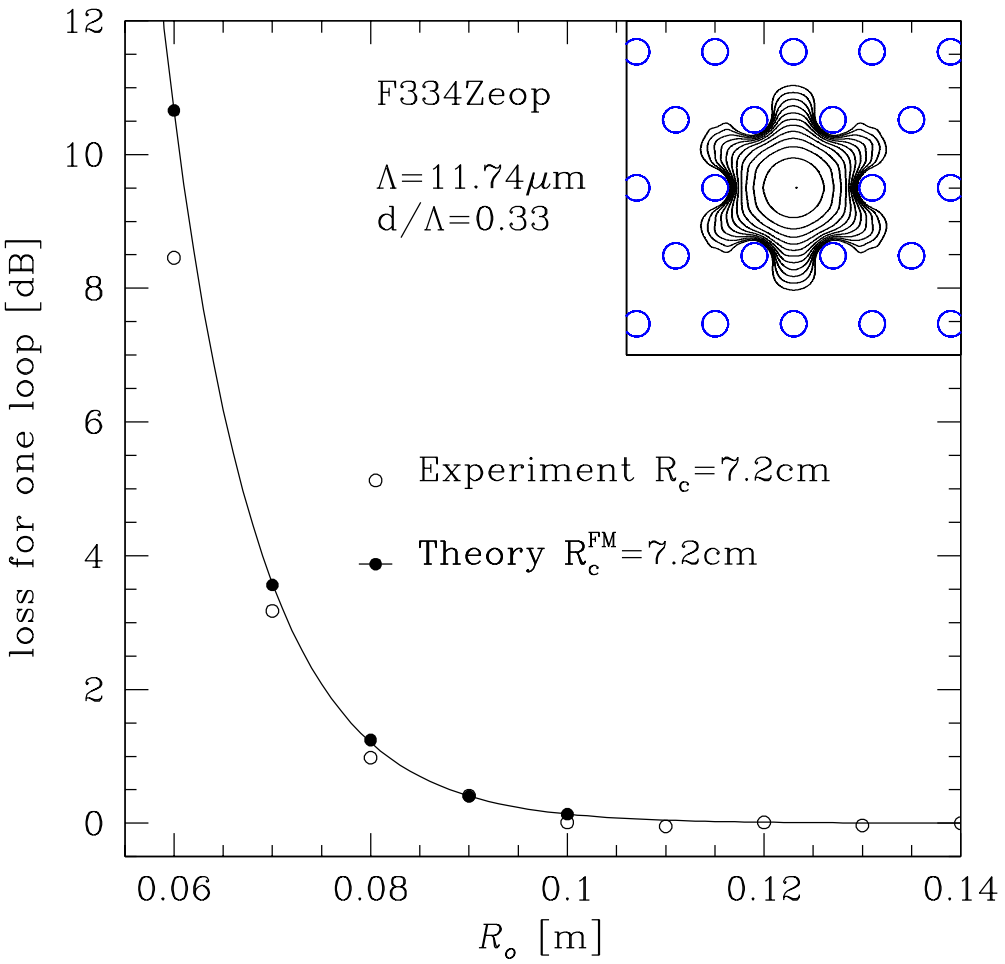

Figure 5.22: Bend loss for one loop of fibre in dB as a function of radius for fibre F334Zeop. The experimental data is shown by open circles, the theoretical predictions are shown by closed circles and the solid line. The predicted mode profile together with the idealised refractive index profile used in calculations is shown in the insert. The contour lines are separated by 2 dB and the width of the box shown is 50 μm. The fibre parameters are shown in Table 5.3.

shown in Fig. 5.16 (b). As a result, the bend loss as a function of bend radius can be used to infer information regarding the number of modes excited in the fibre. For a single-mode fibre, the bend loss as a function of bend radius should increase in a smooth exponential-like fashion. In this study, I have chosen to use Eq. 5.2 to determine if a holey fibre is single-mode or multi-mode, as described in Sections 5.2.3 and 5.9. By this definition, fibre F334Zeop is single-mode, which is confirmed by the measured bend loss, shown in Fig. 5.22 (and also in Fig. 5.24 (a)).

In Fig. 5.24 (b), (c) and (d), the measured bend loss is also shown for the other three

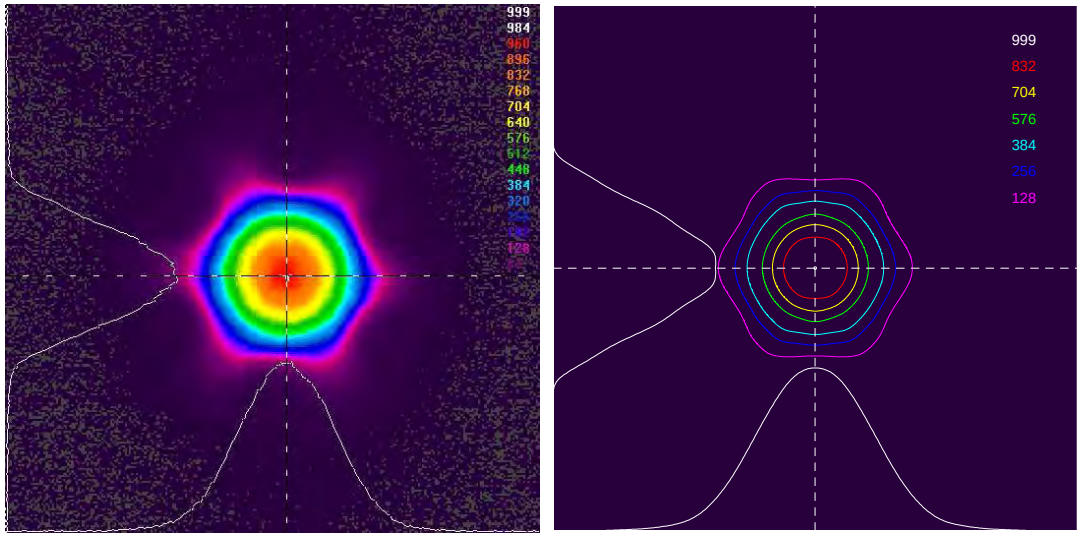

(a) (b)

Figure 5.23: (a) Near-field modal intensity profile for fibre F334Zeop, imaged with a CCD camera. (b) Modal intensity profile from the corresponding numerical simulation. Cross-sections of the modal intensity in the horizontal and vertical directions, shown by the dashed lines, are plotted along the bottom and left hand side of each figure respectively. Contour levels are indicated on each figure.

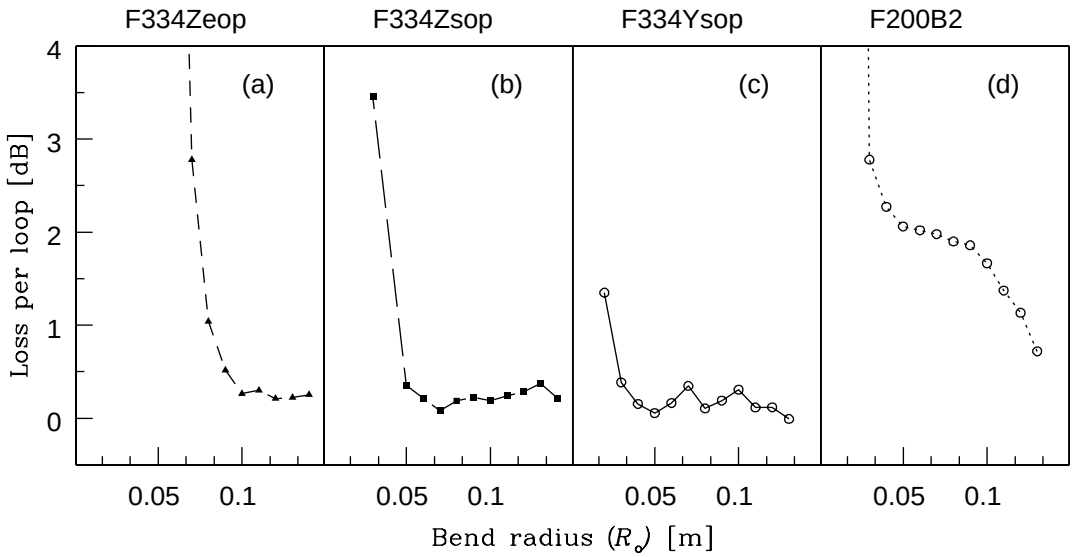

Figure 5.24: Measured bend loss (for one loop of fibre) at 1064 nm as a function of bend radius (R_o) for the four fibres listed in Table 5.3.

fibres listed in Table 5.3. Fibres F334Zsop, F334Ysop and F200B2 are all, in theory, multi-mode. However, the bend loss curves for fibres F334Zsop and F334Ysop are not typical of multi-mode fibres. This could result from the fact that the higher-order modes were not excited at the launch, but may also indicate that these fibres are effectively single-mode at 1064 nm. A fibre is defined to be effectively single-mode if the higher-order modes present in

the fibre are not observed due to the fact that the confinement losses are high, as described in Section 5.3. This is further discussed in Section 7.3, in which additional experimental results are presented for fibres F334Zsop and F334Ysop.

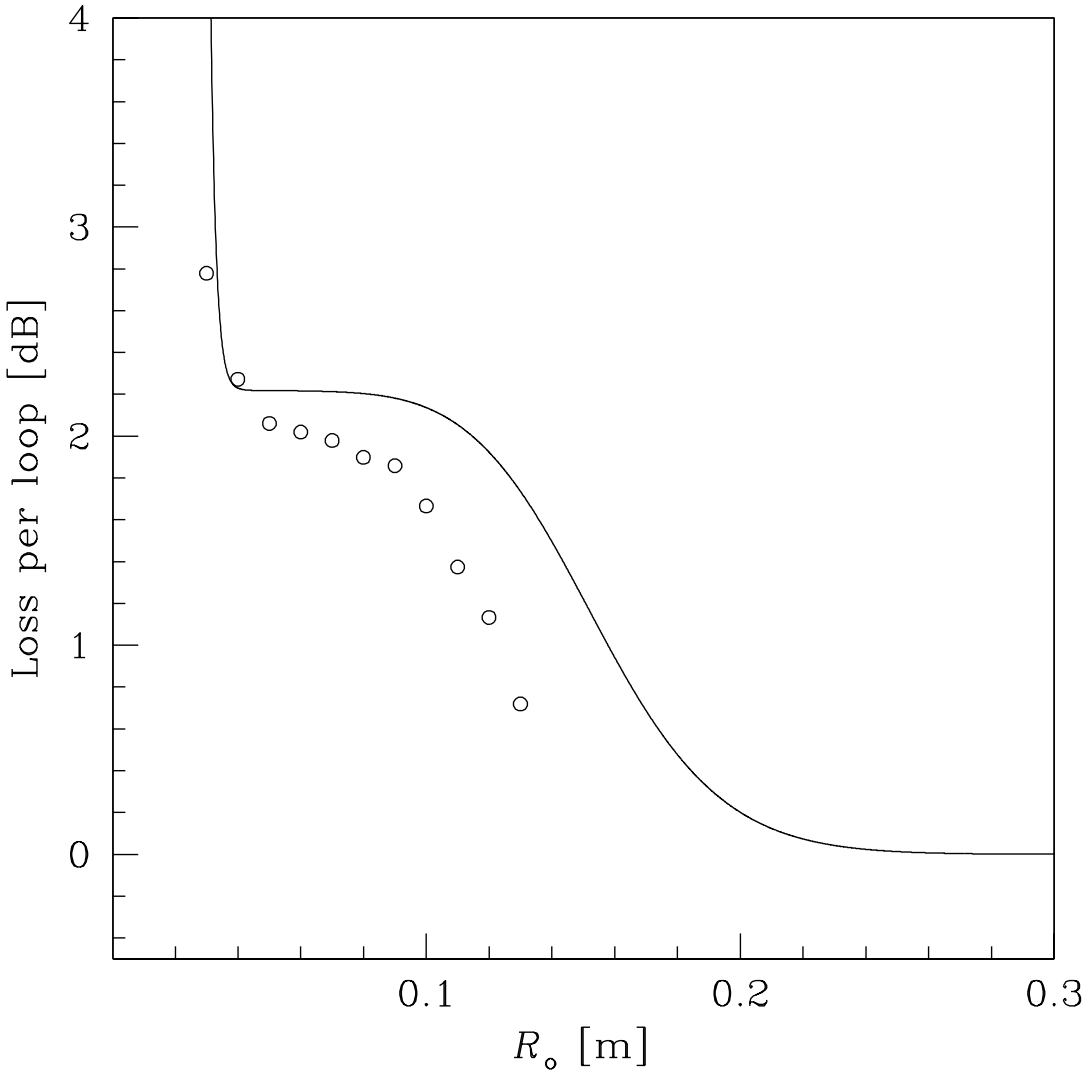

Figure 5.25: Bend loss as a function of bend radius (R_o). The solid line represents the predicted total loss from the fundamental and higher-order modes for fibre HF_H ($\Lambda = 13.4$ μm, $d/\Lambda = 0.50$). The open circles are measured values of bend loss for a similar fibre, F200B2 ($\Lambda = 13.8$ μm, $d/\Lambda = 0.51$).

In contrast to the F334 fibres, the measured bend loss for F200B2, shown in Fig. 5.24 (d) leaves no doubt that higher-order modes are present within this fibre. The shape of the measured bend loss curve is remarkably similar to the predicted bend loss for the multi-mode fibre HF_H, shown in Fig. 5.16 (b). These two curves are shown together in Fig. 5.25, where the measured bend loss for fibre F200B2 is shown by the open circles and the predicted bend loss for fibre HF_H is shown by the solid line. This solid line corresponds to the sum of

the calculated bend loss arising from the fundamental mode and the LP_{11}^{x} and LP_{11}^{y} modes of fibre HF_H, which possesses similar parameters to fibre F200B2. Note that this predicted loss curve for fibre HF_H is obtained by assuming a power ratio of 3:1:1 for the fundamental and the LP_{11}^{x} and LP_{11}^{y} modes respectively, chosen to provide the best agreement with this experimental data. The validity of this choice is discussed in Section 5.3. For both these fibres, the initial rise in loss at larger bend radii represents loss from the LP_{11} modes, and the second sharper rise in loss corresponds to the fundamental mode. Fibre F200B2 has $\Lambda = 13.8$ μm and $d/\Lambda = 0.51$ and fibre HF_H has $\Lambda = 13.4$ μm, $d/\Lambda = 0.50$ and are both indicated on Fig. 5.20. As these two fibres lie on the same contour line of R_c^{FM} in Fig. 5.20, the fundamental mode in each fibre is expected to suffer similar levels of loss in both fibres. This is confirmed by the experimental results. However, fibre F200B2 has a larger value of Λ and d/Λ than fibre HF_H. As a result, the higher-order modes in fibre F200B2 will possess a stronger level of mode confinement relative to those in fibre HF_H. This would account for the fact that the higher-order modes in fibre HF_H experience higher values of bend loss than those in fibre F200B2. The overall similarities between the predicted bend loss for fibre HF_H and the measured bend loss for the similar fibre F200B2 demonstrate that it is possible to model the effect of higher-order modes in bent holey fibres and also that it is possible to strip all higher-order modes without perturbing the fundamental mode by bending the fibre.

5.4.4 Conclusion

The experimental results in this section are presented from a study of four holey fibres with effective areas of ≈ 200 μm^2 that have different structural parameters, with μm $11.7 < \Lambda < 13.8\,\mu$m and $0.33 < d/\Lambda < 0.51$. The fibres in this selection include both single-mode and multi-mode structures and have been characterised in terms of mode area, mode shape and bend loss at 1064 nm. These results demonstrate three of the guidance regions defined in Section 5.3: fibre F334Zeop is truly single-mode, fibres F334Zsop andF334Ysop appear to be effectively single-mode, whilst fibre F200B2 can be selectively single-mode by introducing a bend of radius 7 cm to remove all power from the higher-order modes. The excellent agreement between these measurements and the numerical predictions made in Sections 5.2 and 5.3 validate the numerical techniques used here and demonstrates that they can be used to accurately determine the properties of the fundamental mode and to study the effects of higher-order modes in bent holey fibres. This is further confirmed by

the results presented in Chapter 7, in which spectral measurements are used to assess the bend loss and modedness of some of the fibres shown here as a function of wavelength.

5.5 Defining the range of practical structures (2): Towards larger mode areas at 1064 nm

5.5.1 Introduction

In Section 5.1, a study into the mode area, the bend loss and the modedness of a range of holey fibres with $0.2 < d/\Lambda < 0.5$ and $7\,\mu\text{m} < \Lambda < 14\,\mu\text{m}$ structures was reported. The results of this study, summarised in Fig. 5.6, lead to the conclusion that single-mode holey fibres with $A_{\text{eff}}^{\text{FM}} \approx 320\ \mu\text{m}^2$ can possess tolerable levels of bending losses. In addition, the results of this study strongly suggested that structures with $\Lambda > 14\ \mu\text{m}$ could be used to create single-mode holey fibres with $A_{\text{eff}}^{\text{FM}} > 320\ \mu\text{m}^2$ and tolerable values of R_{c}^{FM}. In this section I extend the numerical work presented in Section 5.1 in order to determine the maximum tolerable effective area for a single-mode holey fibre at 1064 nm. This numerical study is complemented by experimental results presented in Section 5.6, which once again show the effectiveness of the numerical techniques developed here, and also demonstrate that single-mode holey fibres with $A_{\text{eff}}^{\text{FM}} \approx 400\ \mu\text{m}^2$ at 1064 nm are practical to fabricate.

5.5.2 Numerical results

Table 5.4: Predicted modal properties for a range of single-mode large-mode-area holey fibres.

Fibre	Λ [μm]	d [μm]	d/Λ	$A_{\text{eff}}^{\text{FM}}$ [μm^2]	R_{c}^{FM} [cm]
HF_{D}	12.00	4.80	0.40	188	4.4
HF_{J}	15.20	6.08	0.40	293	8.3
HF_{K}	17.70	7.08	0.40	390	12.7
HF_{L}	19.00	7.60	0.40	445	15.2
HF_{M}	20.00	8.00	0.40	490	17.5

The aim of this section is to produce a graph similar to Fig. 5.6 in Section 5.1, which encompasses all single-mode holey fibres with $R_{\text{c}}^{\text{FM}} < 15$ cm. In order to accomplish this, the range of fibre parameters considered in Section 5.1 ($0.2 < d/\Lambda < 0.5$ and $7\,\mu\text{m} < \Lambda < 14\,\mu\text{m}$) must be extended to include fibres with larger mode areas. However, only single-mode fibres

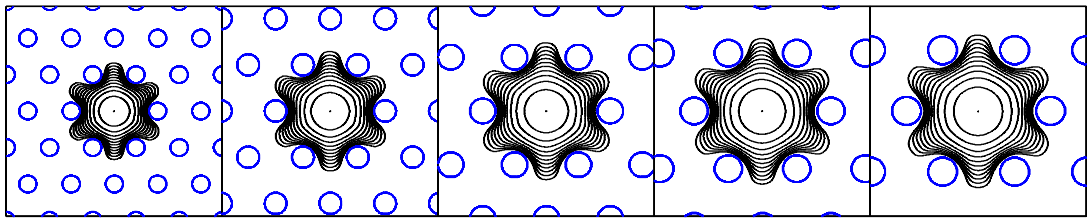

(a) (b) (c) (d) (e)

Figure 5.26: Calculated Modal intensity profiles for fibres (a) HF_D, (b) HF_J, (c) HF_K, (d) HF_L and (e) HF_M. Contours are separated by 2 dB. Fibre parameters are shown in Table 5.4.

are of interest. Since $(d/\Lambda)_c$ flattens to an asymptotic value of 0.406 towards large values of Λ, it is not necessary to extend the range of d/Λ, only the range of Λ. Due to the fact that calculations of R_c^{FM} are relatively time consuming, calculations of bend loss are first performed for four fibres with $d/\Lambda = 0.4$ and increasing values of Λ in order to gauge the maximum value of Λ that it is necessary to consider. A value of $d/\Lambda = 0.4$ is chosen so that these fibres are single-mode, but close to cut-off, and hence possess values of bend loss that are close to the lowest possible value for that given A_{eff}^{FM} in a single-mode fibre. The structural and modal parameters of these four fibres are presented in Table 5.4 together with repeated results for fibre HF_D, shown for comparison.

The modal intensity profiles and structural parameters of these five fibres, which are shown in Fig. 5.26 and Table 5.4 respectively, have $12.0\,\mu m < \Lambda < 20.0\,\mu m$ and possess $190\,\mu m^2 \lessapprox A_{eff}^{FM} \lessapprox 490\,\mu m^2$. It is interesting to note that the shape of the mode for each of these fibres (shown in Fig. 5.26) is almost identical, even though there is more than a factor of 2 between A_{eff}^{FM} for the smallest and largest modes shown. The critical bend radii for the fibres in Table 5.4 range from 4.4 cm up to 17.5 cm, the latter of which is greater than the maximum tolerable R_c^{FM}, defined here to be 15 cm. These results show that extending the range of Λ up to 20.0 μm should therefore encompass all single-mode holey fibres with critical bend radii below 15 cm at 1064 nm.

By calculating A_{eff}^{FM} and R_c^{FM} for $0.2 < d/\Lambda < 0.5$ and $14\ \mu m < \Lambda < 20\ \mu m$ a plot similar to Fig. 5.6 that encompasses all single-mode holey fibres with $R_c^{FM} < 15$ cm can therefore be created. In Section 5.1, numerical results from 32 fibres are used to produce Fig. 5.6 (calculations are spaced by 1 μm in Λ and 0.1 in d/Λ). To extend Λ to 20μm, using the same resolution as before, would require the calculation of A_{eff}^{FM} and R_c^{FM} for a further 24 fibres. This is a reasonably quick calculation for A_{eff}^{FM}, and the results for the fibres within the range $0.2 < d/\Lambda < 0.5$ and $14\ \mu m < \Lambda < 20\ \mu m$ are shown in Fig. 5.27 (a) by the

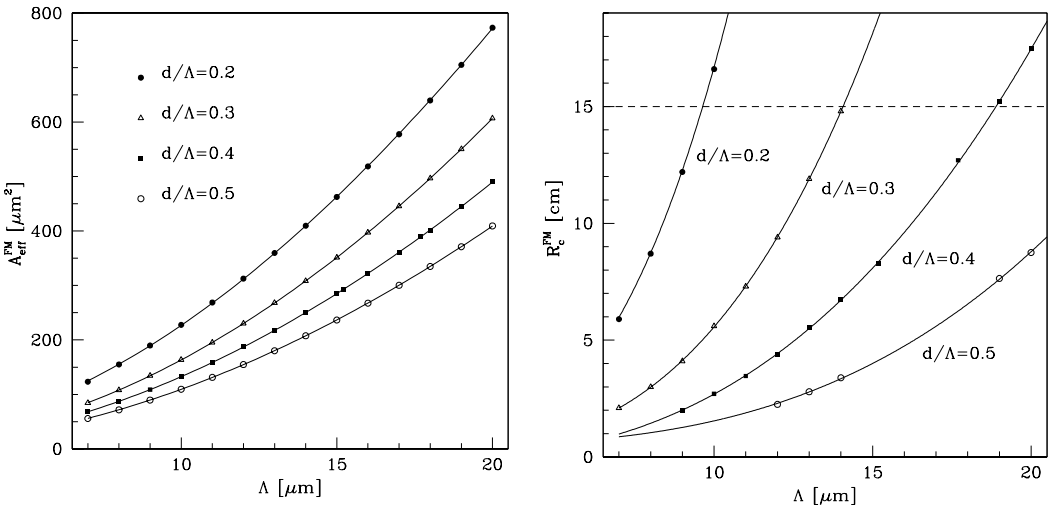

(a) (b)

Figure 5.27: (a) Dots show the predicted effective mode area of the fundamental mode (A_{eff}^{FM}) as a function of the hole-to-hole spacing, Λ, for a range of holes sizes: $0.2 < d/\Lambda < 0.5$ at 1064 nm. The solid line for each value of d/Λ is a fitted curve of the form $y = ax^3 + bx^2 + c$ drawn to guide the eye. (b) Dots show predicted values of the critical bend radius of the fundamental mode (R_c^{FM}) of the fundamental mode as a function of the hole-to-hole spacing, Λ, for a range of relative hole sizes: $0.2 < d/\Lambda < 0.5$ at 1064 nm. The solid line for each value of d/Λ is a fitted curve of the form $y = ax^3 + b$ drawn to guide the eye. The dotted line marks the position of $R_c^{FM} = 15$ cm.

solid and open shapes. Fitted curves for each value of d/Λ are drawn to guide the eye. These calculations are used to create the colour-graded contour plot of A_{eff}^{FM} in Fig. 5.28. Note that the maximum A_{eff}^{FM} within this range is ≈ 800 μm^2. However, in order to define contour lines for the bend radii of interest ($R_c^{FM} \lesssim 15$ cm) it is only necessary to ensure that R_c^{FM} is reasonably well defined for fibres in which $R_c^{FM} \lesssim 20$ cm, which dramatically reduces the required number of calculations. This is advantageous as the calculation of R_c^{FM} is fairly time consuming. In Fig. 5.27 (b) calculated values of R_c^{FM} are shown for a range of fibres. The fitted curves of R_c^{FM} vs Λ for each value of d/Λ, shown by the solid lines in Fig. 5.27 (b), demonstrate that R_c^{FM} can be well defined for the range $0.2 < d/\Lambda < 0.5$ and 14 μm $< \Lambda <$ 20 μm with the addition of only 6 further calculations of R_c^{FM} for structures with $\Lambda >$ 14 μm. These fitted curves of R_c^{FM} vs Λ are then used to create the (thick black) contour lines of R_c^{FM} shown in Fig. 5.28. Note that the accuracy in the position of these contour lines for $R_c^{FM} \gtrsim 20$ cm cannot be accurately quantified, as they are based only on the curve fitted to calculations performed for $R_c^{FM} \lesssim 20$ cm. However, fibres with $R_c^{FM} \gtrsim 20$ cm are of little interest and the additional contour lines on Fig. 5.28 serve only to illustrate

this fact.

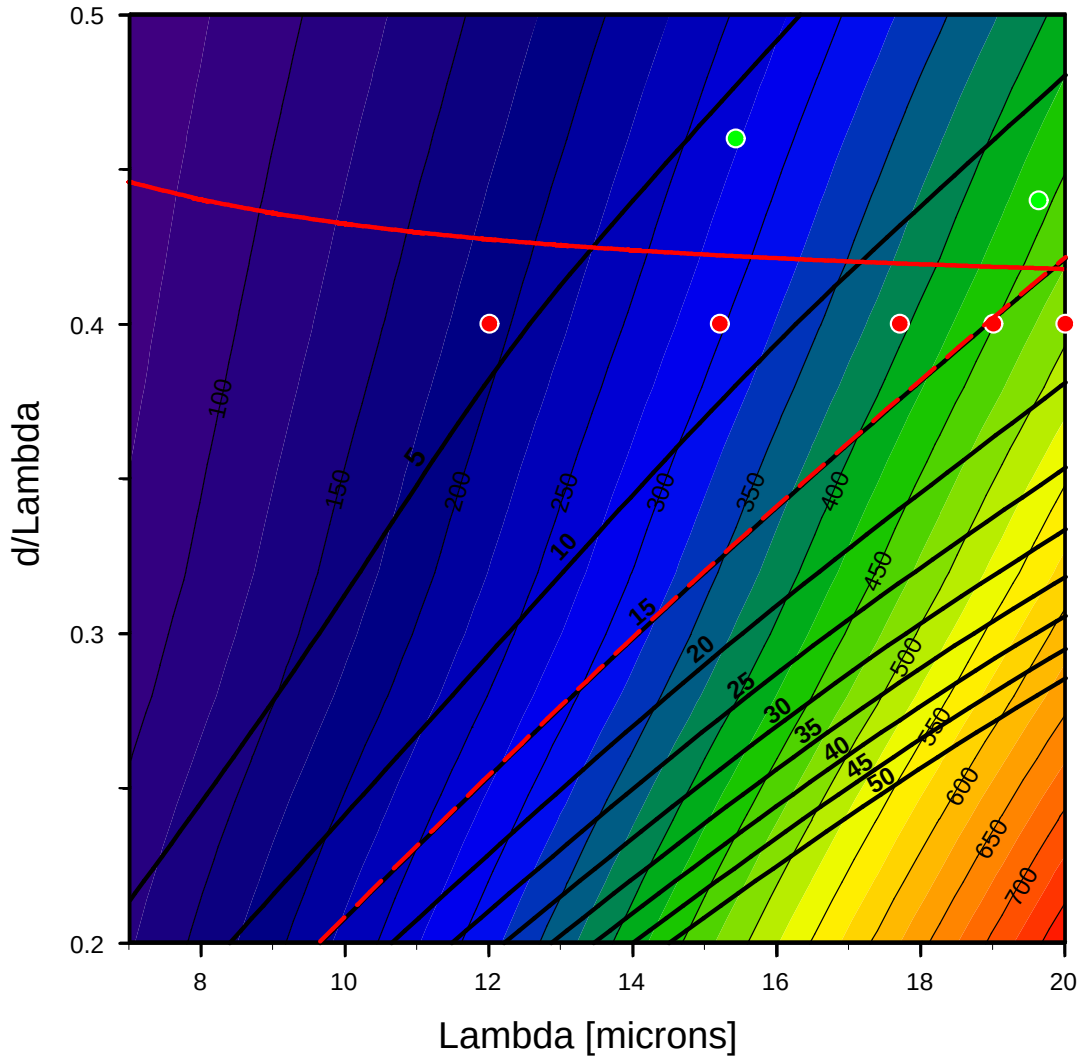

Figure 5.28: Contour plot generated from the data in Fig. 5.27 (a) of effective mode area for the fundamental mode as a function Λ and d/Λ for holey fibres at 1064 nm. The solid red line shows the predicted single-mode/multi-mode boundary using the approximate formula derived in Ref. [19]. The thick black contour lines represent R_c^{FM} in cm (generated from the data in Fig. 5.27 (b)) and the dashed red and black line shows the position of the R_c^{FM} = 15 cm contour line. The red dots show the parameters of some holey fibres that are studied in this section. The green dots show the parameters of two holey fibres studied in the experimental section below.

Also shown on Fig. 5.28 is the boundary between single-mode and dual-mode structures, calculated using Eq. 5.2, represented by the red line. The red dots in Fig. 5.28 represent the five fibres listed in Table 5.4 and the green dots represent the two fibres from the next, experimental, section. This figure shows that for $R_c^{FM} < 15$ cm , the maximum A_{eff}^{FM} attainable in a single-mode holey fibre is $\approx 450\ \mu m^2$. Moreover, this figure is an invaluable

design tool for single-mode structures at 1064 nm, in that it is possible to ascertain the fibre parameters required to create any given value of $A_{eff}^{FM} \lesssim 450\ \mu m^2$ and determine the R_c^{FM} for that fibre.

5.5.3 Discussion

In Sections 5.3 and 5.4 it was demonstrated, using both numerical and experimental results, that for values of $d/\Lambda > (d/\Lambda)_c$ it is possible to make use of effectively and selectively single-mode regimes, to achieve single-mode guidance within a multi-mode fibre. For $A_{eff}^{FM} \approx 190\ \mu m^2$ these regions were defined in terms of d/Λ. This has not been considered in the numerical work presented in this section purely for reasons of time. As a result, the predicted value for the maximum practical mode area of $\approx 450\ \mu m$ is defined here for a truly single-mode holey fibre and can be taken as a somewhat conservative estimate. The experimental results presented in Section 5.6, demonstrate both effectively and selectively single-mode guidance in holey fibres with $A_{eff}^{FM} \approx 300 - 450\ \mu m^2$, and so give some idea of the values of d/Λ for which effectively and selectively single-mode guidance can be achieved for these larger mode areas.

5.6 Experimental study (2): $A_{eff}^{FM} > 300\ \mu m^2$

5.6.1 Introduction

Within this section, results are presented from an experimental study into the modal properties of two holey fibres with $A_{eff}^{FM} > 300\ \mu m^2$ at 1064 nm. Both fibres considered here are technically multi-mode structures and have been characterised in terms of mode area, and bend loss at 1064 nm. Note that unless otherwise indicated the experimental results presented in this section correspond to measurements made using a CW single-mode laser with a wavelength of 1064 nm as the source illumination. These measurements are used to demonstrate the validity of the numerical predictions made in Sections 5.5.2, in addition to providing information into the selectively single-mode regime for larger mode areas. Note that all the numerical predictions presented within this section are calculated using the scalar version of the model presented in Section 3.2, and that the constant of proportionality, τ, defined in Eq.3.17, is equal to 2.0 (see also Section 4.5.3).

5.6.2 The fibres

In Table 5.5 the properties of two fibres that were fabricated and characterised as part of this study are listed. The structural parameters of these fibres are also indicated by the green dots on the contour plot in Fig. 5.28. (please refer to the figure caption for more details). Fibre F409Ysop was fabricated by John Hayes at the ORC and fibre F437Zeop was fabricated by Marco Petrovich, also at the ORC. Both of these fibres are made entirely from pure silica rods and tubes of F300 synthetic silica glass from Heraeus Tenevo AG. SEM images of these two fibres are shown in Fig. 5.29.

Table 5.5: Measured (^{m}) and predicted (^{p}) modal properties for holey fibres. * fibre is found to be effectively single-mode at 1064 nm.

Fibre	Λ [μm]	d [μm]	d/Λ	A^m_{eff} [μm^2]	A^p_{eff} [μm^2]	R_c^m [cm]	R_c^p [cm]	Modes
F409Ysop	15.43	7.07	0.46	270	270	≈ 5	5.5	MM*
F437Zeop	19.64	8.67	0.44	430	440	≈ 12	12.0	MM*

5.6.3 Results and discussion

The measured values of $A_{\text{eff}}^{\text{FM}}$ for fibres F409Ysop and F437Zeop are 270 and 430 μm^2 respectively, which are in excellent agreement with theoretical predictions that are also shown in Table 5.5. SEM images of these two fibres are shown in Fig. 5.29. Note that the innermost ring of holes in both fibres shown in Fig. 5.29 are elliptical in shape. As for the fibres detailed in Section 5.4, the nature of this ellipticity does not break the 6-fold symmetry of the fibre and so it is reasonable to assume that it will not induce significant birefringence. As before, we find that the ellipticity can be taken into account in the modelling by defining an ideal fibre structure that has an equivalent air filling fraction to the real fibre. Note that the fibre parameters quoted in Table 5.3 refer to the equivalent, idealised, profiles used in numerical calculations.

The measured bend loss for fibres F409Ysop and F437Zeop is shown in Fig. 5.30. The predicted bend loss for the fundamental mode is shown by the closed circles and the solid line in each plot. The insets in Figs 5.30 (a) and (b) show the predicted mode profile for the fundamental mode together with the idealised refractive index profile used in the calculations of bend loss for each fibre. Although these two fibres are both technically

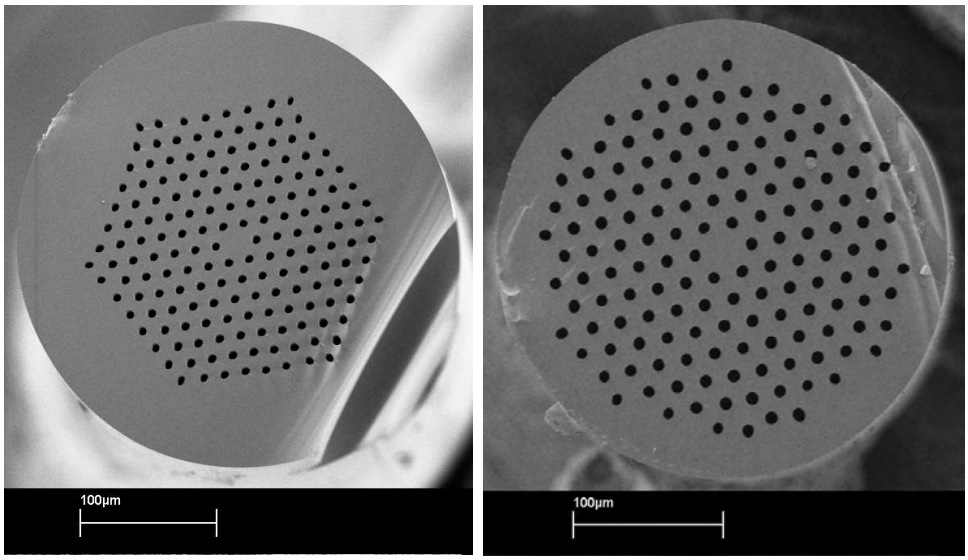

(a) (b)

Figure 5.29: (a) SEM image of fibre F409Ysop. (b) SEM images of fibre F437Zeop. Fibre parameters are shown in Table 5.5.

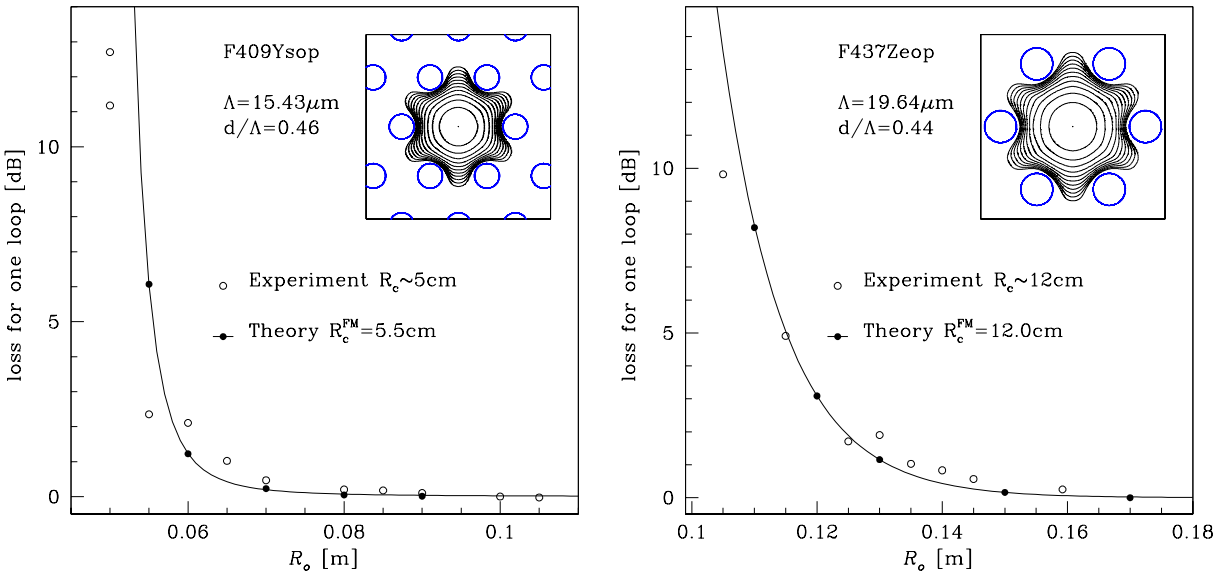

(a) (b)

Figure 5.30: Bend loss for one loop of fibre in dB as a function of radius for (a) fibre F409Ysop and (b) fibre F437Zeop. The experimental data is shown by open circles, the theoretical predictions are shown by closed circles and the solid line. The predicted mode profile together with the idealised refractive index profile used in calculations is shown in the insert. The contour lines are separated by 2 dB and the width of the box shown is 50 μm. The fibre parameters are shown in Table 5.5.

multi-mode structures, we see that the predicted bend loss for the fundamental mode alone is in excellent agreement with the measured bend loss. The absence of any evidence in the bend loss for the presence of higher-order modes indicates that these fibres are effectively single-mode at 1064 nm. A fibre is defined to be effectively single-mode if the higher-order modes present in the fibre are not observed due to the fact that they are significantly lossy, as described in Section 5.3. This is further discussed in Section 7.3.

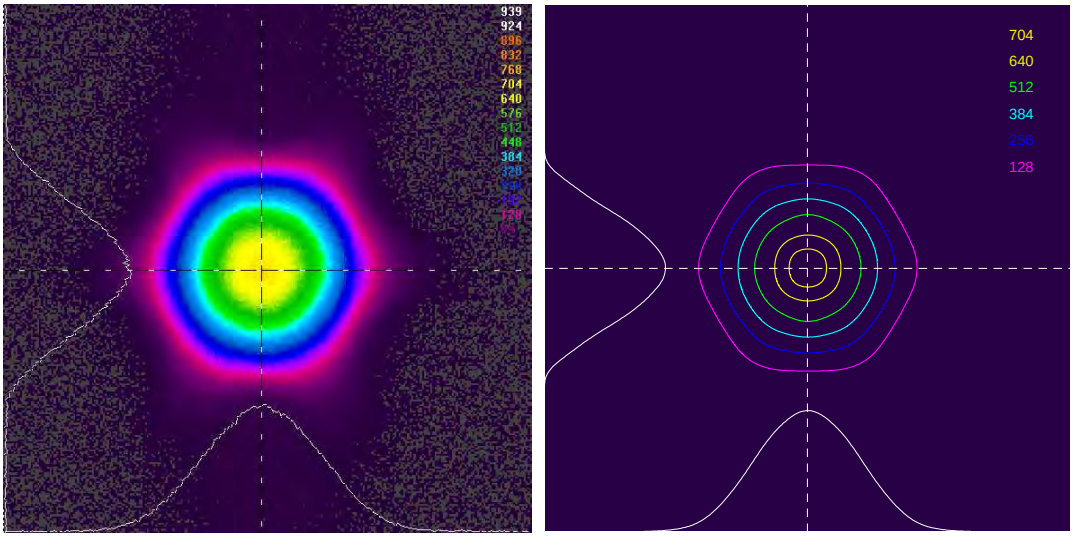

(a) (b)

Figure 5.31: (a) Near-field modal intensity profile for fibre F409Ysop, imaged with a CCD camera. (b) Modal intensity profile from the corresponding numerical simulation of the fundamental mode. Cross-sections of the modal intensity in horizontal and vertical directions, which are indicated by the dashed lines, are plotted along the bottom and left hand side of each figure respectively. Contour levels are indicated on each figure.

Further evidence that fibre F409Ysop is effectively single-mode at 1064 nm is presented in Fig. 5.31, in which the near field mode profile of fibre F409Ysop is shown for: (a) the actual fibre, with a bend radius of approximately 14 cm and (b) the numerical simulation for the fundamental mode of the straight fibre. In Fig. 5.31 (a), the near field is imaged by focussing the far field output from the fibre onto a COHU 7512 CCD camera. The contour levels are indicated on each plot. The contour lines in Fig. 5.31 (b) have been chosen to match some of the camera levels from Fig. 5.31 (a) to aid comparison. In both Fig. 5.31 (a) and (b), Cross-sections of the modal intensity in horizontal and vertical directions, which are indicated by the dashed lines, are plotted along the bottom and left hand side of each figure respectively. These cross-sections are also plotted together in Fig. 5.32 (a). These figures show that the observed near-field modal profile for fibre F409Ysop is an excellent

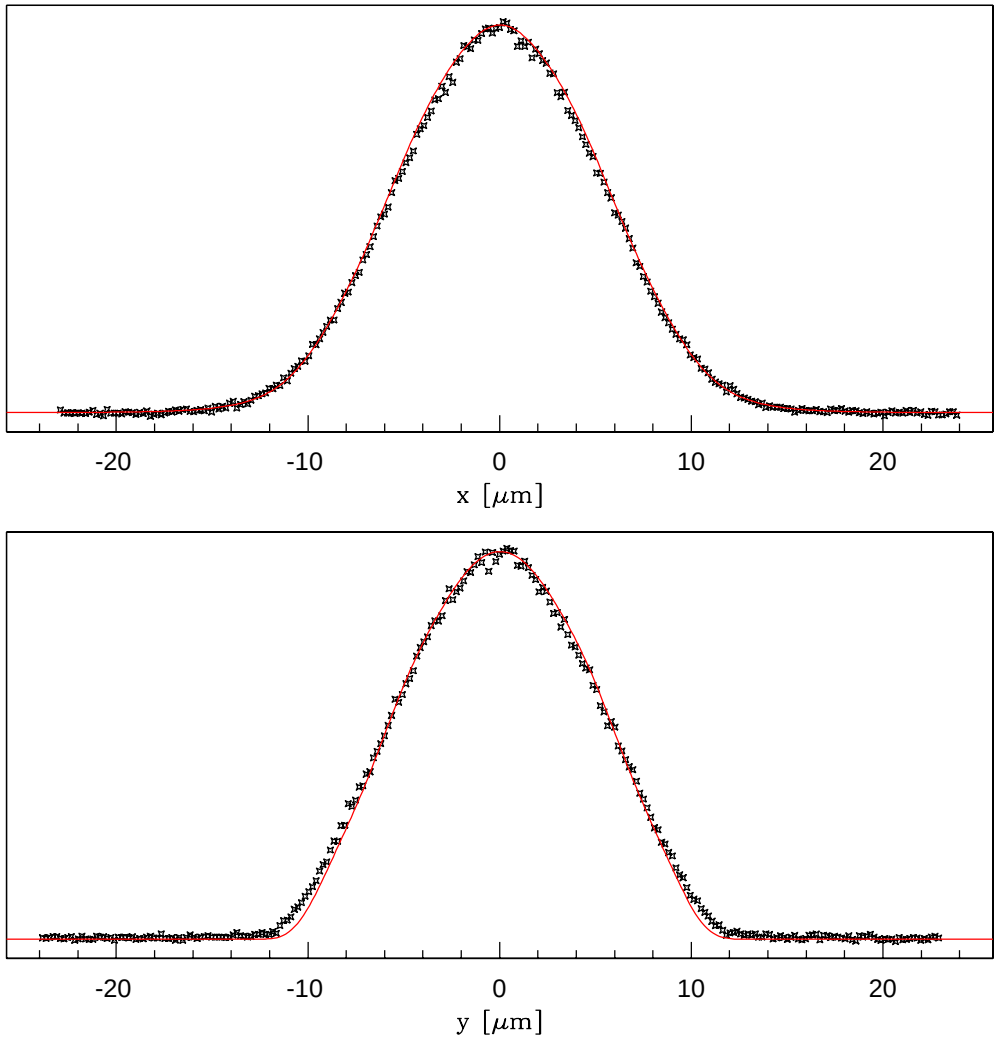

Figure 5.32: Cross-sections of the near field modal intensity in horizontal and vertical directions (top and bottom figures respectively). The crosses indicate the measured near-field modal intensity profile for fibre F409Ysop, imaged with a CCD camera (shown in Fig. 5.31 (a)), and the solid line corresponds to the modal intensity profile from the corresponding numerical simulation of the fundamental mode only (shown in Fig. 5.31 (b)).

match to the theoretical prediction for the fundamental mode alone and confirms that fibre F409Ysop is effectively single-mode at 1064 nm.

The fact that these two fibres can be considered to be effectively single-mode at 1064 nm demonstrates that the estimate of 450 μm^2 as the maximum tolerable effective area at 1064 nm is somewhat conservative. Fibre F437Zeop has $A_{eff}^{FM} \approx 430$ μm^2, $d/\Lambda = 0.44$, and $R_c^{FM} \approx 12$ cm, which indicates that holey fibres that are effectively single-mode at 1064 nm with modes areas up to approximately 500 μm^2 may be practical in terms of bend loss.

5.7 Comparison with step-index fibres

5.7.1 Introduction

In the previous sections of this chapter, results from a detailed study into the modal properties of large-mode-area holey fibres at 1064 nm have been presented. Within this study, the parametric dependencies of mode area, bend loss, and modedness have been established using both experimental and numerical techniques. These results have enabled the practical limits of holey fibres for use in the large-mode, single-mode regime to be ascertained. However, in order to properly evaluate the potential of these novel fibres, it is essential to place their performance in context by comparing the modal properties of their conventional counterparts.

In this section, the modal properties of step-index fibres in the large-mode, single-mode regime at 1064 nm are evaluated numerically in order to assess the potential offered by holey fibres in this same regime. In order to present a meaningful comparison between the two fibre types it is important to consider fibres that are *equivalent* in both modedness and mode size. Traditionally, an *equivalent* step-index (ESI) fibre is used as a crude way of modelling the modal properties of a holey fibre at a given wavelength [4, 16]. (This technique is discussed in more detail in Section 1.4.2). Typically, the core and cladding indices of the ESI fibre equal the refractive index of pure silica and the effective refractive index of the holey fibre cladding (n_{FSM}) respectively. These are both representative choices, but the core radius is then chosen rather arbitrarily. (A core radius of 0.625Λ has been empirically shown to produce a reasonable approximation to the modal properties of a holey fibre [18]). Whilst this technique has proven to be a useful tool for gauging certain modal properties of a holey fibre, it is not an accurate way of creating an *equivalent* fibre due to the arbitrary way in which the core radius is defined. However, in this study, the modal properties of the holey fibres to which comparisons are to be made are already well known. Consequently, the core radius of an ESI fibre can be better defined. For example, the core radius of an ESI fibre can be selected such that the associated A_{eff}^{FM} is equal to that of the comparison holey fibre. Since the aims of the study are to assess the potential offered by holey fibres in the large-mode-area limit, it would seem sensible to consider holey and conventional fibres with similar mode sizes. As a result, and unless otherwise indicated, the parameters of the comparison step-index fibres are chosen to create structures that are equivalent in terms of cladding index and mode area.

In Section 5.7.2, the bending losses of three holey fibres that have been studied in

previous sections are compared with the bending losses of their ESI fibres, as defined above. Section 5.7.3 then explores how the bending losses of these two fibre types can be optimised via the fibre parameters. In Section 5.7.4 I aim to ascertain the maximum mode size that is practical to use (i.e. $R_c^{FM} < 15$ cm) in a single-mode step-index fibre at 1064 nm. The similarities between the modal properties of holey and conventional fibres at 1064 nm are then discussed in Section 5.7.5.

5.7.2 Equivalent step-index fibres and their bending losses

The processes by which the ESI parameters are chosen is discussed within Section 5.7.1, and are summarised in the following; $n_{core} \equiv n_{glass}$, $n_{clad} \equiv n_{FSM}$ and $A_{eff}^{FM}(ESI) \equiv A_{eff}^{FM}(HF)$. The effective cladding index n_{FSM} of each holey fibre is calculated using the commercial software BandSOLVE^{TM}, as described in Section 3.5. The core size (a) of each ESI fibre is calculated via the exact solutions for step-index fibres from Ref. [53]. The bending losses of each ESI fibre are then calculated using the methods that have been developed here to evaluate the bending losses of holey fibres, which are described in Chapter 3. In these calculations, the distance from the centre of the core to the outer edge of the cladding (D) is taken to be the same value as that used for the equivalent holey fibre, in which 7 rings of holes are assumed. Although simpler techniques exist for evaluating the bending losses of step-index fibres [106, 151, 152, 126], each involves various different assumptions and for the purposes of a comparative study it is preferable to use the same set of assumptions for every fibre considered.

In this section, the bending losses of three pairs of holey and ESI fibres are compared at 1064 nm. The fibre parameters and modal properties of these six fibres are shown in Table 5.6. The three single-mode holey fibres, HF_E, HF_J and HF_K have $A_{eff}^{FM} \approx 190$, 290 and 390 μm^2. The effective cladding indices (n_{FSM}) of these holey fibres are 1.448606, 1.448989 and 1.449165 respectively, which are also, by definition, the cladding indices (n_{clad}) of the three ESI fibres, ESI_E, ESI_J and ESI_K. The core radii of these three ESI fibres are chosen as 6.55, 7.84 and 8.55 μm respectively in order to create fibres with the same values of A_{eff}^{FM} as their corresponding holey fibres. Note that the core index in each case is taken to be 1.449631, which is equal to that of pure silica at 1064 nm, as defined by the Sellmeier equation [135]. The NA, and the V-parameter, V, which are defined as NA$= \sqrt{n_{core}^2 - n_{clad}^2}$ and $V = 2\pi a \mathrm{NA}/\lambda$ respectively, are also shown for each of the ESI fibres in Table 5.6. All three step-index fibre satisfy the condition that $V < 2.405$ for a single-mode fibre. The

Table 5.6: The predicted modal properties for a range of single-mode large-mode-area holey fibres and their equivalent step-index (ESI) fibres at 1064 nm. All modal properties are calculated using the methods developed here, which are described in Chapter 3.

Fibre	Λ [μm]	d [μm]	d/Λ	n_{FSM}	A_{eff}^{FM} [μm^2]	R_c^{FM} [cm]
HF_E	12.20	4.00	0.42	1.448606	187	4.0
HF_J	15.20	6.08	0.40	1.448989	293	8.3
HF_K	17.70	7.08	0.40	1.449165	390	12.7
Fibre	a [μm]	n_{clad}	NA	V	A_{eff}^{FM} [μm^2]	R_c^{FM} [cm]
ESI_E	6.55	1.448606	0.055	2.11	187	5.2
ESI_J	7.84	1.448989	0.043	2.00	293	11.1
ESI_K	8.55	1.449165	0.037	1.86	390	21.5

critical bend radius of the fundamental mode, R_c^{FM}, is calculated for each of the six fibres in Tables 5.6 using the methods developed here for holey fibres (see Chapter 3). These values are also shown in Table 5.6 and demonstrate that the bending losses of holey fibres can be less than step-index fibres that are equivalent in terms of A_{eff}^{FM} and n_{clad} at 1064 nm. Indeed, the R_c^{FM} of each of the three holey fibres is $\approx$ 77, 75 and 59% of their ESI fibre equivalents for the $A_{eff}^{FM} \approx$ 190, 290 and 390 μm^2 fibre pairs respectively.

However, the values of R_c^{FM} presented in Table 5.6 do not correspond to optimum values for either fibre type due to the fact that all six fibres are below cut-off at 1064 nm. Furthermore, it should be noted that the ESI fibres are relatively further from cut-off than their holey fibre counterparts (this is explained in more detail in the following sections). As a result, this does not represent a fair comparison of the performance of these two fibre types in the single-mode regime and demonstrates that the ESI approach used here is not an effective way of comparing these two fibre types. Consequently, we look towards comparing the optimum bending losses in both fibre types: i.e. the bending losses for a given mode area in fibres which are close to cut-off. In Section 5.7.3, the way in which the bending losses can be optimised via the fibre structure are explored, in the single-mode limit, for both holey and step-index fibres. The potential offered by holey fibres relative to their conventional counterparts is then reassessed for these optimum values in the single-mode limit.

5.7.3 Optimising bend loss in single-mode fibres at 1064 nm

As mentioned above, the values of R_c^{FM} shown in Table 5.6 do not represent the lowest possible bending losses for single-mode holey or step-index fibres for the particular values of A_{eff}^{FM} considered. In Section 5.5.2 it was demonstrated that for a given value of A_{eff}^{FM}, the bending losses of a holey fibre improve as d/Λ increases (See Fig. 5.9). The optimum bending losses in a single-mode holey fibre thus occur for $d/\Lambda = (d/\Lambda)_c$, where $(d/\Lambda)_c$ represents the maximum value of d/Λ for which a holey fibre is single-mode and is given by Eq. 5.2. The optimum values of R_c^{FM} for $A_{eff}^{FM} \approx 200$, 300 and 400 μm^2 are extracted in Section 5.7.3 below.

For step-index fibres, systematic studies have shown that macro-bending losses can be minimised by increasing the NA and decreasing the core radius [153, 154]. Since the A_{eff}^{FM} typically increases with core radius and decreases with NA, the obvious way of creating a single-mode fibre with a specific value of A_{eff}^{FM} is to use the smallest core radius and highest NA that results in single-mode guidance. This is analogous to using the smallest value of Λ and the largest value of d/Λ that results in the desired mode area and single-mode guidance in a holey fibre. However, at the low values of NA required for single-mode guidance at 1064 nm, the A_{eff}^{FM} of a step-index fibre does not always increase with core radius. This phenomenon and the effect that this has on choosing optimum parameters for minimal bend loss are illustrated in Section 5.7.3. The potential offered by holey fibres relative to their conventional counterparts is then reassessed for optimal parameters in both fibre types.

Holey fibres

Table 5.7: Predicted modal properties for a range of single-mode large-mode-area holey fibres.

Λ [μm]	d [μm]	d/Λ	A_{eff}^{FM} [μm^2]	R_c^{FM} [cm]
12.3	5.68	0.43	190	≈ 4
15.7	6.60	0.42	300	≈ 8
18.2	7.64	0.42	400	≈ 12

In order to assess the optimum values of R_c^{FM} for $A_{eff}^{FM} \approx 200$, 300 and 400 μm^2 a more detailed version of Fig. 5.27 is plotted for a smaller range of parameters in Fig. 5.33. In this graph, the black lines correspond to contour lines of A_{eff}^{FM} in μm^2, the blue lines correspond

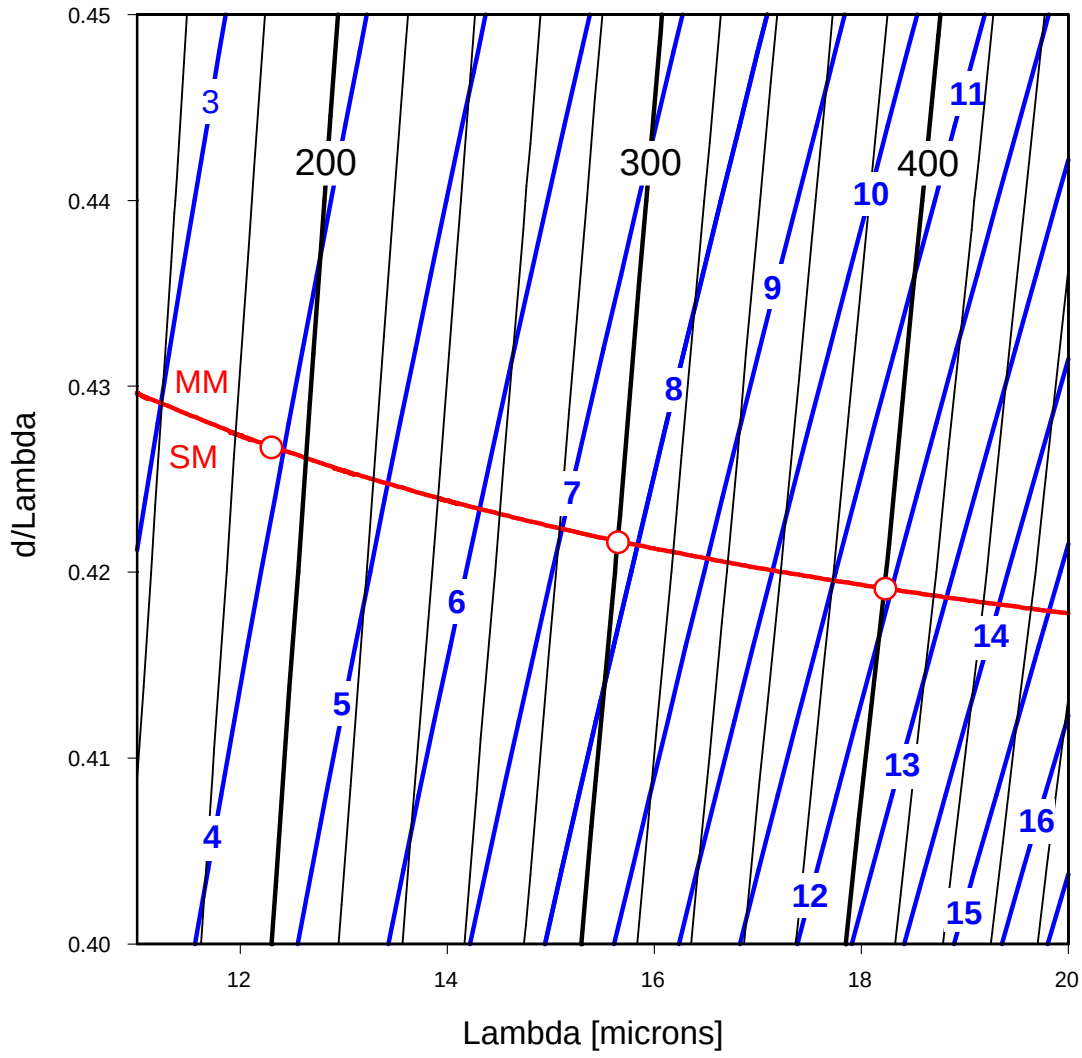

Figure 5.33: Black lines correspond to contour lines of A_{eff}^{FM} in μm^2 generated from the data in Fig. 5.27 (a). The red line shows the predicted single-mode/multi-mode boundary using the approximate formula derived in Ref. [19]. The blue lines correspond to contour lines of R_c^{FM} in cm generated from the data in Fig. 5.27 (b). The red circles along the red line indicate the parameters of the holey fibres in Table 5.7.

to contour lines of R_c^{FM} in cm and the red line shows the predicted single-mode/multi-mode boundary using the approximate formula derived in Ref. [19]. The red circles in Fig. 5.33 show the optimum parameters for single-mode holey fibres with $A_{eff}^{FM} \approx 190, 300$ and 400 μm^2 at 1064 nm. The corresponding R_c^{FM} for these three fibres is $\approx 4, 8$ and 12 cm respectively. These parameters are listed in Table 5.7.

Step-index fibres

In order to determine how the bending losses of step-index fibres can be optimised in the large-mode, single-mode regime at 1064 nm, it is helpful to visualise how the fibre para-

meters influence A_{eff}^{FM}, R_c^{FM} and the modedness (given by the V-parameter defined above). To accomplish this I choose to construct a graph of A_{eff}^{FM} and R_c^{FM} as a function of the fibre parameters as this has proven to be a good way of visualising these relationships in holey fibres (See Fig. 5.28). However, the construction of such a graph requires many calculations. For example, Fig. 5.27 was constructed using the results of modal calculations from 64 separate fibres. Whilst calculations of A_{eff}^{FM} are fairly quick, the methods developed here to calculate bending losses are more time consuming. In order to calculate R_c^{FM} for a wide range of fibre parameters more efficiently, I choose to use an approximate method developed by Marcuse from Ref. [126], in which a loss formula for the fundamental mode of infinitely clad step-index fibres is derived for weakly-guiding fibres. In this approach, which is briefly discussed in Section 2.2, the loss coefficient is determined by calculating the power outflow from the field in the cladding, which is expressed in terms of a superposition of cylindrical outgoing waves. The loss coefficient is given as;

$$\alpha = \frac{\sqrt{\pi}\kappa^2 e^{-\frac{2}{3}R_o\gamma^3/\beta^2}}{4\gamma^{3/2}V^2\sqrt{R_o}(\ln\gamma a)^2} \tag{5.3}$$

where $\kappa = \sqrt{n_{core}^2k^2 - \beta^2}$, $\gamma = \sqrt{\beta^2 - n_{clad}^2k^2}$, β is the propagation constant of the fundamental mode of the straight fibre, R_o is the radius of curvature and $k = 2\pi/\lambda$, where λ is the wavelength of light in free space. Marcuse states that while the above formula gives the correct parametric dependency on bend loss, the exact values of loss are not accurate. However, the purposes of this particular study are to determine how the bending losses can be optimised via the fibre parameters, and accurate values are not required to accomplish this. Note that values of R_c^{FM} calculated using this approximate approach are compared against those calculated using the techniques outline in Chapter 3 for a selection of fibres in Section 5.7.4.

The fibre properties A_{eff}^{FM}, R_c^{FM}, and V are calculated for 80 separate fibres with parameters at evenly spaced intervals of n_{clad} and core radius (a) within the range $1.4485 < n_{clad} < 1.4492$, and 6 μm $< a <$ 12 μm (n_{core}=1.449631). This corresponds to 0.035 <NA< 0.057 and $1.25 < V < 4.06$ and was chosen to create single-mode fibres with 170 $\mu m^2 \lesssim A_{eff}^{FM} \lesssim$ 500 μm^2. The resulting data is plotted as a function of n_{clad} and core radius in Fig. 5.34, where the colour contour plot refers to A_{eff}^{FM} in μm^2, the red line shows the V=2.405 single-mode/multi-mode boundary and the thick black lines correspond to contour lines of R_c^{FM} in cm. (Note that the small degree of oscillation present in the higher level contour lines of R_c^{FM} is not a real phenomenon and is an artefact introduced by the fitting software used to construct this graph.) The contour plot of A_{eff}^{FM} in Fig. 5.34 shows that A_{eff}^{FM} increases as the

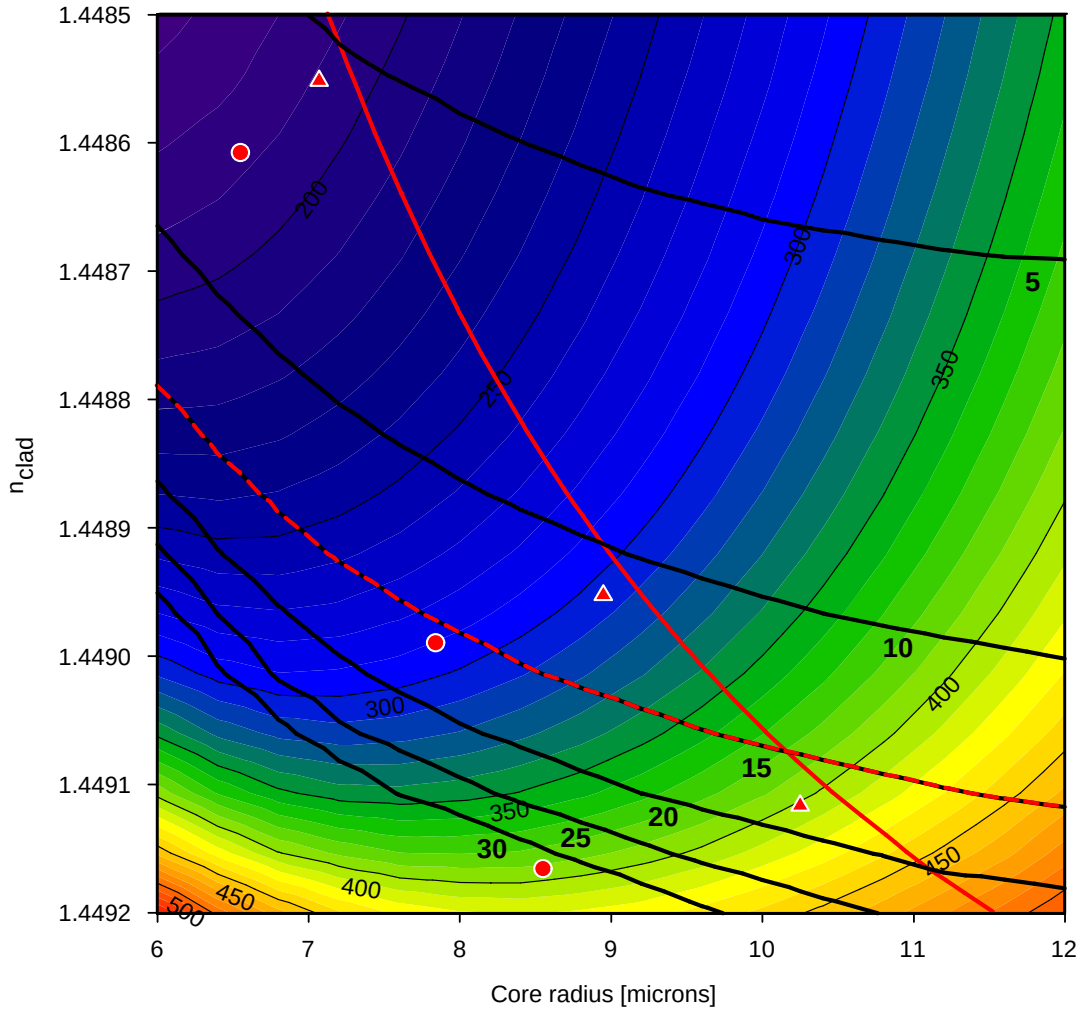

Figure 5.34: Colour contour plot of A_{eff}^{FM} in μm^2 as a function of core radius (a) and n_{clad} for conventional step-index fibres at 1064 nm. The solid red line shows the V=2.405 single-mode/multi-mode boundary. Both A_{eff}^{FM} and V are calculated using exact solutions [53]. The thick black lines correspond to contour lines of R_c^{FM} in cm, calculated using the model in Ref.[126] and the dashed red and black line shows the position of the R_c^{FM} = 15 cm contour line. The small red circles and triangles show the parameters of some step-index fibres that are studied in this section.

value of n_{clad} rises (as the NA decreases) and that there is a minimum value of A_{eff}^{FM} for any given value of n_{clad}. This minimum A_{eff}^{FM} increases with n_{clad} (as the NA decreases). The contour lines of R_c^{FM}, represented by the thick black lines on Fig. 5.34, show that the bending losses improve as the core size is increased and as n_{clad} decreases for all fibres in this range. This demonstrates that for a given value of A_{eff}^{FM} in a single-mode fibre, optimal bending losses can be achieved via the largest core size and smallest value of n_{clad} (corresponding to the largest NA) that results in V$<$ 2.405 and the desired mode size. Essentially, this means that for a given mode area, one should aim to create a fibre with V$\approx$ 2.4. Note that

the functional form of this graph is, at first sight, quite different from the graph shown in Fig. 5.6, in which the same modal properties were plotted in a similar way for holey fibres. This is discussed more in Section 5.37.

However, while the method used to construct the contour lines of R_c^{FM} in Fig. 5.34 gives useful information about the parametric dependencies of bend loss in a step-index fibre (see Eq. 5.3 and surrounding text), it is not sufficiently accurate to enable comparisons of absolute values with similar holey fibres. As mentioned previously, for direct comparison, I choose to calculate the bending losses of step-index fibres using the methods that have been developed here for holey fibres, described in Chapter 3. To enable a comparison between the optimal bending losses of single-mode holey and conventional fibres, I have included here the predicted values of R_c^{FM} for step-index fibres ESI_M, ESI_N and ESI_O. The parameters of these fibres are shown in Table 5.8 alongside the parameters of fibres ESI_E, ESI_J and ESI_K, which were shown in Section 5.7.2 to possess bending losses greater than equivalent holey fibres. Note that these two sets of fibres comprise similar mode areas, but different values of V. Fibres ESI_E, ESI_J and ESI_K have V$\approx$ 2.0 and fibres ESI_M, ESI_N and ESI_O have V$\approx$ 2.3 and are therefore closer to cut-off. Consequently, the bending losses of fibres ESI_M, ESI_N and ESI_O are less than the similarly sized fibres ESI_E, ESI_J and ESI_K. This can be seen from Fig. 5.34, on which the six fibres in Table 5.8 are represented by solid circles (fibres ESI_E, ESI_J and ESI_K) and triangles (fibres ESI_M, ESI_N and ESI_O) and from the predicted values of R_c^{FM} shown in Table 5.8.

The results presented in Table 5.8 show that fibres ESI_M, ESI_N and ESI_O possess $A_{eff}^{FM} \approx 190,300$ and 400 μm^2 at 1064 nm, and $R_c^{FM} = 4.6, 9.5$ and 14.4 cm respectively. This is similar to the lowest values of R_c^{FM} for holey fibres with $A_{eff}^{FM} \approx 190,300$ and 400 μm^2 at 1064 nm, which were shown to be $\approx$ 4, 8 and 12 cm respectively in Section 5.7.3. Note that fibres ESI_M, ESI_N and ESI_O are the ESI fibres of three holey fibres from Chapter 6. Whilst these step-index fibres have V$\approx$ 2.3, and so do not represent the lowest possible bending losses in the single-mode limit (minimal bend loss for single-mode fibre occurs at cut-off, for which V= 2.405), the values of R_c^{FM} are not likely to dramatically decrease between V= 2.3 and V= 2.4. As a result, one can see that the optimal bending losses for single-mode operation are likely to be similar in similarly sized holey and conventional fibres, despite the fact that the bending losses of holey fibres can be significantly less than step-index fibres that are equivalent in terms of A_{eff}^{FM} and n_{clad} at 1064 nm. This illustrates that the practice of selecting ESI parameters by defining $n_{core} \equiv n_{glass}$, $n_{clad} \equiv n_{FSM}$ and

$A_{eff}^{FM}(ESI) \equiv A_{eff}^{FM}(HF)$ does not result in an accurate representation of the modal properties of a holey fibre even though the core radius is not chosen in an arbitrary manner. This is consistent with studies that have shown that both the core and cladding regions of a holey fibre have effective indices that vary with wavelength and that an ESI approach cannot be used to accurately model the modal properties of a holey fibre [87].

Table 5.8: Predicted modal properties for a range of ESI fibres. Critical radius predicted using the numerical methods outlined in Chapter 3.

Fibre	a [μm]	n_{clad}	NA	V	A_{eff}^{FM} [μm^2]	R_c^{FM} [cm]
ESI_E	6.55	1.448606	0.055	2.11	187	5.2
ESI_J	7.84	1.448989	0.043	2.00	293	11.1
ESI_K	8.55	1.449165	0.037	1.86	390	21.5
ESI_M	7.07	1.448552	0.056	2.34	191	4.6
ESI_N	8.95	1.448953	0.044	2.34	305	9.5
ESI_O	10.25	1.449117	0.039	2.34	401	14.4

5.7.4 Maximum practical mode area in a step-index fibre at 1064 nm

Table 5.9: Predicted modal properties for a range of ESI fibres. Critical radius predicted using * method developed in Chapter 3 and ** method from Ref. [126].

Fibre	a [μm]	n_{clad}	NA	V	A_{eff}^{FM} [μm^2]	R_c^* [cm]	R_c^{**} [cm]
ESI_E	6.55	1.448606	0.055	2.11	187	5.2	7.1
ESI_J	7.84	1.448989	0.043	2.00	293	11.1	16.4
ESI_K	8.55	1.449165	0.037	1.86	390	21.5	32.3
ESI_M	7.07	1.448552	0.056	2.34	191	4.6	5.5
ESI_N	8.95	1.448953	0.044	2.34	305	9.5	11.5
ESI_O	10.25	1.449117	0.039	2.34	401	14.4	17.8

In Section 5.7.3 contour plots of A_{eff}^{FM} and R_c^{FM} as a function of n_{clad} and core radius were constructed in order to illustrate how the bending losses of step-index fibres can be optimised in the large-mode area single-mode regime at 1064 nm. For reasons of time, an approximate method was used to calculate R_c^{FM} for the large number of step-index

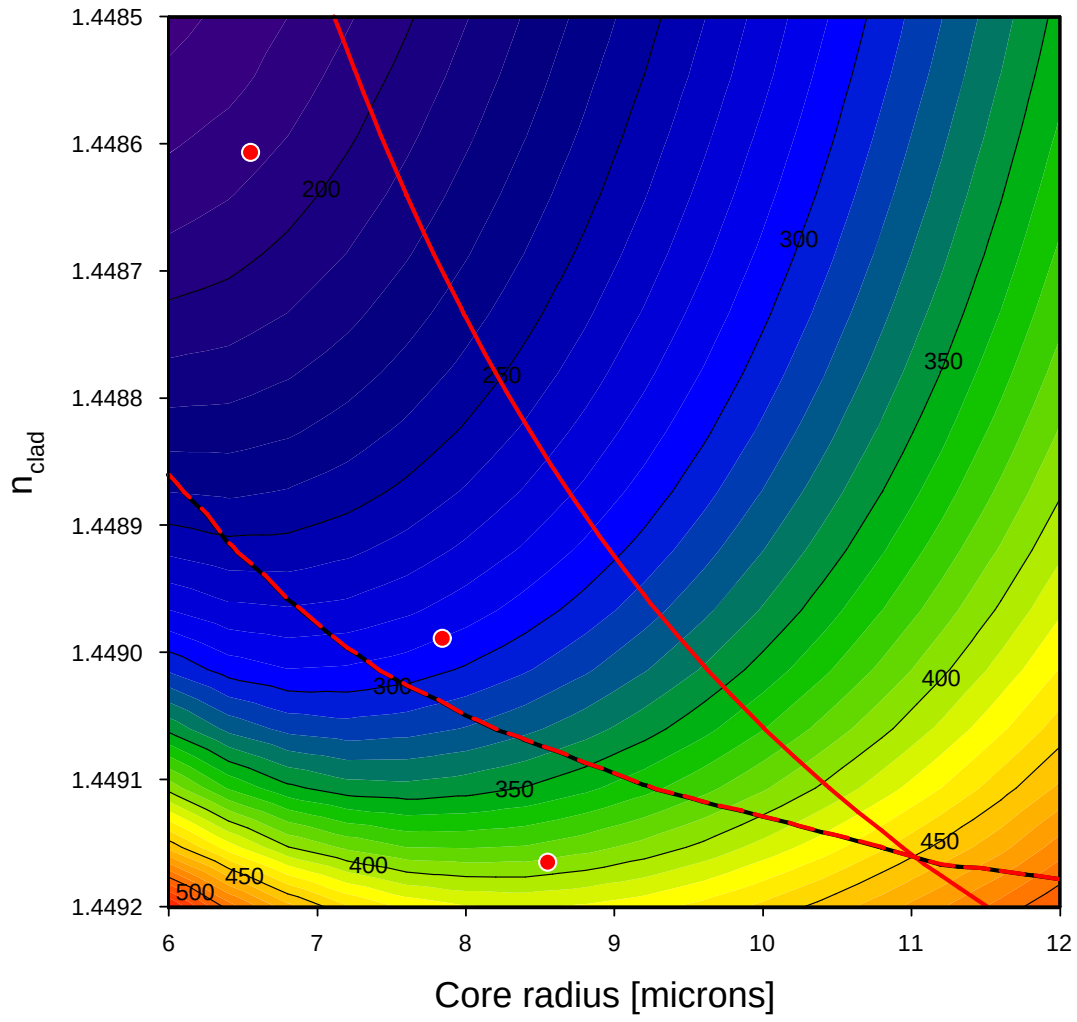

Figure 5.35: Contour plot of A_{eff}^{FM} as a function of n_{clad} and core radius (a) for conventional step-index fibres at 1064 nm. The red line shows the V=2.405 single-mode boundary. The dashed red and black line shows the contour line for which the critical bend radius of the fundamental mode is equal to 15 cm. The red dots show the parameters of three step-index fibres that are equivalent to the three holey fibres indicated in Fig. 5.36, in terms of A_{eff}^{FM} and n_{clad}.

fibres required to form an adequate description of the bend loss over the parameter range considered ($\approx$ 80 fibres were considered at even spaced intervals of n_{clad} and core radius). Although this method, which is described by Eq. 5.3 and the surrounding text, gives the correct parametric dependency on bend loss, the exact values of loss are not accurate and R_c^{FM} is overestimated. This can be seen in Table 5.9, which lists values of R_c^{FM} for 6 step-index fibres, calculated using both Eq. 5.3 and the more accurate methods developed here. This demonstrates that Eq. 5.3 consistently overestimates R_c^{FM} relative to the predictions made using the methods developed here by approx 20-50% (average of $\approx$ 34%). This overestimation can be approximately corrected by scaling the values of R_c^{FM} calculated using

Eq. 5.3 by 0.76 to better agree with the values of R_c^{FM} calculated using the more accurate methods developed here. Due to the fact that this is a crude method of correction, only the $R_c^{FM} = 15$ cm contour line is corrected in this way, and is shown by the thick black line in Fig. 5.35 (See caption for further information). $R_c^{FM} = 15$ cm was previously defined as the upper limit on practicality in Section 5.1 and so gives an approximate idea of the maximum tolerable A_{eff}^{FM} in a step-index fibre at 1064 nm, which can be seen here to be ≈ 450 μm^2. This is the same value of maximum practical mode size as estimated for single-mode holey fibres at 1064 nm in Section 5.5.2. However, despite this similarity, there are some striking differences between Fig. 5.35 and the equivalent graph for holey fibres, shown previously in Fig. 5.28 and repeated here in Fig 5.36. These differences are discussed in the following section.

5.7.5 Comparing parametric dependence of modal properties in holey and step-index fibres

The minima in the contour plot of A_{eff}^{FM} for the conventional fibres, shown in Figs 5.34 and 5.35 and the subsequent effect that this has on the bending losses arises from the fact that the fibres within this range have low values of NA ($0.035 \lesssim \mathrm{NA} \lesssim 0.057$), which causes the fibres to become more weakly guiding as the core size is reduced. Whilst this behaviour is well known in step-index fibres and results from the fact that the fibres are becoming weakly guiding, it prompts the question of why this is not observed within the contour plot of A_{eff}^{FM} and R_c^{FM} for the similar range of holey fibres, repeated here in Fig. 5.36. The three red dots in Fig. 5.36 represent the parameters of three holey fibres that are equivalent in A_{eff}^{FM} and n_{clad} to the three step-index fibres represented by the red dots in Fig. 5.35. One reason for these difference may be the way in which the results are presented. Indeed, if we plot the holey fibre results as a function of n_{FSM} instead of d/Λ, as for the step-index fibres, we observe a more similar pattern of results. A rough plot of this is shown in Fig. 5.37 (a), in which the A_{eff}^{FM} is represented by the dashed contour lines and R_c^{FM} is represented by the solid contour lines. Note that these contour lines are only approximate, since there are fewer results within a grid defined by n_{FSM} than d/Λ. However, even in this crude form, we can see that for a constant value of n_{FSM}, the bending losses improve as Λ (which is approximately equivalent to the core diameter of a step-index fibre) is increased, as in Fig. 5.35. However, a similar minimum in A_{eff}^{FM} is not observed. This may be due to the fact that Λ in a holey fibre and the core radius of a step-index fibre are not entirely equivalent.

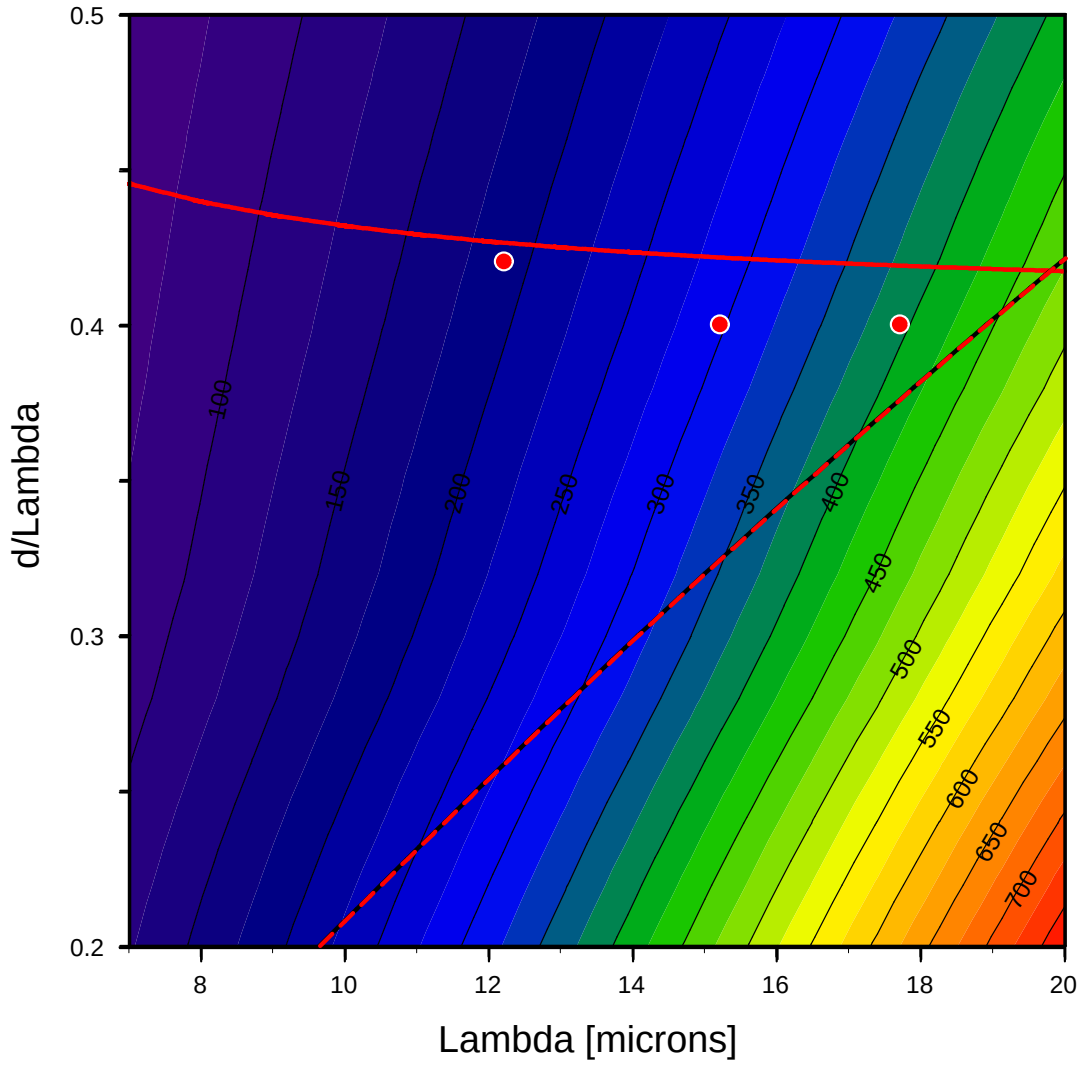

Figure 5.36: Contour plot of A_{eff}^{FM} as a function Λ and d/Λ for holey fibres at 1064 nm. The red line shows the predicted single-mode/multi-mode boundary using the approximate formula derived in Ref. [19]. The dashed red and black line shows the contour line for which the critical bend radius of the fundamental mode is equal to 15 cm. The red dots show the parameters of three holey fibres that are studied in this chapter.

A better approximation is to use $\Lambda - (d/2)$ in place of Λ in the contour plot of A_{eff}^{FM}, as shown in Fig. 5.37 (b). This plot of A_{eff}^{FM} is closer to the form for the step-index fibres than Fig. 5.37 (a), but still does not exhibit a minimum at any point. This may again result from the fact that even $\Lambda - d/2$ is a poor approximation of an equivalent core radius, or it may represent some fundamental difference between holey and conventional fibres, or it could simply result from the fact that the resolution is poor for this representation. Further investigation would be required in order to determine this.

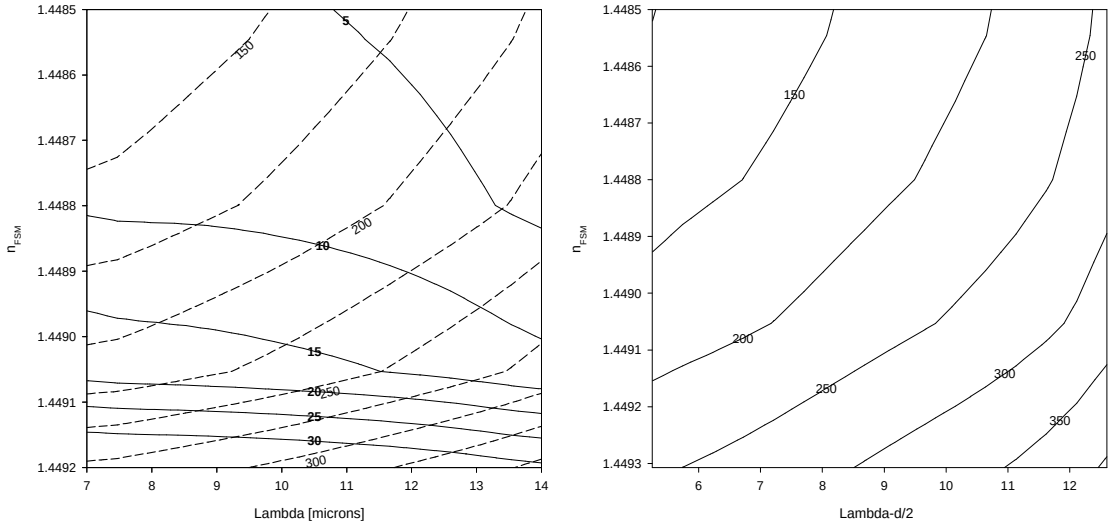

Figure 5.37: (a) Dashed lines represent contour plot of A_{eff}^{FM} in μm^2 as a function Λ and n_{FSM} for holey fibres at 1064 nm. Solid contour lines represent R_c^{FM} in cm. Contour lines are generated from the data shown in Figs 5.27 and 6.1. Note that these plots are only approximate, due to the fact that are fewer results within a grid defined by n_{FSM} than d/Λ, as previously used.

5.7.6 Bending losses of higher-order modes

As discussed in Section 5.3, the technique of removing unwanted higher-order modes by bending the fibre is well known in conventional fibres [149, 150], and can also be achieved in holey fibres. This method exploits the fact that the fundamental mode is the least sensitive to bend induced loss and that the bend loss is exponentially dependent on the radius of curvature. As a result, for certain bend radii ($R_c^{FM} < R_o < R_c^{HOM}$), the higher-order modes suffer catastrophic loss, but the fundamental mode is unperturbed. This is a useful technique as it enables larger mode area fibres to be used for a given bend radius, due to the fact that the R_c^{FM} decreases as the fibre becomes multi-mode.

In this section I present a brief comparison between the bending losses of higher-order modes in holey and step-index fibres by comparing the predicted results for the bending losses of the multi-mode fibre HF_H from Section 5.13 with the bending losses of an equivalent multi-mode step-index fibre. As mentioned in Section 5.7.1 the equivalent step-index (ESI) profile is determined by matching the A_{eff}^{FM} of the holey fibre with the condition that $n_{clad} = n_{FSM}$ and that the core index is equal to that of pure silica. This is accomplished by calculating the modal properties of a step-index fibre using the exact solutions from [53]. Fibre HF_H has $\Lambda = 13.4$ μm, $d/\Lambda = 0.5$ and $n_{FSM} = 1.448420$ at 1064 nm. The effective mode area for the fundamental mode of this fibre (A_{eff}^{FM}) is ≈ 190 μm^2. A core radius of

7.52 μm is found to reproduce the A_{eff}^{FM} of holey fibre HF_H ($n_{core} = 1.446931$). The critical bend radii of each mode of this ESI fibre are calculated using the numerical techniques outlined in Chapter 3. The results for fibre HF_H and the equivalent step-index fibre, ESI_H, are shown in Table 5.10.

Table 5.10: Predicted modal properties for a multi-mode holey fibre, HF_H ($\Lambda = 13.4$ μm and $d/\Lambda = 0.5$), and the ESI fibre, ESI_H (a=7.52 μm, $n_{clad} = 1.448420$, NA=0.059 and $V = 2.63$), calculated using the methods outlined in Chapter 3 in each case. FM refers to a property of the fundamental mode, HOM refers to a property of the first higher-order mode

Fibre	A_{eff}^{FM} [μm^2]	n_{FM}	n^{HOMx}	n^{HOMy}	R_c^{FM} [cm]	R_c^{HOMx} [cm]	R_c^{HOMy} [cm]
HF_H	190	1.449167	1.448538	1.448540	3.0	14.5	17.1
ESI_H	190	1.449126	1.448491	1.448491	3.2	≈ 38	≈ 50

The results in Table 5.10 show that the critical bend radii of the fundamental mode (R_c^{FM}) of fibres HF_H and ESI_H are similar, as expected (See Section 5.7.3), but that the critical bend radii of the higher-order modes are not. (Here ^{HOMx} and ^{HOMy} refer to the two orthogonal LP_{11} modes.) Indeed, R_c^{HOMx} and R_c^{HOMy} are significantly smaller for holey fibre HF_H than for the ESI fibre, demonstrating that the removal of higher-order modes could be achieved at larger bend radii in the step-index fibre. If this trend continues for all multi-mode holey and conventional fibres, it has implications for the technique of selectively guiding only the fundamental mode within a multi-mode fibre by inducing a bend. Based on the preliminary results presented here, it would seem that conventional step-index fibres have the advantage in this application.

The reason for this difference can be seen in the spacing of the modal indices, which are given in Table 5.10 and plotted in Fig. 5.38. In a bent fibre, bending losses arise due to coupling between the fundamental and higher-order and cladding modes, amongst others. Consequently, the magnitude of the bend loss is inversely proportional to the spacing between the modal indices of these various modes. The bending losses of the higher-order modes in fibres HF_H and ESI_H, will therefore be inversely proportional to the distance between their modal indices (n^{HOMx} and n^{HOMy}) and the cladding index ($n_{FSM} \equiv n_{clad}$). As we can see from Fig. 5.38, the higher-order modes of the ESI fibre are closer to the cladding index than for the holey fibre, and should thus result in greater loss, as predicted.

Note that the scalar version of the orthogonal function method (OFM) was used to

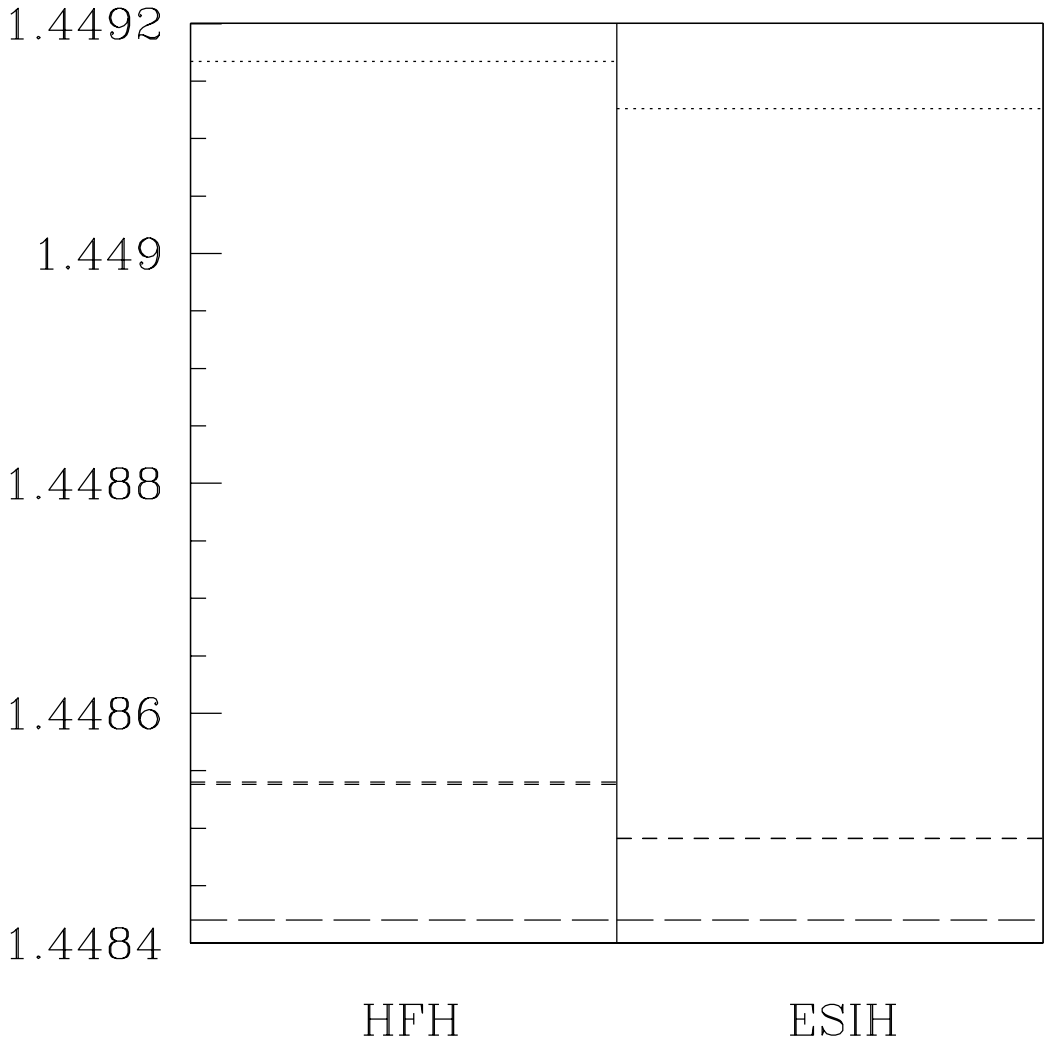

Figure 5.38: Effective modal indices for fibres HF_H and ESI_H: The dotted lines represent the fundamental mode, the short dashed lines represent the first higher-order mode. For HF_H, the long dashed line represents the effective index of the fundamental cladding mode and for ESI_H the long dashed line represents the cladding index. The fibre parameters and modal properties are shown in Table 5.10 and caption.

evaluate the higher-order modal fields and propagation constants in both of these fibres and the bend loss predictions are, as a result, only approximate. However, fully vectorial calculations made using the multipole method (via Vittoria Finazzi) for holey fibre HF_H and the exact solutions for the step-index fibre ESI_H are in good agreement with the calculations made using the scalar OFM, indicating that the scalar approach is appropriate in this example.

5.7.7 Conclusion

In this section, the aim was to explore how the bending losses of step-index fibres at 1064 nm compare with holey fibres in the large-mode-area single-mode regime using numerical techniques. The results presented in Section 5.7.1, demonstrate that the bending losses of holey fibres can be significantly less than those of their *equivalent* step-index (ESI) fibres, whose parameters were chosen by matching values of A_{eff}^{FM} and n_{clad} assuming a core index of pure silica. Section 5.7.3 illustrated how the bending losses of both fibre types could be optimised via the fibre structure for a given mode area, and demonstrated that the bending losses of holey and step-index fibres close to cut-off are similar. This has important implications for bend loss techniques that use an ESI approach, and demonstrates that it is difficult to define an ESI fibre that is truly equivalent. Making use of an approximate study presented in Section 5.7.4, the maximum practical mode size (defined for $R_c^{FM} < 15$ cm) that it is possible to achieve in a single-mode step-index fibre at 1064 nm was estimated as $\approx 450\ \mu m^2$, which is identical to the estimate of the maximum practical A_{eff}^{FM} that can be achieved in a single-mode holey fibre at 1064 nm, as discussed in Section 5.5.2. Furthermore, the results presented in Section 5.7.5 demonstrate that the parametric dependencies of A_{eff}^{FM} and bending losses in holey and conventional fibre are similar, in general, in the large-mode, single-mode regime at 1064 nm.

However, the same cannot be said for multi-mode holey and conventional fibres. In Section 5.7.6, a brief comparison was made between the bending losses of a multi-mode holey and an equivalent step-index fibre. While the bending losses of the fundamental mode were found to be similar in the holey and conventional fibre, the higher-order modes are significantly more susceptible to bending in the step-index fibre. If this is true for all multi-mode fibres, it has implications for the technique of selectively guiding the fundamental mode within a multi-mode fibre by inducing a bend. Based on the preliminary results presented here, it would seem that conventional step-index fibres may have an advantage in this application. However, note that these conclusions are drawn from only one fibre pair and should be treated with caution since the method of defining an ESI profile has been shown to be inaccurate.

5.8 Conclusion

The main aims of this chapter were to evaluate the practical limits of holey fibres for use in the large-mode-area, single-mode regime and to place their performance in context against conventional step-index fibres at 1064 nm. Due to the fact that bending losses represent the fundamental limiting factor on mode area in any optical waveguide, the first step of this analysis was to gain an understanding of the relationships between the structural parameters d and Λ, the mode size, the bend loss and the number of modes present in a holey fibre. This was undertaken using the numerical techniques described in Chapter 3 and was broken down into three calculation stages, in which the three key parameters; A_{eff}^{FM}, R_c^{FM} and the modedness of the fibre were evaluated for the following range of fibre parameters: $7.0\,\mu m < \Lambda < 20.0\,\mu m$ and $0.2 < d/\Lambda < 0.5$. Note that in order to determine the modedness of such a large range of structures, a simple analytical formula from Ref. [19] was employed. This is discussed in detail in Sections 5.2.3 and 5.9. The lower limit on d/Λ is defined by the observation that values of $d/\Lambda < 0.2$ can result in impractically large bending losses and the maximum value of d/Λ is determined by considering the upper limit on single-mode operation. The choice of Λ then determines the effective areas of the fibres considered, which, for this parameter subspace, range from $\approx 60\ \mu m^2$ to $\approx 800\ \mu m^2$. By assessing the subset of fibres within this parameter range that are both single-mode and possess tolerable bending losses (the upper limit for tolerable bend loss is defined here as a critical bend radius (R_c^{FM}) of 15 cm), the range of holey fibre structures that result in practical large-mode-area, single-mode fibres could be determined. Note that this three-step evaluation process is split across two sections within this thesis: in an initial study, presented in Section 5.2, fibres with A_{eff}^{FM} up to $\approx 400\ \mu m^2$ are considered, and in Section 5.5.2, this work is extended to include structures with A_{eff}^{FM} up to $\approx 800\ \mu m^2$ in order to determine the largest practical mode size attainable in a holey fibre at 1064 nm. The results of this study are best summarised in Fig. 5.27, which demonstrates that the fundamental mode area increases towards increasing values of Λ and decreasing values of d/Λ. This is somewhat intuitive, since it is equivalent to increasing the core size and decreasing the NA in a conventional fibre. This figure also shows how the bend loss worsens (i.e. R_c^{FM} increases) with increasing Λ and decreasing d/Λ, presenting a trade off between mode area and bend loss. For any given mode area, the bend loss decreases steadily as d/Λ is increased, demonstrating that the optimum structural parameters are defined by the maximum value of d/Λ that results in single-mode guidance, which can be determined from Eq. 5.2. In this section, the maximum tolerable mode area

possible in a strictly single-mode holey fibre at 1064 nm is shown to be $\approx 450\ \mu m^2$ (defined for $R_c^{FM} < 15$ cm). In addition, the A_{eff}^{FM} and R_c^{FM} 'map' presented in Fig. 5.28 for fibres in the range $7\,\mu m < \Lambda < 20\,\mu m$ and $0.2 < d/\Lambda < 0.5$ is an invaluable design tool and enables basic fibre properties to be determined at-a-glance.

The calculations presented in the initial study in Section 5.2 also provide the basis for a more detailed study into the effect of the fibre structure on modal properties for $A_{eff}^{FM} = 190\ \mu m^2$, presented in Section 5.3. By focussing on a fixed value of A_{eff}^{FM} it becomes possible to gain detailed information regarding the relationships between fibre structure and modal properties and enables valid comparisons to be made in terms of bending losses. In this section, nine holey fibres with $0.2 < d/\Lambda < 0.63$ and $A_{eff}^{FM} \approx 190\ \mu m^2$ at 1064 nm are considered in detail. An A_{eff}^{FM} of $190\ \mu m^2$ was chosen such that the fibres within this range all possessed practical levels of bend loss. For $A_{eff}^{FM} = 190\ \mu m^2$, the single-mode cut-off is shown to occur at $d/\Lambda \approx 0.43$. Consequently, the range of structures encompasses five single-mode and four multi-mode fibres. The aim of this study was to evaluate how the modes of these fibres and their associated losses change as the relative hole size increases. For the nine holey fibres considered here in which $9.0\,\mu m < \Lambda < 15.0\,\mu m$ and $0.2 < d/\Lambda < 0.63$, the critical bend radius of the fundamental mode, R_c^{FM}, was found to decrease from 12.2 to 1.8 cm respectively. Inspection of the modal fields for this range of fibres reveals that the shape of the fundamental mode changes as the relative hole size increases, with the modal field becoming more confined to the core and less filamented in shape.

Furthermore, it can also be seen that the modal deformation in the bent fibre is dependent on the relative hole size, as illustrated in Fig. 5.10. In holey fibres with relatively small holes, the mode deforms in a gradual manner as the bend is tightened, steadily extending further into the cladding region and experiencing greater loss. In contrast, in holey fibres with large holes, the mode undergoes a sudden deformation for R_o close to R_c^{FM}, resulting in a sharp increase in bend loss as a function of bend radius. Due to the fact that the onset of bend loss in response to decreasing curvature becomes much sharper as d/Λ increases, it becomes possible to operate closer to R_c^{FM} without incurring significant bend loss in fibres with large holes. However, we find that the mode deformation for R_o close to R_c^{FM} can significantly alter the mode area, even at radii at which the bend loss is minimal. This results from the fact that for large values of d/Λ, the mode of the bent fibre becomes squashed against the inner ring of holes in the direction of the bend, which acts to decrease the effective area of the mode. Although the bend loss can be minimal in this situation due

to the fact that the mode is still confined to the core region, the effective mode area can be reduced by as much as 15%, reducing the power handling capabilities of the fibre.

Of the nine fibres considered in Section 5.3, four are determined to be multi-mode structures. However, studies of the confinement and bending losses of the higher-order modes present in these fibres demonstrate that multi-mode holey fibres can still be effectively or selectively single-mode in practice. Within this section, four regimes of guidance are defined and the range of d/Λ that results in single-mode guidance in practice is extended. These four regimes are: (1) True single-mode guidance, which is defined for holey fibres in which only the fundamental mode is supported. (2) *effective* single-mode guidance, which is defined for multi-mode holey fibres in which the higher-order modes possess such high confinement losses that they would not be observed for any significant length of fibre. (3) *selective* single-mode guidance, in which higher-order modes can be selectively removed by bending the fibre (a technique well established in conventional fibres, which relies on the fact that the fundamental mode is the least sensitive to bend induced loss and that the bend loss is exponentially dependent on the radius of curvature [149, 150]). (4) Robust multi-mode guidance, in which the higher-order modes are well confined and possess similar values of R_c^{FM} to the fundamental mode and so cannot be selective removed without perturbing the fundamental mode. For $A_{eff}^{FM} \approx 190\ \mu m^2$ at 1064 nm, these regimes are defined by the following values of d/Λ: (1) $< 0.43 <$ (2) $< 0.45 <$ (3) $< 0.63 <$ (4). Note that the values of d/Λ that define these regimes will increase for mode areas larger than 190 μm^2 and decrease for mode areas smaller than this value.

This numerical study is complemented by experimental results presented in Sections 5.4 and 5.6, which validate these numerical predictions and demonstrate that the large-mode-area structures considered here are practical to fabricate. For the range of fibres studied in this section, strictly, effectively and selectively single-mode guidance are all observed. However, note that for the case of selectively single-mode guidance, a significant fraction of power ($\approx$ 2 dB) is lost when removing the higher-order modes by inducing a bend. However, it may be possible to minimise this loss by adjusting the fraction of power coupled into the higher-order modes, via the launch conditions for example. Whilst this is not studied here for reasons of time, it is obviously an important consideration. Experimental results in Section 5.6, also show that a holey fibre with $d/\Lambda = 0.44$, $A_{eff}^{FM} = 430\ \mu m^2$ and $R_c^{FM} = 12.0$ cm is effectively single-mode at 1064 nm. This demonstrates that the predicted value for the maximum practical mode area of $\approx 450\ \mu$m at 1064 nm, which is defined for a

truly single-mode holey fibre, can be taken as a somewhat conservative estimate and that mode areas up to approximately 500 μm^2 could be practical in terms of bending losses for silica holey fibres at 1064 nm.

In order to understand how holey fibres compare with conventional step-index fibres in this large-mode-area, single-mode regime, a numerical study is also undertaken for similarly sized conventional fibres and the results of this are presented in Section 5.7. In order to present a meaningful comparison between the two fibre types it is important to consider fibres that are *equivalent* in both modedness and mode size. This is achieved by defining the equivalent step-index (ESI) profile in the following way: $n_{core} \equiv n_{glass}$, $n_{clad} \equiv n_{FSM}$ and $A_{eff}^{FM}(ESI) \equiv A_{eff}^{FM}(HF)$ (see Sections 1.4.2, 5.7.1 and 5.7.2 for more details). Note that several techniques are used to evaluate the A_{eff}^{FM} and the bend loss of the conventional fibres considered in Section 5.7. For accurate comparisons between the two fibre types, the models applied to holey fibres are applied to the conventional fibres also. Although simpler techniques exist for step-index fibres, for the purposes of a comparative study it is preferable to use the same set of assumptions for every fibre considered. However, for calculations that involve a wide range of structures, conventional techniques are instead used to evaluate these parameters, as discussed in Section 5.7.3. Initial results from this comparative study show that the bending losses of holey fibres can be up to 60% less than step-index fibres that are equivalent in terms of A_{eff}^{FM} and n_{clad} at 1064 nm. However, further study indicates that the practice of selecting ESI parameters by defining $n_{core} \equiv n_{glass}$, $n_{clad} \equiv n_{FSM}$ and $A_{eff}^{FM}(ESI) \equiv A_{eff}^{FM}(HF)$ does not result in an accurate representation of the modal properties of a holey fibre even though the core radius is not chosen in an arbitrary manner. By instead considering holey and conventional fibres with similar mode areas that are both close to cut-off, it can be seen that the optimal bending losses for single-mode operation are similar in similarly sized holey and conventional fibres. Furthermore, it is shown that the maximum practical mode area for strictly single-mode guidance is also found to be $\approx 450\ \mu m^2$, as for holey fibres.

Despite these similarities, at first sight the structural dependencies on R_c^{FM} and A_{eff}^{FM} seem very different in holey and conventional fibres as there are striking differences between the contour plots of A_{eff}^{FM} and R_c^{FM} for holey and conventional fibres, shown in Fig. 5.36 and Fig. 5.35 respectively. For example, at a given value of n_{clad} in a conventional fibre, there exists a minimum A_{eff}^{FM}. In addition, for the step-index fibres, the bend loss improves for increasing values of core radius. This seems contrary to the situation observed in holey

fibres, in which no minimum is observed for any particular value of d/Λ, and bend loss is seen to worsen for increasing values of Λ. However, the majority of differences in the contour plots of A_{eff}^{FM} and R_c^{FM} in these two fibre types arise from the fact that n_{clad} and a are not equivalent to d/Λ and Λ. Indeed, far more similar functionalities can be achieved by instead using n_{FSM} and $\Lambda - d/2$ as the axes for the contour plot of the holey fibre parameters, demonstrating that the fundamental modes of holey and step-index fibres possess similar parametric dependencies on A_{eff}^{FM} and bend loss.

The similarities between the bending losses of higher-order modes in holey and conventional fibres are explored in Section 5.7.6. In this study, the bending losses of the higher-order modes present in one holey and one approximately equivalent conventional fibre are investigated. The results of this study demonstrate that the higher-order modes of the ESI fibre suffer greater bending losses than those of the holey fibre, despite the fact that the bending losses of the fundamental mode in both fibres are similar. For applications in which it is necessary to selectively guide only the fundamental mode by inducing a bend, step-index fibre may have an advantage. However, note that these conclusions are drawn from only one fibre pair and should be treated with caution since the method of defining an ESI profile has been shown to be inaccurate. Also note that the scalar version of the orthogonal function method was used to evaluate the higher-order modal fields in both of these examples and the bend loss predictions are, as a result, only approximate. However, full vectorial calculations of the propagation constants of these fibres indicate that the scalar approximation is valid.

In summary, the results presented in this chapter have shown that large-mode-area holey fibres possess similar bending losses to their conventional counterparts at 1064 nm and that the maximum tolerable mode area (defined for $R_c^{FM} < 15$ cm) is approximately 450 μm^2 in both fibre types for strictly single-mode guidance. However, it is well known that the bending losses of conventional fibre types can be improved by using a more complex refractive index profiles [123, 155, 156]. In the following chapter this theme is explored for holey fibres, in which the refractive index profile can be adjusted simply by altering the stacking elements in the preform.

Chapter 6

Improved holey fibre designs for 1064 nm

6.1 Introduction

As mentioned in Section 1.2.4, holey fibres are typically fabricated by heating and pulling a preform into fibre using a conventional fibre drawing tower. The preform of a silica holey fibre is typically constructed by stacking many silica capillaries around a central solid silica rod. In the final fibre, the central solid rod forms the core, and the surrounding glass capillaries in the preform form the microstructured cladding. This method of fabrication permits a high level of design flexibility. For example, the fibre design can be radically altered simply by choosing different stacking elements in the preform. This approach has been used to create multiple-core holey fibres [33], in which multiple solid rods in the preform form many separate cores in the final fibre, and birefringent holey fibres in which a 2-fold symmetric core is formed by two adjacent rods in the preform [56]. The multiple-rod approach has also been used to create large-mode-area holey fibres with triangular shaped cores by using three adjacent rods in the preform [34]. It has also been shown that this triangular core fibre structure can be used to enlarge the mode area by $\approx 30\%$ without increasing the bending losses [34]. Due to the fact that bending losses limit the maximum mode sizes that are practical to use, this preliminary work indicates that multiple-rod holey fibres may offer a route towards practical single-mode fibres with larger mode areas than can be created with traditional single-rod designs.

In this chapter, I aim to explore the reasons why multiple-rod holey fibres offer improved bending losses relative to single-rod designs and to accurately quantify the magnitude of

the improvement in bend loss in the single-mode regime at 1064 nm using the numerical techniques described in Chapter 3.

6.2 Holey fibres with cores formed by multiple rods

6.2.1 Introduction

As mentioned above, results have shown that by using three adjacent rods to form the core of a holey fibre, instead of the usual one, it is possible to enlarge the mode area by $\approx 30\%$ without increasing the bending losses [34]. In Ref. [34] this improvement is assessed via an experimental study of the bending losses of two holey fibres: (1) a traditional single-rod core holey fibre with $\Lambda = 10$ μm and $d/\Lambda = 0.45$ and (2) a triangular three-rod core holey fibre with $\Lambda = 6$ μm and $d/\Lambda = 0.25$. The authors state that both fibres represent the upper limit of endlessly single-mode guidance. The maximum permissable d/Λ for single-mode guidance in holey fibres with multiple-rod cores decreases with each additional rod due to the fact that the core size has increased relative to Λ. This is discussed in more detail in Section 6.2.2. The triangular core holey fibre ($\triangle$HF) has an $A_{eff}^{FM} \approx 30$ % larger than the conventional holey fibre (HF), but the bending losses of the two fibres are shown to be similar for a bend radius of 16 cm. In Ref. [34] the authors also present a qualitative theoretical analysis of the bending losses in these two fibre types, which further supports these initial experimental results. However, the two fibres considered within the study from Ref. [34], described above, are not endlessly single-mode. Using Eq. 5.1, which has been validated against the theoretical methods used here, it can be seen that the conventional holey fibre with $\Lambda = 10$ μm and $d/\Lambda = 0.45$ is only single-mode for wavelengths $\gtrsim 1.7$ μm. There is currently no simple method of assessing the modedness of a $\triangle$HF structure, but my calculations presented in Section 7.5 show that higher-order modes are present at 308 nm in $\triangle$HF structures with $\Lambda \approx 5$ μm and $d/\Lambda = 0.2$. Since the $\triangle$HF reported in Ref. [34] has larger values of both Λ and d/Λ, these results imply that this fibre cannot be endlessly single-mode.

The study presented in Ref. [34] highlighted that these more complex holey fibre designs have the potential to improve bend loss in single-mode structures, but the information presented to date does not allow the advantages of these novel structures to be accurately quantified, which is essential to enable this technique to be optimised for future fibre design. The theoretical methods developed in Chapter 3 have been shown to be capable of

accurately predicting the bending losses of holey fibres (for example, see Sections 5.4 and 5.6). Since there are very few limitations on the types of fibre that can be modelled using these techniques, these methods can be applied to △HFs. My aim is to quantify the improvement in bending losses that these △HF structures can offer for single-mode operation by comparing the bending losses of pairs of holey fibres and △HFs that are equivalent in terms of A_{eff}^{FM} and n_{FSM} at 1064 nm.

6.2.2 △HF structures: single-mode considerations

As mentioned in Section 6.2.1, the maximum value of d/Λ that results in single-mode guidance, ($(d/\Lambda)_c$), decreases in structures in which more than one rod is used to form the core. For example, in order to create a single-rod and multiple-rod holey fibre with the same mode area, a smaller value of Λ must be used in the latter. If the same value of d/Λ is used in both fibres, the effective cladding index (n_{FSM}) of the multiple-rod fibre will be lower than that of the holey fibre for any given wavelength, even though the air-filling fraction is identical, since the overall structure scale is smaller for the multiple-rod fibre (and the wavelength of light has not changed). This fact can be seen in Fig. 6.1 (b), which shows a contour plot of n_{FSM} as a function of Λ and d/Λ at 1064 nm and demonstrates that n_{FSM} decreases towards larger values of d/Λ and smaller values of Λ for a fixed wavelength (1064 nm). (Fig. 6.1 (b) was created from the data points of n_{FSM} shown in Fig. 6.1 (a).) Since the core index (pure silica) is identical in both fibre types, it is necessary to use smaller values of d/Λ in a multiple-rod holey fibre relative to a single-rod holey fibre to achieve single-mode guidance.

As an example, we consider the case of a holey fibre with $\Lambda = 12.0$ μm and $d/\Lambda = 0.40$, which has an A_{eff}^{FM} of ≈ 190 μm^2 at 1064 nm. In order to define a △HF structure that is equivalent to this holey fibre in terms of A_{eff}^{FM} and n_{FSM}, both Λ and d/Λ must be decreased from these original parameters, as explained above. The n_{FSM} of the holey fibre with $\Lambda = 12.0$ μm and $d/\Lambda = 0.40$ is indicated on Fig. 6.1 (b) by the circular blue point. To maintain n_{FSM} whilst decreasing Λ and d/Λ, one must follow the same contour level as the original holey fibre down the graph, until the parameters of a △HF fibre with an equivalent A_{eff}^{FM} is reached. (Note that A_{eff}^{FM} is not indicated on Fig. 6.1 (b)). This is represented by the blue triangular point on Fig. 6.1 (b), which represents an (approximately) equivalent triangular-core holey fibre (△HF), in which three rods form the core, with $\Lambda = 7.4$ μm, $d/\Lambda = 0.2$, and $A_{eff}^{FM} \approx 190$ μm^2.

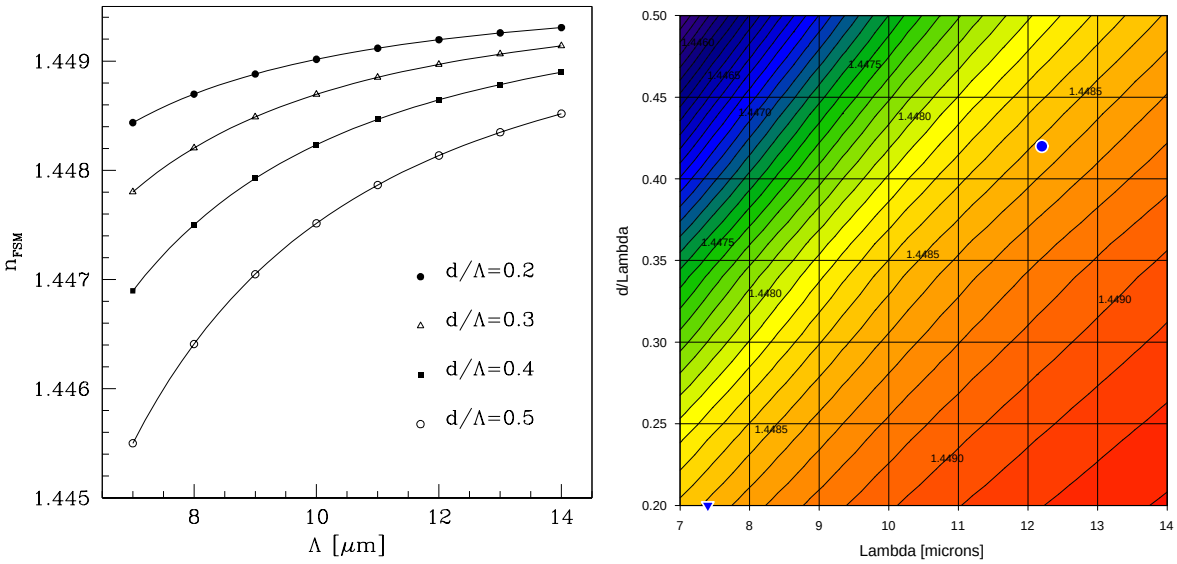

(a) (b)

Figure 6.1: (a) Effective index of the fundamental space filling mode (n_{FSM}) of the holey fibre cladding as a function of Λ, for a range of holes sizes: $0.2 < d/\Lambda < 0.5$ at 1064 nm (calculated using BandSOLVE^{TM} [134]). (b) Contour plot of n_{FSM} generated from the data in (a) as a function of Λ and d/Λ.

6.2.3 △HF: Theoretical comparisons with equivalent holey fibre structures

In this section, the bending losses of three pairs of holey fibres and △HFs that are each approximately equivalent in terms of A_{eff}^{FM} and n_{FSM} are evaluated and compared. The effective cladding index n_{FSM} of the fibres are calculated using the commercial software BandSOLVE^{TM}, as described in Section 3.5 [134]. The parameters of these six fibres are shown in Table 6.1. The three holey fibres have Λ=12.0, 15.2 and 17.7 μm, with $d/\Lambda = 0.4$, and the equivalent △HFs have $\Lambda = 7.4$, 9.5 and 11.0 μm respectively, with $d/\Lambda = 0.2$. The A_{eff}^{FM} of these three fibre pairs are $\approx$ 190, 300 and 400 μm^2 respectively. The fundamental modal intensity profile of each fibre is shown in Fig. 6.2. Note that the modes of the three △HFs reflect the core geometry, being somewhat triangular in shape. However, these △HF modes can still be well approximated by a Gaussian function, with an overlap of $\approx 97.7\%$. In comparison, the overlap between the three holey fibre modes in Fig. 6.2 and a pure Gaussian function of optimum width is $\approx 98.0\%$. This overlap is evaluated numerically, using the overlap integral defined in Eq. 3.11, where E_b is replaced by a Gaussian function.

Finding an equivalent △HF is not a trivial process, and can involve the calculation of A_{eff}^{FM} and n_{FSM} for many structures. I have found that the n_{FSM} of a holey fibre with $d/\Lambda =$

Table 6.1: Predicted modal properties for a range of holey fibres. △HF refers to triangular core structures.

Fibre	Λ [μm]	d [μm]	d/Λ	n_{FSM}	Modes	C_{loss}^{HOM} for 5 rings [dB/m]	A_{eff}^{FM} [μm^2]	R_c^{FM} [cm]
HF_D	12.0	4.80	0.40	1.448645	SM	-	188	4.0
HF_J	15.2	6.08	0.40	1.448989	SM	-	293	8.3
HF_K	17.7	7.08	0.40	1.449165	SM	-	390	12.7
$\triangle HF_M$	7.40	1.48	0.20	1.448552	MM	18.6	191	2.8-3.0
$\triangle HF_N$	9.50	1.90	0.20	1.448953	MM	-	305	5.8-6.2
$\triangle HF_O$	11.00	2.20	0.20	1.449117	MM	8.10	401	8.8-9.3

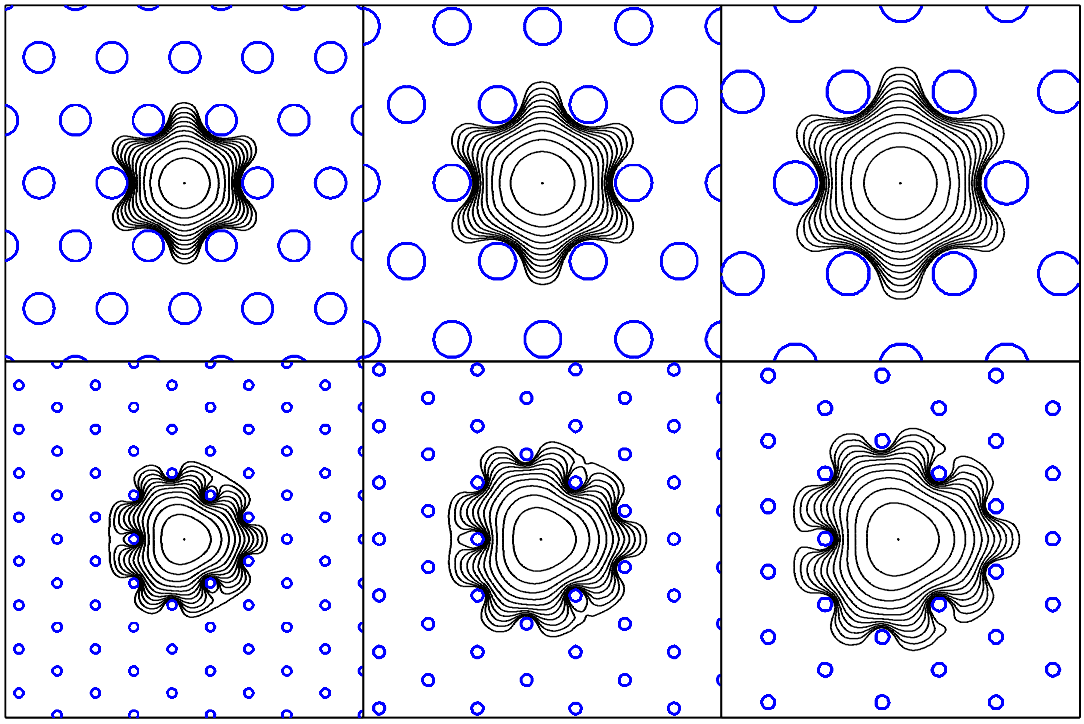

(a) (b) (c)

Figure 6.2: Modal intensity profiles for some of the holey fibres and △HFs listed in Table 6.1, together with the refractive index profile of the fibre. Top row: (a) fibre HF_D, (b) fibre HF_J and (c) fibre HF_K. Bottom row: (a) fibre $\triangle HF_M$, (b) fibre $\triangle HF_N$ and (c) fibre $\triangle HF_O$. The dimensions of the box in each modal plot are 60 μm × 60 μm. The contour lines are separated by 2 dB

0.4 can be approximately matched by a △HF of similar mode area with $d/\Lambda = 0.2$. However, the fibre pairs created in this way are only approximately equivalent in terms of n_{FSM}. Preliminary calculations (based on the V-number of an equivalent step-index fibre of each

$\triangle$HF), showed the $\triangle$HFs in Table 6.1 to be single-mode, with V=2.34. However, further, more accurate calculations have shown that each of the $\triangle$HFs are actually multi-mode. This was determined by Vittoria Finazzi using the multipole technique described in Section 5.13. However, the higher-order modes present in the $\triangle$HFs possess large confinement losses for 5 rings of holes, and as such would not be guided in any significant length of fibre (Confinement losses for fibres $\triangle HF_M$ and $\triangle HF_O$ are shown in Table 6.1 for 5 rings of holes.). However, to ensure that the confinement losses are negligible for the fundamental mode it is estimated that approximately $8-9$ rings of holes would be required for $\triangle$HFs. This would, of course, also act to lower the confinement losses of any higher-order modes present. However, the $\triangle$HFs considered here are only just multi-mode, and single-mode guidance can be achieved with a modest reduction in hole size (early estimates indicate $d/\Lambda = 0.18$ should be sufficient). As a result, the bending losses of the fundamental mode of these structures should not be greatly different than those of truly single-mode $\triangle$HFs, and as such should still give a reasonable approximation of the improvement offered by using a $\triangle$HF structure instead of a single-rod core design at 1064 nm.

The critical bend radii of the fundamental modes (R_c^{FM}) of the 6 holey fibres considered here are shown in Table 6.1. Note that two values of R_c^{FM} are shown for the $\triangle$HFs in Table 6.1, which correspond to bends in the $\phi = 60^o$ and $\phi = 0^o$ directions respectively. In Section 4.5, a study into the bending losses of standard single-rod holey fibres at 1550 nm as a function of the angular orientation (ϕ) of the fibre found that the bend loss varied little with respect to ϕ. Indeed, for all the single-rod holey fibres considered in this thesis, the variation in R_c^{FM} with respect to ϕ is calculated to be less than 2%. As a result, the value of R_c^{FM} for holey fibres is only ever reported for a bend in the direction of $\phi = 0^o$. However, the variation in R_c^{FM} with respect to ϕ is found to be greater in the $\triangle$HFs than in the single-rod holey fibres as a result of the fact that the core geometry is less circularly symmetric. The calculated bend loss as a function of ϕ is shown for holey fibre HF_J and the equivalent triangular core fibre $\triangle HF_N$ in Fig. 6.3 (a) and (b) for bend radii of 7.6 and 5.0 cm respectively. Both fibres have $A_{eff}^{FM} \approx 300\ \mu m^2$ at 1064 nm. The solid circles in Fig. 6.3 (a) and (b) represent the bend loss in dB per loop, whilst the open circles indicate the relative positions of the innermost ring of holes within the fibre. These plots demonstrate that the bending losses reflect the refractive index profile and that the degree of variation in loss is greater for the $\triangle$HF relative to the holey fibre. For the holey fibre HF_J, the calculated values of R_c^{FM} vary by less than 1%, which is in agreement with all previous results and

illustrates that the effect of ϕ on the bend loss may be safely ignored in single-rod holey fibres. For the equivalent $\triangle$HF however, the calculated values of R_c^{FM} vary by $\approx 6\%$ at 1064 nm. The maximum and minimum values of R_c^{FM} for this $\triangle$HF occur for bends in the $\phi = 0^o$ and $\phi = 60^o$ directions respectively, which correspond to the values shown in Table 6.1.

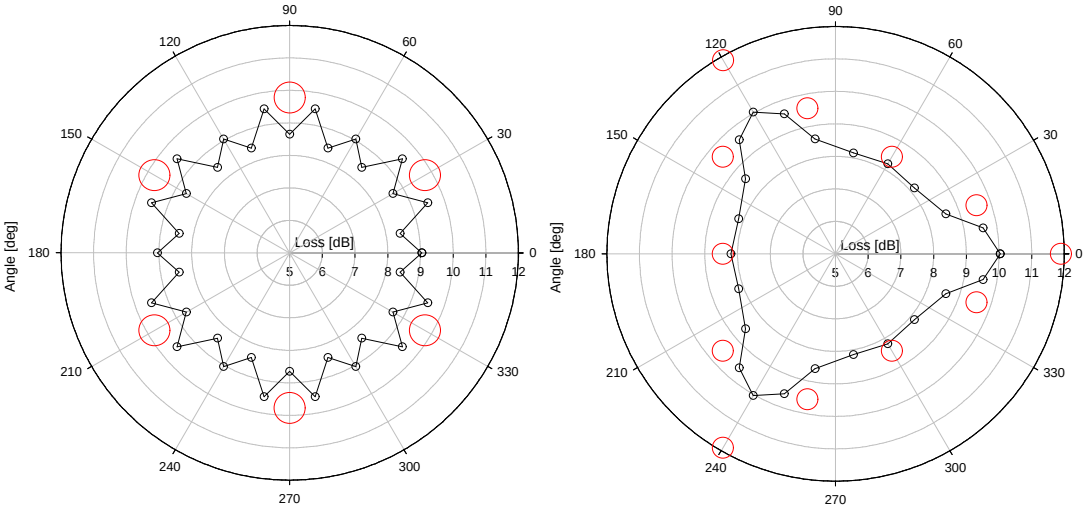

(a) (b)

Figure 6.3: Black points and line shows the bend loss as a function of angular orientation for (a) holey fibre HF_J (R_c^{FM} = 8.3 cm) and (b) Triangular core holey fibre $\triangle HF_N$ (R_c^{FM} = 6.0 cm) at 1064 nm. The respective bend radii for each data set shown in (a) and (b) are 7.6 and 5.0 cm. The red circles show the relative positions of the innermost holes in each case.

Assuming that the triangular core fibres $\triangle HF_M$, $\triangle HF_N$ and $\triangle HF_O$ are bent in the $\phi = 0^o$ direction, which represents the worst bend loss for these fibres, the R_c^{FM} is equal to $\approx$ 75, 75 and 73% of that of the holey fibres HF_D, HF_J, and HF_K respectively. This corresponds to a relative increase in A_{eff}^{FM} of $\approx 30\%$ for a $\triangle$HF structure with the same R_c^{FM} as a traditional single-rod holey fibre at 1064 nm. This is consistent with the results presented in Ref. [34], in which a $\triangle$HF was shown to exhibit similar bending losses to a single-rod holey fibre at 16 cm, despite a 30% larger A_{eff}^{FM}.

However, recall that the $\triangle$HFs considered here are not truly single-mode, and as such represent values of R_c^{FM} lower than that of a truly single-mode $\triangle$HF. A better like-for-like comparison can be made for the smallest of the three $\triangle$HFs using results from Section 5.3, in which a detailed study into the bending losses of holey fibres with $A_{eff}^{FM} \approx 190\ \mu m^2$ was presented. The parameters of holey fibre HF_F from Section 5.3 are a better match to fibre $\triangle HF_M$ than fibre HF_D. Note that fibre HF_F is a multi-mode structure in which the higher-

order modes are found to suffer high confinement losses for 6 rings of holes. The details of fibre HF_F are included in Table 6.2.3 together with fibre $\triangle HF_M$. For this more equivalent fibre pair, we see that the R_c^{FM} of the $\triangle$HF is $\approx 81\%$ of the holey fibre. Assuming a similar ratio for all mode areas, this corresponds to a relative increase in A_{eff}^{FM} of $\approx 15-20\%$ for a $\triangle$HF structure with the same R_c^{FM} as a traditional single-rod holey fibre at 1064 nm.

Table 6.2: Predicted modal properties for holey fibre HF_F and the equivalent $\triangle HF_M$.

Fibre	Λ [μm]	d [μm]	d/Λ	n_{FSM}	Modes	C_{loss}^{HOM} for 6 rings [dB/m]	A_{eff}^{FM} [μm^2]	R_c^{FM} [cm]
HF_F	12.56	5.53	0.44	1.448566	MM	3.4	189	3.7
Fibre	Λ [μm]	d [μm]	d/Λ	n_{FSM}	Modes	C_{loss}^{HOM} for 5 rings [dB/m]	A_{eff}^{FM} [μm^2]	R_c^{FM} [cm]
$\triangle HF_M$	7.40	1.48	0.20	1.448552	MM	18.6	191	2.8-3.0

Since fibre HF_F and $\triangle HF_M$ possess similar mode areas and core and cladding indices, the differences in the bend loss of these two fibres must result solely from the cladding geometry, with the many smaller, closely spaced holes of the $\triangle$HF being more effective at confining the bent mode to the core than the fewer, larger, and more widely spaced holes of the single-rod holey fibre. By comparing the mode shape of the bent fibre for these two fibres we see that this is indeed the case. The modal intensity profiles for fibres HF_F and fibre $\triangle HF_M$, which both possess $A_{eff}^{FM} \approx 190$ μm^2 at 1064 nm are shown in Figs 6.4 (a) and (b) respectively for bends in the $\phi = 0^o$ direction. The bend radius is 3.5 cm in each case. The shape of the bent modes in Figs 6.4 (a) and (b) show conclusively that the $\triangle$HF structure is better able to confine the bent mode to the fibre core than the single-rod holey fibre at a given bend radius. Based on the calculations in this section I would estimate that the maximum practical A_{eff}^{FM} (defined for $R_c^{FM} = 15$ cm) for a $\triangle$HF at 1064 nm is ≈ 550 μm^2, which is $\approx 20\%$ larger than the estimate of the maximum tolerable mode size for a conventional single-rod holey fibre, which was determined to be ≈ 450 μm^2 in Section 5.5.2.

However, it is important to note that while the $\triangle$HF structure offers improved bending losses, more elements are required in a $\triangle$HF preform in order to achieve the same level of confinement losses as a similarly sized single-rod holey fibre. This results from the fact that the confinement losses of the fundamental mode in any holey fibre are inversely proportional

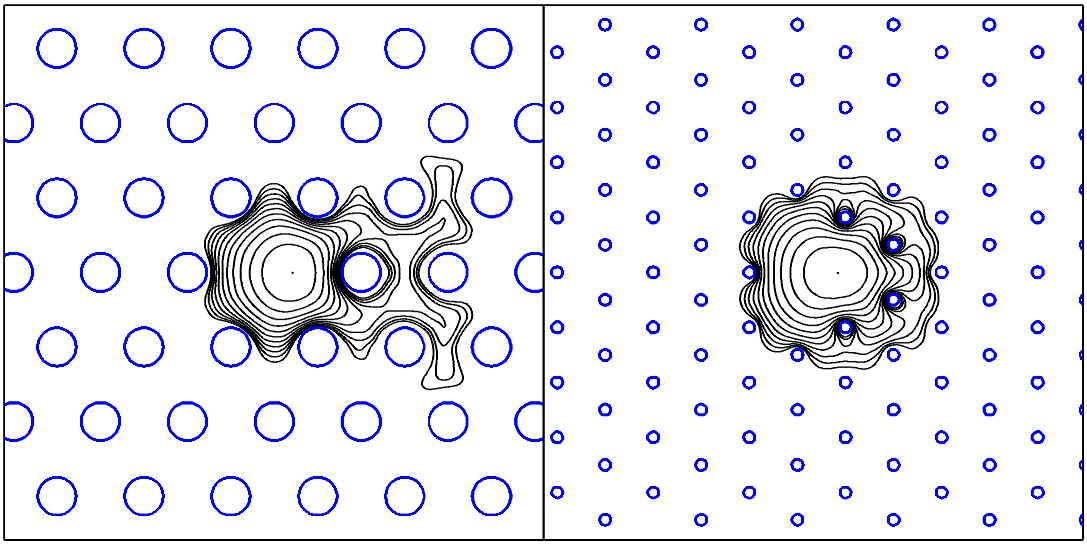

(a) (b)

Figure 6.4: Modal intensity profile for (a) fibre HF_F ($R_c^{FM} = 3.7$ cm) and (b) fibre $\triangle HF_M$ ($R_c^{FM} = 3.0$ cm for $\phi = 0^o$) at 1064 nm for bends in the $\phi = 0^o$ direction. The bend radius is 3.5 cm in each case. Contour levels are separated by 2 dB.

to the width of the cladding region and proportional to d/Λ. For example, the confinement losses of the fundamental mode of a holey fibre with $\Lambda = 12$ μm and $d/\Lambda = 0.4$ at 1064 nm are negligible ($< 1 \times 10^8$ dB/m) for 6 to 7 rings of holes, which are typical. To achieve a similar level of mode confinement in a similarly sized $\triangle$HF ($\Lambda = 7.4$ μm, d/Λ=0.2), 8 to 9 rings of holes are required. This equates to over 200 additional elements within the preform. Consequently, the fabrication process is more time consuming for $\triangle$HFs, but as shown in the following section, large-mode area $\triangle$HFs are practical to fabricate.

6.2.4 Experimental work

In this section, some preliminarily work is presented that demonstrates that large-mode area single-mode $\triangle$HF fibres can be fabricated. The fibres in this section have been fabricated by John Hayes at the ORC from rods and tubes of F300 synthetic silica glass from Heraeus Tenevo AG.

As mentioned above, in a $\triangle$HF, more than 200 additional elements are required in order to achieve similar levels of mode confinement as in a similarly sized single-rod holey fibre. We initially thought that a good way of reducing the number of elements required may be to use a double-clad structure, with larger values of Λ and d/Λ in the outer cladding. An example of this structure is shown in Fig. 6.5 (a), which is an optical microscope image of

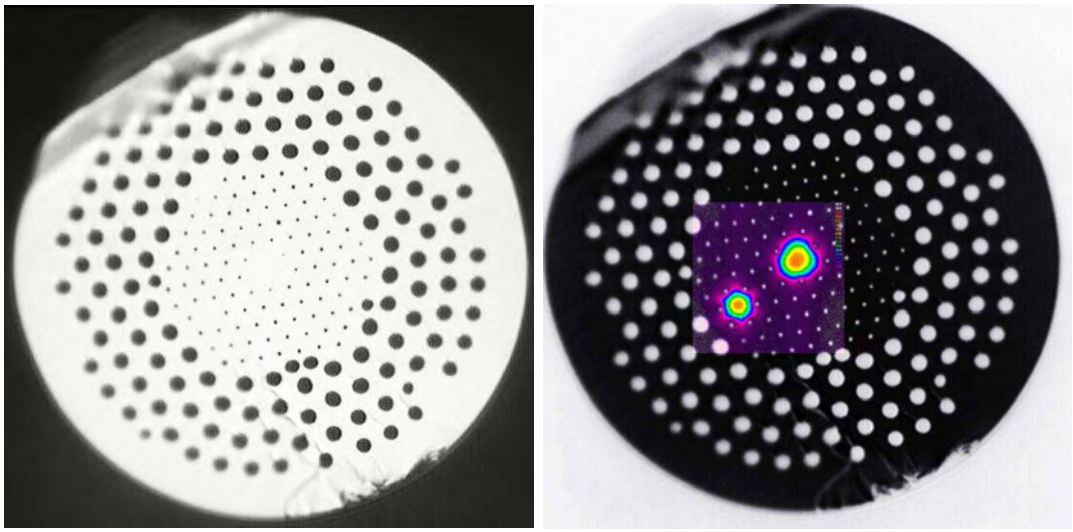

(a) (b)

Figure 6.5: (a) Optical microscope image of fibre $\triangle HF_{444}$. Inner cladding: $\Lambda \approx 11.4$ μm and $d/\Lambda \approx 0.2$ with 5 rings of holes. Outer cladding: $\Lambda \approx 19$ μm and $d/\Lambda \approx 0.4$ with 4 rings of holes. (b) Near-field modal profiles for the two cores present in this fibre superimposed on a negative colour image of (a)

fibre $\triangle HF_{444}$. In the preform of fibre $\triangle HF_{444}$, 4 rings of capillaries with dimensions designed to produce $\Lambda \approx 18$ μm and $d/\Lambda \approx 0.4$ in the final fibre were stacked around a central region containing 5 rings of capillaries with dimensions designed to produce $\Lambda \approx 11$ μm and $d/\Lambda \approx 0.2$ in the final fibre. In this way, the number of additional elements required (relative to that in a typical single-rod holey fibre preform) is reduced to approximately 70. The parameters of the outer cladding were chosen such that the n_{FSM} remains constant (see Fig. 6.1 (b)). As such, the modedness of the fibre should not be adversely affected by the change in cladding parameters. The final fibre shown in Fig. 6.5 (a) has an inner cladding with $\Lambda \approx 11.4$ μm and $d/\Lambda \approx 0.2$ with 5 rings of holes and a outer cladding with $\Lambda \approx 19$ μm and $d/\Lambda \approx 0.4$ with 4 rings of holes. Whilst this method was successful in creating the $\triangle$HF fibre shown in Fig. 6.5 (a), the hole arrangement is somewhat disorganised due to the fact that the two cladding parameters do not stack neatly together. In addition, note that one hole in the penultimate ring in the inner cladding has collapsed during fabrication, effectively creating an additional core. The near-field mode profiles of the two cores present in this fibre are shown in Fig. 6.5 (b), superimposed on a negative colour image of the fibre. Using the CCD camera to monitor the output from this fibre, as shown in Fig. 6.6, it was established that the two cores could not be independently addressed via the launch conditions at 1064 nm. As a result, it was not possible to perform quantitative characterisations of A_{eff}^{FM} or R_c^{FM} using the techniques outlined in Section 4. However, the near-field modal

profiles of the central, triangular, core can be used to demonstrate the similarities in mode shape between the actual fibre and the numerical predictions, as shown in Fig. 6.7 (a) and (b) for 1064 nm respectively.

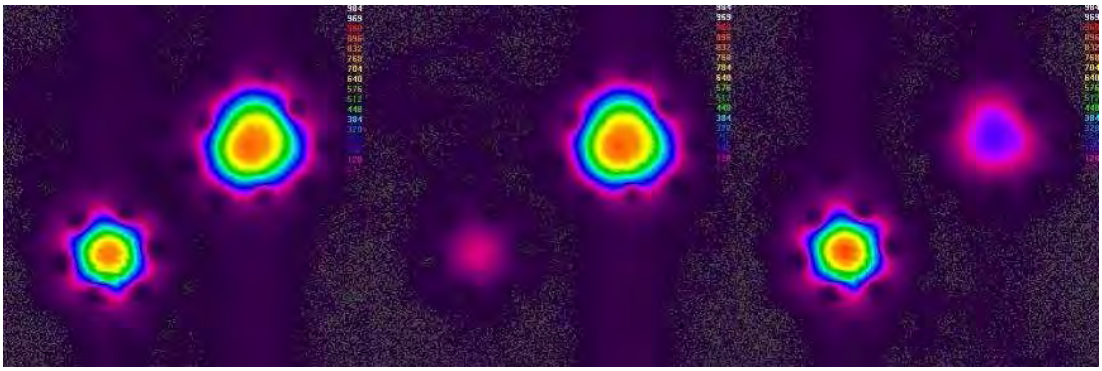

(a) (b) (c)

Figure 6.6: Near-field modal profiles images with a COHU 7512 silicon CCD camera for different launch conditions.

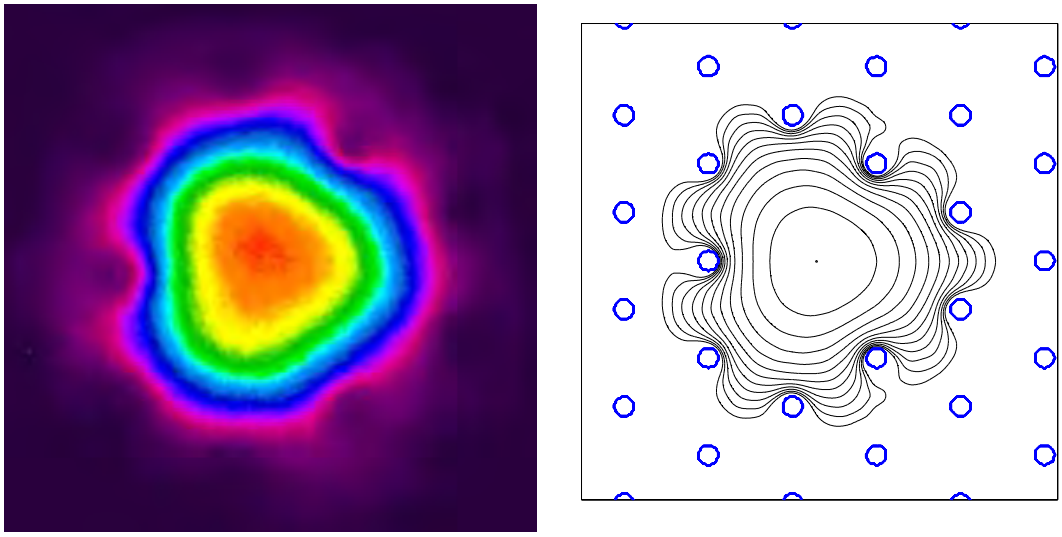

(a) (b)

Figure 6.7: (a) Near-field modal profile of central triangular core in fibre $\triangle HF_{444}$, imaged with a COHU 7512 silicon CCD camera. (b) Predicted mode profile for similar $\triangle$HF with $\Lambda = 11.0$ μm and $d/\Lambda = 0.2$.

Due to the fact that the double-clad approach results in a somewhat disorganised hole arrangement, a simple 9 ring $\triangle$HF structure was attempted. This involves stacking many more capillaries in the preform (approximately 130 more) than the double-clad approach, and is thus more time consuming. However, the uniformity of the final fibre is greatly improved, as is shown by the SEM of $\triangle HF_{498}$ in Fig. 6.8.

Fibre $\triangle HF_{498}$, shown in Fig. 6.8 has $\Lambda \approx 11$ μm and $d/\Lambda \approx 0.1$ with 9 rings of holes.

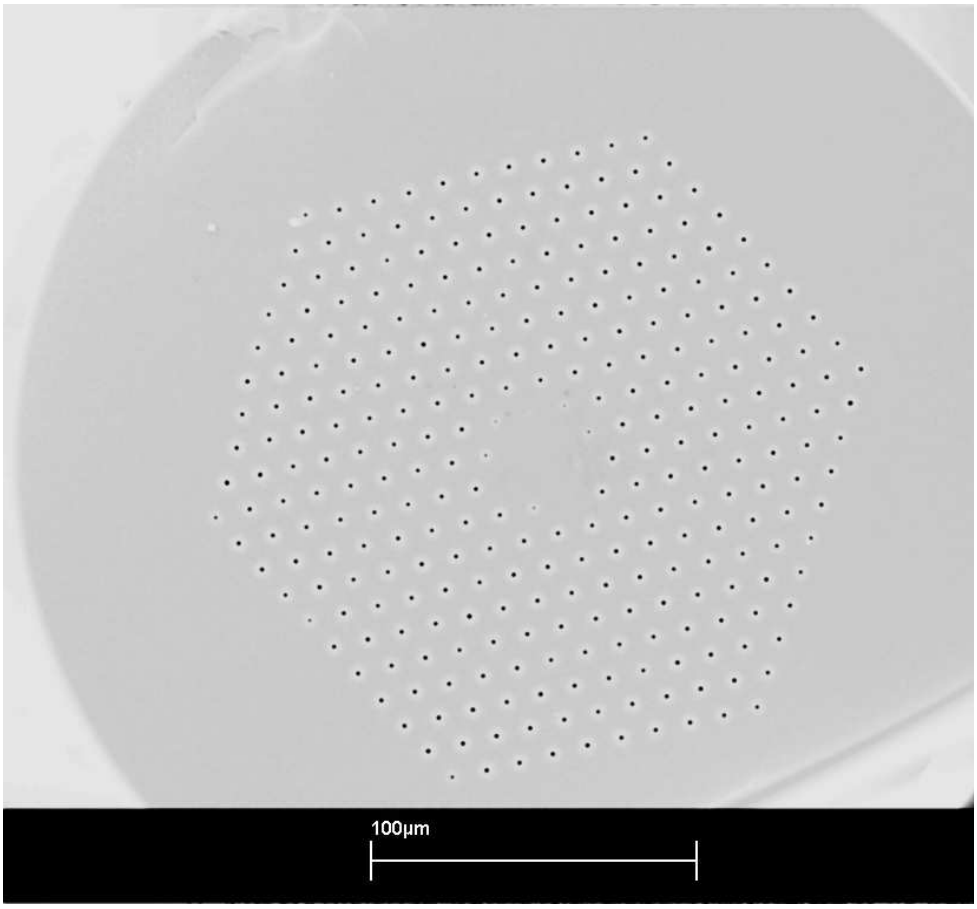

Figure 6.8: SEM image of fibre $\triangle HF_{498}$ fabricated at the ORC with $\Lambda \approx 11$ μm and $d/\Lambda \approx 0.06 - 0.1$ with 10 rings of holes.

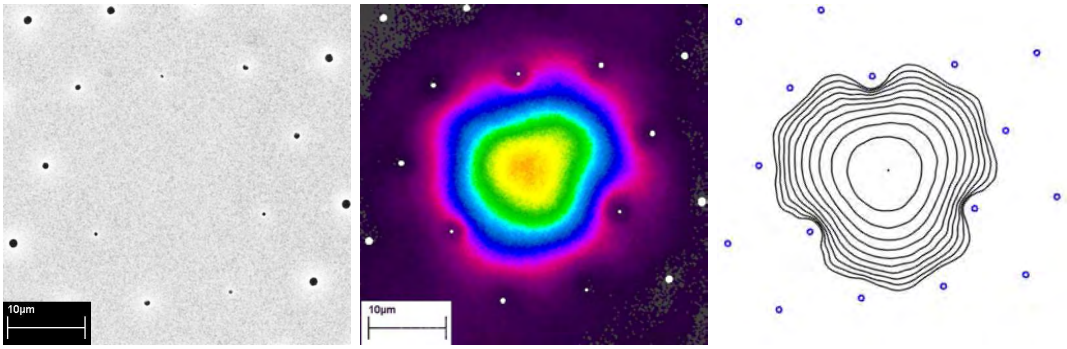

(a) (b) (c)

Figure 6.9: (a) SEM image of core region of fibre $\triangle HF_{498}$ fabricated at the ORC with $\Lambda \approx 11$ μm and $d/\Lambda \approx 0.06 - 0.1$. (b) Near-field modal intensity profile at 1064 nm imaged with a CCD camera. Mode is superimposed on SEM image shown in (a). (c) Predicted modal intensity profile for $\Lambda \approx 11$ μm and $d/\Lambda = 0.06$. Contour levels are separated by 2 dB.

A larger scale SEM image of the core region of fibre $\triangle HF_{498}$ is shown in Fig. 6.9 (a), which shows that some of the holes in the innermost ring are smaller, with a minimum

$d/\Lambda \approx 0.06$. The A_{eff}^{FM} of this fibre is measured at 1064 nm to be ≈ 560 μm^2. This is consistent with numerical simulations, which predict an A_{eff}^{FM} in the range of 530-570 μm^2 for $d/\Lambda = 0.06 - 0.1$. The mode profile of this fibre at 1064 nm, imaged with a COHU 7512 silicon CCD camera, is shown in Fig. 6.9 (b), which is superimposed on the fibre SEM of the core region, shown separately in Fig. 6.9 (a). This mode profile demonstrates the effect of the differing hole sizes in the inner ring of holes on the mode shape. Relative to the idealised predicted mode, which is shown in Fig. 6.9 (c) for $d/\Lambda = 0.06$, we can see that the differing hole sizes act to distort the mode shape, but that the mode is still well confined to the core.

Unfortunately, only a short length of this fibre was available for characterisation due to problems in the coating stage of fabrication during this trial. However, for the length of fibre studied (≈ 70 cm), the power fluctuations that are often exhibited in large-mode-area holey fibres with high bending losses were not observed. This suggest that this structure is practical in terms of bend loss. However, more work is obviously required in order to confirm this, which is currently ongoing at the ORC.

Note that preliminary results for a new $\triangle$HF fabricated at the ORC show that for a single-mode $\triangle$HF with an A_{eff}^{FM} of ≈ 480 μm^2 at 1064 nm, the R_c^{FM} is ≈ 13 cm. From Fig. 5.33, it can be seen that the best possible value of R_c^{FM} for a single-rod holey fibre with this mode area is expected to be ≈ 16 cm, demonstrating a $\approx 20\%$ improvement in R_c^{FM}, which is in excellent agreement with the numerical predictions presented in Section 6.2.3 for the closely matched fibre pair HF_F and $\triangle HF_M$.

6.3 Discussion and conclusion

Preliminary work has shown that multiple-rod holey fibres may offer a route towards practical single-mode fibres with larger mode areas than can be created with traditional single-rod designs [34]. This study highlighted that more complex holey fibre designs, in which three adjacent rods are used to form the core, have the potential to improve bend loss in single-mode structures. However, the advantages of these novel $\triangle$HF structures have not been accurately quantified, which is essential to enable this technique to be optimised for future fibre design.

In order to quantify the improvement in bending losses that these $\triangle$HF structures can offer for single-mode operation it is necessary to compare the bending losses of pairs of holey fibres and $\triangle$HFs that are equivalent in terms of A_{eff}^{FM} and n_{FSM} at 1064 nm. For a given mode area, the overall scale of the microstructured cladding must be decreased relative to a conventional single-rod holey fibre. As a result, the relative hole size in the $\triangle$HF must also decrease in order to maintain single-mode guidance. This is explained in detail in Section 6.2.2. It is found here that holey fibres with $d/\Lambda = 0.4$ are approximately equivalent in terms of A_{eff}^{FM} and n_{FSM} to $\triangle$HF structures with $d/\Lambda = 0.2$ and values of Λ approximately 60% that of the single-rod design. However, note that the fibre pairs created in this way are only approximately equivalent in terms of A_{eff}^{FM} and n_{FSM} and that finding structures that are well matched in terms of these two parameters is not a trivial process.

In this chapter, the bending losses of three pairs of holey fibres and $\triangle$HF that are approximately equivalent are evaluated using the methods developed in Chapter 3, which have very few restrictions on the type of fibre profile than can be modelled. Initial results demonstrate that $\triangle$HF structures offer a $\approx 30\%$ improvement in mode area for the same value of R_c^{FM} as a single-rod holey fibre at 1064 nm. This is consistent with the findings presented in Ref. [34]. However, further investigation, considering more closely matched structures, indicates that the level of improvement in mode area is probably less than this, at around 15-20%, allowing the maximum tolerable A_{eff}^{FM} for strict single-mode operation to rise to $\approx 500\ \mu m^2$ at 1064 nm. In addition, the numerical methods used here, which are capable of considering the effect on the bend loss of the angular orientation of the fibre structure, show that for $\triangle$HFs, the R_c^{FM} can vary by $\approx 6\%$ (Note that previous results quoted for percentage improvements in loss are calculated assuming worst-case orientation). This is much larger than the variation in bend loss with respect to angular orientation predicted for single-rod holey fibres, which is typically less than 1% at 1064 nm.

Furthermore, it is important to note that while the △HF structure offers improved bending losses, over 200 additional elements are required within the preform in order to achieve the same level of confinement losses as a similarly sized single-rod holey fibre. Consequently, the fabrication process is more time consuming for △HFs, but as shown in Section 6.2.4, large-mode area △HFs are practical to fabricate. Preliminary results for a single-mode △HF with an A_{eff}^{FM} of ≈ 480 μm^2 at 1064 nm show that R_c^{FM} is ≈ 13 cm. From Fig. 5.33, it can be seen that the best possible value of R_c^{FM} for a single-rod holey fibre with this mode area is expected to be ≈ 16 cm, demonstrating a $\approx 20\%$ improvement in R_c^{FM}, which is in excellent agreement with the numerical predications presented in this chapter.

Note that it has been demonstrated that the bending losses of conventional solid fibres can be improved by introducing a dip and subsequent rise in the refractive index profile of the fibre cladding [123]. The dip in refractive index improves the bend loss of the fibre and the rise in index compensates for the associated reduction in the cladding index. This method has been shown to significantly improve the bending losses of step-index fibres and could be applied to a holey fibre simply by using different sized capillaries in the preform. In this way, it should be possible to create a holey fibre with different hole sizes that would act to modulate the effective cladding index of the holey fibre. This is something that has not been considered here for reasons of time, but will be investigated in future studies.

Up until this point, the work presented in this thesis has focussed on single-wavelength characterisation of holey fibres at near-IR wavelengths, which has allowed our theoretical methods to be validated. However, the novel property of endlessly single-mode guidance offers obvious advantages for broad-band applications. In addition, this property may also present a more practical route towards large-mode-area, single-mode fibres for short wavelength applications, in which conventional fibre fabrication techniques are limited by the low values of NA required to maintain single-mode guidance. However, while the bending losses of holey and conventional fibres have been shown to be similar at 1550 nm and 1064 nm, it is unclear how this relationship may change towards shorter wavelengths. The relationships between holey fibre structure and bend loss as a function of wavelength are explored in the following chapter.

Chapter 7

Large-mode-area holey fibres for UV to mid-IR wavelengths

7.1 Introduction

One of the most well known properties of silica holey fibres is their ability to remain single-mode at all wavelengths [4]. This property, known as endlessly single-mode guidance has been shown to occur in holey fibres for $d/\Lambda \lesssim 0.4$ [19]. This property offers obvious advantages for broad-band applications but also presents a practical route towards large-mode-area, single-mode fibres for short wavelength applications. However, as discussed in Section 2.3, the bending losses of a holey fibre increase towards both long and short wavelengths, and it is these losses that limit the window of useful wavelength operation.

It has been shown empirically that the mid-point in wavelength between the long and short bend loss edges in a silica holey fibre is approximately given by $\Lambda/2$ [32]. Each of the large-mode-area holey fibres considered within this study possess $\Lambda > 7$ μm, which corresponds to mid-point wavelengths $\gtrsim 3.5$ μm. However, the theoretical minimum loss in silica glass is bounded by Rayleigh scattering in the short wavelength limit and infrared absorption in the long wavelength limit, rising to ≈ 100 dB/km at ≈ 300 nm and ≈ 2.2 μm. For high power and transmission applications, where fibre losses are critical, silica fibres are therefore only useful for wavelengths between ≈ 300 nm and 2.2 μm [157, 158] (see Section C.2 for some examples of spectral attenuation in silica glass). Consequently, we do not expect to observe the long wavelength loss edge in any of the holey fibres considered here. This implies that the maximum tolerable $A_{\text{eff}}^{\text{FM}}$ decreases with decreasing wavelength for large-mode, single-mode silica holey fibres for all wavelengths of interest. Whilst this is

well known, it is not currently understood what impact this will have on the practicality of fibres designed for UV transmission, which represents the shortest wavelengths that are transparent in silica. In this chapter, I aim to use the numerical techniques developed in Chapter 3, which have been shown to be capable of accurate predictions (see Chapter 5), to investigate whether the bending losses in holey fibres at 308 nm are prohibitively large. The results from this study are presented in Section 7.2.1.

As discussed in Section 2.3, conventional step-index fibres exhibit only one bend loss edge at long wavelengths. This results from the fact that the NA decreases with increasing wavelength as the mode extends further into the cladding, resulting in a more weakly guided mode that suffers greater bend loss. Towards short wavelengths, the NA of a conventional fibre increases, and the bending losses fall. At first sight, this suggests that conventional fibres are more bend resistant than holey fibres towards short wavelengths. However, whilst a holey fibre can guide a single-mode over a broad wavelength range, the number of modes guided in a step-index fibre increases rapidly towards short wavelengths. In order to make a meaningful comparison between the bending losses of the two fibre types in the single-mode regime it is necessary to consider a different *equivalent* step-index (ESI) fibre for every wavelength at which the holey fibre is considered. A comparison between the bending losses of a holey fibre and a number of equivalent conventional fibres is undertaken in Sections 7.2.1 and 7.2.2 for a holey fibre with $\Lambda = 7.5$ μm and $d/\Lambda = 0.4$ in the wavelength range 308 nm to 1550 nm.

The effect of the holey fibre structure on A_{eff}^{FM} and R_c^{FM} has been studied extensively at 1064 nm using both numerical and experimental techniques in Chapter 5. In Sections 7.2.3 and 7.3, some of this work is extended to consider the effect of wavelength also. In Section 7.2.3, the results from a numerical study into the effect of the fibre structure on A_{eff}^{FM} and R_c^{FM} for wavelengths between 308 to 1600 nm are presented for a selection of fibre structures with $60 \approx A_{eff}^{FM} \lesssim 400$. This numerical work is complemented by the experimental results presented in Section 7.3, which further validate the numerical technique developed here and give additional information regarding the modedness of holey fibres as a function of wavelength.

An approach that is often used when studying holey fibre properties as a function of wavelength is to assume a constant refractive index of silica so that Maxwell's equations become scale invariant [4, 16, 17]. This approach is advantageous as it vastly reduces the number of calculations required to evaluate a wide range of fibre structures over many

different wavelengths. However, bend loss is a sensitive function of the fibre parameters and this scaling approach has not previously been evaluated for bend loss. In Section 7.4, numerical and experimental results from previous sections are used to evaluate the accuracy of this scaling technique for bend loss in holey fibres.

In Chapter 6, the triangular core holey fibre ($\triangle$HF) was shown to exhibit improved bending losses relative to traditional holey fibre designs at 1064 nm. In Section 7.5, I look briefly at how the improvement offered by the $\triangle$HF structure varies as a function of wavelength and consider if this type of structure offers a way of accessing larger mode areas towards short wavelengths.

Up until this point, all work in this thesis has focussed solely on silica holey fibres. However, holey fibres can also be made from mid-IR transmitting materials such as tellurite and chalcogenide glasses, also known as soft-glasses [22, 25, 24]. In Section 7.6 of this chapter, I look briefly at the modal properties of large-mode-area holey fibres made from a high index compound soft glass, called Gallium-Lanthanum-Sulphide (GLS). Conventional fibre fabrication techniques have met with limited success due to problems matching core and cladding materials and also due to crystallisation at the core/cladding interface. Since holey fibres can be made from a single-material these problems can be minimised, allowing the creation of GLS fibres for mid-IR applications. However, like most soft-glasses, GLS is highly nonlinear. Indeed, GLS possesses an n_2 that is approximately 100 times that of silica glass [159]. For transmission applications nonlinear effects are an unwanted phenomena. The nonlinear effects can be minimised by using large mode areas and it is therefore necessary to assess the maximum practical mode sized that can be achieved in a GLS holey fibre. In Section 7.6, I use the numerical techniques outlined in Chapter 3, to gain an understanding of the range of practical mode areas that can be created in holey fibres made from GLS glass at a wavelength of 2.2 μm.

7.2 Numerical study of the bending losses of holey and conventional fibres from UV to IR wavelengths

7.2.1 Holey fibres vs step-index fibres at 308 nm

As mentioned in the introduction above, although holey fibres can be endlessly single-mode, the bend loss worsens towards short wavelengths, increasingly limiting the mode areas that are practical to use. This will obviously have the greatest impact on fibres designed for

UV transmission, which represents the shortest wavelengths that are transparent in silica. In this section, I use the numerical techniques developed in Chapter 3, which have been shown to be capable of accurate predictions (See Chapter 5), to investigate if the bending losses in holey fibres at 308 nm are prohibitively large. A holey fibre with a modest A_{eff}^{FM} of 66 μm^2 at 308 nm is chosen for this study, as the bending losses at this wavelength are expected to be much larger than those at 1064 nm, which have been studied in the previous two chapters. A comparison between the bending losses of this holey fibre and equivalent step-index fibres is also presented. Note that the bending losses of the ESI fibres within this section are calculated using the numerical techniques developed in Chapter 3 to enable direct comparison of the absolute values.

Note that the attenuation losses in silica glass increase sharply towards UV wavelengths due to Rayleigh scattering. This intrinsic loss can be reduced by using a silica glass with a high OH content, down to values of ≈ 0.1 dB/m for wavelengths around 300 nm [160] (see Section C.2). This level of loss can be acceptable for lengths of fibre up to a few 10's of metres. However, this is not considered in any detail here.

The structural parameters and modal properties of the holey fibre HF_P studied in this section are listed in Table 7.1. Fibre HF_P has $\Lambda = 7.5$ μm and $d/\Lambda = 0.4$ and as such is endlessly single-mode. The critical bend radius of the fundamental mode, R_c^{FM}, is found to be 10.6 cm at 308 nm. Whilst this is not prohibitive, it is considerably larger than would be expected at 1064 nm, which would be < 2 cm. For example, from Fig. 5.33 we can see that this value of R_c^{FM} would equate to $A_{eff}^{FM} \approx 370$ μm^2 at 1064 nm for a structure with $\Lambda \approx 17.5$ μm. This large value of R_c^{FM} indicates that mode areas greater than ≈ 100 μm^2 are likely to be impractical at 308 nm.

Table 7.1: Predicted modal properties for the endlessly single-mode holey fibre HF_P: $\Lambda = 7.5$ μm, $d/\Lambda = 0.4$ and some step-index fibres at 308 nm.

Fibre	Λ [nm]	d/Λ	n_{FSM}	NA	A_{eff}^{FM} [μm^2]	R_c^{FM} [cm]
HF_P	7.5	0.4	1.485420	0.025	66	10.6
Fibre	a [μm]	n_{clad}	V	NA	A_{eff}^{FM} [μm^2]	R_c^{FM} [cm]
ESI_P	3.40	1.485420	1.76	0.025	68	> 20
SIF_P	4.20	1.485374	2.40	0.028	66	11.8

As described in Section 5.7.1, the bending losses of holey fibres can be compared to those

of conventional step-index fibres only by considering step-index fibres that are equivalent to the holey fibres in question. Throughout this thesis the parameters of equivalent step-index (ESI) fibres have been calculated by assuming $n_{clad} \equiv n_{FSM}$, $n_{core} = n_{glass}$ and by choosing the core radius such that the ESI fibre possesses the same value of A_{eff}^{FM} as the holey fibre to which the comparison is to be made. However, at this short wavelength it is not always possible to create a step-index fibre that is equivalent to a holey fibre in terms of A_{eff}^{FM} and n_{FSM}. The reasons for this can be seen in Fig. 7.1, which shows a contour plot of A_{eff}^{FM} as a function of core radius (a) and n_{clad} for step-index fibres at 308 nm. The red line in Fig. 7.1 indicates the V=2.405 boundary between single-mode and multi-mode guidance and the two red dots correspond to the parameters of the two step-index fibres in Table 7.1. As in Section 5.7, we see that there exists a minimum value of A_{eff}^{FM} for each value of n_{clad}. A direct result of this minimum in the A_{eff}^{FM} is that it is not possible to create a step-index fibre with the same cladding index and A_{eff}^{FM} as holey fibre HF_P ($n_{FSM} = 1.485420$, $A_{eff}^{FM} = 66\ \mu m^2$). From Fig. 7.1 it can be seen that the minimum A_{eff}^{FM} for a step-index fibre with $n_{clad} = 1.485420$ at 308 nm $\approx 68\ \mu m^2$, which is represented by fibre ESI_P in Table 7.1, for which $R_c^{FM} > 20$ cm. This value of R_c^{FM} is significantly larger than for the equivalent holey fibre, even though both fibres possess identical values of NA. (Note that the NA for a holey fibre is defined here as $\sqrt{{n_{glass}}^2 - {n_{FSM}}^2}$).

However, the V-parameter of fibre ESI_P is considerably less than 2.405, which is the minimum requirement for single-mode operation in a step-index fibre. Since holey fibre HF_P is close to cut-off ($(d/\Lambda)_c \approx 0.416$ for this fibre at 308 nm) it seems more sensible to compare the bending losses of holey fibre HF_P with the bending losses of a step-index fibre that is also close to cut-off. As a result, I choose a second method of defining an ESI fibre for holey fibres close to cut-off; once again $n_{core} = n_{glass}$, but n_{clad} and the core radius (a) are both free parameters. The core radius and n_{clad} are then chosen to match the A_{eff}^{FM} of the holey fibre with the condition that V=2.4. In this way, fibre SIF_P is defined to be roughly equivalent to holey fibre HF_P and represents the best bending losses that can be achieved in a truly single-mode step-index fibre. The R_c^{FM} of this second ESI fibre is 11.8 cm and is comparable with the R_c^{FM} of holey fibre HF_P, which is 10.6 cm at 308 nm, as shown in Table 7.1. In addition, the fact that holey fibre HF_P is endlessly single-mode, together with the fact that the bending losses improve towards longer wavelengths, mean that fibre HF_P can be defined as a practical fibre for all wavelengths longer than 308 nm. The A_{eff}^{FM} and the bend loss of this fibre is further explored in the following section.

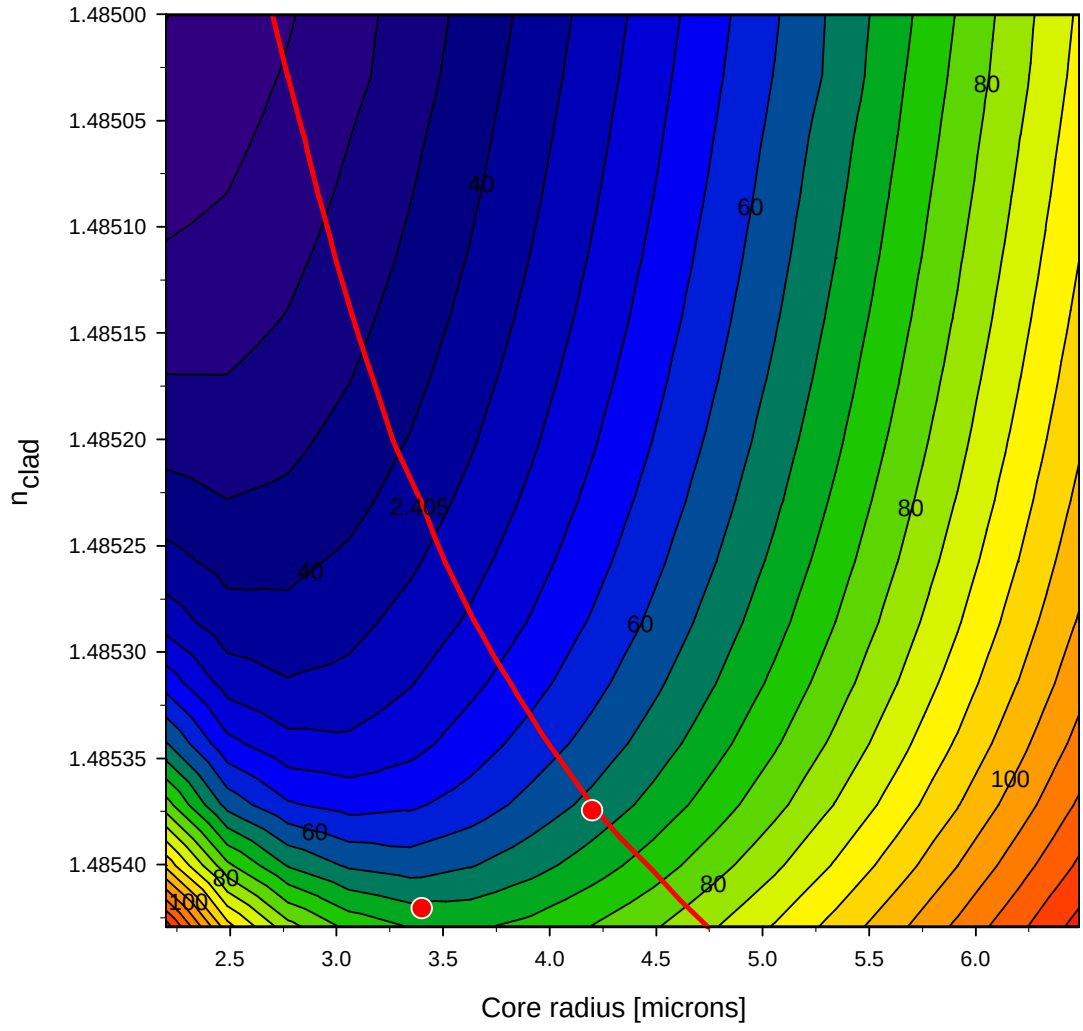

Figure 7.1: Contour plot of A_{eff}^{FM} as a function of n_{clad} and core radius (a) for conventional step-index fibres at 308 nm. The red line shows the V=2.405 single-mode boundary. The red dots show the parameters of the step-index fibres ESI_P and SIF_P in Table 7.1.

7.2.2 Holey fibres vs step-index fibres at 308 to 1550 nm

In this section I aim to extend the work presented in Sections 5.7.3 and 7.2.1 to include wavelengths within the range 308 nm to 1550 nm. In this way, I aim to investigate the similarities in the spectral dependencies on mode area and bend loss for single-mode holey and equivalent conventional fibres. This is accomplished by comparing the bending losses of a holey fibre with $\Lambda = 7.5$ μm and $d/\Lambda = 0.4$ (fibre HF_P), with those of equivalent step-index (ESI) fibres in the wavelength range 308 to 1550 nm. An ESI fibre is, by definition, only equivalent to any particular holey fibre at a single wavelength, and in order to make a meaningful comparison between the bending losses of the two fibre types it is necessary to consider a different *equivalent* step-index (ESI) fibre for every wavelength. Here, the

bending losses of holey fibre HF_P and a different ESI fibre are evaluated at five discreet wavelengths of 308, 633, 1064, 1310 and 1550 nm. The parameters of each ESI fibre studied in this section are found using the second ESI method described above, in which the V-parameter is set to 2.4 and n_{FSM} and the core radius are chosen to match the A_{eff}^{FM} to that of the comparison holey fibre. (Note that the results for 308 nm are repeated from the previous section.) This technique is chosen as a result of the fact that the usual method of defining an ESI fibre, by matching the cladding index, can result in a very weakly guided ESI fibre (as described in the previous section). Since a holey fibre with a d/Λ of 0.4 is considered to be close to cut-off at all wavelengths, a fairer comparison is to consider step-index fibres with similar mode area that are also close to cut-off. In this way, the bending losses of holey fibre HF_P can be compared to the best possible bend loss attainable in a single-mode step-index fibre with similar values of A_{eff}^{FM} for each wavelength considered. As in Section 5.7.3, the A_{eff}^{FM} and V-parameter for each ESI fibre is calculated using the exact solutions from Ref. [53] and the bending losses are evaluated using an approximate model from Ref. [126], which is described by Eq. 5.3 and the surrounding text. This method is found to overestimate R_c^{FM} by $\approx 20-50\%$ at 1064 nm. However, since the aim of this section is not to compare absolute values, but to explore the similarities in the parametric dependencies for these two fibre types, this technique is perfectly adequate.

The predicted modal properties for the endlessly single-mode holey fibre HF_P, which has $\Lambda = 7.5$ μm and $d/\Lambda = 0.4$, are shown in Table 7.2 for 5 wavelengths in the range 308 - 1550 nm. Note that the A_{eff}^{FM} is relatively constant over the wavelength range considered; from 308 to 1550 nm, the A_{eff}^{FM} increases from 66 μm^2 to 81 μm^2, corresponding to an increase of $\approx 20\%$ over more than 1200 nm. (The A_{eff}^{FM} of this fibre is plotted as a function of wavelength in Fig. 7.5). Also shown in Table 7.2 is the NA of holey fibre HF_P, defined here as $\sqrt{{n_{glass}}^2 - {n_{FSM}}^2}$. These values show that the NA increases with wavelength, from ≈ 0.03 at 308 nm to ≈ 0.12 at 1550 nm. This increase in NA leads to a dramatic drop in R_c^{FM} towards long wavelengths, from 10.6 cm at 308 nm to 0.60 cm at 1550 nm.

The predicted modal properties for the five ESI fibres considered here are shown in Table 7.1. Each ESI fibre corresponds to one of the five wavelengths at which the bending losses of holey fibre HF_P were evaluated, as shown in Table 7.2. The fibre parameters and modal properties listed in Table 7.1 show that in order to match the A_{eff}^{FM} of fibre HF_P for V=2.4, the core radius of the ESI fibres must increase with wavelength. Note that the choice of V=2.4 results from the desire to compare the bending losses of holey and

Table 7.2: Predicted modal properties for the endlessly single-mode holey fibre HF_P: $\Lambda = 7.5$ μm, $d/\Lambda = 0.4$ at five different wavelengths. Modal properties are calculated using the numerical techniques presented in Chapter 3.

λ [nm]	n_{FSM}	NA	A_{eff}^{FM} [μm^2]	R_c^{FM} [cm]
308	1.485420	0.025	66	10.6
633	1.456118	0.051	73	3.00
1064	1.447227	0.084	77	1.22
1310	1.443266	0.101	79	0.86
1550	1.439213	0.118	81	0.60

conventional fibres that are both close to cut-off, as discussed above and in Section 7.2.1. In addition, we see that the NA increases from ≈ 0.03 to ≈ 0.13 from 308 to 1550 nm, mimicking the behaviour of the holey fibre. Moreover, we find that the functional form of R_c^{FM} is also imitated, decreasing from 14.8 cm at 308 nm to 0.58 cm at 1550 nm.

Table 7.3: Predicted modal properties for five different step-index fibres which possess V=2.4 and are equivalent to holey fibre HF_P ($\Lambda = 7.5$ μm, $d/\Lambda = 0.4$) in terms of A_{eff}^{FM} at five discreet wavelengths. A_{eff}^{FM} and V are calculated using the exact solutions from Ref. [53] and R_c^{FM} is evaluated using Eq. 5.3.

λ [nm]	a [μm]	n_{clad}	NA	V	A_{eff}^{FM} [μm^2]	R_c^{FM} [cm]
308	4.20	1.485374	0.028	2.40	66	14.58
633	4.45	1.456000	0.054	2.40	73	3.52
1064	4.56	1.446890	0.089	2.40	77	1.23
1310	4.63	1.442750	0.110	2.40	79	0.80
1550	4.67	1.438500	0.130	2.40	81	0.58

The predicted values of R_c^{FM} for holey fibre HF_P and the five ESI fibres are shown in Fig. 7.2 as a function of wavelength (open and closed circles respectively). This plot demonstrates that the bending losses for both the holey fibre and the ESI fibres are very similar as a function of wavelength, indicating that the parametric dependencies on mode area and bend loss are similar for these two fibre types as a function of wavelength. In addition, the fact that comparative studies in Sections 5.7.3 and 7.2.1 have shown that the absolute values of R_c^{FM} for fibres close to cut-off are similar at both 308 and 1064 nm, indicates that the performance of single-mode holey and conventional step-index fibres, in

terms of mode area and bend loss, is similar at any given wavelength.

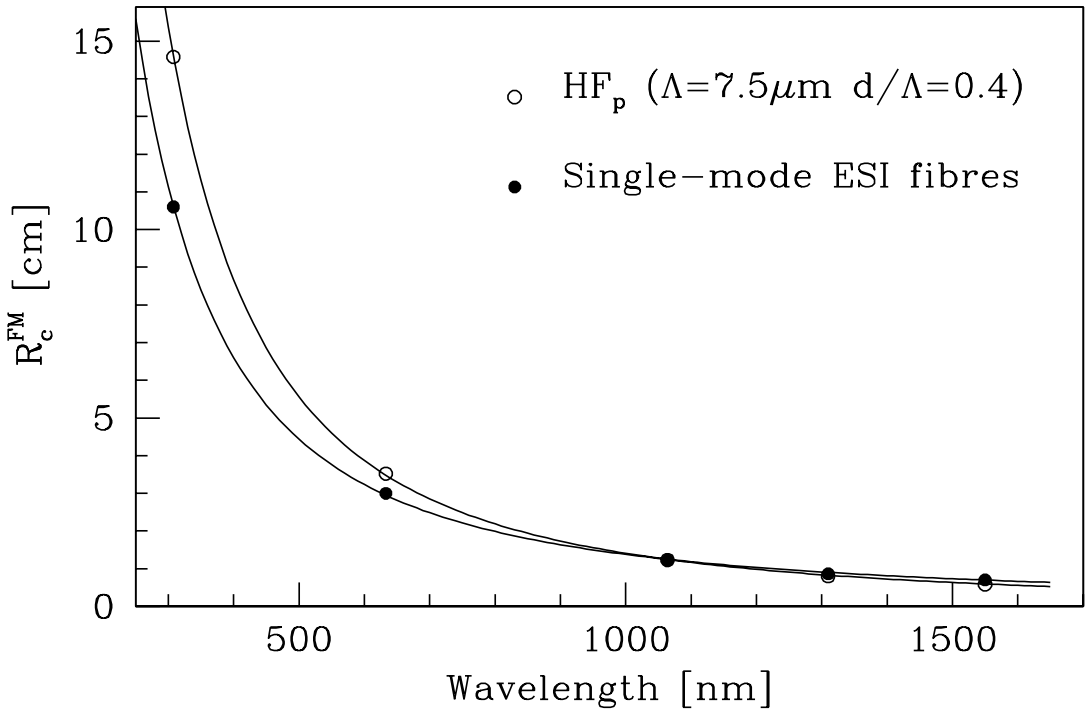

Figure 7.2: Critical bend radius (R_c^{FM}) as a function of wavelength. Open circles correspond to the endlessly single-mode holey fibre HF_P and the closed circles each correspond to a different ESI fibre at each wavelength. At each wavelength, an ESI fibre is chosen that possesses V=2.4 and the same mode area as the holey fibre HF_P at that given wavelength. The holey and ESI fibre parameters are shown in Tables 7.2 and 7.3.

In this section the effect of wavelength has been considered on the bending losses of a holey fibre with $\Lambda = 7.5$ μm and $d/\Lambda = 0.4$ which has a rather conservative mode area of ≈ 70 μm^2. This study has shown that this fibre is practical in terms of bending losses ($R_c^{FM} < 15$ cm) in the range 308 to 1550 nm. In the following section I look at the effect of wavelength on the bending losses of a selection of holey fibres with A_{eff}^{FM} up to 400 μm^2.

7.2.3 The effect of the holey fibre structure

In this section the bending losses of seven different holey fibres are investigated as a function of wavelength using the numerical techniques developed in Chapter 3 in order to aid understanding of how the fibre geometry influences the bend loss as a function of wavelength. The fibre parameters of each of the seven holey fibres studied in this section are listed in Table 7.4 together with the value of A_{eff}^{FM} at 1064 nm. The fibres in Table 7.4 have been chosen in order to represent the range of holey fibres that has been considered within

this thesis. These seven fibres have $7.5\mu\text{m} < \Lambda < 17.7$ μm, $0.28 < d/\Lambda < 0.45$ and $A_{\text{eff}}^{\text{FM}}$ at 1064 nm ranging from 66 μm^2 to 390 μm^2. Note that all these fibres are endlessly single-mode with the exception of fibre HF_G, which has been shown to be effectively single-mode at 1064 nm (and hence for all wavelengths greater than 1064 nm), in Section 5.3, due to the fact that the higher-order modes possess high confinement losses.

Table 7.4: Predicted modal properties for a range of single-mode large-mode-area holey fibres.

Fibre	Λ [μm]	d [μm]	d/Λ	$A_{\text{eff}}^{\text{FM}}$@1064 nm [$\mu\text{m}^2$]
HF_P	7.50	3.00	0.40	66
HF_B	10.70	3.04	0.28	190
HF_C	11.30	3.84	0.34	190
HF_D	12.00	4.80	0.40	188
HF_G	12.70	5.73	0.45	188
HF_J	15.20	6.60	0.40	293
HF_K	17.70	7.64	0.40	390

As previously discussed in Section 2.3, bending losses in a holey fibre increase towards both long and short wavelengths, and it is these losses that limit the window of useful wavelength operation. However, it has been shown empirically that the mid-point in wavelength between the long and short bend loss edges in a silica holey fibre is approximately given by $\Lambda/2$ [32]. For the fibres considered here this corresponds to mid-point wavelengths ranging from ≈ 3.8 to ≈ 8.9 μm. Since even the smallest of these is well beyond those wavelengths that are transparent in silica, we do not expect to observe the long wavelength loss edge in any of the holey fibres considered here. This implies that the bend loss of every holey fibre considered here should increase as the wavelength decreases, for all wavelengths considered.

The bending losses of these seven holey fibres are plotted in two graphs, Fig. 7.3, which includes all fibres in the selection with $A_{\text{eff}}^{\text{FM}} \approx 190$ μm^2 shown for 600 nm$\lesssim \lambda \lesssim$1600 nm and Fig. 7.4, which includes all fibres in the selection with $d/\Lambda = 0.4$ shown for 300 nm$\lesssim \lambda \lesssim$1600 nm. These two figures show that the bending losses increase towards short wavelengths for each holey fibre considered here. In addition, it can be seen that as d/Λ increases and as Λ decreases, the magnitude of bend loss decreases at all wavelengths, widening the window of useful wavelength operation. This demonstrates that the optimum way of creating a single-mode holey fibre with minimal bending losses is to use $d/\Lambda = (d/\Lambda)_c$

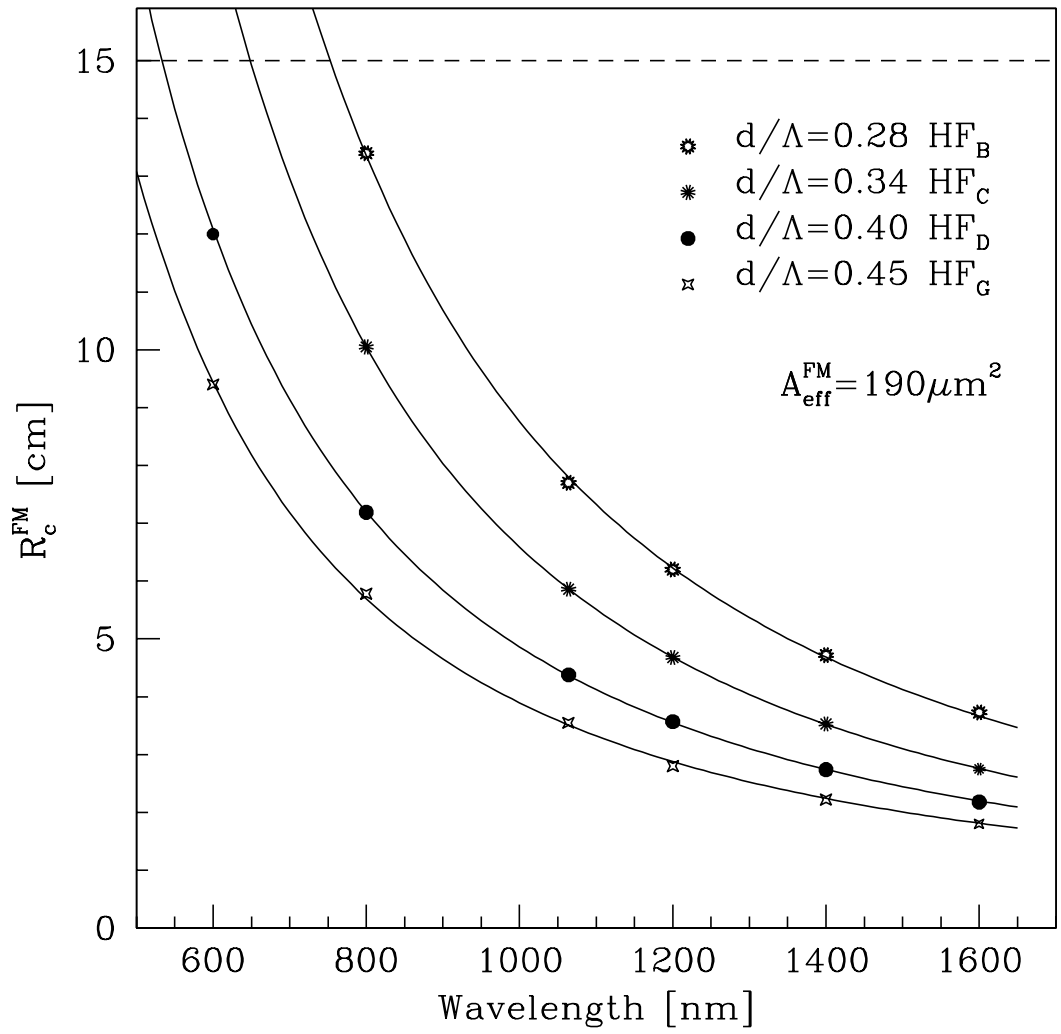

Figure 7.3: Critical bend radius (R_c^{FM}) as a function of wavelength for four holey fibres with $A_{eff}^{FM} \approx 190\ \mu m^2$ at 1064 nm. The dashed line marks the position of $R_c^{FM} = 15$ cm. The fibre parameters are shown in Tables 7.4.

(where $(d/\Lambda)_c$ is the maximum value of d/Λ that results in single-mode guidance as defined in Eq. 5.2) for any wavelength of interest. The value of Λ chosen then simply defines the A_{eff}^{FM}. Note that these findings correspond to what may be expected intuitively, since it is equivalent to using a high NA in a conventional fibre.

In Table 7.4, the A_{eff}^{FM} is given only for a wavelength of 1064 nm. This is a reasonable approximation for all wavelengths considered here due to the fact that the mode size in large-mode-area silica holey fibres is found to be weakly dependent on the wavelength [17],[132]. The A_{eff}^{FM} of the four fibres in Fig. 7.4 are plotted in Fig. 7.5 to illustrate this point. Over the wavelength range shown, which spans more than 1200 nm, the A_{eff}^{FM} of each of the four

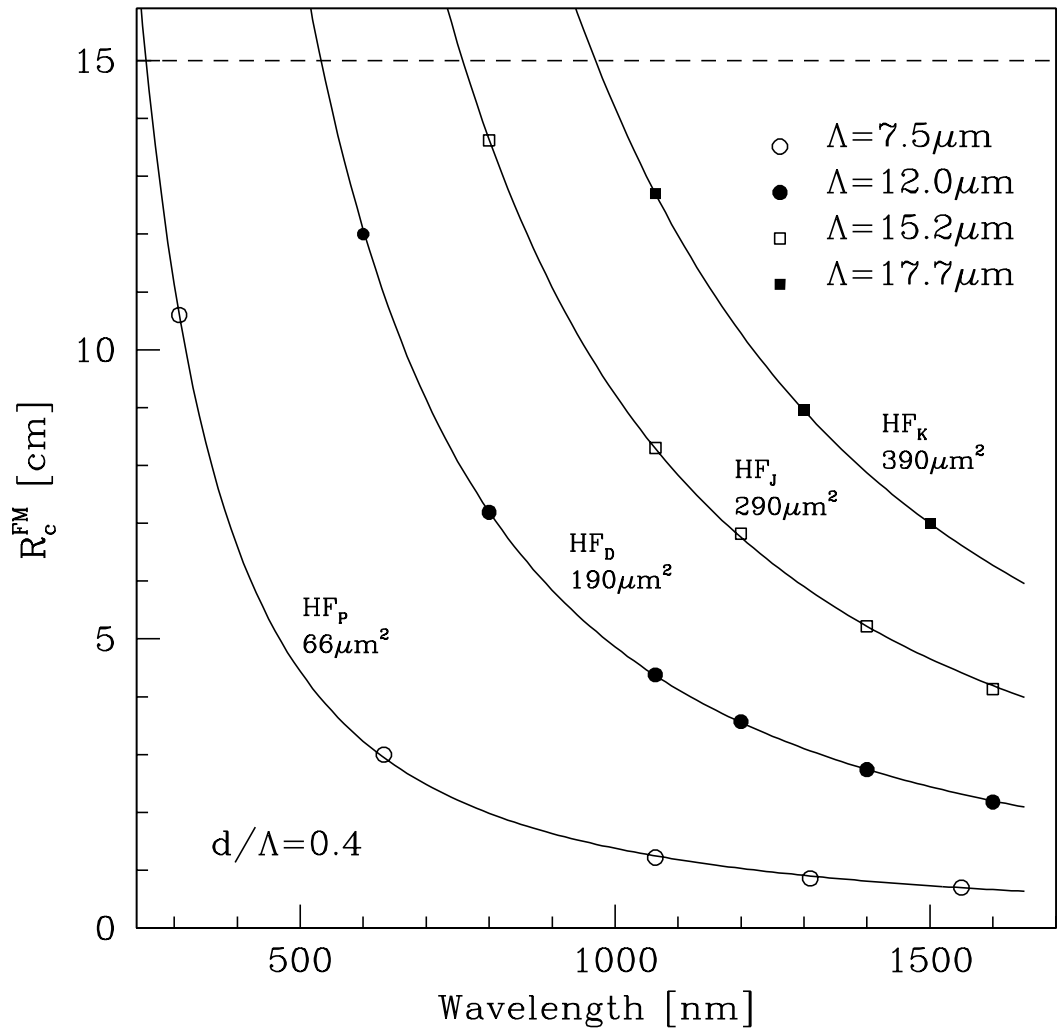

Figure 7.4: Critical bend radius (R_c^{FM}) as a function of wavelength for four holey fibres with $d/\Lambda = 0.4$ and increasing values of Λ and A_{eff}^{FM}. The values of A_{eff}^{FM} marked on the graph correspond to 1064 nm. The dashed line marks the position of $R_c^{FM} = 15$ cm. The fibre parameters are shown in Tables 7.4.

fibres varies by less than 20%.

Fig. 7.4 shows that the wavelength at which the maximum tolerable value of R_c^{FM} is reached, defined here as 15 cm, increases with the A_{eff}^{FM} of the fibre, as is expected. The A_{eff}^{FM} of the fibre is plotted against this maximum tolerable wavelength in Fig. 7.6, in which the open circles represent values extracted from Fig. 7.4 and Fig. 7.5, and the solid line is a fit drawn to guide the eye. This demonstrates that the maximum tolerable A_{eff}^{FM} steadily decreases towards short wavelengths, from ≈ 650 μm^2 at 1550 nm to ≈ 80 μm^2 at 308 nm. This is consistent with the previous estimate from Section 7.2.1, which stated that $A_{eff}^{FM} \approx 100$ μm^2 at 308 nm was likely to be impractical, and is also consistent with reports of a

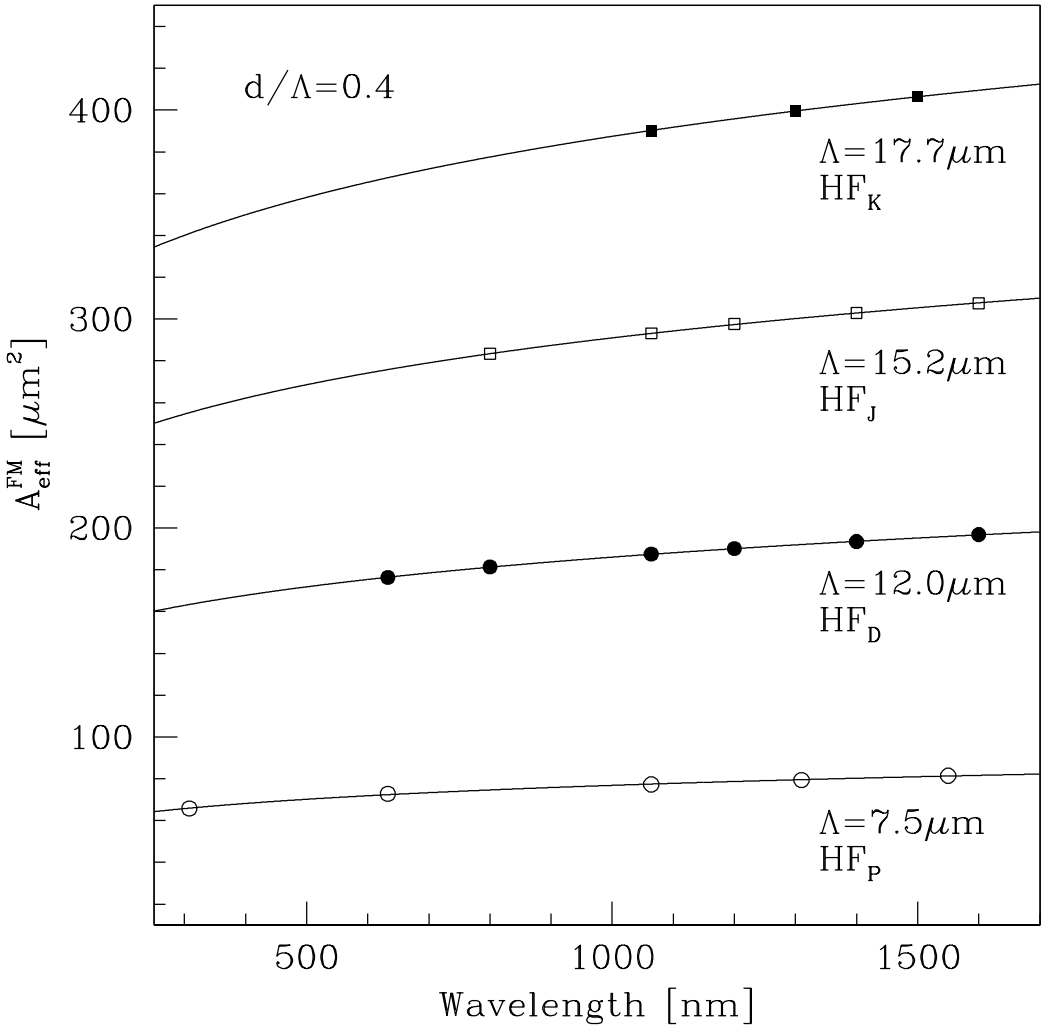

Figure 7.5: A_{eff}^{FM} as a function of wavelength for four holey fibres with $d/\Lambda = 0.4$ and increasing values of Λ, and A_{eff}^{FM}. Values of A_{eff}^{FM} marked on figure correspond to 1064 nm. Note that the fibre parameters are shown in Tables 7.4.

practical single-mode holey fibre with $A_{eff}^{FM} \approx 600$ μm^2 at 1550 nm [10]. Note however, that the estimates of the maximum tolerable A_{eff}^{FM} shown in Fig. 7.6 correspond to $d/\Lambda = 0.4$. Consequently, they represent conservative estimates, especially towards long wavelengths due to the fact that $(d/\Lambda)_c$ increases with wavelength. Furthermore, it has been shown that multi-mode fibres can be effectively single-mode in practice for $d/\Lambda > (d/\Lambda)_c$. Experimental results presented in Chapter 5 demonstrated that at 1064 nm, fibres with $A_{eff}^{FM} \approx 200$ μm^2 could be effectively single-mode for values of d/Λ up to 0.5. This work is extended in Section 7.3, in which experimental results of bend loss measurements from a range of holey fibres illuminated with a white-light source are used to infer information regarding the

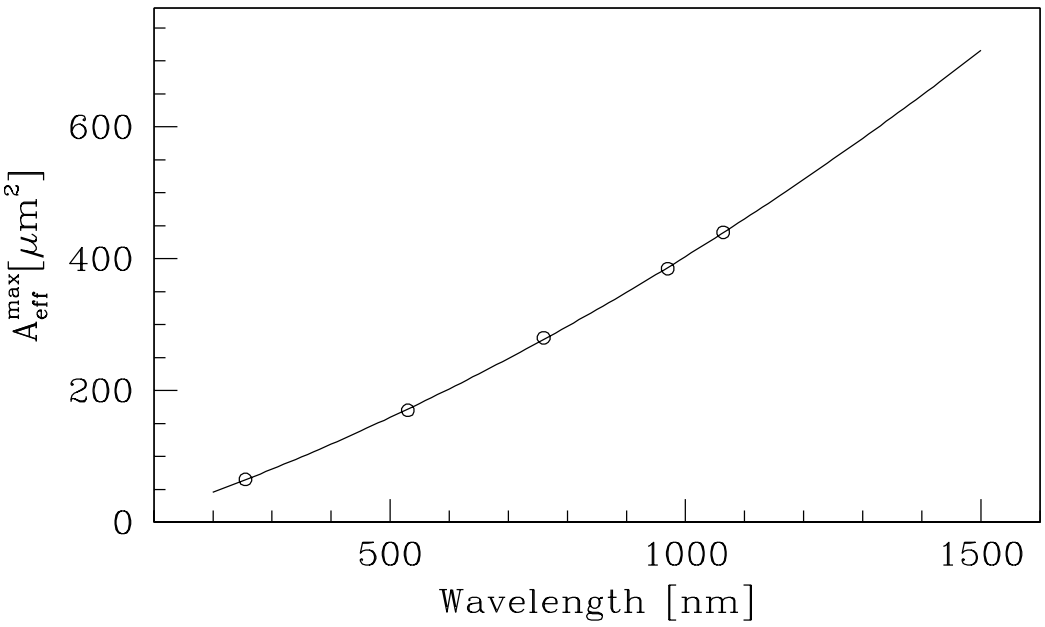

Figure 7.6: Maximum tolerable A_{eff}^{FM} as a function of wavelength for holey fibres. Maximum tolerable A_{eff}^{FM} defined as the A_{eff}^{FM} at which $R_c^{FM} = 15$ cm. Open circles represent data extracted from Fig. 7.4 and Fig. 7.5. The solid line is a fit to this data of the form $y = a * x^2 + b * x + c$.

modedness of the fibre as a function of wavelength.

Note also that the values of the maximum tolerable A_{eff}^{FM} shown in Fig. 7.6 could be improved by using a $\triangle$HF, in which three adjacent rods are used to form the core, as discussed in Chapter 6. The benefits offered by the $\triangle$HF structure as a function of wavelength are explored in Section 7.5.

7.3 Experimental results from white light bend loss measurements

7.3.1 Introduction

In this section, experimental results are presented from a series of bend loss measurements made on a selection of holey fibres using a white-light source of illumination. These measurements are made using the experimental set-up described in Section 4.4.3 and have been performed by Matteo Fuocci and Marco Petrovich at the ORC. Note that all results have been obtained for one full loop of fibre. The results from these experiments, presented in Section 7.3.2 below, can be used to infer information regarding the modedness of the fibres, in addition to the bending losses as a function of wavelength, as explained previously in

Sections 5.3 and 5.4.

These results are also used to further validate the numerical techniques developed here to model the bending losses of holey fibres, as described in Chapter 3. In Section 7.3.3, the R_c^{FM} as a function of wavelength is extracted from the white-light bend loss measurements of a holey fibre with $\Lambda = 12.1$ μm and $d/\Lambda = 0.34$. Comparison with numerical predictions of R_c^{FM}, calculated using the scalar version of the modal model in Section 3.2 for a range of wavelengths, demonstrate the accuracy of these techniques as a function of wavelength.

7.3.2 Experimental clues to the modedness of holey fibres

To explain how information regarding the modedness of the fibre can be extracted we look first at three fibres with $A_{eff}^{FM} \approx 200$ μm^2 and increasing values of d/Λ, which have been studied in detail at 1064 nm in previous sections. The structural parameters and modal properties at 1064 nm of these fibres are shown in Table 7.5 (repeated from Section 5.4). SEM images of these fibres are shown in Fig. 5.21. The spectral response to bending for each of these three fibres is shown in Figs 7.7, 7.8 and 7.9 as a function of wavelength. In each of these three figures, (a) shows the power transmitted in dBm and (b) shows the data from (a) which has been normalised against the power in the straight fibre. Please refer to figure captions and legends for more details. For all fibres considered here, the bend loss is expected to occur first at short-wavelengths for gentle bends, extending to longer wavelengths as the bend radii are decreased. This is observed for all fibres considered.

Table 7.5: Measured (^{m}) and predicted (^{p}) modal properties for a range of holey fibres at 1064 nm. * indicates that the fibre is effectively single-mode at 1064 nm.

Fibre	Λ [μm]	d [μm]	d/Λ	$A^m{}_{eff}$ [μm^2]	$A^p{}_{eff}$ [μm^2]	R_c^m [cm]	R_c^p [cm]	Modes
F334Zeop	11.74	3.84	0.33	200	210	7.1	7.2	SM
F334Zsop	11.93	5.39	0.45	165	170	3.3	-	MM*
F334Ysop	12.63	6.48	0.51	165	170	< 2	-	MM*

The modedness of the three fibres in Table 7.5 are determined using Eq. 5.2, as discussed in Section 5.3. Fibre F334Zeop is determined to be endlessly single-mode and fibres F334Zsop and F334Ysop are determined to be multi-mode for all wavelengths transparent in silica. Single-wavelength bend loss measurements at 1064 nm, presented in Section 5.4

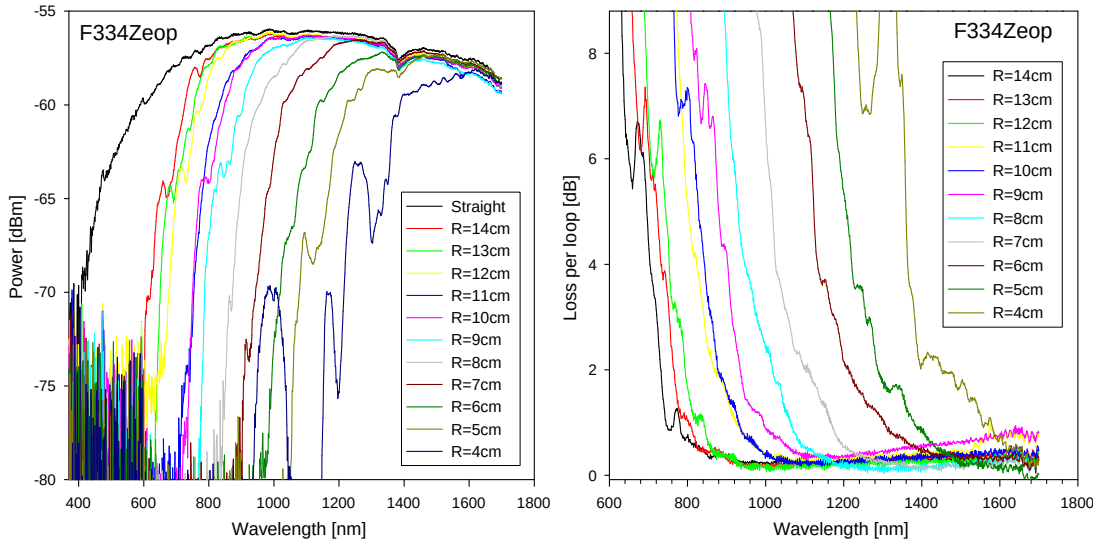

(a) (b)

Figure 7.7: (a) Power transmitted through holey fibre F334Zeop for white light illumination at launch. (b) The data from (a) normalised against the power in the straight fibre. The fibre parameters are shown in Table 5.3.

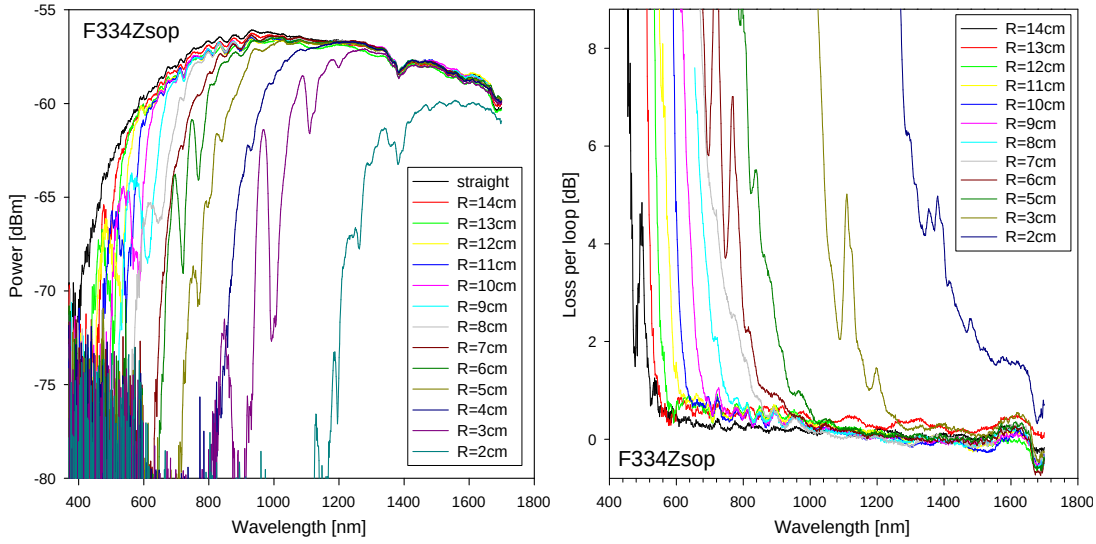

(a) (b)

Figure 7.8: (a) Power transmitted through holey fibre F334Zsop for white light illumination at launch. (b) The data from (a) normalised against the power in the straight fibre. The fibre parameters are shown in Table 5.3.

confirmed that fibre F334Zeop was single-mode and indicated that fibres F334Zsop and F334Ysop were effectively single-mode at 1064 nm. The lack of evidence for higher-order modes in fibres F334Zsop and F334Ysop was attributed to the fact that the higher-order modes possessed high levels of confinement loss (calculated to be $\approx$ 0.5 dB/m for simi-

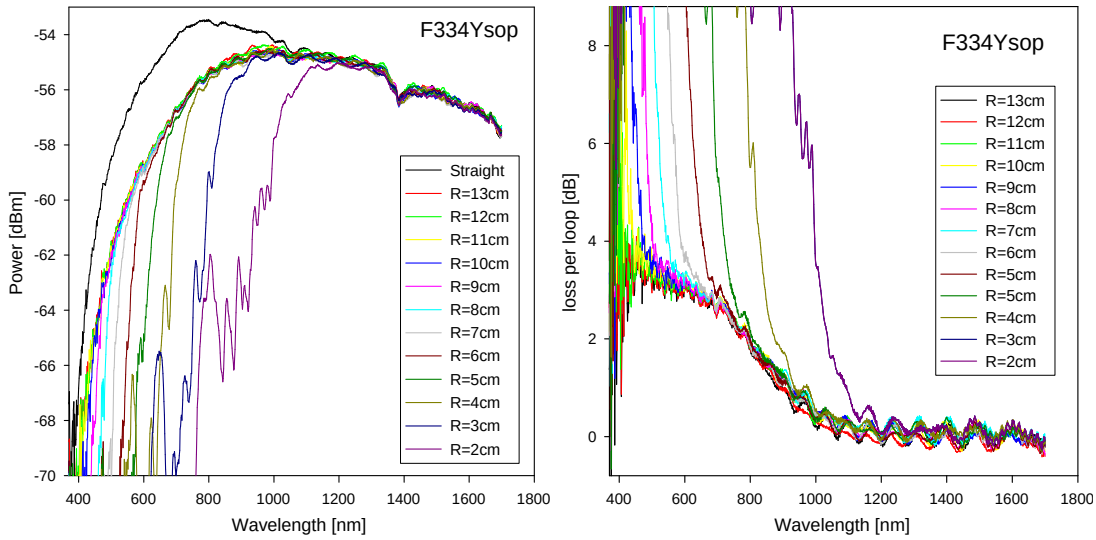

(a) (b)

Figure 7.9: (a) Power transmitted through holey fibre F334Ysop for white light illumination at launch. (b) The data from (a) normalised against the power in the straight fibre. The fibre parameters are shown in Table 5.3.

lar structures in Section 5.3). Using the data from the white-light bend loss experiments shown in Figs 7.7, 7.8 and 7.9 these conclusions can be confirmed and additional information regarding the modedness at other wavelengths can be inferred, as discussed in the following.

The transmitted power in Fig. 7.7 (a) for the endlessly single-mode fibre F334Zeop shows a smooth reduction towards short wavelengths from one radius to the next, indicating that power is lost steadily as the bend radius is reduced. In contrast, the transmitted power in Fig. 7.9 (a) for the multi-mode fibre F334Ysop shows a marked reduction in power from the straight fibre to the largest bend for wavelengths $\lesssim$1050 nm. This large power loss for $\lambda < 1050$ nm is indicative of higher-order modes that possess low enough confinement losses to be observed in the straight fibre for $\lambda < 1050$ nm, but possess such high bending losses that they are stripped completely from the fibre for $R_o < 13$ cm. The fact that this loss can be attributed solely to higher-order modes, and the fact that we deduce that all power is lost from these higher-order modes for $R_o < 13$ cm is determined from the observation that the subsequent few smaller bend radii show relatively constant power levels for $\lambda < 1050$ nm. This indicates that the $R_c^{FM} \ll 13$ cm$\ll R_c^{HOM}$, where R_c^{HOM} is the critical bend radius of the higher-order modes. Fibre F334Ysop is therefore defined to be selectively single-mode for $R_o < 13$ cm for $\lambda \lesssim 1050$ nm and effectively single-mode for $\lambda \gtrsim 1050$ nm, which is

consistent with the interpretation made at 1064 nm in Section 5.4.

Fibre F334Zsop lies in between fibres F334Zeop and F334Ysop in terms of fibre parameters and was determined to be effectively single-mode at 1064 nm in Section 5.4. Indeed, the graph of transmitted power as a function of wavelength, shown in Fig. 7.8 (a), looks similar to the equivalent plot for the endlessly single-mode fibre F334Zeop, which is shown in Fig. 7.7 (a), indicating that fibre F334Zsop may be effectively single-mode across the entire wavelength range shown. However, evidence of higher-order modes for $\lambda \lesssim 850$ nm is present in the data displayed in Fig. 7.8, but it is not easy to see. By extracting the loss for individual wavelengths, as shown in Fig. 7.10, the characteristic 'step' in bend loss that indicates the presence of higher-order modes can be clearly seen for the wavelength of 600 nm. In contrast, the bend loss at 850 nm shows no sign of higher-order modes. The onset of this 'step' occurs gradually between these two wavelengths, and only becomes clearly representative of a single-mode fibre at 850 nm. As a result, fibre F334Zsop is defined to be effectively single-mode for $\lambda \gtrsim 850\ nm$. This fibre is also likely to be selectively single-mode for $\lambda \lesssim 850\ nm$ below some bend radius, but this is not obvious from the data presented here.

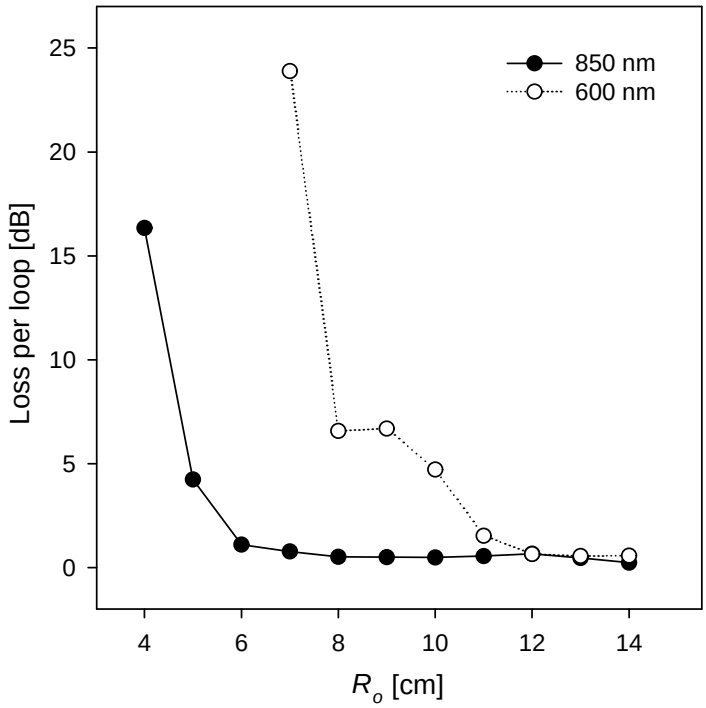

Figure 7.10: Bend loss (per loop) for holey fibre F334Zsop at 850 and 600 nm, extracted from the data in Fig. 7.8. Fibre parameters are shown in Table 5.3.

The critical bend radii (R_c) as a function of wavelength can be extracted for fibres F334Zeop, F334Zsop and F334Ysop from the data shown in Figs 7.7 (b), 7.8 (b) and 7.9 (b) respectively, in which the power transmitted through each fibre is normalised against the power transmitted through the corresponding straight fibre. These critical bend radii are shown in Fig. 7.11 (the fitted curves in Fig. 7.11 are drawn to guide the eye). Note that two different values of R_c are shown for fibre F334Ysop. The first of these corresponds to the loss for all modes present in this multi-mode fibre, extracted from 7.9 (b). The additional R_c curve correspond to the loss from the fundamental mode (FM) alone and is extracted in the following way. Previously, fibre F334Ysop was defined to be a multi-mode fibre that can be selectively single-mode for $R_o < 13$ cm, with negligible power lost from the fundamental mode at this radius (i.e. $R_c^{FM} \ll 13$ cm$\ll R_c^{HOM}$). Therefore, by normalising the loss spectra shown in Fig. 7.9 (a) against the power in the fibre at $R_o = 13$ cm, as shown in Fig. 7.12, the loss due to the fundamental mode alone can be extracted.

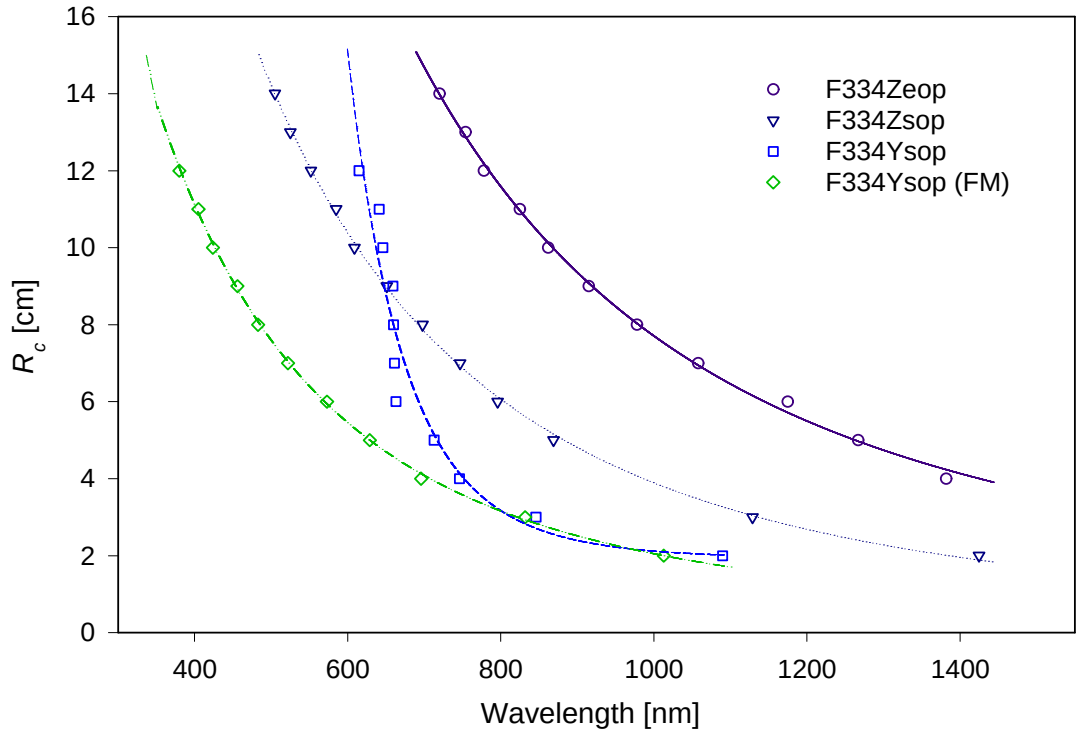

Figure 7.11: R_c for holey fibres F334Zeop, F334Zsop and F334Ysop as a function of wavelength. The critical bend radius is shown for fibre F334Ysop for all modes of the fibre (solid squares) and for the fundamental mode (FM) alone (open diamonds). The data shown here is extracted from the data shown in Figs 7.7, 7.8 and 7.9. The fibre parameters are shown in Table 5.3.

Considering only the fundamental mode, the results presented in Fig. 7.11 illustrate how

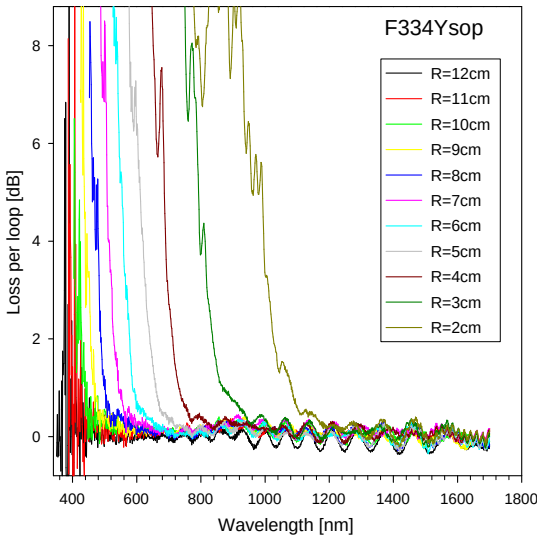

Figure 7.12: Power transmitted through holey fibre F334Ysop for white light illumination at launch, normalised against the power in the fibre at $R_o = 13$ cm. The fibre parameters are shown in Table 5.3.

the R_c^{FM} increases towards short wavelengths and as d/Λ decreases, as is expected. However, the collective R_c, which corresponds to all the modes present in fibre F334Ysop, increases relative to the R_c of the fundamental mode as the wavelength decreases. This indicates that towards short wavelengths, the fraction of power lost from higher-order modes in a bent holey fibre increases relative to the fraction of power lost from the fundamental mode. Consequently, for $\lambda \lesssim 645$ nm, the overall R_c of fibre F334Ysop, which has $d/\Lambda \approx 0.51$ and $A_{eff}^{FM} \approx 165$ μm^2 at 1064 nm, becomes larger than the R_c of fibre F334Zsop, which has $d/\Lambda \approx 0.45$ and $A_{eff}^{FM} \approx 165$ μm^2 at 1064 nm. This implies that a multi-mode holey fibre can possess greater bending losses than a single-mode holey fibre, with a similar A_{eff}^{FM}, towards short wavelengths as a direct result of the fact that power is coupled into the (more lossy) higher-order modes from the fundamental mode. However, note that it may be possible to minimise the power lost through the bending losses of higher-order modes via selective launch conditions. It was not possible to investigate this with the white-light source of illumination used here, due to the fact that the spot size incident on the fibre at launch was many times that of the fibre diameter. Single-mode sources would enable further investigation in this area, which is necessary in order to properly evaluate the conditions for selectively single-mode guidance in a holey fibre. This has not been performed here for reasons of time, but is obviously something to consider in future investigations.

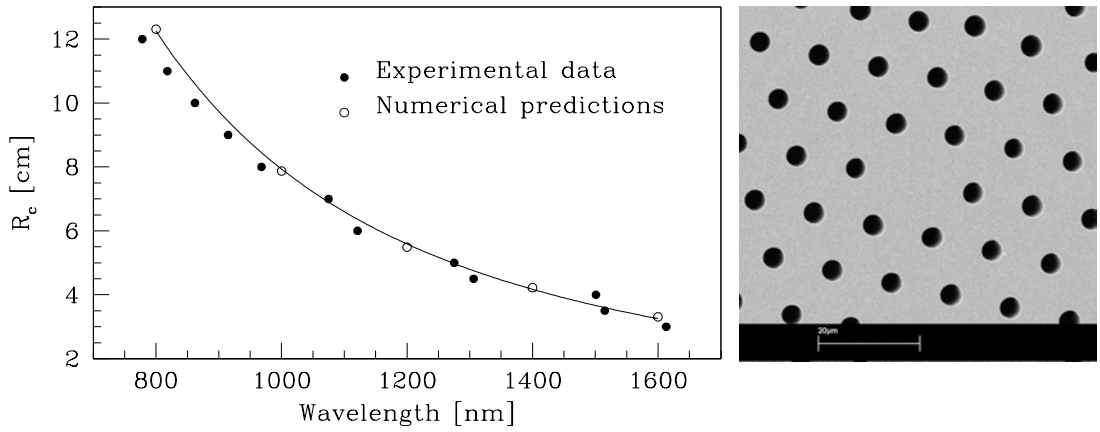

(a) (b)

Figure 7.13: (a) Critical bend radius (R_c^{FM}) as a function of wavelength for holey fibre F200D1 with $\Lambda = 12.1$ μm and $d/\Lambda = 0.34$. (b) SEM of holey fibre F200D1. $A_{eff}^{FM} \approx 220$ μm^2 @ 1064 nm.

7.3.3 Comparison with numerical predictions

In this section the measured values of R_c^{FM} as a function of wavelength are compared with numerical predictions for fibre F200D1, which has $\Lambda = 12.1$ μm and $d/\Lambda = 0.34$. Fibre F200D1 was fabricated from pure silica rods and tubes of F300 synthetic silica glass from Heraeus Tenevo AG, by Kentaro Furusawa, at the ORC. Note that for all the numerical predictions presented within this section, the constant of proportionality, τ, defined in Eq. 3.17, is equal to 2.0 (see also Section 4.5.3). As in the previous section, the values of R_c^{FM} are extracted from bend loss measurements made using a white-light source of illumination and show that the bending losses worsen towards short wavelengths. The predicted values of R_c^{FM} are calculated using the techniques developed here, which are described in Chapter 3. The SEM of fibre F200D1 is shown in Fig. 7.13 (b) and the A_{eff}^{FM} of this fibre at 1064 nm is measured as 215 μm^2. This is in excellent agreement with the predicted value of 220 μm^2. The measured values of R_c^{FM} for this fibre are shown in Fig. 7.13 (a) together with the predicted values. The excellent agreement between experiment and theory demonstrates that the numerical methods developed here can be used to accurately predict the bending losses of holey fibres as a function of wavelength.

7.4 Scaling predicted values of R_c^{FM} in silica holey fibres

7.4.1 Introduction

As mentioned briefly in Section 1.2.2, if a constant refractive index is assumed, Maxwell's equations become scale invariant. Consequently, for this assumption, the modal properties of a holey fibre with a hole-to-hole spacing of $\Lambda = \Lambda_1$ and a relative hole size of $d_1/\Lambda_1 = \delta$ are exactly replicated in a structure with a different Λ (Λ_2), if the relative hole size is maintained ($d_2/\Lambda_2 = \delta$) and if the wavelength is also scaled proportionately, i.e. $\lambda_2 = \lambda_1(\Lambda_2/\Lambda_1)$. This approach is advantageous as it vastly reduces the number of calculations required to evaluate a wide range of fibre structures over many different wavelengths.

By assuming a constant refractive index for an air/silica holey fibre, the wavelength dependence of the refractive index of silica is neglected. However, the refractive index of silica is a weak function of wavelength, varying by approximately 3% in the wavelength range $300 - 1600$ nm (as illustrated in Section C) and this approximation is often used successfully to evaluate certain holey fibre properties [4, 16, 17]. However, bend loss is a sensitive function of the fibre parameters and this scaling approach has not previously been evaluated for bend loss. In the following, results from previous sections are used to evaluate the accuracy of this scaling technique for bend loss in holey fibres.

In the following two sections, the predicted values of R_c^{FM} presented in Chapter 5, which were calculated for a range of holey fibre structures at 1064 nm, are used (via appropriate scaling) to evaluate the R_c^{FM} for several holey fibres that have been considered previously in this chapter as a function of wavelength. In Section 7.4.2, values of R_c^{FM} obtained via this scaled approach are compared with predictions made using a wavelength dependent refractive index (shown previously in Section 7.2.3) and in Section 7.4.3, predicted values of R_c^{FM} obtained via this scaled approach are compared with experimentally measured values.

7.4.2 Comparison with other predicted values

In Sections 5.2 and 5.5.2, the A_{eff}^{FM} and R_c^{FM} for holey fibres with structural parameters in the range $7.0\,\mu\text{m} < \Lambda < 20.0\,\mu\text{m}$ and $0.2 < d/\Lambda < 0.5$ were evaluated numerically using the methods developed in Chapter 3. These results were then used to construct contour plots of A_{eff}^{FM} and R_c^{FM} over this range of Λ and d/Λ (see for example Fig. 5.28). For reference, the refractive index used for the calculations presented in Chapter 5 was 1.449631. Here, these results are recast to produce a scale invariant version of the same contour plot, as shown

in Fig. 7.14.

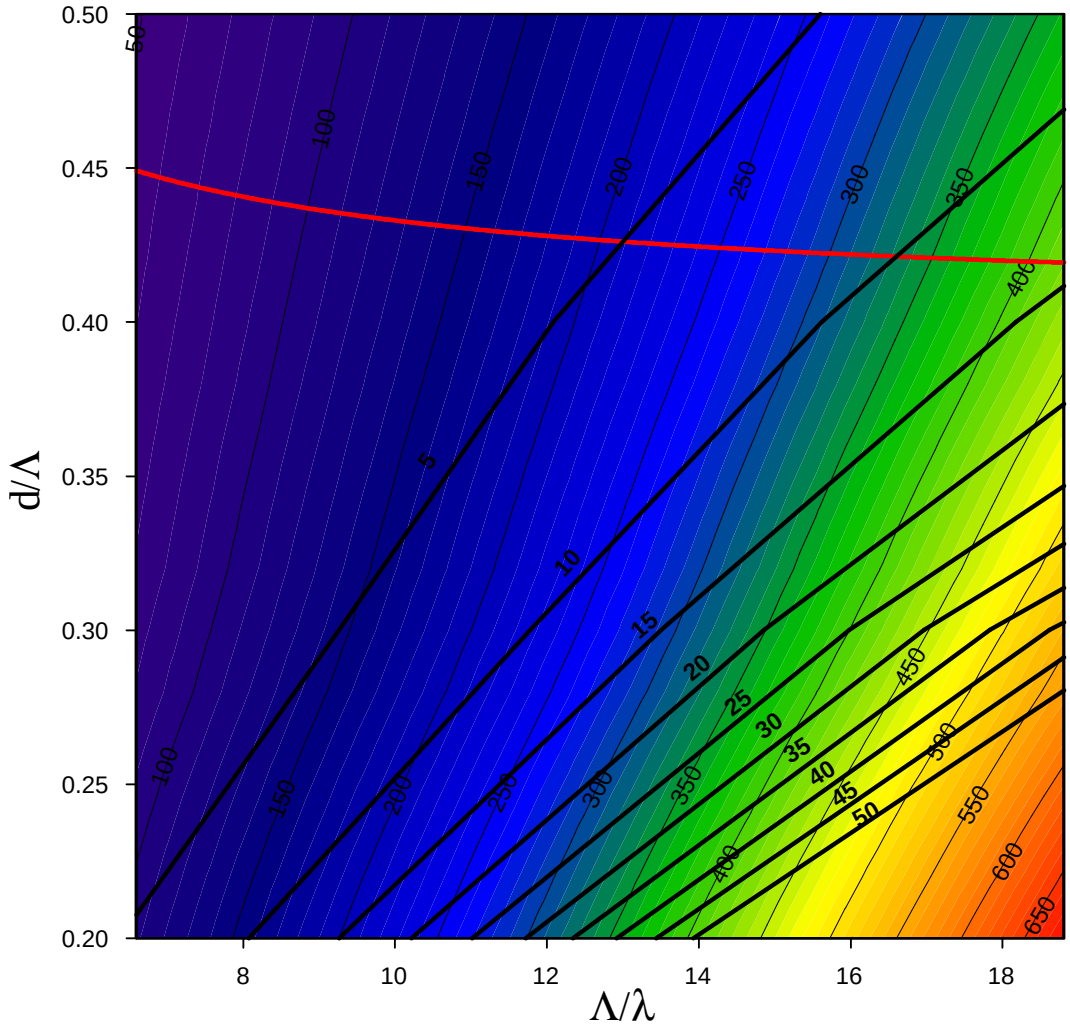

Figure 7.14: Contour plots from which A_{eff}^{FM}, R_c^{FM} and the modedness of the fibre can be extracted. The colour contour lines show A_{eff}^{FM}/λ^2. The solid black contour lines represent R_c^{FM}/λ and the solid red line indicates the single-mode/multi-mode cut-off. These values are plotted as a function of Λ/λ and d/Λ.

In Fig. 7.14, the colour contours correspond to $A_{eff}^{FM}/(\lambda^2)$, the solid black contour lines represent R_c^{FM}/λ and the solid red line indicates the single-mode/multi-mode cut-off (calculated using Eq. 5.2). These values are plotted as a function of Λ/λ and d/Λ. Values of A_{eff}^{FM} and R_c^{FM} can thus be extracted from this graph for $6.6 \lesssim \Lambda/\lambda \lesssim 18.8$ and $0.2 < d/\Lambda < 0.5$. By comparing these values with previously calculations in which the wavelength dependence of the refractive index of silica was included, the accuracy of this scaling approach for predicting R_c^{FM} can be evaluated. This is done here for the following two holey fibres;

HF_B and HF_G, which have $\Lambda = 10.7$ μm, $d/\Lambda = 0.28$ and $\Lambda = 12.7$ μm, $d/\Lambda = 0.45$ respectively and the results are shown in Tables 7.6 and 7.7. In Tables 7.6 and 7.7, values of R_c^{FM} and A_{eff}^{FM} that have been extracted from Fig. 7.14 are shown together with values that have been calculated with the wavelength dependent refractive index of silica included, via the Sellmeier equation. It has been previously shown that the A_{eff}^{FM} of a holey fibre can be found with good accuracy using a scale invariant approach [17], and the values of A_{eff}^{FM} in Tables 7.6 and 7.7 confirm this. In addition, the agreement between the two values of R_c^{FM} demonstrates that scaling calculations made at other wavelengths can result in accurate predictions of R_c^{FM}. In the following section, this scaling approach is further validated against experimentally measured values of R_c^{FM}.

Table 7.6: Scaled R_c^{FM} and A_{eff}^{FM} for fibre HF_B: $\Lambda = 10.7$ μm, $d/\Lambda = 0.28$.

λ [nm]	Λ/λ	R_c^{FM}/λ ± 0.2	R_c^{FM} [cm] (scaled)	R_c^{FM} [cm] (Sellmeier)	A_{eff}^{FM}/λ^2 ± 2	A_{eff}^{FM} [μm^2] (scaled)	A_{eff}^{FM} [μm^2] (Sellmeier)
800	13.4	17.1	13.7	13.4	297	188	186
1064	10.0	7.2	7.7	7.70	171	192	190
1200	8.9	5.2	6.2	6.20	138	196	196
1400	7.6	3.3	4.6	4.72	103	198	201
1600	6.7	2.4	3.8	3.73	81	205	206

Table 7.7: Scaled R_c^{FM} and A_{eff}^{FM} for fibre HF_G: $\Lambda = 12.7$ μm, $d/\Lambda = 0.45$.

λ [nm]	Λ/λ	R_c^{FM}/λ ± 0.2	R_c^{FM} [cm] (scaled)	R_c^{FM} [cm] (Sellmeier)	A_{eff}^{FM}/λ^2 ± 2	A_{eff}^{FM} [μm^2] (scaled)	A_{eff}^{FM} [μm^2] (Sellmeier)
800	15.9	7.3	5.8	5.8	287	184	183
1064	11.9	3.4	3.6	3.6	166	188	188
1200	10.6	2.5	3.0	3.0	133	192	191
1400	9.1	1.6	2.2	2.2	100	196	196

7.4.3 Comparison with measured values

In this section, values of R_c^{FM} measured as a function of wavelength are compared to predicted results extracted from Fig. 7.14, which has been constructed with the assumption that the refractive index of silica is constant, as described above (in this case $n_{silica} = 1.449631$). Four fibres are considered here in detail and are listed together with their structural parameters in Table 7.8. With the exception of fibre F409Ysop, all the experimental results shown here are repeated from Section 7.3, in which only the results for fibre F200D1 were compared to numerical predictions.

Table 7.8: Structural parameters of the four fibres shown in Fig. 7.15.

Fibre	Λ [μm]	d/Λ	A_{eff}^{FM}@1064 nm [μm^2]
F334Zeop	11.7	0.33	200
F334Zsop	11.9	0.45	165
F200D1	12.1	0.34	220
F409Ysop	15.4	0.46	270

The measured values of R_c^{FM} (open circles) are shown together with predicted values (closed circles), extracted from Fig. 7.14, in Fig. 7.15. The insets in each part of Fig. 7.15 show the SEM of the appropriate fibre. The agreement between the (scaled) predictions and measured values of R_c^{FM} in Figs 7.15 (a), (c) and (d) demonstrates that, for the holey fibres considered here, R_c^{FM} is essentially scale invariant and a scaling approach can be used to form accurate predictions of this parameter. For fibre F409Ysop, (Fig. 7.15 (a)), the agreement between the scaled predictions and measured values of R_c^{FM} can be seen to diverge for $\lambda \lesssim 850$ nm. This results from the fact the bend loss in this fibre at $\lambda \lesssim 850$ nm has contributions from both the fundamental core mode and the higher order core modes of the fibre (The scaled predicted values of R_c^{FM} correspond to the fundamental mode only). This is supported by the results from Section 7.3, in which multi-mode behaviour was observed in this fibre for $\lambda \lesssim 850$ nm (the vertical dashed line in Fig. 7.15 (b) indicates $\lambda = 850$ nm).

7.4.4 Conclusion

In conclusion, the results in this section demonstrate that in calculations of R_c^{FM}, the assumption of a constant refractive of silica can be used to produce accurate predictions for holey fibres and that R_c^{FM} is essentially scale invariant. In addition, the contour plot of

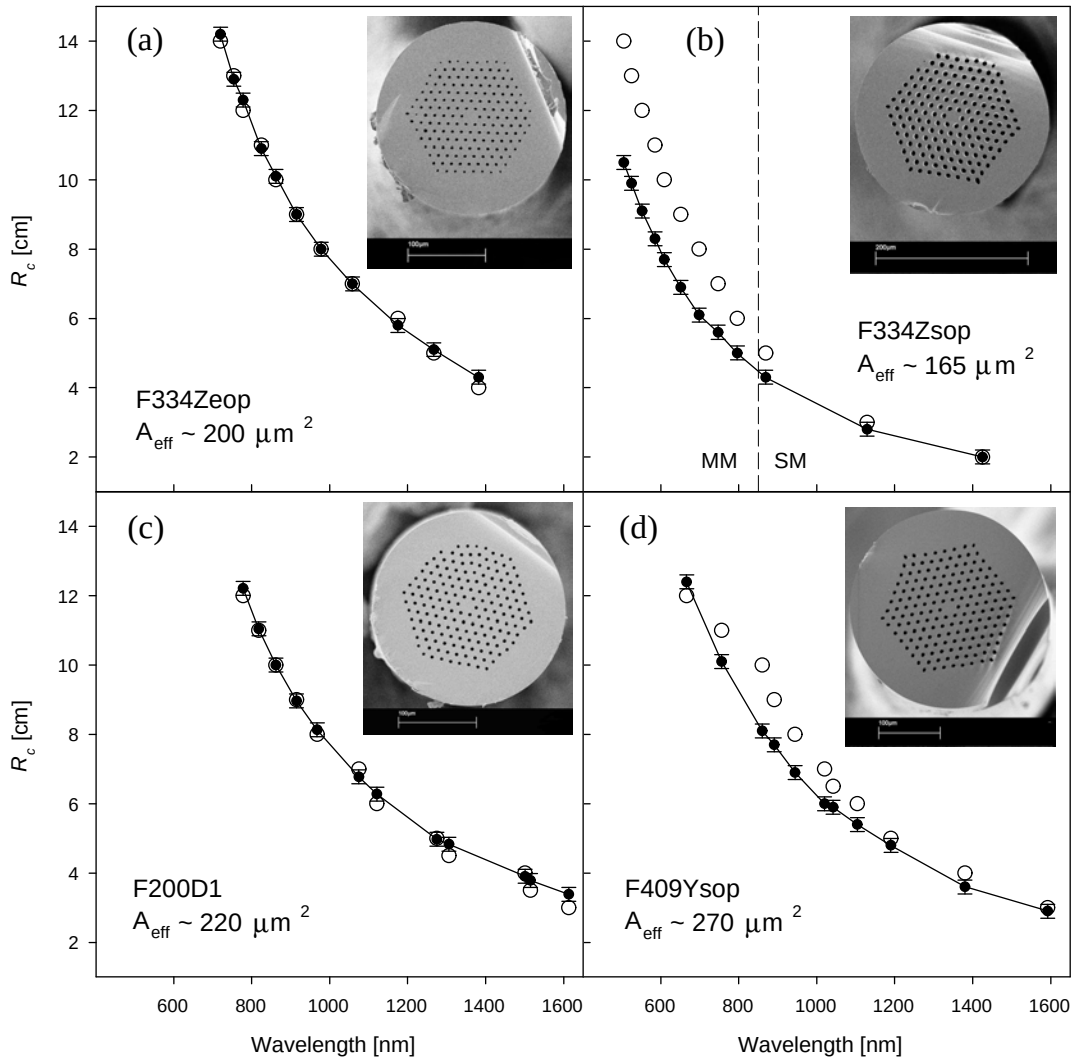

Figure 7.15: Critical bend radius (R_c^{FM}) as a function of wavelength for four holey fibres studied experimentally within this thesis. (a) F334Zeop, (b) F334Zsop, (c) F200D1, and (d) F409Ysop. Open circles correspond to experimental measurements and solid circles correspond to predicted values, extracted from Fig 7.14. The vertical dashed line in (b) indicates the wavelength at which this fibre was observed to be multi-mode (see Section 7.3). A SEM of each holey fibre shown in the inset of each part. The structural parameters of the four fibres considered in this figure are shown in Table 7.8.

$A_{eff}^{FM}/(\lambda^2)$ and R_c^{FM}/λ presented in Fig. 7.14 is an invaluable design tool and enables basic fibre properties to be determined at-a-glance for $6.6 \lesssim \Lambda/\lambda < 18.8$ and $0.2 < d/\Lambda < 0.5$.

7.5 Bend loss of a △HF as a function of wavelength: A numerical study

As discussed in Chapter 6, experimental results have shown that by using three adjacent rods to form the core of a holey fibre (referred to here as a △HF), instead of the usual single-rod, it is possible to enlarge the mode area without increasing the bending losses [34]. In Chapter 6, the improvement offered by single-mode △HFs was evaluated in detail using the numerical techniques developed in Chapter 3. These calculations demonstrated that at 1064 nm a △HF structure can be used to increase the A_{eff}^{FM} by $\approx 15-20\%$ without increasing the R_c^{FM}, relative to a traditional single-rod holey fibre at 1064 nm. In this section I aim to further understand how this relative improvement in bend loss varies as a function of wavelength. Here I choose to consider the largest fibre pair studied in Chapter 6; holey fibre HF_K and triangular core fibre $\triangle HF_O$, which both possess $A_{eff}^{FM} \approx 400\ \mu m^2$. Note that the parameters of these two fibres were chosen to create approximately similar values of n_{FSM} and A_{eff}^{FM} at 1064 nm. However, this choice is a non-trivial process, and as a result, the n_{FSM} of $\triangle HF_O$ is slightly lower than that of HF_K, resulting in the fact that fibre $\triangle HF_O$ is just multi-mode at 1064 nm. This unfortunately means that the fibres are not as similar as would be preferred for a direct comparison. However, via investigation of the bending losses for a more closely matched HF/△HF fibre pair in Section 6.2.3, it has been shown that the improvement offered by △HF in terms of bend loss is real, and is not seen merely as a result of non-equivalent structures. Furthermore, in this section, I aim only to look at the functional dependence of the bend loss with respect to wavelength in the two fibre types, and the absolute values of loss are less important. The structural parameters and predicted values of A_{eff}^{FM} at 1064 nm for these two fibres are listed in Table 7.9.

Table 7.9: Structural parameters and predicted modal properties at 1064 nm for holey fibre HF_K and triangular core holey fibre $\triangle HF_O$.

Fibre	Λ [μm]	d [μm]	d/Λ	A_{eff}^{FM} @ 1064 nm [μm^2]
HF_K	17.70	7.08	0.40	390
$\triangle HF_O$	11.00	2.20	0.20	401

In Chapter 6 the structural parameters of the fibre pair HF_K and $\triangle HF_O$ were deliberately chosen to create approximately equivalent values of A_{eff}^{FM} and n_{FSM} at 1064 nm to

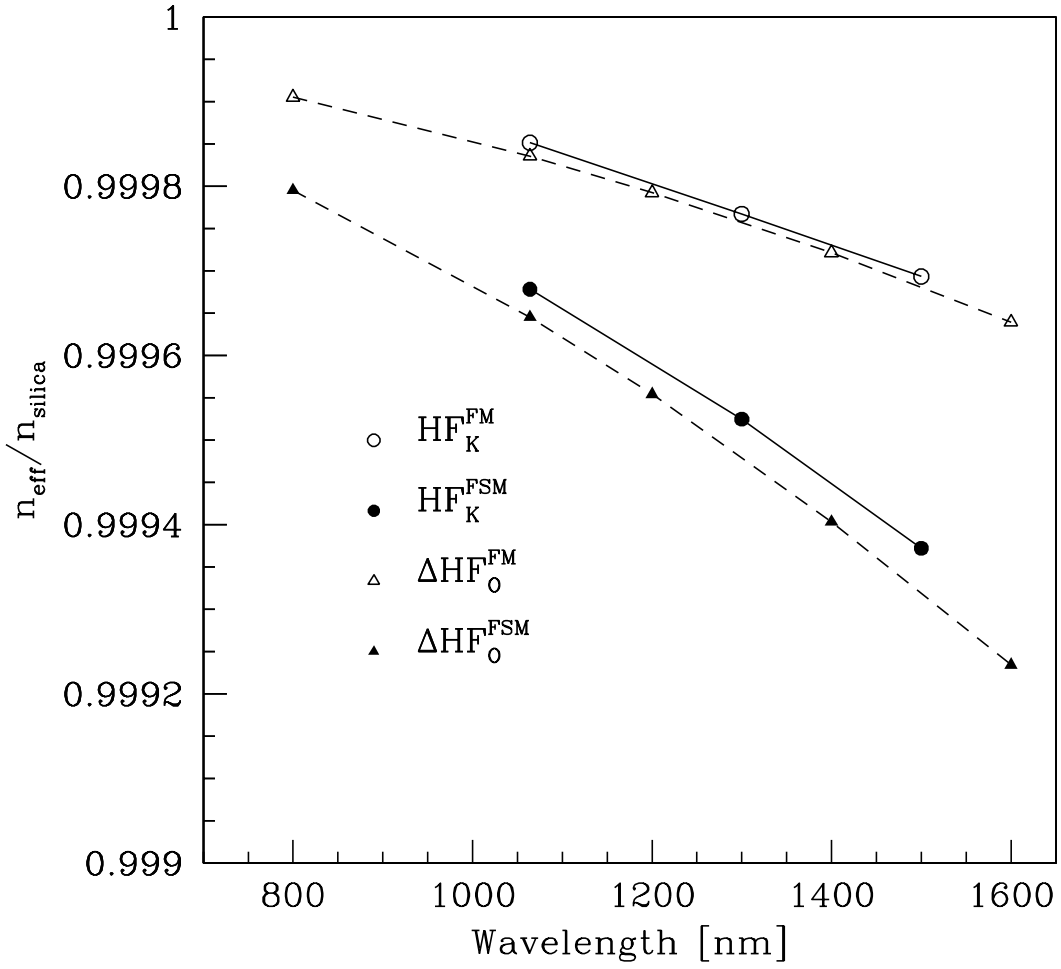

Figure 7.16: Effective modal index of the fundamental core and cladding modes of holey fibre HF_K (round shapes) and triangular core fibre $\triangle HF_O$ (triangular shapes) as a function of wavelength. Modal indices are normalised against the refractive index of silica (calculated using the Sellmeier equation). Open shapes correspond to the effective modal index of the fundamental mode (FM) and the closed shapes correspond to the effective modal index of the fundamental space filling mode of the cladding (FSM). Fibre parameters are shown in Table 7.9

enable a comparative study of bend loss. In order to consider the comparative bending losses of these two fibres as a function of wavelength it is therefore important to understand how the A_{eff}^{FM} and n_{FSM} vary as a function of wavelength. This is necessary in order to gauge the range of wavelengths over which any HF/$\triangle$HF pair could be considered equivalent structures. In Fig. 7.16, the effective modal indices of the fundamental mode (FM) and the fundamental space filling mode of the cladding (FSM) are shown for fibre HF_K and $\triangle HF_O$ as a function of wavelength. This plot shows that the degree of variation in n_{FSM} as a function of wavelength is very similar for the two fibres and that the degree of equivalence in

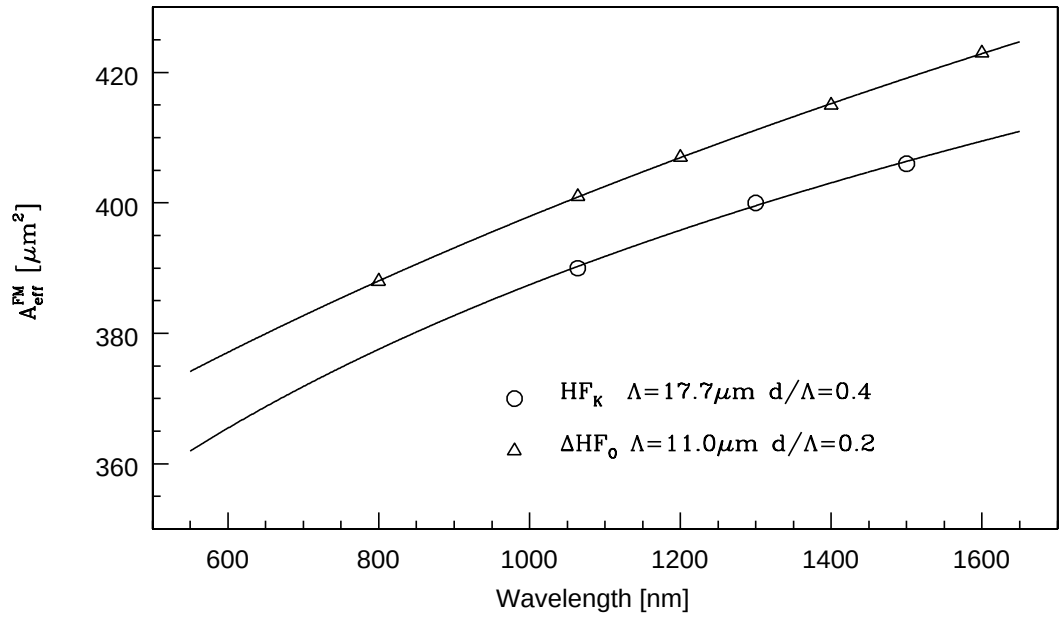

Figure 7.17: A_{eff}^{FM} as a function of wavelength for holey fibre HF_K and triangular core fibre $\triangle HF_O$. The fibre parameters are shown in Tables 7.9.

n_{FSM} can therefore be considered approximately constant over the wavelength range shown. The inclusion of the effective modal index of the fundamental core mode (FM) in Fig. 7.16 serves to illustrate the fact that the spacing between the FM and the FSM narrows towards short wavelengths in both fibres, increasing the coupling between these two modes as the wavelength is decreased. Since macro-bending losses arise from bend induced coupling between the core and cladding modes (amongst others), this demonstrates that the bending losses of both fibres are expected to increase towards short wavelengths by approximately similar amounts. Note that this can also be thought of in terms of the NA of the fibre: as the wavelength reduces the cladding index increases, resulting in a lower NA and a more weakly guided mode that is more susceptible to bend induced loss. Fig. 7.17 shows that although fibre $\triangle HF_O$ has a slightly larger A_{eff}^{FM} than HF_K, the degree of variation in A_{eff}^{FM} with respect to wavelength is similar for both fibres. This fact, together with the n_{FSM} data from Fig. 7.16, demonstrates that the degree of equivalence of these two fibres can be considered to be approximately constant over the wavelength range shown.

The R_c^{FM} for fibres HF_K and $\triangle HF_O$ are shown as a function of wavelength in Fig. 7.18. The solid shapes represent numerical calculations and the solid line represents a fit drawn to guide the eye. This plot demonstrates that the R_c^{FM} of the $\triangle HF$ is less than that of the approximately equivalent holey fibre at all wavelengths considered. Part of this reduction results from the fact that fibre $\triangle HF_O$ has a slightly higher NA than fibre HF_K,

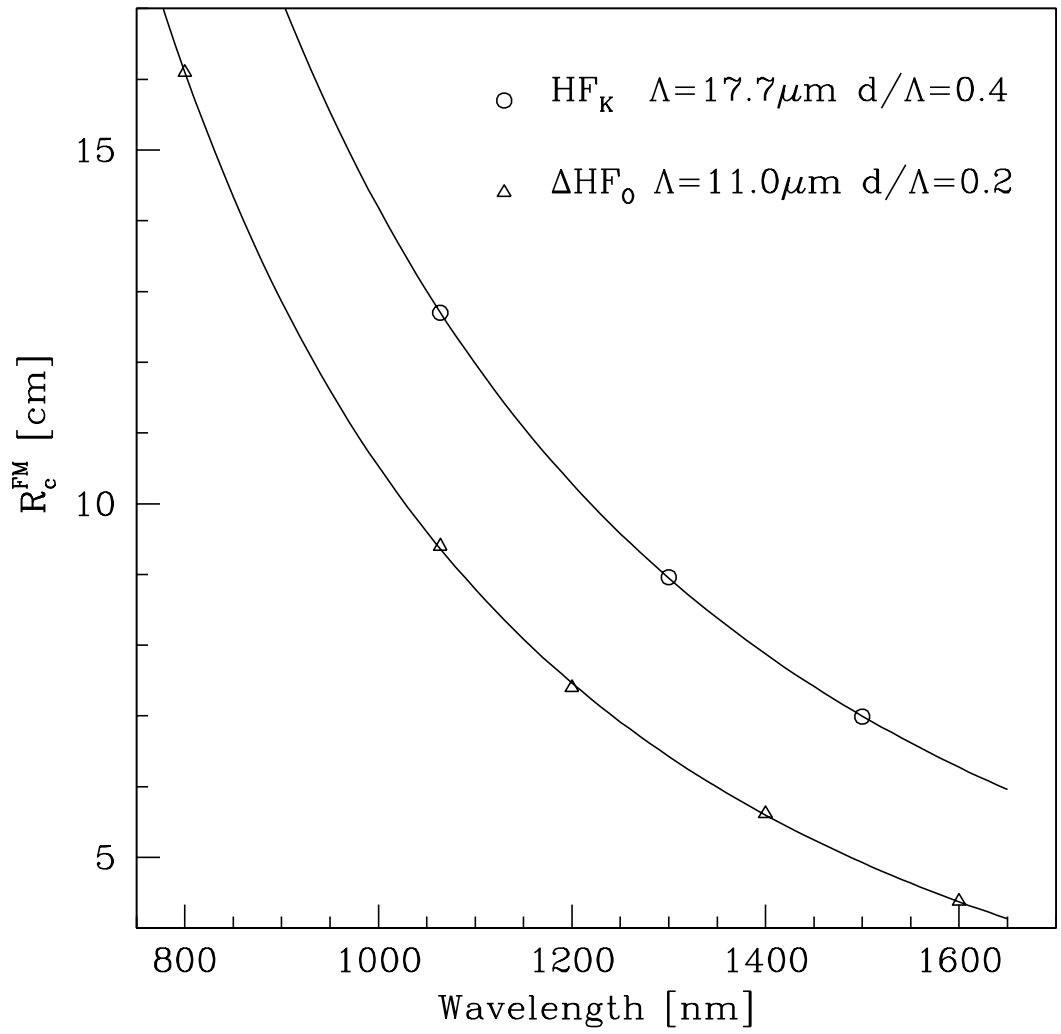

Figure 7.18: R_c^{FM} as a function of wavelength for holey fibre HF_K and $\triangle HF_O$. Fibre parameters are shown in Table 7.9

although the A_{eff}^{FM} of fibre $\triangle HF_O$ is also slightly larger then HF_K and the numerical results presented in Section 6.2.3 indicate that the majority of this improvement arises from the more complex geometry of the $\triangle$HF structure and not the mismatch in NA. Moreover, this plot demonstrates that the spectral dependency on bend loss in the two fibre types is similar and that the relative improvement offered by the $\triangle$HF increases towards short wavelengths. This suggests that $\triangle$HFs may offer a particularly attractive route towards large-mode-area single-mode fibres in the short wavelengths extreme. Indeed, preliminary investigations at 308 nm show that a $\triangle$HF with $\Lambda = 4.65$ μm with $d/\Lambda = 0.2$, which possesses $A_{eff}^{FM} = 68$ μm^2, has a low value of R_c^{FM} (< 2 cm). However, this fibre is found to be robustly multi-mode at 308 nm. In order to assess the potential benefit offered by

△HF structures towards short wavelengths it is necessary to first ascertain the conditions required for single-mode guidance in these fibres and to determine if endlessly single-mode guidance is possible in △HFs. This work is continuing at the ORC.

7.6 Non-silica holey fibres for large mode areas at 2.2 μm

7.6.1 Introduction

Up until this point, all work in this thesis has focussed solely on silica holey fibres. However, holey fibres can also be made from non-silica glasses, such as tellurite and chalcogenide glasses, which offer unique optical properties, such as mid-IR transmission and high values of nonlinearity. The majority of non-silica holey fibres fabricated to date are small-core, high NA structures designed to maximise the high intrinsic nonlinearities of these glasses [24, 23, 25, 26]. However, for transmission applications, single-mode fibres with low nonlinearities, and hence large-mode-areas are required. In this section, the aim is to investigate the *fundamental* factors that limit practical mode sizes in non-silica soft-glass holey fibres. In order to do this it is necessary to ascertain the structural parameters that result in large-mode-areas, and to determine the subset of these structures that result in single-mode guidance with practical levels of bend loss and low levels of effective nonlinearity. For simplicity, one glass is considered here for one wavelength of transmission: a high index compound soft glass, called Gallium-Lanthanum-Sulphide (GLS) which had a refractive index of 2.37 is considered here at 2.2 μm.

The nonlinear figure of merit in an optical fibre is defined as $\gamma = 2\pi n_2/\lambda A_{\text{eff}}$, where n_2 the nonlinear index coefficient. The typically value of n_2 for silica is $2.6\times10^{-20}\text{m}^2\text{W}^{-1}$, which in conventional single-mode step-index fibre (Corning SMF-28), equates to $\gamma \approx 1\ \text{W}^{-1}\text{km}^{-1}$. The intrinsic nonlinearity of GLS glass is ≈ 100 times that of silica [159]. Consequently, in order for a GLS fibre to have an equivalent level of nonlinearity, an effective area of $\approx 6000\ \mu\text{m}^2$ would be required. This is obviously fairly extreme, and higher values of nonlinearity could be tolerated for short lengths of fibre. For example, for $A_{\text{eff}}^{\text{FM}} = 600\ \mu\text{m}^2$, the nonlinear figure of merit γ, is of the order of 10 $\text{W}^{-1}\text{km}^{-1}$ at 2.2 μm in a GLS fibre. The first step in assessing if GLS glass is a practical material to create holey fibres designed for transmission at 2.2 μm, is therefore to evaluate the types of structures that result in large-mode-areas and investigate the associated bending losses. A brief study of these fibre properties in GLS fibres is presented in Section 7.6.2, using the numerical methods outlined

in Chapter 3.

7.6.2 Practical effective areas in GLS holey fibres

The refractive index of GLS, at 2.37, is significantly larger than that of silica. In addition, the wavelength of transmission studied here, which is 2.2 μm, is much longer than the wavelengths at which silica glass is typically considered. Due to the fact that holey fibre properties, such as mode area and bend loss are sensitive functions of both the fibre structure and the wavelength of operation, it is difficult to gauge the types of structural parameters that will result in large-mode-area, single-mode structures with practical levels of bend loss. In this section, the effective area, modedness and bend loss of a few holey fibre structures are evaluated in order to determine useful holey fibre parameters in GLS glass. These results are presented in Table 7.10.

Table 7.10: Structural parameters and predicted modal properties at 2.2 μm for GLS holey fibres.

Fibre	Λ [μm]	d [μm]	d/Λ	A_{eff}^{FM} [μm^2]	R_c^{FM} [cm]
HF_Q	10.00	4.00	0.40	133	1.6
HF_R	12.00	4.80	0.40	188	2.7
HF_S	15.20	6.08	0.40	293	5.1
HF_T	17.70	7.08	0.40	391	7.7

The results in Table 7.10 shows calculated values of A_{eff}^{FM} and R_c^{FM} at 2.2 μm in GLS holey fibre with $10.0\,\mu m < \Lambda < 17.7\,\mu m$ and $d/\Lambda = 0.4$. The choice of d/Λ results from numerical work performed by Vittoria Finazzi using the multipole method, which shows that GLS holey fibres are single-mode and close to cut-off for $d/\Lambda < 0.4$ at 2.22 μm. The effective mode areas of these fibres range from $\approx 130\ \mu m^2$ for $\Lambda = 10.0\ \mu$m to $\approx 400\ \mu m^2$ for $\Lambda = 17.7\ \mu$m. Note that this is astonishingly similar to the effective areas on would expect in a silica holey fibre with similar parameters at 1064 nm (see Table 5.1 for comparison). This similarity must result from the balance between the influences of the higher refractive index, which results in a smaller mode that is more confined to the glass core, and the longer wavelength, which acts to increases the mode size. However, while the values of A_{eff}^{FM} are almost identical, the bending losses are lower in GLS, as a result of the higher index contrast between the air/glass regions. For the range of fibres considered here, in which $130\,\mu m^2 \lesssim A_{eff}^{FM} \lesssim 400\,\mu m^2$, 1.6 cm$< R_c^{FM} <$ 7.7 cm. This represents values of R_c^{FM} that are,

on average, $\approx 60\%$ of those for similarly sized silica holey fibres at 1064 nm. In other words, in a GLS holey fibre at 2.2 μm, the effective mode area can be ≈ 1.3 times larger than that of a silica holey fibre at 1064 nm for a similar value of R_c^{FM}. Recall that in Section 5.5.2, it was shown that an $A_{eff}^{FM} = 450$ μm^2 represented the largest practical mode area that could be achieved in a single-mode silica holey fibre at 1064 nm (practical mode area defined for $R_c^{FM} < 15$ cm). Consequently, it can be seen that mode areas up to ≈ 600 μm^2 should be practical, in terms of bend loss in single-mode GLS holey fibres. Note that for $d/\Lambda = 0.4$ mode areas of ≈ 600 μm^2 can be created using $\Lambda \approx 21 - 22$ μm.

7.7 Conclusion

Although holey fibres can be endlessly single-mode, the wavelength range of useful operation is limited by the fact that the bending losses worsen towards short wavelengths. This will have the greatest impact on fibres designed for UV transmission, which represents the shortest wavelengths that are transparent in silica. In the sections above, I have demonstrated that the bending losses at 308 nm are not prohibitive for holey fibres with $A_{eff}^{FM} \approx 80$ μm^2 and that the maximum tolerable A_{eff}^{FM} (defined for $R_c^{FM} = 15$ cm) increases steadily with wavelength from ≈ 80 μm^2 at 308 nm to $\lesssim 650$ μm^2 at 1550 nm. In addition, the numerical results presented in the above sections show that for all wavelengths, optimal bending losses in large-mode single-mode holey fibres are achieved by using the largest value of d/Λ that results in single-mode guidance ($d/\Lambda \approx 0.4$).

The numerical work presented in this chapter also demonstrates that although the bending losses and the modedness of holey and step-index fibres are very different as a function of wavelength, the performance of single-mode holey and conventional step-index fibres, in terms of mode area and bend loss, are similar at any given wavelength. However, holey fibres possess an advantage for broadband applications due to the property of endlessly single-mode guidance. In addition, unlike conventional fibres, which require dopants to create guidance, holey fibres can be single-material structures, which may be beneficial from a power handling perspective.

In Section 7.3, experimental results presented from a series of bend loss measurements made on a selection of holey fibres using a white-light source are used to infer information regarding both the bend loss and the modedness of single and multi-mode holey fibres as a function of wavelength. These results demonstrate that a multi-mode holey fibre can possess greater bending losses than a single-mode holey fibre with a similar A_{eff}^{FM} towards

short wavelengths. In addition, comparison between the measured and predicted values of R_c^{FM} for a range of wavelengths demonstrates that the numerical methods developed here can be used to accurately predict the bending losses of holey fibres as a function of wavelength. Furthermore, it is shown in Section 7.4 that R_c^{FM} is essentially scale invariant and a scaling approach can be used to form accurate predictions of this parameter. As a result, the contour plot of $A_{eff}^{FM}/(\lambda^2)$ and R_c^{FM}/λ presented in Fig. 7.14 is shown to be an invaluable design tool and enables basic fibre properties to be determined at-a-glance for $6.6 \lesssim \Lambda/\lambda < 18.8$ and $0.2 < d/\Lambda < 0.5$.

One interesting thing to note from the experimental observation of bend loss as a function of wavelength in the holey fibres considered here is that large oscillations in loss with respect to wavelength are consistently not observed. This is in direct contrast to conventional step-index fibres, in which oscillations in bend loss spectra are frequently observed [137, 121, 136, 122]. The oscillations are attributed to the frequency dependence of the coupling between core and cladding modes, and are often explained in terms of the interference between the core modes and 'whispering gallery' modes of the cladding, which are produced by reflection at the cladding/coating interface [137, 122]. In a holey fibre, the cladding/coating interface is different. For example, the microstructured cladding and the fibre coating are generally separated by a region of solid silica. In addition, and perhaps most importantly, the outer boundary of the microstructured cladding region is not well defined and is also typically irregular due to imperfections in the lattice placement of the holes. It is most probable that these factors are responsible for the fact that these oscillations in loss with respect to wavelength are not observed in the holey fibres considered here. The lack of these spectral fluctuations in bend loss observed in holey fibres may have advantages for applications such as wavelength filtering and sensing applications that involve bend induced attenuation.

It has been previously shown that the bending losses of holey fibres can be improved by using three adjacent rods to form the core, as discussed in Chapter 6 [34]. The benefit offered by this $\triangle$HF structure is shown here to improve slightly towards short wavelengths. However, conditions required to maintain single-mode guidance in $\triangle$HFs as a function of wavelength are unknown and require investigation before further work can proceed.

Although the majority of work in this thesis focuses on silica holey fibres, holey fibres can also be made from mid-IR transmitting materials such as tellurite and chalcogenide glasses, also known as soft-glasses [22, 25, 24]. In Section 7.6 of this chapter, the modal

properties of large-mode-area holey fibres made from a high index compound soft glass, called Gallium-Lanthanum-Sulphide (GLS) were briefly considered. The work presented in this section demonstrates that single-mode GLS holey fibres with A_{eff}^{FM} up to 600 μm^2 should be practical structures in terms of bend loss (defined as $R_c^{FM} < 15$ cm). Note that the effective nonlinearity of a GLS fibre with a mode area of 600 μm^2 is of the order of 10 $W^{-1}km^{-1}$, which is approximately 10 times that of conventional single-mode fibre. Depending on the application, this may prove a suitable level of nonlinearity, but for high powers a multi-mode solution may well be necessary in order to minimise nonlinear effects. Note that this estimation is based on a very crude (wavelength independent) estimate of the nonlinearity of GLS, a factor which is likely to be strongly wavelength dependent.

Chapter 8

Conclusion

In high power fibre applications, large mode areas are required in order to avoid damage to the fibre and to minimise nonlinear effects that would otherwise distort the signal. Holey fibre technology presents an attractive alternative to conventional technology, due to the fact that it is possible to create extremely large-mode-area fibres that are single-mode over a broad wavelength range. In a silica holey fibre, the condition of endlessly single-mode guidance ($d/\Lambda \lesssim 0.4$) is essentially scale invariant [4, 30], which offers huge potential in the large-mode-area single-mode regime. However, as with any fibre, the macro-bending losses place a fundamental upper limit on the mode sizes that are practical to use and are therefore an important consideration in the design of large-mode-area holey fibres. At the start of this project in July 2000, knowledge of the factors that influence bend loss in holey fibres was limited and there had been little development towards theoretical techniques that could be used to accurately predict these losses. Such techniques are essential for future fibre design and for assessing what benefits holey fibres may offer over their conventional counterparts in the large-mode-area, single-mode regime.

The aims of the study presented here were thus threefold: (1) to develop methods of accurately predicting bend loss that can be applied to both holey and conventional fibres, (2) to use these techniques to explore the potential offered by holey fibres in the large-mode-area, single-mode regime, and (3) to place their performance in context against conventional step-index fibres. In order to fulfil these aims, it is also essential to be able to accurately predict the effective mode area and modedness of both fibre types. Furthermore, reliable methods of characterising the bend loss, the effective mode area and the bending losses of holey and conventional fibres are also essential to enable comparative studies and also to validate the theoretical techniques developed here.

The numerical models and experimental techniques that have been developed as part of this study to characterise large-mode-area holey and conventional fibres are described in detail in Chapter 3 and Chapter 4 respectively and focus on the three key properties required when considering large-mode-area single-mode holey fibres: the effective mode area, the bend loss and the number of modes supported by the fibre. The theoretical approaches to bend loss developed here are adapted from methods designed for conventional waveguides and, importantly, do not assume a circularly symmetric refractive index profile. These methods do, however, require that the core modes (and associated propagation constants) of the straight and bent fibre be known. Here these properties are calculated using the orthogonal function method from Refs [86, 94, 95, 13], as described in Section 1.4.3 and 3.2. In the case of the bent fibre, a well established conformal transformation is applied to the refractive index profile, which allows the mode of the bent fibre to be calculated in the same way. The orthogonal function technique was chosen for this purpose as it is both an efficient and accurate method for evaluating these properties, as discussed in Section 3.1 and references therein. Once the modal fields of the fibre are known, the transition loss is calculated as a splice loss between the mode of the straight fibre and the distorted mode of the bent fibre, as described in Section 3.4. The pure bend loss is calculated by evaluating the fraction of the modal field in the bent fibre that has to travel faster than the local speed of light to negotiate the bend, as described in Section 3.5. These techniques enable the transition losses and the pure bend losses to be evaluated for any holey fibre, using the full refractive index profile, and for any given angular orientation of bend.

The orthogonal function method is also used to evaluate the effective mode area of each fibre considered via numerical integration of the modal fields. The modedness of holey fibres can be evaluated using several techniques, as described in Sections 5.2.3 and 5.9, but the method of choice is a simple analytical formula from Ref. [19], which, via comparison with other techniques used here, has proved to be sufficiently accurate for the purposes of this study. Using these theoretical methods we have demonstrated excellent agreement with experimentally measured values for a range of holey fibre structures over a wide range of wavelengths, as shown in Chapters 4, 5, 6 and 7. Note that the experimental methods developed in Section 4 have also proved to be robust and repeatable measurement techniques. The numerical predictions and experimental results presented in Section 4 demonstrate that transition loss is a small overall contribution to macro-bend loss in a holey fibre. These results also show that the 6-fold symmetry of the holey fibre cladding

does influence the bend loss with respect to the angular orientation of the fibre in the bend, but that this effect is an order of magnitude less than variations that arise as a result of irregularities in the positions of the outermost holes in the fibre cladding.

In Chapter 5, the modal properties of holey fibres are explored at 1064 nm, which represents one of the most widely used wavelengths in laser applications. The range of structural parameters that give rise to single-mode, large-mode-area holey fibres with practical levels of bend loss are evaluated numerically using the techniques from Chapter 3. The effective mode area, bend loss and modedness is evaluated for the following range of fibre parameters: $7.0\,\mu\text{m} < \Lambda < 20.0\,\mu\text{m}$ and $0.2 < d/\Lambda < 0.5$. The results from this study illustrate the trade-offs between mode area and bend loss and show that the maximum tolerable effective mode area in a strictly single-mode holey fibre at 1064 nm is $\approx 450\ \mu\text{m}^2$. In this case, the maximum tolerable mode area is defined by a maximum practical critical bend radius of 15 cm. This upper limit is defined via experimental observations, in which fibres with $\text{R}_\text{c}^\text{FM} \gtrsim 15$ cm are seen to become extremely sensitive to low level vibrations and air-currents in the laboratory environment, exhibiting rapidly fluctuating power levels. In addition, a comparative study between holey and step-index fibres in the large-mode-area single-mode regime at 1064 nm demonstrates that at this particular wavelength, the performance of the two fibre types in terms of mode area and bend loss is similar. Throughout this chapter, experimental results from holey fibres fabricated as part of this study are used to validate the numerical methods and demonstrate that fibres with $\text{A}_\text{eff}^\text{FM}$ up to at least $\approx 430\ \mu\text{m}^2$ at 1064 nm are practical to fabricate.

In Chapter 6, the possibility of improving bend loss in holey fibres at 1064 nm, by using different arrangement of holes in the cladding is explored numerically and experimentally. The numerical results from this section lead to the conclusion that by using three rods in the preform to form a triangular fibre core, the critical bend radius of the fundamental mode can be reduced by $\approx 20\%$. This level of reduction is demonstrated experimentally for a single-mode triangular-core fibre with an effective mode area of $\approx 480\ \mu\text{m}^2$, which possesses a critical bend radius of ≈ 13 cm. Numerical predictions also indicate that the critical bend radius of the fundamental mode in these triangular-core fibres varies by $\approx 6\%$ at 1064 nm as a function of the angular orientation in the bend as a result of the shape of the core and inner cladding. In conventional single-rod holey fibres the predicted variation in the critical bend radius of the fundamental mode with respect to angular orientation is typically less then 1%.

In Chapter 7 the spectral dependence on mode area and bend loss in holey fibres is considered both numerically and experimentally. Although holey fibres can be endlessly single-mode, the wavelength range of useful operation is limited by the fact that the bending losses worsen towards short wavelengths. In this chapter, the numerical results demonstrate that the maximum tolerable A_{eff}^{FM} (defined for $R_c^{FM} = 15$ cm) increases steadily with wavelength from ≈ 80 μm^2 at 308 nm to $\lesssim 650$ μm^2 at 1550 nm. It is also shown, in Section 7.4, that R_c^{FM} is essentially scale invariant and a scaling approach can be used to form accurate predictions of this parameter. The numerical work presented in this chapter also demonstrates that although the bending losses and the modedness of holey and step-index fibres exhibit very different spectral dependencies, the performance of single-mode holey and conventional step-index fibres, in terms of mode area and bend loss, are similar at any given wavelength.

The majority of work in this thesis focuses on silica holey fibres to enable the experimental validation of the numerical techniques developed here. However, holey fibres can also be made from other glasses that offer properties not available in silica glass, such as mid-IR transmission. Such glasses include tellurite and chalcogenide glasses, which are also typically highly nonlinear. As a result, it is important to evaluate whether sufficiently large-mode-areas can be created with these materials in order to reduce nonlinear effects, which are unwanted in transmission applications. The modal properties of large-mode-area holey fibres made from a high index compound soft glass, called Gallium-Lanthanum-Sulphide (GLS) were briefly considered in Section 7.6. The work presented in this section demonstrates that single-mode GLS holey fibres with A_{eff}^{FM} up to 600 μm^2 should be practical structures in terms of bend loss (defined as $R_c^{FM} < 15$ cm). The effective nonlinearity of a GLS fibre with this mode area is approximately 10 times greater than that of conventional single-mode fibre due to the high intrinsic nonlinearity of GLS glass [159]. Depending on the application, this may prove a suitable level of nonlinearity, but for high powers a multi-mode solution may be necessary in order to sufficiently minimise nonlinear effects.

In conclusion, experimental techniques that have enabled robust and repeatable characterisation of the basic components of bend loss in large-mode-area holey fibres have been developed. Numerical techniques of modelling bend loss that retain the full refractive index profile and include the effect of the angular orientation of the cladding have been developed and experimentally validated. Together, these techniques present us with powerful tools that can be used to study the bending losses of any large-mode-area fibre, which is

essential in the task of developing novel holey fibre structures with greater resistance to bending. In this study these techniques have been applied to the problem of understanding the factors that influence bend loss in a holey fibre. They have been used to determine the range of practical structures and mode areas in the wavelength range 308 to 1550 nm and have been used to show that, at any given wavelength, the performance of holey fibres and step-index fibres are similar in terms of effective mode area and bend loss. However, holey fibres possess an obvious advantage for broadband applications due to their unique ability to remain single-mode at all wavelengths. In addition, unlike conventional fibres, which require dopants to create guidance, holey fibres can be single-material structures, which may be beneficial from a power handling perspective.

The research presented in this thesis has also illustrated several areas that warrant further investigation. In Section 4.5, it is demonstrated that holey fibres with an outer region of slightly lower index silica experience lower bending losses than single-material structures. This improvement in bend loss probably results from the same process by which W-fibre profiles in conventional fibres act to improve bend loss [155, 156]. In these structures a depressed cladding region is used to more effectively confine the fibre mode to core, resulting in a lower bend loss. However, numerical predictions of this type of structure, calculated using the bend loss model developed here, do not indicate any improvement in bend loss. This is thought to arise from the fact that the model of bend loss developed here neglects all coupling effects between the various fibre modes. However, more computationally intensive methods such as beam propagation or finite-element methods are capable of evaluating the improvement offered by this approach [123].

In addition, in Sections 5.3.4, 5.4 and 7.3, it is shown that the higher-order modes in multi-mode holey fibres can be removed without perturbing the fundamental mode by bending the fibre. Unfortunately, for the fibres studied here, experimental observations show that $\approx$ 2 dB of power is lost in this process of mode selection, which represents a significant fraction of power in the fibre. However, it may be that this loss can be minimised by reducing the fraction of power coupled into the higher-order modes at launch, and further investigations are necessary in order to determine this. In addition, preliminary numerical work presented in Section 5.7.6 indicates that the process of selectively guiding only the fundamental mode by inducing a bend may be more efficient in step-index fibres. However, this work involves the study of a single holey/conventional fibre pair and obviously requires further investigation before anything more definitive can be inferred. Note that

conventional fibres with a helical core geometry can exhibit preferentially higher bending losses for higher-order modes in the same way as a bent conventional fibre. Holey fibre technology offers an attractive route towards a helical core geometry due to the fact that the process of offsetting the fibre core is simple to achieve during the holey fibre fabrication process. Recent work has also shown that holey fibres can be successfully spun without degrading the cladding structure [58].

The work presented in this thesis also demonstrates that analysis of the conditions for single-mode and endlessly single-mode condition in more general holey fibres structures are required. Numerical results presented in Section 7.5 indicate that holey fibres in which the core is formed by multiple adjacent rods in the preform offer improved bending losses relative to the more traditional single-rod core design, especially in the short wavelength limit. However, the condition for single-mode guidance is not well established for this more complex holey fibre design and it is not known if these multiple-rod designs will exhibit endlessly single-mode guidance. As the number of rods used to form the fibre core is increased, the value of Λ required to create a given core size decreases. In order to maintain single-mode guidance, the value of d/Λ must also decrease due to the fact that the overall scale of the cladding has been effectively reduced relative to the wavelength of light. (This is discussed in detail in Section 6.2.2). In the extreme limit, as the number of rods used approaches infinity, the refractive index profile can be seen to approach the case of a step-index fibre, in which endlessly single-mode guidance is not observed. For example, in a three-rod holey fibre core, the condition of single-mode guidance is met at 1064 nm for $d/\Lambda \lesssim 0.20$. However, numerical results show that this does not hold towards shorter wavelengths and further investigation is required in order to determine if these fibres exhibit endlessly single-mode guidance.

Large-mode-area fibres are required primarily for high power and transmission applications. The study presented here has focused on the practical limits that bend loss imposes on large-mode-area holey fibres designed for single-mode operation. However, in order to fully evaluate the potential offered by large-mode-area holey fibres for high power and transmission applications it is just as important to consider the power handling capabilities of these fibres. Preliminary high power laser tests have shown that large-mode-area holey fibres show good performance in terms of damage for industrial applications [138]. Furthermore, holey fibres can be made from pure silica, which may have benefits in terms of power handling that has yet to be assessed.

Part IV

Appendix

Appendix A

Predicting bend loss

A.1 Derivation of the critical point x_r

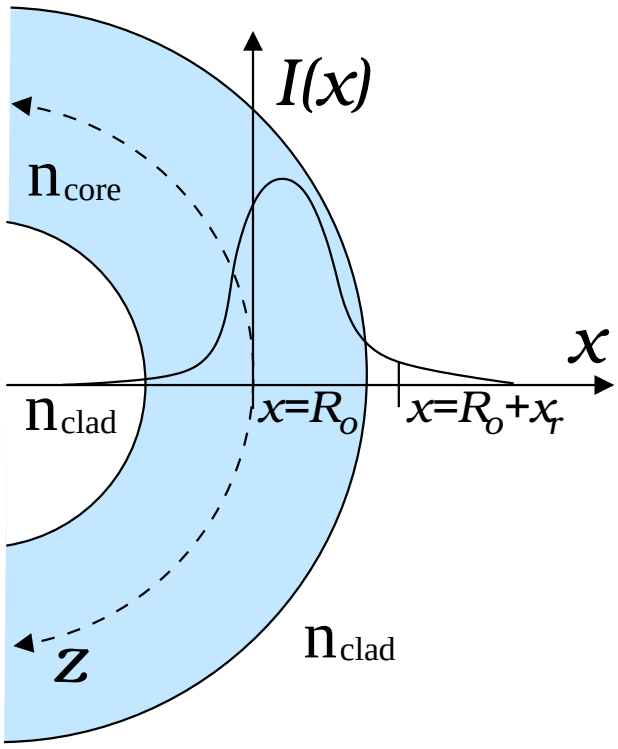

Figure A.1: Sketch of mode propagating in the z direction around a bend of radius R_o in the x direction.

Fig. A.1 shows a sketch of a guided mode propagating along a waveguide with a core index of n_{core} and a cladding index of n_{clad}. The mode is propagating in the z direction around a bend in the x direction with a radius of curvature R_o. For the mode to propagate along a curved trajectory without suffering loss, the angular velocity, Ω, of the modal phase

front must be constant. The angular velocity is given by

$$\Omega = \frac{v}{x}, \tag{A.1}$$

where v is the local velocity of the modal phase front. Consequently, at some distance towards the outside of the bend, defined here to be $x = R_o + x_r$, the required velocity will exceed the local speed of light and the fraction of power at $x > R_o + x_r$ is lost as radiation. (Note that in the bend loss calculation the local coordinate system used defines the centre of the fibre to be $x = 0$, as opposed to the centre of curvature.) At the centre of the mode, $x = R_o$, the velocity of the phase front is defined by the propagation constant of the mode such that

$$v = v_o = \frac{ck}{\beta_b}, \tag{A.2}$$

where c is the velocity of light in free space, β_b is the propagation constant of the bent mode and $k = 2\pi/\lambda$. Since the tails of the mode propagate in the cladding of the fibre, their maximum speed is given by $\mathrm{c/n_{clad}}$, where $\mathrm{n_{clad}}$ is the refractive index of the cladding region. In a holey fibre, the cladding index is assumed to be equal to the effective index of the fundamental space filling mode ($\mathrm{n_{clad}} = \mathrm{n_{FSM}}$). Note that only the $\mathrm{n_{FSM}}$ of the straight fibre is required in this calculation since it is this quantity that represents the maximum (effective) local speed of the microstructured cladding region. The maximum local speed of light for the tails of the mode is thus given by:

$$v_{max} = \frac{c}{\mathrm{n_{clad}}} = \frac{ck}{\beta_{\mathrm{FSM}}} \tag{A.3}$$

where β_{FSM} is the propagation constant of the fundamental mode of the cladding. The value of x_r can then be determined in the following way:

$$\Omega = \frac{v}{x} = \frac{v_o}{R_o} = \frac{v_{max}}{R_o + x_r} \tag{A.4}$$

$$v_{max} R_o = v_o (R_o + x_r) \tag{A.5}$$

$$v_o x_r = R_o (v_{max} - v_o) \tag{A.6}$$

$$x_r = \left(\frac{\beta_b}{\beta_{\mathrm{FSM}}} - 1 \right) R_o \tag{A.7}$$

which is Eq. 3.12.

A.2 Modelling bend loss in holey fibres via an ESI approximation

As discussed in Section 2.3.2, a simple method of modelling bend loss in a holey fibre based on a step-index fibre analogy was proposed in recent months [132]. A comparison of the results obtained using this simple approach with those obtained using the numerical models developed here is presented within this appendix in order to avoid interrupting the flow of the rest of the material presented in this thesis. Note that the simple model proposed in Ref. [132], is described here in some detail in order to highlight the many approximations used and the associated limitations. However, I am keen to stress that this simple approach represents a valuable way of estimating bend loss in large-mode-area holey fibres, and can be reasonably accurate for fibres with relatively large air holes.

In this approach, a simplified formula developed to approximate the pure bend loss of single-mode step-index fibres from Ref. [129] is applied to holey fibres. This simplified formula can be expressed solely in terms of $\mathrm{A}_{\mathrm{eff}}^{\mathrm{FM}}$, R_o, $\mathrm{n_{FM}}$ and $\mathrm{n_{FSM}}$ and the bend loss of a holey fibre can be evaluated without the need to define an ESI refractive index profile. The expression for the pure bend loss attenuation coefficient from Ref. [132] is:

$$\alpha = \frac{\lambda}{8(\sqrt{6\pi})n_{\mathrm{FM}}\mathrm{A}_{\mathrm{eff}}^{\mathrm{FM}}} F\left[\frac{R_o\lambda^2}{6\pi^2 n_{\mathrm{FM}}^2}\left(\frac{V_{\mathrm{PCF}}}{\Lambda}\right)^3\right] \tag{A.8}$$

where

$$F(x) = \frac{exp(-x)}{\sqrt{x}} \tag{A.9}$$

and

$$V_{\mathrm{PCF}} = \frac{2\pi}{\lambda}\Lambda\sqrt{n_{\mathrm{FM}}^2 - n_{\mathrm{FSM}}^2} \tag{A.10}$$

Note that α is expressed in Np/m (see Section 3.5 for definition) and for conversion to dB/m, α should be multiplied by 8.686. The key parameters in the above expressions, $\mathrm{A}_{\mathrm{eff}}^{\mathrm{FM}}$ and $\sqrt{n_{\mathrm{FM}}^2 - n_{\mathrm{FSM}}^2}$, are then approximated by analytical expressions in terms of λ, Λ and d/Λ only. These approximate definitions are based on functions fitted to data generated using a plane-wave approach and can be found in Refs [145] and [161]. The expression for V_{PCF} is given as:

$$V_{\mathrm{PCF}} \approx \frac{\mathcal{A}(d/\Lambda)}{\mathcal{B}(d/\Lambda) \times exp\left[\mathcal{C}(d/\Lambda) \times (\lambda/\Lambda)\right] + 1} \tag{A.11}$$

where

$$\mathcal{A} = d/\Lambda + 0.457 + \frac{3.405(d/\Lambda)}{0.904 - (d/\Lambda)} \tag{A.12}$$

$$\mathcal{B} = 0.200(d/\Lambda) + 0.100 + 0.027(1.045 - d/\Lambda)^{-2.8} \tag{A.13}$$

$$\mathcal{C} = 0.630 \times exp\frac{0.755}{0.171 + (d/\Lambda)} \tag{A.14}$$

For $\lambda/\Lambda < 2$ and $V_{\mathrm{PCF}} > 0.5$ the expression return values of V_{PCF} that deviate $< 3\%$ from values obtained via a plane-wave approach. The expression for $\mathrm{A_{eff}}$ is given as:

$$\mathrm{A_{eff}} = \pi \mathrm{w}^2 \tag{A.15}$$

where

$$w/\Lambda = \frac{A}{V_{\mathrm{PCF}}^{2/(2+g)}} + \frac{B}{V_{\mathrm{PCF}}^{2/3}} + \frac{C}{V_{\mathrm{PCF}}^{6}} \tag{A.16}$$

where $A = 0.7078$, $B = 0.2997$, $C = 0.0037$ and $g = 8$. Maximal deviation between the fit and actual values of $\mathrm{A_{eff}}$ calculated using a plane-wave approach are estimated to be $< 1\%$. Note that the parameter V_{PCF} is defined to be the V-parameter of a holey fibre, with the single-mode condition satisfied for $V_{\mathrm{PCF}} < \pi$. Note also that a fixed value of 1.444 is used for the refractive index of silica, which is necessary in order to preserve the scale invariance of the wave equation. Where $\mathrm{n_{FM}}$ appears on its own in the approximate loss formula shown in Eq.A.8, the assumption $\mathrm{n_{FM}} = \mathrm{n_{glass}}$ is made, which is approximately equivalent in the large-mode-area regime. In this way, all parameters in Eq. A.8 can be determined without the use of complex numerical models and require knowledge of $\mathrm{n_{glass}}$, λ, Λ and d/Λ only.

The results presented within Ref. [132] show good agreement with experimental data for the fibres considered. However, the assumption of $\mathrm{n_{FM}} = \mathrm{n_{glass}}$ is only valid for large values of Λ/λ and d/Λ and leads to increasing inaccuracy as d/Λ decreases in the large-mode-area regime. This is demonstrated here via comparison with some of the numerical results for holey fibres at 1064 nm presented in Section 5.3, which were calculated using the numerical techniques developed in Chapter 3. These results are presented in Table A.1, which lists the fibre parameters and modal properties for a selection of fibres at 1064 nm for which $9.0\,\mu\mathrm{m} < \Lambda < 15.0\,\mu\mathrm{m}$ and $0.2 < d/\Lambda < 0.63$. Each of the fibres in this selection has $\mathrm{A_{eff}^{FM}} \approx 190\ \mu\mathrm{m}^2$ at 1064 nm. The modedness of each of these fibres, calculated using the multipole method by Vittoria Finazzi [54], is indicted by the column labelled 'modes', where SM indicates a single-mode fibre and MM indicates a multi-mode structure (see Section 5.3 for more details). Properties labelled with [132] indicate values calculated using the simplified method from Ref. [132]. All other results presented are calculated using the numerical methods for holey fibres from Chapter 3. Note that the methods from Chapter 3 have been validated against experimental measurements (see Sections 4.5, 5.4, 5.6 and 7.3.3), and have been shown to be capable of accurate predictions. A comparison between

these methods is best made graphically, as shown in Fig. A.2, which is discussed in the following.

Table A.1: Calculated modal properties for a range of holey fibre structures. SM indicates a single-mode fibre and MM indicates a multi-mode structure, evaluated by Vittoria Finazzi using the multipole method. ^{FM} refers to a property of the fundamental mode. $^{[132]}$ refers to a calculation using the method from Ref. [132].

Fibre	Λ [μm]	d [μm]	d/Λ	A_{eff}^{FM} [μm^2]	R_c^{FM} [cm]	Modes	$A_{eff}^{FM\ [132]}$ [μm^2]	$R_c^{FM\ [132]}$ [cm]	$V_{PCF}^{[132]}$
HF_A	9.00	1.80	0.20	190	12.2	SM	207	22.6	1.23
HF_B	10.70	3.04	0.28	190	7.7	SM	207	11.0	1.66
HF_C	11.30	3.84	0.34	190	5.9	SM	196	6.4	1.77
HF_D	12.00	4.80	0.40	188	4.4	SM	192	3.7	2.17
HF_E	12.20	5.09	0.42	187	4.0	SM	191	3.1	2.66
HF_F	12.56	5.53	0.44	189	3.7	MM	192	2.6	2.72
HF_G	12.70	5.73	0.45	188	3.6	MM	193	2.4	2.81
HF_H	13.40	6.70	0.50	190	3.0	MM	195	1.5	3.68
HF_I	15.00	9.46	0.63	189	1.8	MM	195	0.37	5.53

In Fig. A.2, the critical bend radii from Table A.1 (R_c^{FM}) are plotted as a function of d/Λ. The closed circles represent the values of R_c^{FM} calculated using the methods developed in Chapter 3, while the open circles represent values calculated using the simplified expression from Ref. [132], shown in Eq. A.8 above. Fitted curves to these values of R_c^{FM} are drawn to guide the eye. The vertical straight lines mark the predicted cut-off position at which the fibres change from being single-mode to multi-mode structures. The solid straight line marks the position of $d/\Lambda = 0.43$, evaluated in Section 5.3. The dashed straight line represents the predicted cut-off calculated using the condition $V_{PCF} = \pi$ from Ref. [132]. Note that the definition of $V_{PCF} = \pi$ for cut-off in a holey fibre overestimates the value of d/Λ for which a holey fibre remains single-mode. This graph also shows that the simplified method from Ref. [132] can be used to approximate the R_c^{FM} of holey fibre with fair accuracy for large-mode-area holey fibres with large air holes ($d/\Lambda \gtrsim 0.35$), although the overall loss is, in general, underestimated in this regime. However, for smaller hole sizes, this method becomes increasingly inaccurate. This may result from the fact that the approximation $n_{FM} = n_{glass}$ becomes increasingly invalid for fibres with small values d/Λ due to the

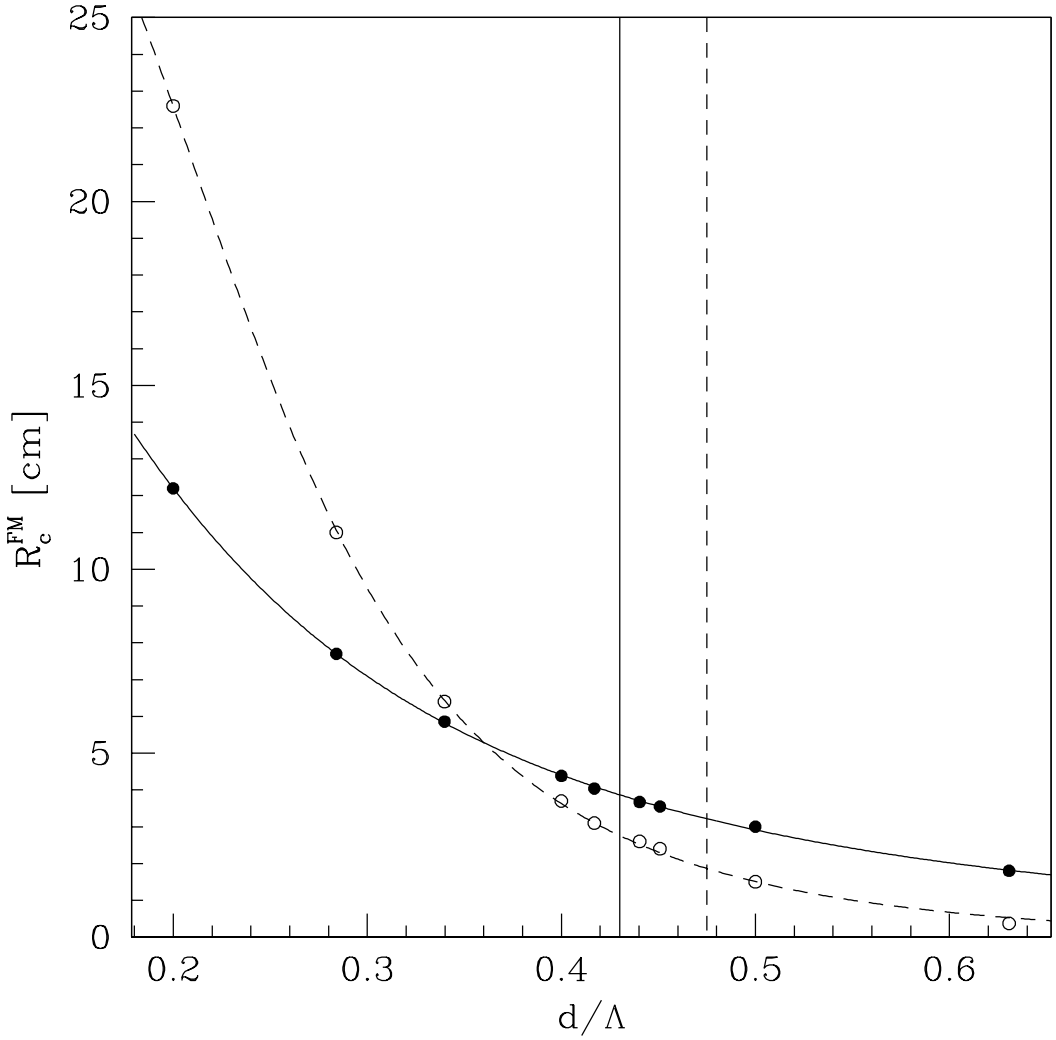

Figure A.2: Critical bend radius of the fundamental mode (R_c^{FM}) as a function of d/Λ at 1064 nm. The points represent the values of R_c^{FM} for the fibres listed in Table A.1, all of which possess $A_{eff}^{FM} \approx 190\ \mu m^2$. The closed circles represent the values of R_c^{FM} calculated using the methods developed in Chapter 3, while the open circles represent values calculated using the simplified expression from Ref. [132], shown in Eq. A.8 above. Fitted curves to these values of R_c^{FM} are drawn to guide the eye. The vertical straight lines mark the predicted cut-off position at which the fibres change from being single-mode to multi-mode structures. The solid straight line marks the position of $d/\Lambda = 0.43$, evaluated in Section 5.3. The dashed straight line represents the predicted cut-off calculated using the condition $V_{PCF} = \pi$ from Ref. [132]

fact that the mode can extend further into the cladding region, lowering n_{FSM}. However, one may expect this approximation to underestimate the losses, due to the fact that the assumption of $n_{FM} = n_{glass}$ results in an overestimated NA in the small d/Λ limit. Indeed, this method contains many approximations, and it is therefore difficult to determine which of these may contribute in what way to inaccuracy of the final result.

In addition, and as discussed in Section 2.3.2, this simplified method is restricted solely to holey fibres with a perfect triangular arrangement of air holes in which the core is formed by the omission of a single hole. This is a significant disadvantage since holey fibre geometry can vary significantly from this basic design, as illustrated in Fig. 1.6 in Section 1.2.4, including different air/glass geometries in addition to hybrid and solid holey fibre types. Furthermore, due to the approximations present in the original formula from Ref. [129], this method ignores the symmetry differences between holey and step-index fibres: holey fibres typically possess a 6-fold symmetric cladding geometry, but can be more complex, such as the case of a triangular core formed by three adjacent rods in the preform [34]. Indeed, the methods developed here, in which the full complex refractive index profile of a holey fibre can be taken into account, predict an angular variation of $\approx 6\%$ in R_c^{FM} for the triangular core holey fibres. Furthermore, since this technique is based on a formula derived for single-mode step-index fibres it cannot be used to evaluate the bending losses associated with higher-order modes. In Sections 5.13 and 5.4, the influence of the bending losses of higher-order modes present in multi-mode holey fibres is assessed using the techniques presented in Chapter 3. It was demonstrated that for $d/\Lambda > 0.5$, the bending losses of higher-order modes can have a significant influence on the overall bending losses of the fibre and so must be considered. However, the simplified method described here has the virtues of being both quick and simple to evaluate and is accurate enough to gauge the practicalities of large-mode-area fibre design for simple triangular lattice geometries close to cut-off.

Appendix B

Fibres studied experimentally

B.1 Introduction

This appendix contains details of the structural parameters (Λ and d/Λ), A_{eff}^{FM} and R_c of all the single-rod holey fibres studied experimentally within the research reported in this thesis. In case where these fibres have also been studied theoretically, the predicted values of A_{eff}^{FM} and R_c^{FM} are also included. Note that predicted values correspond to the fundamental mode only.

B.2 Summary of measurements

Table B.1: Structural parameters, fundamental mode area (A_{eff}^{FM}) and critical bend radius (R_c) for the endlessly single-mode holey fibres HF_1 – HF_4. Predicted values are indicated in brackets.

fibre	Λ [μm]	d/Λ	A_{eff}^{FM} [μm^2]	R_c [cm]
HF_1	7.6	0.23	130 (140)	0.21 (0.23)
HF_2	9.7	0.23	215 (212)	0.46 (0.44)
HF_3	11.3	0.24	230 (259)	0.66 (0.58)
HF_4	9.5	0.25	180 (190)	-

Four holey fibres were studied experimentally in Section 4.5; HF_1, HF_2, HF_3 and HF_4. The structural parameters, measured and predicted values for these four fibres are shown in Table B.1. Predicted quantities are indicated in brackets. Note that these four holey fibres were not made from a single-grade of silica. As a result, the modal properties are not

consistent with those of all other holey fibres considered in this study, which are fabricated from pure silica (see Section 4.5 for more details).

Seven holey fibres were studied experimentally in Chapters 5 and 7 and the structural parameters, measured and predicted values for these seven fibres are shown in Table B.2. Predicted quantities are indicated in brackets.

Table B.2: Structural parameters, fundamental mode area (A_{eff}^{FM}) and critical bend radius (R_c) for a selection of pure silica holey fibres studied at 1064 nm. Predicted values are indicated in brackets. * fibre is found to be effectively single-mode at 1064 nm. ** fibre is found to be selectively single-mode for $R_o \lesssim 7$ cm at 1064 nm.

Fibre	Λ [μm]	d/Λ	A_{eff}^{FM} [μm^2]	R_c [cm]	Modes
F334Zeop	11.7	0.33	200 (210)	7.1 (7.2)	SM
F334Zsop	11.9	0.45	165 (170)	3.3 (3.0)	MM*
F334Ysop	12.6	0.51	165 (170)	< 2	MM*
F200D1	12.1	0.34	215 (220)	6.9 (6.8)	SM
F200B2	13.8	0.51	195 (210)	< 2	MM**
F409Ysop	15.4	0.46	270 (270)	≈ 5 (5.5)	MM*
F437Zeop	19.6	0.44	430 (440)	≈ 12 (12.0)	MM*

The bend loss of five of the fibres in Table B.2 was also measured as a function of wavelength using a white light source. These five fibres are F334Zeop, F334Zsop, F334Ysop, F200D1 and F409Ysop. The results of these white light measurements can be found in Sections 7.3 and 7.4 and are also summarised here in Fig. B.1. Fig. B.1 shows contour plots of predicted values of $A_{eff}^{FM}/(\lambda^2)$ and R_c^{FM}/λ as a function of Λ/λ and d/Λ (assuming scale invariance, as discussed in Section 7.4). Each solid circle in Fig. B.1 represents a value of R_c^{FM} that has been extracted from measurements of bend loss made on the seven fibres listed in Table B.2 (including those measured with a white source of illumination).

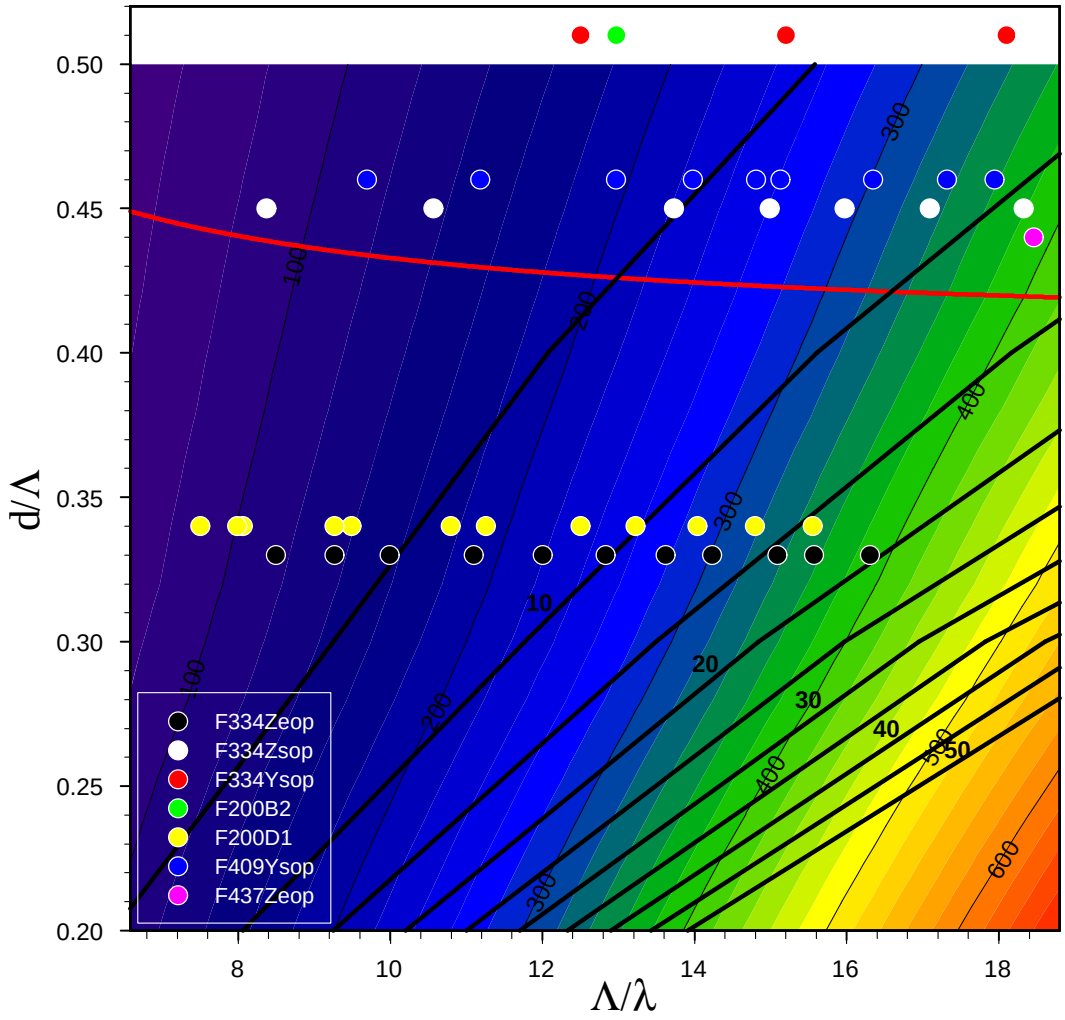

Figure B.1: Contour plots from which predicted values of the fibre parameters A_{eff}^{FM}, R_c^{FM} and moded-ness can be extracted as a function of Λ/λ and d/Λ (assuming scale invariance). The colour contour lines show predicted values of A_{eff}^{FM}/λ^2. The solid black contour lines represent predicted values of R_c^{FM}/λ and the solid red line indicates the predicted single-mode/multi-mode cut-off. The filled circles indicate the range of holey fibres and wavelengths that have been characterised experimentally as part of the research presented within this thesis. The structural parameters of these holey fibres are listed in Table 7.8.

Appendix C

Properties of Silica

C.1 Refractive index

The refractive index of silica glass varies with wavelength. This property is referred to a chromatic dispersion and, on a fundamental level, originates from the resonance frequencies at which the silica absorbs light through oscillations of bound electrons. Far from these resonances, the refractive index of silica is well approximated by the Sellmeier equation:

$$\mathrm{n_{silica}} = 1 + \sum_{\mathrm{j=1}}^{\mathrm{m}} \frac{\mathrm{B_j}\omega_{\mathrm{j}}^2}{\omega_{\mathrm{J}}^2 - \omega^2} \tag{C.1}$$

where ω_j is the resonance frequency and B_j is the strength of the jth resonance. The parameters ω_j and B_j are found experimentally by fitting the measured dispersion curve to Eq. C.1 with m=3. For bulk fused silica these parameters are found to be $B_1 = 0.6961663$, $B_2 = 0.4079426$, $B_3 = 0.8974794$, $\lambda_1 = 0.0684043$, $\lambda_2 = 0.1162414$, and $\lambda_3 = 9.896161$, where $\lambda_j = 2\pi c/\omega_j$ and c is the speed of light in vacuum. The refractive index of fused silica as determined by this equation with these parameters is shown in Fig. C.1. These represent the values used in all calculations within this thesis.

C.2 Attenuation

Theoretical minimum loss in silica glass is bounded by Rayleigh scattering in the short wavelength limit and infrared absorption in the long wavelength limit. In addition, large peaks in the absorption spectrum of silica glass are also observed due to OH contamination. The following two figures show typical attenuation for two types of silica glass as a function of wavelength taken from Ref. [157, 158]. Fig. C.2, corresponds to F300 synthetic silica

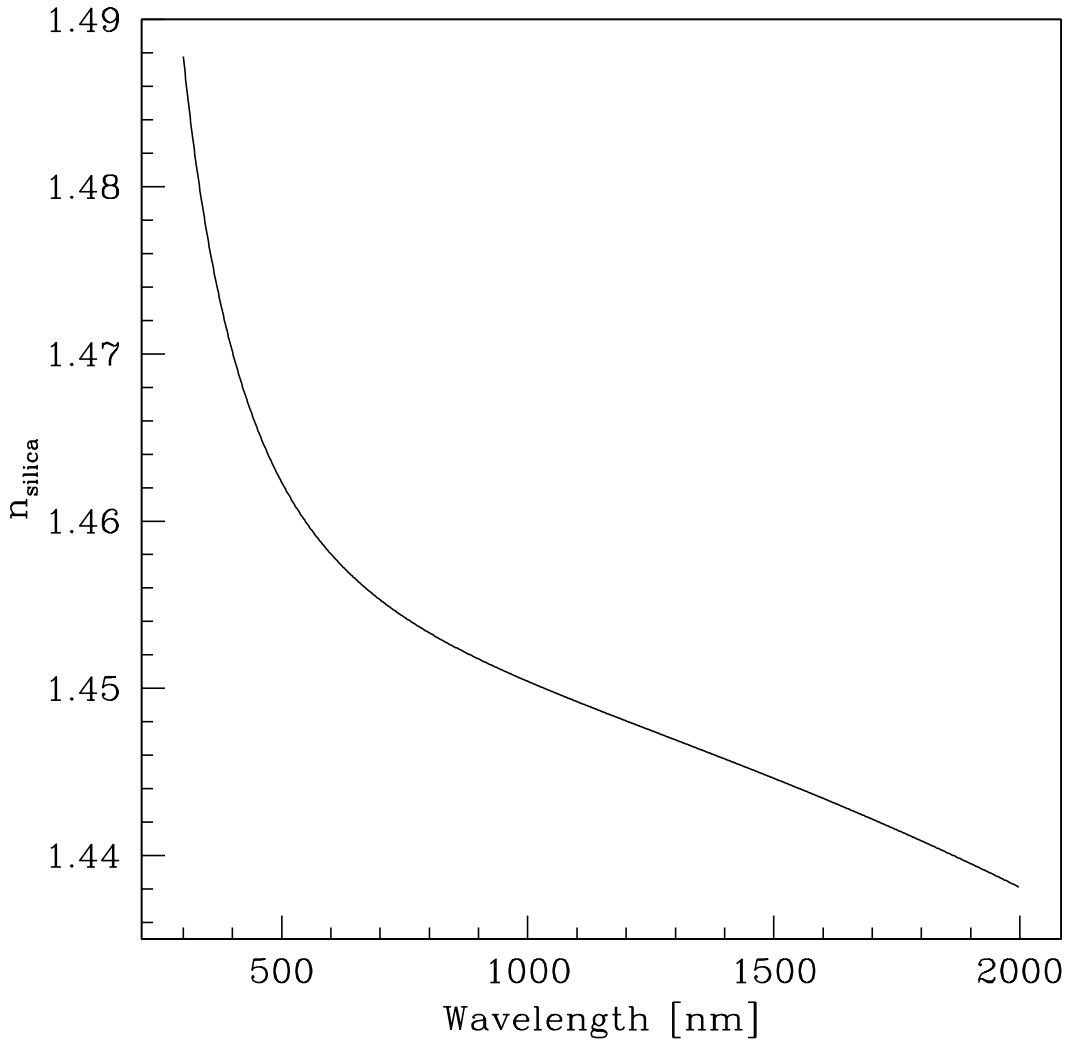

Figure C.1: Variation the refractive index of fused silica as a function of wavelength as described by Eq. C.1.

glass from Heraeus Tenevo AG, which is used to make the holey fibres included in this study. Fig. C.3, corresponds to F100 synthetic silica glass from Heraeus Tenevo AG, which has a higher OH content and lower loss in the short wavelength limit.

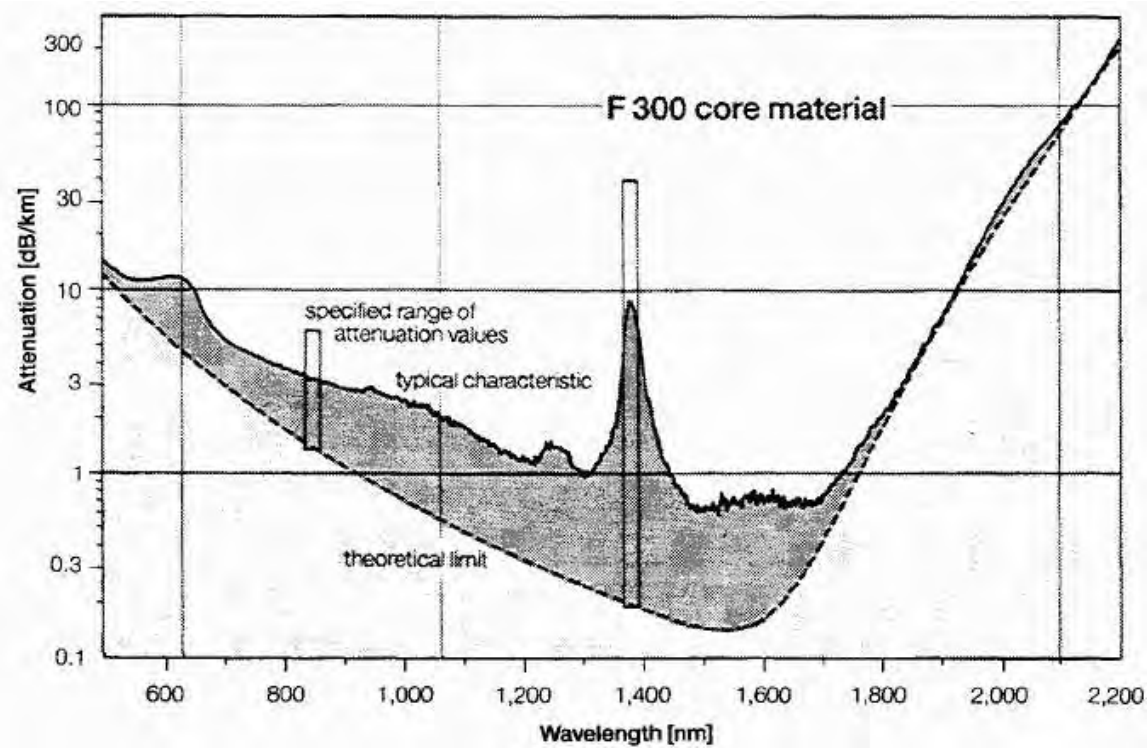

Figure C.2: Typical attenuation for F300 synthetic silica glass from Heraeus Tenevo AG taken from Ref. [157].

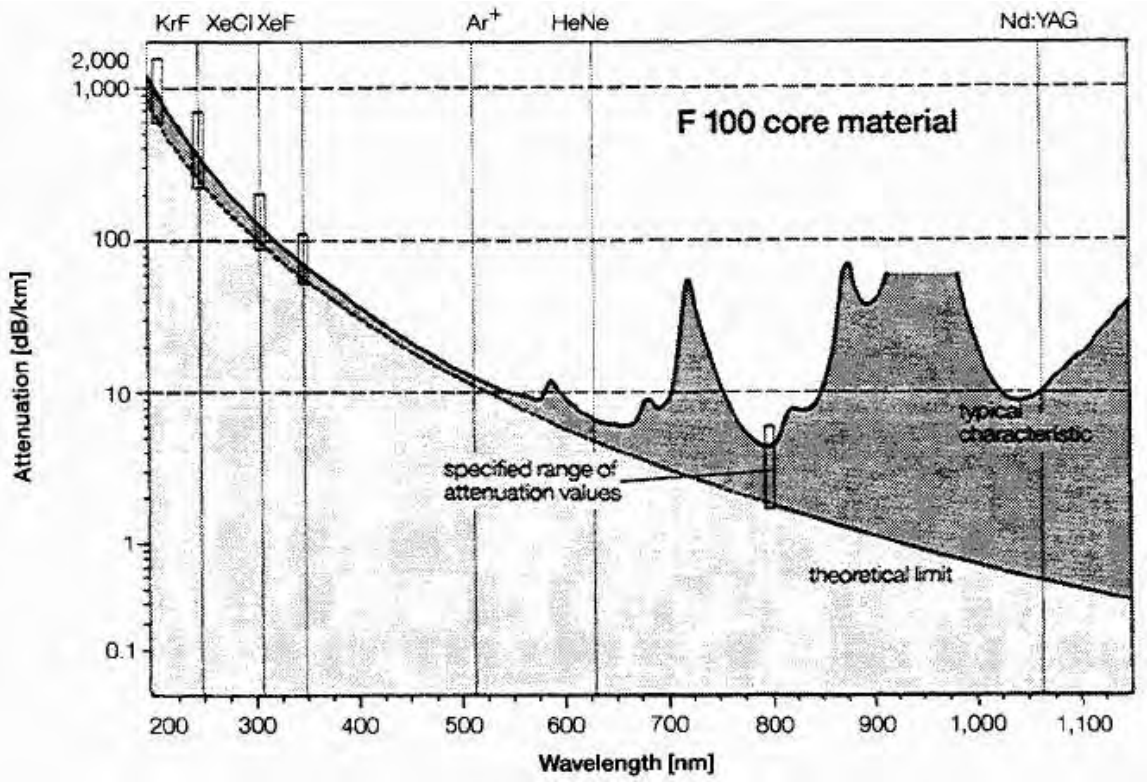

Figure C.3: Typical attenuation for F100 synthetic silica glass from Heraeus Tenevo AG taken from Ref. [157].

Bibliography

[1] P Kaiser, E. A. J. Marcatili, and S. E. Miller. A new optical fiber. *Bell Sys. Tech. J.*, 52:265–269, 1973.

[2] P. Kaiser and H. W. Astle. Low-loss single-material fibres made from pure fused silica. *Bell Syst. Tech. J.*, 54:1021–1039, 1974.

[3] J. C. Knight, T. A. Birks, P. St. J. Russell, and D. M. Atkin. All-silica single-mode optical fiber with photonic crystal cladding. *Opt. Lett.*, 21:1547–1549, 1996.

[4] T. A. Birks, J. C. Knight, and P. St. J. Russell. Endlessly single-mode photonic crystal fiber. *Opt. Lett.*, 22:961–963, 1997.

[5] T. A. Birks, D. Mogilevtsev, J. C. Knight, and P. St. J. Russell. Dispersion compensation using single material fibers. *IEEE Photon. Tech. Lett*, 11:674–676, 1999.

[6] D. Mogilevtsev, T. A. Birks, and J. Russell, P. St. Group-velocity dispersion in photonic crystal fibers. *Opt. Lett.*, 23:1662–1664, 1998.

[7] J. C. Knight, J. Arriaga, T. A. Birks, A. Ortigosa-Blanch, J. W. Wadsworth, and P. St. J. Russell. Anomalous dispersion in photonic crystal fiber. *IEEE Photon. Tech. Lett.*, 12:807–809, 2000.

[8] A. Ferrando, E. Silvestre, J.J. Miret, J.A. Monsoriu, M. V. Andres, and P. St. J Russell. Designing a photonic crystal fibre with flattened chromatic dispersion. *Electron. Lett.*, 35:325–327, 1999.

[9] P. Petropoulos, T. M. Monro, W. Belardi, K. Furusawa, J. H. Lee, and Richardson D. J. 2R-regenerative all-optical switch based on a highly nonlinear holey fiber. *Opt. Lett.*, 26:1233–1235, 2001.

[10] M. D. Nielsen, J. R. Folkenberg, and N. A. Mortensen. Single-mode photonic crystal fiber with an effective area of 600 square-microns and low bending loss. *Electron. Lett.*, 39:1802–1803, 2003.

[11] T. A. Birks, P. J. Roberts, P. St. J. Russell, D. M. Atkin, and T. J. Shepherd. Full 2-D photonic bandgaps in silica/air structures. *Electron. Lett.*, 31:1941–1943, 1995.

[12] R. F. Cregan, B. J. Mangan, J. C. Knight, T. A. Birks, P. St. J. Russell, P. J. Roberts, and D. C. Allan. Single-mode photonic band gap guidance of light in air. *Science*, 285:1537–1539, 1999.

[13] T. M. Monro, P. J. Bennett, N. G. R. Broderick, and D. J. Richardson. Holey fibres with random cladding distributions. *Opt. Lett.*, 25:206–208, 2000.

[14] Z. Zhu and T. G. Brown. Analysis of the space filling modes of photonic crystal fibers. *Opt. Express*, 8:547–554, 2001. http://www.opticsexpress.org/abstract.cfm?URI=OPEX-8-10-547.

[15] Michele Midrio, Mukesh P. Singh, and Carlo G. Someda. The space filling mode of holey fibers: an analytical vectorial solution. *J. Lightw. Tech.*, 18:1031–1037, 2000.

[16] J. Broeng, D. Mogilevstev, S. E. Barkou, and A. Bjarklev. Photonic crystal fibers: A new class of optical waveguides. *Opt. Fiber Tech.*, 5:305–330, 1999.

[17] N. A. Mortensen. Effective area of photonic crystal fibers. *Opt. Express*, 10:341–348, 2002. http://www.opticsexpress.org/abstract.cfm?URI=OPEX-10-7-341.

[18] T. A. Birks, D. Mogilevtsev, J. C. Knight, P. St. J. Russell, J. Broeng, P. J. Roberts, J. Atal, F. West, D. C. Allan, and J. C. Fajardo. The analogy between photonic crystal fibres and step index fibres. In *Optical Fiber Communication Conference*, volume 4, pages 114–116. OFC'99, San Diego, California, 1999. Paper FG4.

[19] B. T. Kuhlmey, R. C. McPhedran, and C.M. de Sterke. Modal cutoff in microstructured optical fibres. *Opt. Lett.*, 27:1684–1686, 2002.

[20] K. Tajima, M. Ohashi, K. Shiraki, T. Tatede, and S. S. Shibata. Low rayliegh scattering P_2O_5–F–SiO_2 glasses. *J. Lightw. Tech.*, 10:1532–1535, 1992.

[21] K. Tajima, J. Zhou, K. Kurokawa, and K. Nakajima. Low water peak photonic crystal fibers. In Italy ECOC 2003, Rimini, editor, *29 th European conference on optical communication*, pages 42–43. postdealine paper Th4.1.6, 2003.

[22] T. M. Monro, Y. D. West, D. W. Hewak, N. G. R. Broderick, and D. J. Richardson. Chalcogenide holey fibres. *Electron. Lett.*, 36:1998–2000, 2000.

[23] T. M. Monro, K. M. Kiang, J. H. Lee, K. Frampton, Z. Yusoff, R. Moore, J. Tucknott, D. W. Hewak, H. N. Rutt, and D. J. Richardson. High nonlinearity extruded single-mode holey optical fibres. In *Optical Fiber Communications conference*, page FA1. OFC 2002, Anahiem, CA 19-21 March 2002, 2002. Postdeadline paper.

[24] K. M. Kiang, K. Frampton, T. M. Monro, R. Moore, J. Tucknott, D. W. Hewak, D. J. Richardson, and H. N Rutt. Extruded single-mode non-silica glass holey optical fibres. *Electron. Lett.*, 38:546–547, 2002.

[25] V. R. K. Kumar, A. K. George, W. H. Reeves, J. C. Knight, P. St. J. Russell, F. G. Omenetto, and A. J. Taylor. Extruded soft glass photonic crystal fiber for ultrabroad supercontinuum generation. *Opt. Express*, 10:1520–1525, 2002. http://www.opticsexpress.org/abstract.cfm?URI=OPEX-10-25-1520.

[26] V. R. K. Kumar, A. K. George, J. C. Knight, and P. St. J. Russell. Tellurite photonic crystal fiber. *Opt. Express*, 11:2641–2645, 2003. http://www.opticsexpress.org/abstract.cfm?URI=OPEX-11-20-2641.

[27] K. Furusawa, A. N. Malinowski, J. H. Price, T. M. Monro, J. K. Sahu, J. Nilsson, and D. J. Richardson. Cladding pumped ytterbium-doped fiber laser with holey inner and outer cladding. *Opt. Express*, 9:714–720, 2001. http://www.opticsexpress.org/abstract.cfm?URI=OPEX-9-13-714.

[28] D. B. S. Soh, C. Codemard, J. K. Sahu, J. Nilsson, S. Baek, S. Wang, and F. Laurell. 18-mW 488.7 nm cw-frequency doubled fiber MOPA source. In *Photonics West 2004, San Jose, CA 26-28 January 2004*, Proceedings of SPIE, pages 5335–10, 2004. http://www.spioptics.com/Tech_Papers/Frequency-doubled%20980%20nm%20MOPA%20.pdf.

[29] K. Furusawa, T. M. Monro, P. Petropoulos, and D. J. Richardson. A mode-locked laser based on ytterbium doped holey fiber. *Electron. Lett.*, 37:560–561, 2001.

[30] J.C. Knight, T.A. Birks, R.F. Cregan, P. St. J. Russell, and J. P. de Sandro. Large mode area photonic crystal fiber. *Electron. Lett.*, 34:1346–1347, 1998.

[31] J. C. Baggett, T. M. Monro, K. Furusawa, and D. J. Richardson. Comparative study of bend loss in large mode holey and conventional fibers. *Opt. Lett.*, 26:1045–1047, 2001.

[32] T. Sorensen, J. Broeng, A. Bjarklev, E. Knudsen, S. E. Barkou, and S. E. B. Libori. Macro-bending loss properties of photonic crystal fiber. *Electron. Lett.*, 37:287–289, 2001.

[33] B. J. Mangan, J. C. Knight, T. A. Birks, and P. St. J. Russell. Experimental study of dual-core photonic crystal fibre. *Electron. Lett.*, 36:1358–1359, 2000.

[34] N. A. Mortensen, M. D. Nielsen, J. R. Folkenberg, A. Petersson, and H. R. Simonsen. Improved large-mode-area endlessly single-mode photonic crystal fibers. *Opt. Lett*, 28:393–395, 2003.

[35] J. Limpert, T. Schreiber, S. Nolte, H. Zellmer, T. Tunnermann, R. Iliew, F. Lederer, J. Broeng, G. Vienne, A. Petersson, and C. Jakobsen. High-power air-clad large-mode-area photonic crystal fiber laser. *Opt. Express*, 11:818–823, 2003. http://www.opticsexpress.org/abstract.cfm?URI=OPEX-11-7-818.

[36] J. Limpert, T. Schreiber, A. Liem, S. Nolte, H. Zellmer, T. Peschel, V. Guyenot, and A. Tünnermann. Thermo-optical properties of air-clad photonic crystal fiber lasers in high power operation. *Opt. Express*, 11:2982–2990, 2003. http://www.opticsexpress.org/abstract.cfm?URI=OPEX-11-22-2982.

[37] J. Limpert, A. Liem, M. Reich, T. Schreiber, S. Nolte, H. Zellmer, A. Tünnermann, J. Broeng, A. Petersson, and C. Jakobsen. Low-nonlinearity single-transverse-mode ytterbium-doped photonic crystal fiber amplifier. *Opt. Express*, 12:1313–1319, 2004. http://www.opticsexpress.org/abstract.cfm?URI=OPEX-12-7-1313.

[38] W. J. Wadsworth, J. C. Knight, W. H. Reeves, and P. St. J. Russell. Yb3+-doped photonic crystal fibre laser. *Electron. Lett.*, 36:1452–1453, 2000.

[39] W. J. Wadsworth, G. Percival, R. M. Bouwmans, J. C. Knight, and P. St. J. Russell. High power air-clad photonic crystal fibre laser. *Opt. Express*, 11:48–53, 2003. http://www.opticsexpress.org/abstract.cfm?URI=OPEX-11-1-48.

[40] N. Platonov, V. P. Gapontsev, O Shkurihin, and I. Zaitsev. 400W low-noise single-mode cw ytterbium fiber laser with an integrated fiber delivery. In *Conference*

on Lasers and Electro-Optics, postdeadline paper, page CThPDB9. CLEO 2003, Washighton, D.C., 2003.

[41] C. A. Codemard, L. M. B. Hickey, K. Yelen, D. B. S. Soh, R. Wixey, M. Coker, M. N. Zervas, and J. Nilsson. 400 mW 1060 nm ytterbium doped fiber DFB laser. In *Photonics West 2004 San Jose 24-29 Jan 2004*, 2004.

[42] J. Limpert, A. Liem, H. Zellmer, and A. Tünnermann. 500 W continuous-wave fibre laser with excellent beam quality. *Electron. Lett.*, 39:645–646, 2003.

[43] J.K. Sahu, C.C. Renaud, K. Furusawa, J.A. Selvas, R. adn Alvarez-Chavez, D.J. Richardson, and J. Nilsson. Jacketed air-clad cladding pumped ytterbium-doped fibre laser with wide tuning range. *Electronics Lett.*, 37:1116–1117, 2001.

[44] T Hasegawa, E. Sasaoka, M. Onishi, M. Nishimura, Y. Tsuji, and M. Koshiba. Hole-assisted lightguide fiber for large anomalous dispersion and low optical loss. *Opt. Express*, 9:681–686, 2001. http://www.opticsexpress.org/abstract.cfm?URI=OPEX-9-13-681.

[45] T. Okuno, M. Onishi, T. Kashiwada, S. Ishikawa, and M. Nishimura. Silica-based functional fibers with enhanced nonlineraity and their applications. *IEEE J. Sel. Top. Quant.*, 5:1385–1391, 1999.

[46] J. H. Lee, W. Belardi, K. Furusawa, P. Petropoulos, Z. Yusoff, T. M. Monro, and D. J. Richardson. Fourwave mixing based 10-Gb/s tunable wavelength conversion using a holey fiber with a high sbs threshold. *IEEE Photon. Technol. Lett.*, 15:440–442, 2003.

[47] T. M. Monro, K. M. Kiang, J. H. Lee, K. Frampton, Z. Yusoff, R. Moore, J. Tucknott, D. W. Hewak, H. N. Rutt, and D. J. Richardson. Extreme nonlinearities in holey fibres.

[48] K. M. Hilligsøe, T. V. Andersen, H. N. Paulsen, C. K. Nielsen, K. Mølmer, S. Keiding, R. Kristiansen, K. P. Hansen, and J. J. Larsen. Supercontinuum generation in a photonic crystal fiber with two zero dispersion wavelengths. *Opt. Express*, 12:2004, 1045-105. http://www.opticsexpress.org/abstract.cfm?URI=OPEX-12-6-1045.

[49] W. J. Wadsworth, J. C. Knight, A. Ortigosa-Blanch, J. Arriaga, E. Silvestre, and P. St. J. Russell. Soliton effects in photonic crystal fibres at 850 nm. *Electron. Lett.*, 36:53–55, 2000.

[50] J. Herrmann, U. Griebner, N. Zhavoronkov, A. Husakou, D. Nickel, J. C. Knight, W. J. Wadsworth, P. St. J. Russell, and G. Korn. Experimental evidence for supercontinuum generation by fission of higher-order solitons in photonic fibers. *Phys. Rev. Lett.*, 88:173901, 2002.

[51] A. V. Husakou and J. Herrmann. Supercontinuum generation, four-wave mixing, and fission of higher-order solitons in photonic-crystal fibers. *J. Opt. Soc. Am. B*, 19:2171–2182, 2002.

[52] J. K. Ranka, R. S. Windeler, and A. J. Stentz. Visible continuum generation in air silica microstructured optical fibers with anomalous dispersion at 800nm. *Opt. Lett.*, 25:25–27, 2000.

[53] Katsunari Okamoto. *Fundamentals of Optical Waveguides*. Academic Press, 1 edition, 2000.

[54] V. Finazzi. *A theoretical study into the fundamental design limits of devices based on one- and two-dimensional structured fibres*. PhD thesis, University of Southampton, Southampton, SO17 1BJ, September 2003.

[55] A. Ortigosa-Blanch, J. C. Knight, W. J. Wadsworth, J. Arriaga, B. J. Mangan, T. A. Birks, and P. St. J. Russell. Highly birefringent photonic crystal fibers. *Opt. Lett.*, 25:1325–1327, 2000.

[56] T. P. Hansen, J. Broeng, S. E. B. Libori, E. Knudsen, A. Bjarklev, J. R. Jensen, and H. Simonsen. Highly birefringent index-guiding photonic crystal fibers. *IEEE Photon. Technol. Lett.*, 13:588–590, 2001.

[57] I. Suzuki, H. Kubota, S. Kawanishi, M. Tanaka, and M. Fujita. Optical properties of a low-loss polarization-maintaining photonic crystal fiber. *Opt. Express*, 9:676–680, 2001. http://www.opticsexpress.org/abstract.cfm?URI=OPEX-9-13-676.

[58] M. Fuochi, J. R. Hayes, K. Furusawa, W. Belardi, J. C. Baggett, T. M. Monro, and D. J. Richardson. Polarization mode dispersion reduction in spun large mode area silica holey fibres. *Opt. Express*, 12:1972–1977, 2004. http://www.opticsexpress.org/abstract.cfm?URI=OPEX-12-9-1972.

[59] J. R. Folkenberg, M. D. Nielsen, N. A. Mortensen, C. Jakobsen, and H. R. Simonsen. Polarization maintaining large mode area photonic crystal fiber. *Opt. Express*, 12:956–960, 2004. http://www.opticsexpress.org/abstract.cfm?URI=OPEX-12-5-956.

[60] T. M. Monro, D. J. Richardson, and P. J. Bennett. Developing holey fibres for evanescent field devices. *Electron. Lett.*, 35:1188–1189, 1999.

[61] Y. L. Hoo, W. Jin, H. L. Ho, D. N. Wang, and R. S. Windeler. Evanescent-wave gas sensing using microstructure fiber. *Optical Engineering*, 41:8–9, 2001.

[62] Y. L. Hoo, W. Jin, H. L. Ho, and D. N. Wang. Measurement of gas diffusion coefficient using photonic crystal fiber. *IEEE Photon. Tech. Lett.*, 15:1434–1436, 2003.

[63] J. C. Baggett, T. M. Monro, W. Belardi, K. Furusawa, and D. J. Richardson. Assorted core air-clad fibre. *Electron. Lett.*, 36:2065–2066, 2000.

[64] X. Feng, A. K. Mairaj, D. W. Hewak, and T. M. Monro. Towards high-index glass based monomode holey fibre with large mode area. *Electron. Lett.*, 40:167–168, 2004.

[65] M. A. van Eijkelenborg, M. C. J. Large, A. Argyros, J. Zagari, S. Manos, N. A. Issa, I. M. Bassett, S. C. Fleming, R. C. McPhedran, C. M. de Sterke, and N. A. P. Nicorovici. Microstructured polymer optical fibre. *Opt. Express*, 9:319–327, 2001. http://www.opticsexpress.org/abstract.cfm?URI=OPEX-9-7-319.

[66] M. A. van Eijkelenborg, A. Argyros, G. Barton, I. M. Bassett, M. Fellew, G. Henry, N. A. Issa, M. C. J. Large, S. Manos, W. Padden, L. Poladian, and J. Zagari. Recent progress in microstructured polymer optical fibre fabrication and characterisation. *Opt. Fiber Tech.*, 9:199–209, 2003.

[67] H. Mehmud, S. Kilinc, T. Kumkum, and F. Kalyani. Polymer optical fibers. In *International Conference for Upcoming Engineers, May 2003*, Raman session papers. Ryerson University, Toronto, Ontario, 2003. http://www.icue.ca/icuexplore/Raman_07.pdf.

[68] B. Temelkuran, S. D. Hart, G. Benoit, J. D. Joannopoulos, and Y. Fink. Wavelength-scalable hollow optical fibres with large photonic bandgaps for co2 laser transmission. *Nature*, 420:650–653, 2002.

[69] X. Feng, T. M. Monro, P. Petropoulos, V. Finazzi, and D. W. Hewak. Solid microstructured optical fiber. *Opt. Express*, 11:2225–2230, 2003. http://www.opticsexpress.org/abstract.cfm?URI=OPEX-11-18-2225.

[70] V. Rastogi and K. S. Chiang. Propagation characteristics of a segmented cladding fiber. *Opt. Lett.*, 26:491–493, 2001.

[71] V. Rastogi and K. S. Chiang. Analysis of segmented cladding fiber by the radial-effective-index method. *J. Opt. Soc. Am. B*, 21:258–265, 2004.

[72] B. J. Eggleton, C. Kerbage, P. Westbrook, R. S. Windeler, and A. Hale. Microstructured optical fiber devices. *Opt. Express*, 9:698–713, 2001. http://www.opticsexpress.org/abstract.cfm?URI=OPEX-9-13-698.

[73] T. T. Larsen, D. S. Hermann, J. Broeng, and A. Bjarklev. A novel photonic crystal fibre switch. In *Conference on Lasers and Electro Optics, Europe*, Postdeadline paper, pages CEP1–9–THU. CLEO/Europe'03, Munich, Germany, 2003.

[74] T. T. Larsen, A. Bjarklev, D. S. Hermann, and J. Broeng. Optical devices based on liquid crystal photonic bandgap fibres. *Opt. Express*, 11:2589–2596, 2003. http://www.opticsexpress.org/abstract.cfm?URI=OPEX-11-20-2589.

[75] T. T. Larsen, D. S. Hermann, J. Broeng, and A Bjarklev. Photonic bandgaps in a photonic crystal fiber filled with a cholesteric liquid crystal. In *Proceedings of the 29 th European Conference on Optical Communication*. ECOC 2003, Rimini, Italy, 2003.

[76] J. Broeng, S. E. Barkou, T. Sndergaard, and A. Bjarklev. Analysis of air-guiding photonic bandgap fibers. *Opt. Lett.*, 25:96–98, 2000.

[77] L. B. Shaw, J. S. Sanghera, I. D. Aggarwal, and F. H. Hung. As-S and As-Se based photonic band gap fiber for ir laser transmission. *Opt. Express*, 11:3455–3460, 2003. http://www.opticsexpress.org/abstract.cfm?URI=OPEX-11-25-3455.

[78] J. A. West, J. C. Fajardo, M. T. Gallagher, K. W. Koch, N. F. Borrelli, and D. C. Allan. Demonstration of an IR-optimized air-core photonic bandgap fiber. In *Proceedings of the 27 th European Conference on Optical Communication*, ECOC 2001, Amsterdam, Netherlands, page Paper ThA2, 2001.

[79] M. Charlene, M. Smith, N. Venkataraman, M. T. Gallagher, D. Müller, J. A. West, N. F. Borrelli, D. C. Allan, and K. W. Koc. Low-loss hollow-core silica/air photonic bandgap fibre. *Nature*, 424:657–659, 2003. doi:10.1038/nature01849.

[80] T. P Hansen, J. Broeng, C. Jakobsen, G. Vienne, H. R. Simonsen, M. D. Nielsen, P. M. W. Skovgaard, J. R. Folkenberg, and A. Bjarklev. Air-guiding photonic bandgap fibers: Spectral properties, macrobending loss, and pracical handling. *J. Lightw. Tech.*, 22:11–15, 2004.

[81] J. C. Knight, J. Broeng, T. A. Birks, and P. St. J. Russell. Photonic band gap guidance in optical fibers. *Science*, 282:1476–1478, 1998.

[82] S. E. Barkou, J. Broeng, and A. Bjarklev. Silica air photonic crystal fiber design that permits waveguiding by a true photonic bandgap effect. *Opt. Lett.*, 24:46–48, 1999.

[83] K. Saitoh, N. A. Mortensen, and M. Koshiba. Air-core photonic band-gap fibers: the impact of surface modes. *Opt. Express*, 12:394–400, 2004. http://www.opticsexpress.org/abstract.cfm?URI=OPEX-12-3-394.

[84] J. A. West, C. M. Smith, N. F. Borrelli, D. C. Allan, and K. W. Koch. Surface modes in air-core photonic band-gap fibers. *Opt. Express*, 12:1485–1496, 2004. http://www.opticsexpress.org/abstract.cfm?URI=OPEX-12-8-1485.

[85] B. Mangan, L. Farr, P. J. Langford, A. Roberts, D. P. Williams, F. Couny, M. Lawman, M. Mason, S. Coupland, R. Flea, H. Sabert, T. A. Birks, J. C. Knight, and J. Russell, P. St. Low loss (1.7 dB/km) hollow core photonic bandgap fiber. In *OSA Trends in Optics and Photonics (TOPS)*, volume 95 of *Optical Fiber Communication Conference, Technical Digest, Postconference Edition*, 2004.

[86] T. M. Monro, D. J. Richardson, N. G. R. Broderick, and P. J. Bennett. Holey optical fibers: an efficient modal model. *J. Lightw. Tech.*, 17:1093–1102, 1999.

[87] J. Rishede, S. B. Libori, A. Bjarklev, J. Broeng, and E. Knudsen. Photonic crystal fibers and effective index approaches. In *Proceedings of the 27 th European Conference on Optical Communications*, page paper Th.A1.5. ECOC 2001, Amsterdam, The Netherlands, 2001.

[88] D. Mogilevtsev, T. A. Birks, and P. St. J. Russell. Dispersion of modes guided in photonic crystal fibres. In *Conference on Lasers and Electro-optics Europe, 1998*, Paper CFB7, pages 349–349. CLEO/Europe 14-18 September 1998, 1998.

[89] D. Mogilevtsev, T. A. Birks, and P. St J. Russell. Group-velocity dispersion in photonic crystal fibres. *Opt. Lett.*, 21:1662–1664, 1998.

[90] E. Silvestre, M. V. Andrés, and P. Andrés. Biorthonormal-basis method for the vector description of optical-fiber modes. *J. Lightw. Tech.*, 16:923–928, 1998.

[91] A. Ferrando, E. Silvestre, J. J. Miret, P. Andrés, and M. V. Andrés. Full-vector analysis of a realistic photonic crystal fiber. *Opt. Lett.*, 24:276–278, 1999.

[92] S. G. Johnson and J. D. Joannopoulos. Block-iterative frequency-domain methods for Maxwell's equations in a planewave basis. *Opt. Express*, 8:173–190, 2001. http://www.opticsexpress.org/abstract.cfm?URI=OPEX-8-3-173.

[93] M. J. Steel, T. P. White, C. M. de Sterke, R. C. McPhedran, and L. C. Botten. Symmetry and degeneracy in microstructured optical fibers. *Opt. Lett.*, 26:488–490, 2001.

[94] T. M. Monro, D. J. Richardson, N. G. R. Broderick, and P. J. Bennett. Modeling large air fraction holey optical fibers. *J. Lightw. Tech.*, 18:50–56, 2000.

[95] T. M. Monro, N. G. R. Broderick, and D. J. Richardson. Exploring the optical properties of holey fibers. In M. Bertolotti, Bowden C. M., and C. Sibilia, editors, *Nanoscale, linear and nonlinear optics, Erice, Sicily*, volume 560 of *AIP conference proceedings*. International School on quantum Electronics, 2000.

[96] P. J. Bennett, T. M. Monro, and D. J. Richardson. Towards practical holey fibre technology: Fabrication splicing modeling and characterization. *Opt. Lett.*, 24:1203–1205, 1999.

[97] B. J. Eggleton, P. S. Westbrook, R. S. Windeler, S. Splter, and T. A. Strasser. Grating resonances in air-silica microstructured optical fibers. *Opt. Lett.*, 24:1460–1462, 1999.

[98] F. Brechet, J. Marcou, D. Pagnoux, and P. Roy. Complete analysis of the characteristics of propagation into photonic crystal fibers, by the finite element method. *Opt. fiber Tech.*, 6:181–191, 2000.

[99] T. P. White, R. C. McPhedran, C.M. de Sterke, L. C. Botten, and M. J. Steel. Confinement losses in microstructured optical fibers. *Opt. Lett.*, 26:1660–1662, 2001.

[100] M. Heiblum and J. H. Harris. Analysis of curved waveguides by conformal transformation. *IEEE J. Quantum Electron.*, QE_11:75–83, 1975.

[101] W. Berglund and A. Gopinath. WKB analysis of bend loss in optical waveguides. *J. Lightw. Tech.*, 18:1161–1166, 2000.

[102] W. A. Gambling, H. Matsumura, and C. M. Ragdale. Field deformation in a curved single-mode fiber. *Electron. Lett.*, 14:130–132, 1978.

[103] A. Snyder and J. Love. *Optical Waveguide Theory.* Chapman and Hall, 1995.

[104] W. A. Gambling, H. Matsumura, and R. A. Sammut. Mode shift at bends in single-mode fibers. *Electron. Lett.*, 13:695–697, 1977.

[105] W. A. Gambling, H. Matsumura, C. M. Ragdale, and R. A. Sammut. Measurement of radiation loss in curved single-mode fibers. *Micro. Opt. and Acoust.*, 2:134–140, 1978.

[106] J. Saijonmaa and D. Yevick. Beam propagation analysis of loss in bent optical waveguides and fibers. *J. Opt. Soc. Am. A*, 73:1785–1791, 1983.

[107] A. J. Harris and P. F. Castle. Bend loss measurements on high numerical aperture small mode fibers as a function of wavelength and radius of curvature. *J. Lightw. Tech.*, 4:34–40, 1986.

[108] J. Yamauchi, M. Ikegaya, and H. Nakano. Analysis of bent step index fibers by the beam propagation method. *IEE Proc. J. Optoelect.*, 139:201–207, 1992.

[109] M. Mirianashvili, K. Ono, and M. Hotta. Coupled mode analysis of loss in single-mode bent optical fibers. *Jpn. J. Appl. Phys.*, 39:1468–1471, 2000.

[110] D. Donlagic and B. Culshaw. Propagation of the fundamental mode in curved graded index multimode fiber and its application in sensor systems. *J. Lightw. Tech.*, 18:334–342, 2000.

[111] W. A. Gambling, H. Matsumura, and C. M. Ragdale. Curvature and microbending losses in single-mode fibers. *Opt. and Quant. Electron.*, 11:43–59, 1979.

[112] http://syllabus.syr.edu/ELE/kdl/Ele682/smf28.PDF.

[113] E. A. J. Marcatili and S. E. Miller. Improved relations describing directional control in electro-magnetic wave guidance. *The Bell Sys. Tech. J.*, pages 2161–2188, September 1969.

[114] D. Marcuse. Influence of curvature on the losses of doubly clad fibers. *Appl. Opt.*, 21:4208–4213, 1982.

[115] D. Marcuse. Field deformation and loss caused by curvature of optical fibres. *J. Opt. Soc. Am. A*, 66:311–320, 1976.

[116] H. Renner. Bending losses of coated single-mode fibers: a simple approach. *J. Lightw. Tech.*, 10:544–551, 1992.

[117] L. Faustini and G. Martini. Bend loss in single-mode fibers. *J. Lightw. Tech.*, 15:671–679, 1997.

[118] R. A. Sammut. Discrete radiation from curved single mode fibres. *Electron. Lett.*, 13:418–419, 1977.

[119] W. A. Gambling, D. N. Payne, and H Matsumura. Radiation from curved single-mode fibres. *Electron. Lett.*, 12:567–569, 1976.

[120] R. A. Sammut. Intensity modulation of light transmitted in a curved optical fibre. *Electron. Lett.*, 13:545–546, 1977.

[121] Y Murakami and H. Tsuchiya. Bend loss of coated single-mode optical fibres. *IEE J. of Quan. Electron.*, 14:495–501, 1978.

[122] R. Morgan, J. D. C. Jones, P. G. Harper, and J. S. Barton. Observation of secondary bend loss oscillations arising from propagation of cladding modes in buffered monomode optical fibres. *Opt. Comm.*, 85:17–20, 1991.

[123] S. Tomljenovic-Hanic, J. D. Love, and A. Ankiewicz. Low-loss singlemode waveguide and fibre bends. *Electron. Lett.*, 38:220–222, 2002.

[124] C. Vassallo. Scalar field theory and 2D ray theory for bent single mode fibres. *J. of Lightw. Tech.*, 3:416–423, 1985.

[125] I. Valiente and C. Vassallo. New formalism for bending losses in coated single mode optical fibres. *Electron. Lett.*, 25:1544–1545, 1989.

[126] D. Marcuse. Curvature loss formula for optical fibers. *J. Opt. Soc. Am. A*, 66:216–220, 1976.

[127] A. B. Sharma, A. H. Al-Ani, and S. J. Halme. Constant-curvature loss in monomode fibers: an experimental investigation. *Appl. Opt.*, 23:3297–3301, 1984.

[128] J. Sakai and T. Kimura. Bending loss propagation in arbitrary-index profile optical fibers. *Appl. Opt.*, 17:1499–1506, 1978.

[129] J. Sakai. Simplified bending loss formula for single-mode optical fibers. *Appl. Opt.*, 18:951952, 1979.

[130] A. W. Snyder, I. White, and D.J. Mitchell. Radiation from bent optical waveguides. *Electron. Lett.*, 11:332–333, 1975.

[131] T. Sorensen, J. Broeng, A. Bjarklev, E. Knudsen, S. E. Barkou, S. E. B. Libori, H. R. Simonsen, and J. R. Jensen. Macrobending loss properties of photonic crystal fibers with different air filling fractions. In *Proceedings of the 27th European Conference on Optical Communications*, page Paper We.L2.4. ECOC 2001, Amsterdam, The Netherlands, 2001.

[132] M. D. Nielsen, N. A. Mortensen, M. Albertsen, J. R. Folkenberg, A. Bjarklev, and D. Bonacinni. Predicting macrobending loss for large-mode area photonic crystal fibers. *Opt. Express*, 12:1775–1779, 2004. http://www.opticsexpress.org/abstract.cfm?URI=OPEX-12-8-1775.

[133] W. A. Gambling and H. Matsumura. Propagation characteristics of curved fibers. *Trans. IECE Japan*, E61:196–201, 1978.

[134] BandSOLVE^{TM} v1.3 RSoft Design Group, Inc., Ossining, NY. http://www.rsoftdesign.com/products/component_design/BandSOLVE/.

[135] Govind P. Agrawal. *Nonlinear Fiber Optics*. Academic Press, 3 edition, 1995.

[136] G. L. Tangonan, H. P. Hsu, V. Jones, and J. Pikulski. Bend loss measurements for small mode field diameter fibres. *Electron. Lett.*, 25:142–143, 1989.

[137] R. Morgan, J. S. Barton, P. G. Harper, and J. D. C. Jones. Wavelength dependence of bending loss in momomode optical fibers: effect of the fiber buffer coating. *Opt. Lett.*, 15:947–949, 1990.

[138] Photonic Crystal Fibre for Industrial Beam Delivery (PFIDEL). OSDA DTI Link Grant, project coordinator BAE Systems.

[139] S. T. Huntington and J. Lyytikainen, K. Canning. Analysis and removal of fracture damage during and subsequent to holey fiber cleaving. *Opt. Express*, 11:535–540, 2003. http://www.opticsexpress.org/abstract.cfm?URI=OPEX-11-6-535.

[140] M. Artilia, G. Coppa, P. Di Vita, M. Potenza, and A. Sharma. Mode field diameter measurements in single-mode optical fibers. *J. Lightw. Tech.*, 7:1139–1152, 1989.

[141] Frank L. Pedrotti and Leno S. Pedrotti. *Introduction to optics.* Prentice hall international editions, 2 edition, 1996. Section 22-5.

[142] B. T. Kuhlmey, R. C. McPhedran, C.M. de Sterke, P. A. Robinson, G. Renversez, and D. Maystre. Microstructured optical fibers: wheres the edge? *Opt. Express*, 10:1285–1290, 2002. http://www.opticsexpress.org/abstract.cfm?URI=OPEX-10-22-1285.

[143] R. Ghosh, A. Kumar, and J. P. Meunier. Waveguiding properties of holey fibres and effective-V model. *Elecron. Lett.*, 35:1873–1875, 1999.

[144] R. Ghosh, A. Kumar, J. P. Meunier, and E. Marin. Modal characteristics of few-mode silica-based photonic crystal fibres. *Opt. Quant. Elecron.*, 32:963–970, 2000.

[145] M. D. Nielsen and N. A. Mortensen. Photonic crystal fiber design based on the V-parameter. *Opt. Express*, 11:2762–2768, 2003. http://www.opticsexpress.org/abstract.cfm?URI=OPEX-11-21-2762.

[146] J. R. Folkenberg, N. A. Mortensen, K. P. Hansen, T. P. Hansen, K. Lyngby, R. Simonsen, and C. Jakobsen. Experimental investigation of cutoff phenomena in nonlinear photonic crystal fibers. *Opt. Lett.*, 28:1882–1884, 2003.

[147] J. C. Knight, T. A. Birks, P. St. J. Russell, and J. P. de Sandro. Properties of photonic crystal fiber and the effective index model. *J. Opt. Soc. Am. A*, 15:748–752, 1998.

[148] A. Ferrando, E. Silvestre, J. J. Miret, P. Andrés, and M. V. Andrés. Vector description of higher-order modes in phoronic crystal fibers. *J. Opt. Soc. Am. A*, 17:1333–1340, 2000.

[149] Jeffrey P. Koplow, Dahv A. V. Kliner, and Lew Goldberg. Single-mode operation of a coiled multimode fiber amplifier. *Opt. Lett.*, 25:442–444, 2000.

[150] P. Webels and C. Fallnich. Highly sensitive beam quality measurements on large-mode-area fiber amplifiers. *Opt. Express*, 11:3346–3351, 2003. http://www.opticsexpress.org/abstract.cfm?URI=OPEX-11-25-3346.

[151] D. Marcuse. Bend loss of slab and fiber modes computed with diffraction theory. *J. Quant. Electron.*, 29:2957–2961, 1993.

[152] A. W. Snyder, I. White, and D. J. Mitchell. Radiation from bent optical waveguides. *Electron. Lett.*, 11:332–333, 1975.

[153] A. L. Deus and H. R. D. Sunak. Design considerations for minimising macrobending loss in erbium-doped fibre amplifiers. *IEEE Photon. Tech. Lett.*, 3:50–52, 1991.

[154] L. E. Busse and I. D. Aggarwal. Design parametrs for fluoride mutlimode fibres. *J. Lightw. Tech.*, 9:828–831, 1991.

[155] A. V. Belov. Profile structure of single-mode fibers with low nonlinear properties for long-haul communication lines. *Opt. Comm.*, 161:212–216, 1999.

[156] V. V. Steblina, J. D. Love, R. H. Stolen, and J. S. Wang. Cladding mode degeneracy in bent W-fibres beyond cutoff. *Opt. Comm.*, 156:271–274, 1998.

[157] http://www.tenevo.com/downloads/ds_sf-datasheets.pdf.

[158] http://www.tenevo.com/downloads/pub_sf-of_uv_ir.pdf.

[159] J. Requejo-Isidro, A. K. Mairaj, V. Pruneri, D.W. Hewak, M.C. Netti, and J. J. Baumberg. Self refractive non-linearities in chalcogenide based glasses. *J. Non-crystal. Solids*, 317:241–246, 2003.

[160] Fibre optics in astronomy III ASP conference series Vol 152 (1998). http://www.tenevo.com/downloads/pub_sf-broadband_spectroscopy.pdf.

[161] M. D. Nielsen, N. A. Mortensen, J. R. Folkenberg, and A. Bjarklev. Mode-field radius of photonic crystal fibers expressed by the V parameter. *Opt. Lett.*, 28:2309–2311, 2003.